博士論文

GIS-based Susceptibility Analysis and SAR-based Detection for the Landslides Triggered in 2018 Hokkaido Eastern Iburi Earthquake

（2018 年北海道胆振東部地震の土砂災害に関する
GIS を用いた危険度評価と SAR を用いた検出に関する研究）

by
葛 平兰
へ ピンラン

A Dissertation in the Department of Civil Engineering
Presented in Partial Fulfillment of the Requirements
For the Degree of Doctor of Philosophy

The University of Tokyo
2020

Abstract

GIS-based Susceptibility Analysis and SAR-based Detection for the Landslides Triggered in 2018 Hokkaido Eastern Iburi Earthquake

（2018 年北海道胆振東部地震の土砂災害に関する
GIS を用いた危険度評価と SAR を用いた検出に関する研究）

The extensive landslides triggered in 2018 Hokkaido Eastern Iburi Earthquake brought valuable data, information, experience, and lessons for future landslide disaster management, while causing big casualties and damage. This research aimed to make full of these data and experience to understand the landslide event, learn from it, and to suggest a procedure benefitting pre-event and post-event landslide disaster management in the future.

The first objective is to understand the landslide event by collecting and analyzing spatial data of landslide inventory and conditioning factors (topography, geology, soil, surface vegetation, precipitation, and ground motion) as well as previous reports and studies concerning the landslide event.

- It was found that most landslides were shallow, small-sized, densely distributed, and moved down several meters' volcano activity related soil layers with long run-out and high mobility. The slope gradient of the collapsed slopes was relatively lower comparing with other landslides, owing to local topography, geology, and soil characteristics. The earthquake was the direct trigger of the landslide event, and the combinational impact of several conditioning factors, especially the special soft porous soil types, the accumulation of previous precipitation in the soil, and the shaking of the ground motion, was the real cause of these extensive landslides.
- The special characteristics of the landslide event remind us to pay attention to physical properties and dynamic characteristics of the volcano activity related soil. Moreover, areas with special characteristics should also be taken seriously, when landslide triggers occur even with a low intensity, as the combinational impact of several conditioning factors that are not very significant might cause a severe landslide event.

The second objective is to develop a suitable landslide susceptibility model using the collected spatial data of landslide inventory and conditioning factors to facilitate pre-event landslide disaster management in the future. Data collection, data pre-processing, indicator effectiveness and correlation analysis, landslide presence and absence ratio analysis, training and validation dataset preparation, and model construction were carried out step by step.

- It was found that the standard curvature, one-week cumulative precipitation, and peak spectral acceleration of 0.3s were relatively more effective among curvature-, rainfall-, and earthquake-related indicators, owing to the parameter comprehensiveness, local soil water storage capacity and evaporation condition, and predominate period of local soil, respectively.
- The ratio of 1:1 between landslide presence and absence was more ideal for landslide statistical susceptibility analysis and was suggested, as the more non-landslide cells involved in analysis, the lower recall value, that is, the more landslide cells would be classified as non-landslide cells.
- The constructed landslide susceptibility model using the analyzed indicators under the ideal ratio achieved a good accuracy for both training and validation dataset in this case, and is expected to provide some information for understanding future landslide occurrence susceptibility, by updating the changed conditioning factors.

The third objective is to explore favorable SAR-based landslide detection approaches by analyzing different features in captured SAR data to benefit post-event landslide disaster management in the future. Principal analysis, parameter calculation, qualitative interpretation, quantitative analysis, and landslide detection were executed step by step. Moreover, a simple comparison between ALOS-2 and Sentinel-1 products, and a combinational application of landslide susceptibility map and SAR-based landslide detection were also performed.

- It was found that the intensity difference (d) had both lower-value and higher-value pixels in landslide areas, as triggered landslides smoothed hillsides causing backscattering decrease, and roughened foothill areas causing backscattering increase. The correlation (r, Δr) and coherence parameters (γ,

$\Delta\gamma$) had more or less some lower-value pixels in landslide regions due to the relatively larger ground changes and decorrelation induced by landslides.

- The sensitivity of parameters to other minor changes influenced the performance of them for landslide detection in these vegetation areas and also the optimal window size for parameter calculation. The more sensitive the parameter, the more inteference from other minor changes, and therefore the worse the performance and the larger the window size needed to filter and blur these inteference.
- As the calculation window size increased, the performance of the intensity parameters first increased and then decreased. A value around 25%~75% cumulative distribution curve of landslide sizes could achieve relatively favorable results. A relatively smaller value within this range was better for intensity difference, while a relatively larger value within this range was better for correlation coefficient parameters.
- The correlation difference Δr and the new intensity difference parameter d_{abs2} showed favorable performance and were recommended for future application. Particularly, d_{abs2} achieved the best performance and can be derived very easily from only one pre-event and one post-event SAR intensity images.
- Sentinel-1 products did not achieve as good results as ALOS-2 products for landslide detection in this case. It might relate to the lower spatial resolution of the Sentinel-1 products and also the difference between the looking direction, imaging micorwave, and polarization between these two products. If possible, a further study by controlling different variables might be better to understand and compare these influences. Nevertheless, Sentinel-1 products are free data and have a higher temporal resolution than ALOS-2 products. As the intensity difference calculated by them also had some clear different characteristics in landslide areas, they are also valuable data that could be used to understand the general landslide condition following a disaster.
- In a specific case, a comprehensive consideration of different factors (e.g., spatial resolution, temporal resolution, and image coverage) is needed so that appropriate products can be applied to achieve the study or application

purpose properly, as there are always trade-offs among different kinds of resolution and compromise between image resolution and image coverage.

- The combinational application of landslide susceptibility map and SAR-based landslide detection could help improve landslide detection results, limit the scope of SAR image for processing, draw attention to dangerous areas, and provide more reasonable information for rescue and response operations.

Based on these studies and results, corresponding to a disaster process in the future, a following management procedure is suggested: before landslide occurrence, updating predicted or actual rainfall and/or earthquake terms in the landslide susceptibility map to understand landslide occurrence risk in different areas and remind local people for preparation; after the landslide, detecting landslides rapidly by suggested SAR features and combining them with the updated susceptibility map to provide information for arranging rescue and response operations efficiently and effectively.

Acknowledgements

I would like to address my sincere thanks to my supervisor Prof. Kimiro Meguro at Institute of Industrial Science, The University of Tokyo, who has given his inspirational and permanent guidance, encouragement, and support throughout the research. Without his help, I would not be able to finish this research. I will always remember the significant points he has taught such as “always find the hidden essential reasons behind a phenomenon to really understand and solve a problem” and “take the difficult time in life as a chance to grow up”.

I would like to express my deep gratitude to my supervising committee Prof. Yoshiaki Nakano, Prof. Wataru Takeuchi, Prof. Takashi Kiyota, and Prof. Muneyoshi Numada for providing many constructive suggestions, critics, and feedbacks from various perspectives, such as approach generality, physical reason behind different SAR feature performance, landslide mechanism, and data collectability, which helped me to improve and enhance this research.

I would also like to give my thanks to Prof. Hideomi Gokon at Japan Advanced Institute of Science and Technology, who taught me a lot about remote sensing and machine learning, and provided the dataset and software for me to use. I would also like to express my thanks to Prof. Shunichi Koshimura at Tohoku University for kindly providing the SAR data in Hokkaido earthquake in my research.

I am lucky that I got lots of support and help in the lab from the assistant professors, secretaries, and lab members. I will remember the nice discussions and interesting moments shared with everyone.

I also want to express my appreciation for the financial support from the Ministry of Education, Culture, Sports, Science and Technology (MEXT).

Finally, I would like to give my special appreciation to my family members for their continuing support, encouragement, understanding, and patience. Without their love and supporting, I cannot complete my research work.

GE Pinglan

Tokyo, Japan

2020

List of Publications

Reviewed paper

1. Ge, P., Gokon, H., Meguro, K. (2020). A review on synthetic aperture radar-based building damage assessment in disasters. Remote Sensing of Environment, 240, 111693. DOI: https://doi.org/10.1016/j.rse.2020.111693
2. Ge, P., Gokon, H., Meguro, K., Koshimura, S. (2019). Study on the intensity and coherence information of high-resolution ALOS-2 SAR images for rapid massive landslide mapping at a pixel level. Remote Sensing, 11(23), 2808. DOI: https://doi.org/10.3390/rs11232808
3. Ge, P., Gokon, H., Meguro, K. (2019). Building damage assessment using intensity SAR data with different incidence angles and longtime interval. Journal of Disaster Research, 14(3), 456-465. DOI: 10.20965/jdr.2019.p0456

Non-reviewed paper

1. Ge, P., Gokon, H., Meguro, K., Koshimura, S. (2019). Tile-based landslide detection using SAR images: a case study of the 2018 Hokkaido Estern Iburi Earthquake. SEISAN KENKYU, 71(6), 1055-1057. DOI: https://doi.org/10.11188/seisankenkyu.71.1055
2. Ge, P., Gokon, H., Meguro, K., Koshimura, S. (2019). Investigation on the potential of ALOS-2 single look complex data for massive landslide detection. Bulletin of ERS, 52.

Conference

1. Ge, P., Gokon, H., Meguro, K., Koshimura, S. (2019). Analyses on landslide extraction by synthetic aperture radar single look complex images. 18th international symposium on new technologies for urban safety of mega cities in Asia (USMCA2019), December 9-10, Yangon, Myanmar.

Curriculum Vitae

Name: 葛 平兰 (GE Pinglan)

Date of birth: August 15, 1991

Nationality: China

Education:

2010 - 2014 Bachelor's Degree, School of Civil Engineering, Shandong University, China

2014 - 2017 Master Degree, College of Civil Engineering, Tongji University, China

2017 - 2020 Doctoral Course, Department of Civil Engineering, The University of Tokyo, Japan

Table of Contents

List of Figures

List of Tables

List of Acronyms

ALOS-2: Advanced Land Observing Satellite-2

AUC: Area under the Curve

CEOS: Committee on Earth Observation Satellites

DEM: Digital Elevation Model

ESA: European Space Agency

ESRI: Environmental Systems Research Institute

FN: False Negative

FP: False Positive

FPR: False Positive Rate

GIS: Geographic Information System

GRD: Ground Range Detected

GSI: Geospatial Information Authority of Japan

HH: Horizontal Transmit and Horizontal Receive

HV: Horizontal Transmit and Vertical Receive

IDW: Inverse Distance Weighted

JGS: Japanese Geotechnical Society

JMA: Japan Meteorological Agency

JST: Japan Standard Time

LiDAR: Light Detection and Ranging

MLIT: Ministry of Land, Infrastructure, Transport and Tourism

MMI: Modified Mercalli Intensity

NARO: National Agriculture and Food Research Organization

PALSAR-2: Phased Array Type L-band Synthetic Aperture Radar-2

PGA: Peak Ground Acceleration

PGV: Peak Ground Velocity

PSA03: Peak Spectral Acceleration for 0.3s

PSA10: Peak Spectral Acceleration for 1.0s

PSA30: Peak Spectral Acceleration for 3.0s

ROC: Receiver Operating Characteristic

RS: Remote Sensing

Radar: Radio Detecting and Ranging

SAR: Synthetic Aperture Radar

SLC: Single Look Complex

SNAP: Sentinel Application Platform

SPI: Stream Power Index

STI: Sediment Transport Index

TN: True Negative

TOL: Tolerance

TP: True Positive

TPR: True Positive Rate

TWI: Topographic Wetness Index

UBS: Ultra-fine Mode Single Polarization

USGS: U.S. Geological Survey

UTC: Coordinated Universal Time

VH: Vertical Transmit and Horizontal Receive

VIF: Variance Inflation Factor

VV: Vertical Transmit and Vertical Receive

CHAPTER 1

INTRODUCTION

1.1. Background

1.1.1. The 2018 Hokkaido Eastern Iburi Earthquake

On September 6th, 2018, just one day after the powerful Typhoon Jebi passed, an earthquake with a moment magnitude of 6.6 M_w (Japan Meteorological Agency (JMA) scale: 6.7M_j) struck the eastern Iburi region in Hokkaido Prefecture, North Japan, and triggered extensive landslides near the towns of Atsuma, Mukawa, and Abira. This earthquake, officially known as the 2018 Hokkaido Eastern Iburi Earthquake, is an intraplate earthquake occurred at the epicenter of 42.686°N, 141.929°E near Tomakomai with a depth of 35km, at 03: 07: 59 am local time (JST) (UTC: 18: 07: 59 on 5 September 2018) (**Figure 1.1**) (USGS; Wang et al., 2019). It was a reverse dip-slip fault earthquake with a pressure axis in the ENE-WSW direction. Shaking was felt strongly in Hokkaido and Aomori prefecture. The maximum intensity of the earthquake was IX on the U.S. Geological Survey (USGS) scale (**Figure 1.1**) and 7 on the JMA scale.

This earthquake caused 42 fatalities, 762 injuries including 31 serious injuries, 462 totally-collapsed houses, 1,570 severally-damaged houses, and 12,600 slightly-damaged houses according to Japan Geotechnical Society (JGS) (2019). Besides, it has also severely disrupted the electrical service, transportation, and communication in local area, leaving 5.3 million residents without power and causing a damage of over 367.5 billion yen (Mainichi Shimbun, 2018). Due to the fires broke out in the earthquake, the Hokkaido Electric Power Company's coal-fired power plant in Atsuma was heavily destroyed, causing 2.95 million houses in Hokkaido without power. Moreover, some water supply facilities were damaged, leading to 68,249 houses in 44 municipalities without water. Some roads and bridges were also blocked or damaged by the earthquake-triggered landslides or the earthquake-caused liquefaction, becoming impassable. Furthermore, regional economic activities were seriously affected. Farming and fishing industries suffered severe losses owing to transportation closure and no power for operating equipment, cooling, and

refrigerating. Tourism industry was influenced due to the impacts and damage caused by the earthquake and the perception that the area was in danger of aftershocks.

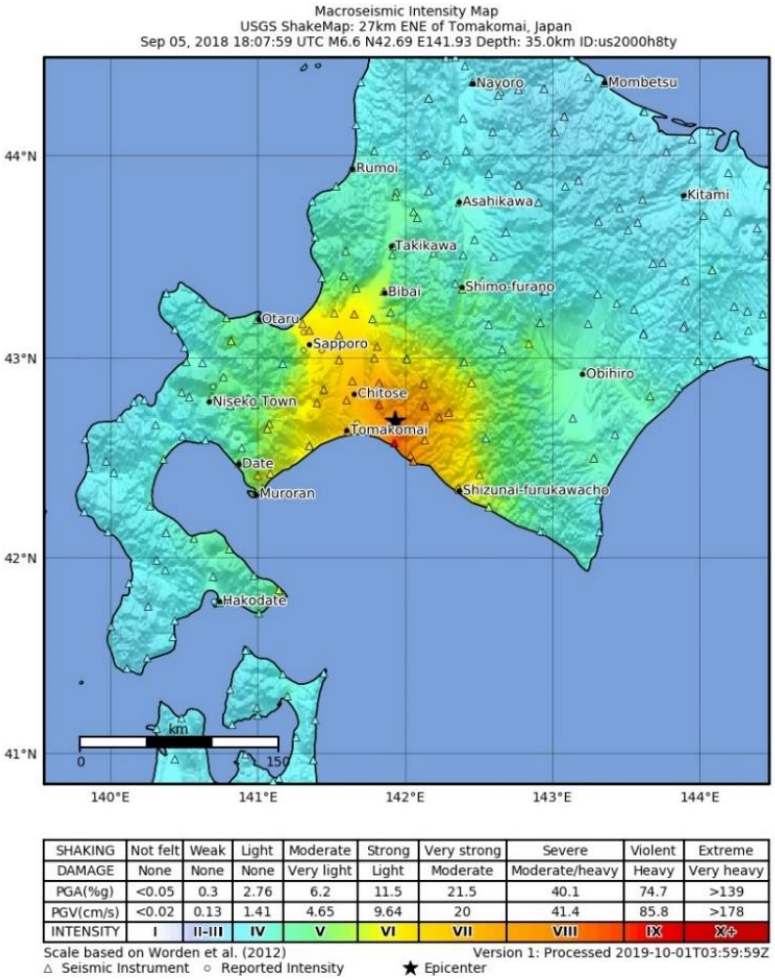

Figure 1.1. Shakemap for the 2018 Hokkaido Eastern Iburi Earthquake (USGS).

1.1.2. Landslides Triggered by the 2018 Hokkaido Eastern Iburi Earthquake

This earthquake triggered extensive densely distributed landslides near the towns of Atsuma, Mukawa, and Abira in the north of the earthquake epicenter, due to the complex interaction between the ground motion, rainfall, and special soil types of volcano ash here. The number and total area of the triggered landslides were approximately 6,000 and 46 km^2, which were said to be the largest in Japan ever since Meji Era (1868-1912) (Osanai et al., 2019). The total volume of the landslides was around 30 milion m^3 according to the Ministry of Land, Infrastructure, Transport and Tourism (MLIT) (2018).

Most of the landslides were shallow, moving down several meters' volcano activity related soil layers with high mobility and long run-out and leaving the upper slip surface exposed without overlapping slide mass. Several deep-seated landslides were also found in the southeast of this area, including one that formed a landslide dam in the Hidaka-Horonai river. The landslides were mainly spoon and planar types occurred in valley topography and planar slopes, respectively, with a small to medium size, similar to the rainfall-induced landslides (Yamagish and Yamazaki, 2018). **Figure 1.2** shows the overall distribution and several different types of the landslides.

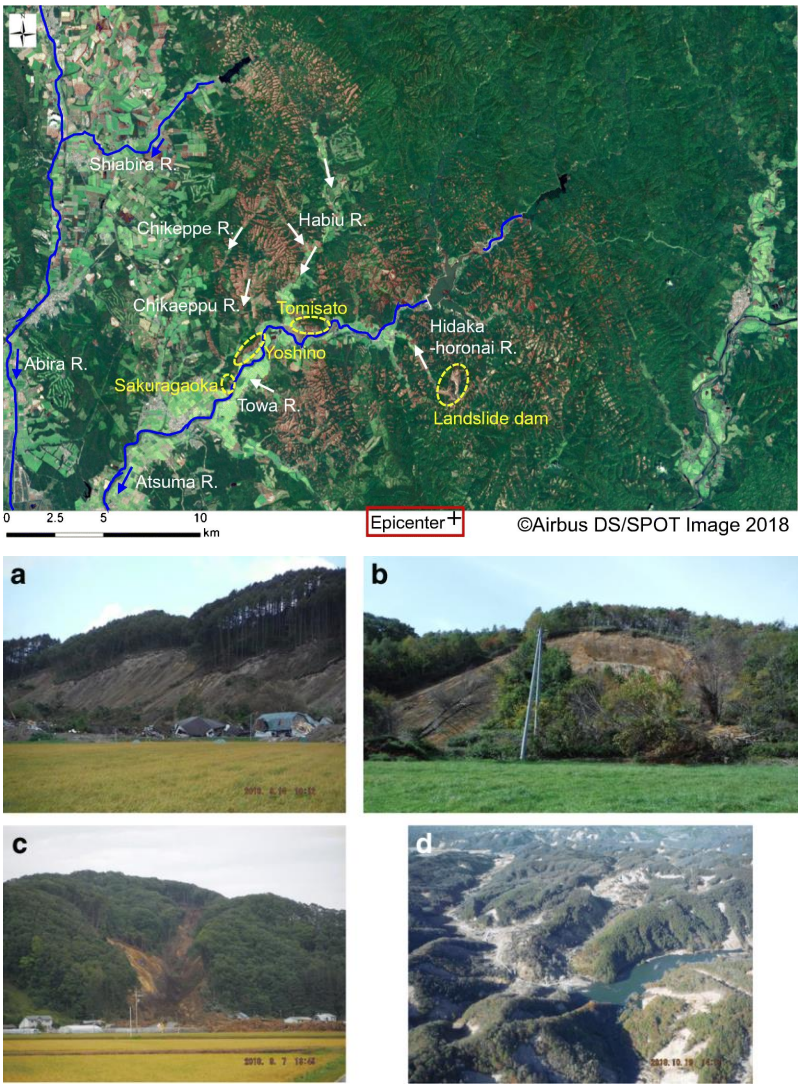

Figure 1.2. Landslides triggered by the 2018 Hokkaido Eastern Iburi Earthquake (Osanai et al., 2019): (a) Translational earth slide in Yoshino area (shallow landslide); (b) Translational earth block slide in Chikeppe River area (shallow landslide); (c) Earth flow in Tomisato area (shallow landslide); (d) Translational rock slide that formed the landslide dam (large deep-seated landslide).

The main landslide materials were several meters' volcano activity related soil layers erupted from several volcanoes in 40km-70km west of the earthquake epicenter (mainly Shikotsu caldera, Eniwa volcano, and Tarumae volcano). The predominant bedrock was Middle to Late Miocene marine and non-marine sediments, which mainly includes sandstone, mudstone, and conglomerate. The soft and porous volcanic soil layers above the hard bedrock inundated by previous accumulated rainfall and then ruptured by the shear force of the earthquake, which might be the mechanism of most induced landslides.

These landslides triggered by the earthquake were thought as an important reason for the big casualties and damage caused by the disaster. Among all of the 42 deaths, 36 people were killed by the earthquake-triggered landslides in Atsuma region. Especially, in Yoshino area (**Figure 1.3**), many houses were swepted away by the landslides, causing 19 of 34 residents killed. Moreover, the debris carried out by the landslides involved many houses, and blocked and damaged some roads, bridges, rivers, and paddies at the foot of the mountains, causing damage to infrastructures and leading to big property damage and economic losses.

Figure 1.3. Landslides in Yoshino area (Google Earth).

1.2.Problem Statement

As is said, present and past are keys to the future. While causing big casualties and damage, this disaster also should make us think about the future, i.e., what caused the damage and how to reduce the damage for such disasters in the future. For instance, if there was a management procedure corresponding to the disaster process, the causalities and damage caused by the disaster might have been reduced. On one hand, before the disaster, if there were some models, systems, or maps that can be used to understand the dangerous condition of landslide occurrence in different areas, local people might have prepared better for the disaster. On the other hand, after the disaster, if there were some rapid ways to understand the landslide condition, more time might have been saved for emergency response and therefore more trapped people might have been saved. Besides, the fact that the disaster occurred in the early morning of local time also reminded us that the rapid way might be more reliable if it could work independent of sun light and weather condition.

Moreover, while bringing casualties and damage, the disaster also provided us with abundant data and information that can be used to understand and learn from the disaster. Collecting relevant data and performing related analyses of the disaster might provide useful information for preferable landslide disaster management in the future. For instance, the spatial dataset of actual landslides and causative factors (e.g., ground motions and precipitation) can be collected and used to understand the characteristics and mechanism of the landslides, and to analyze the susceptibility condition of landslide occurrence in this area. The remote sensing (RS) data captured during the landslide event can be collected and applied to explore rapid landslide detection approaches, benefitting emergency response and rescue for landslide disasters in the future.

To explore how to apply the data and information mentioned above to achieve the thoughts mentioned above, previous research, methodology, and approaches were reviewed and studied. As there were few studies concerning the whole procedure, studies related to each parts were reviewed seperately as follows.

1.2.1. Landslide Susceptibility Analysis for Pre-event Landslide Disaster

Management

There are generally three different kinds of approaches that can be used to construct models, maps, or systems for understanding dangerous condition of landslide occurrence, including deterministic approach, probabilistic approach, and statistical approach. The deterministic approach analyzes the landslide mechanism by infinite slope models and hydrological models. It requires detailed information of soil strength, soil depth, and hydrological parameters, which are difficult to collect for a large-scale area. The probability approach calculates an annual exceedance probability of certain magnitude of landslide failure at a specific slope by probabilistic models according to multi temporal landslide inventories. It requires long-term historical landslide records of similar types, which might be difficult to collect sufficiently and completely. Moreover, different types of landslides might be mixed (e.g., rainfall-induced landslides and earthquake-triggered landslides), if the history records were not very clear. The statistical approach constructs a landslide susceptibility, hazard, or risk model by analyzing the relationship between a series of landslides or an event-based landslide inventory and the corresponding landslide causative factors (e.g., earthquake and geology). It is difficult to be used for predicting landslide magnitude and run-out distance.

As introduced above, different approaches have different advantages and disadvantages, and are suitable for different situations. Considering the fact that in cases like this one, it is difficult to collect the detailed information of soil and hydrological parameters or the series of similar historical landslide records due to the wide distribution and special characteristics of the landslides, the statistical approach is applied. By analyzing the relationship between the event-based landslide inventory and the corresponding landslide conditioning factors such as topography and rainfall, a landslide susceptibility map can be constructed, which may provide some useful information for preferably managing landslide disaster in the future.

Over the years, various analyses have been carried out for the statistical approach-based landslide susceptibility analysis of different types of landslides based on geographic information system (GIS) (Wang et al., 2005; Pardeshi et al., 2013; Lee, 2015). Statistical analysis, such as discriminant analysis and logistic regression, and advanced machine learning approaches, such as decision tree, support vector machine,

and artificial neural networks, have all been explored for statistical landslide susceptibility analysis (Lee et al., 2008; Bai et al., 2010; Lee, 2014; Hong et al., 2015; Hong et al., 2016; Bui et al., 2016). Earthquake-induced landslides (Lee et al., 2008), rainfall-induced landslides (Chau et al., 2004), and storm event-induced landslides (Lee et al., 2008) have all been investigated as study subjects. Yet, most analyses usually only considered one exterior landslide conditioning factor depending on the need of local area (e.g., rainfall, earthquake, or storm), as there was usually only one main triggering factor for each landslide event. This seems to be not very general, especially not very suitable for cases like this one, in which both rainfall and earthquake were considered as important exterior factors for the landslide occurrence.

1.2.2. Landslide Detection for Post-event Landslide Disaster Management

For landslide detection and understanding after a disaster, there are generally three main ways including field survey, optical remote sensing, and synthetic aperture radar (SAR) remote sensing. Field survey can provide very detailed information about a landslide event but takes time, especially for a wide area. Moreover, just after a disaster, it might be dangerous to go to the site, and the disaster area might be inaccessible due to damaged or blocked transportation. Optical remote sensing can provide very clear and intuitive images to understand the condition of landslide occurrence. However, it needs sunlight for imaging and cannot penetrate clouds due to the short wavelength of the applied visible light. As a result, it cannot be used at night and bad weather conditions, which may hamper its application as an emergency tool for landslide detection. For instance, it was said that there were almost no cloud-free images for landslide detection in the first week following the 2015 Nepal earthquake (Burrows et al., 2019). SAR remote sensing actively transmits microwaves to ground targets and then receives the backscattered signals. It can provide data at both night and bad weather condition, as it works independent of sunlight and applies longer wavelength that can penetrate thick clouds. However, SAR data are relatively difficult to interpret comparing with optical images, and might not be able to provide results as accurate as field survey and optical remote sensing.

In this study, considering the purpose of emergency application and the fact that

landslide event often occurred in bad weather condition (particularly rainfall-induced landslides) and sometimes at night like the one in this case, SAR remote sensing is applied. As time goes by after the landslides, when available and applicable, optical images can be applied and field survey can be carried out successively to obtain and more detailed information about the landslide event from other aspects.

Over the years, SAR remote sensing has been widely explored for the monitoring of specific slow-moving landslides in a light-of-sight direction by various inteferometry techniques (Strozzi et al., 2005, Colesanti and Wasowski, 2006, Zhao et al., 2012, Tofani et al., 2013, Confuorto et al., 2017, and Zhao et al., 2018). Yet, the application of it for landsldie detection has not been studied well. Several conducted studies were only concentrated on large individual landslides, catchments (Raspini et al., 2015; Yun et al., 2015; Xue et al., 2018), or dozens of landslides (Konishi and Suga, 2018). A couple of studies (Mondini, 2017; Burrows et al., 2019) focusing on large-scale landslide detection were also not for shallow landslides. The feasibility of SAR data for the detection of the densely distributed small and shallow landslides is not very clear. Moreover, there are several features and parameters in SAR data that can be used to measure ground changes, including intensity-related ones, phase-related ones, and polarimetry-related ones. But there are basically no studies to compare them and to give suggestions on which one is better or cost-effective for application.

1.3. Research Objective

Based on the considerations in section 1.2, the general objective of this research is to make full use of the data, information, experience, and lessons brought by the landslide event to understand it, learn from it, and to suggest some procedure benefiting landslide disaster management in the future. More specifically, based on the landslides triggered in 2018 Hokkaido Eastern Iburi Earthquake, this study aims to:

1. Understand the landslide event by collecting and analyzing the spatial data of landslide inventory and conditioning factors as well as previous reports and studies concerning the landslide event.

2. Develop a suitable landslide susceptibility model using the collected spatial data of landslide inventory and conditioning factors to facilitate pre-event landslide disaster management in the future.
3. Explore favorable SAR-based landslide detection approaches by analyzing different features in captured SAR data to benefit post-event landslide disaster management in the future.

After that, in the future, corresponding to a landslide disaster process, a following management procedure can be applied: before the disaster, updating the predicted or actual dynamic terms (e.g., rainfall and earthquake) in the landslide susceptibility map to understand the dangerous condition of landslide occurrence in different areas and to remind local people for reasonable preparation; after the disaster, detecting the induced landslides rapidly by suggested SAR features and combining them with the updated landslide susceptibility map to provide information for effective and efficient rescue and response operations.

1.4. Research Methodology

To achieve these objectives, the technologies of GIS and SAR remote sensing are applied. GIS is a computer system designed to manipulate various spatial and geographic data, and is very suitable for analyzing the relationship between landslide inventories and conditioning factors. It has become a popular technology applied in calculating and managing natural hazards including landslides since the middle of 1980s (Chau, et al., 2004). By the use of GIS, various types of spatial data can be displayed, inventoried, and analyzed easily and conveniently. In this research, GIS is applied to understand the landslide event by analyzing landslide inventory and conditioning factor layers and to construct a landslide susceptibility model by the statistical analysis of logistic regression.

Statistical analysis can construct a mathematical model by analyzing the relationship between the dependent variable (landslide occurrence in this case) and independent variables (landslide conditioning factors in this case). Comparing with the deterministic approach that explores slope failure mechanism by physical models, it does not require detailed physical parameters, such as soil strength, soil depth, and

hydrological parameters, which are difficult to collect in a large area (Lee, 2015). Moreover, the model constructed by the statistical analysis may be applied for landslide prediction, monitoring, and management in the future by updating the changed causative factors, based on the assumption that future landslides will occur under similar conditions of previous landslides.

As one of statistical analysis approach, logistic regression can be used to model the relationship between a dichotomous dependent variable (landslide presence and absence in this case) and a set of independent variables (landslide conditioning factors in this case). It is efficient, highly interpretable, can be implemented relatively easily and quickly, and does not require the independent variables to have a normal distribution. Continuous data, discrete data, and category data can all be applied as independent variables in a logistic regression. It is applied to construct the landslisde susceptibility model in this case.

Remote sensing is a technology used to acquire information about a phenomenon or object from a distance without physical contact. It can provide a valuable data source for landslide disaster study, owing to the capabilities of rapid response, no contact, and broad coverage. SAR is an important kind of active RS technology that transmits energies to the earth surface by itself and then receives backscattered energies. It is able to work at both night and daytime, as it does not need sun's energy for imaging. Moreover, it applies microwave bands in the electromagnetic spectrum that have a relatively long wavelength and can penetrate clouds, which enables it to work in any weather conditions. Furthermore, several kinds of information in SAR data (e.g., intensity and coherence) have the potential for landslide detection, as they can be used to measure ground changes. In this research, SAR data are applied to explore landslide detection approaches.

In specific implementations:

- First, the spatial data of landslide inventory and conditioning factors (topography, geology, soil, surface vegetation, precipitation, and ground motion) will be collected from different sources, and then processed and analyzed in ArcGIS software to understand the general characteristics of the

extensive landslides, combining with previous reports on field surveys and research on mechanism study of this landslide event.

- Then, based on the collected spatial data of landslide inventory and conditioning factors, the GIS-based statistical analysis will be performed to construct a suitable landslide susceptibility model in the study area. All data, either in a raster format or in a vector format, will be converted into a unified format for analysis. The effectiveness and correlation of the indicators for each conditioning factor will be analyzed to find the relatively effective ones and to eliminate the correlated ones for model construction. The selected and checked data will then be classified into two groups with one used for model training and another used for model validation.
- After that, SAR products acquired for the influenced area during the disaster will be investigated to explore rapid landslide detection approaches. Potential information and parameters that can be derived from the captured products and have the ability to measure ground changes will be selected and calculated based on radar reflection mechanism, to facilitate rapid detection. Qualitative and quantitative analyses of these potential parameters and information will be carried out to find favorable and cost-effective ones for landslide detection. Landslides detected by the favorable SAR information and parameters will be compared with actual landslide inventory to check the reliability and accuracy.

1.5. Structure of the Research

In order to logically introduce how to use the methodologies mentioned in section 1.4 to achieve the objectives mentioned section 1.3, there are totally seven chapters in this thesis. The details of each chapter are described below:

Chapter 1 introduces the basic information of this research, including research background, problem statement, research objective, research methodology, and the structure of the research. The special landslide event caused by 2018 Hokkaido Eastern Iburi Earthquake reminded us to learn from it and to make a management procedure corresponding to landslide process for reducing casualties and damage. Considering the data availability, purpose of emergency application, and actual

situation of landslide disaster, GIS-based landslide susceptibility analysis and SAR-based landslide detection were determined, even though there were several problems to be solved for their application in such cases. To explain how to use these analyses to achieve these objectives systematically and clearly, seven chapters were written orderly and logically in this thesis.

Chapter 2 describes the important concepts and terminologies used in this research, including landslide, GIS, RS, SAR, disaster, and disaster management. The definition, causes, types, and impacts of landslides are first introduced to provide an understanding of the research subject. The concepts, basic knowledge, important terms, and advantages of GIS, RS, and SAR are then presented to explain the major technologies and tools applied in this research and why they are applied. The definition, classification, and impacts of disaster as well as the procedure and cycle for disaster management are finally described to help understand this research in a big picture of disaster study.

Chapter 3 analyzes the characteristics of the landslides by collecting spatial data of landslide inventory and conditioning factors, and studying previous reports and research concerning this landslide event. A landslide inventory is applied to understand the sizes and distribution of the landslides. The raster or vector maps of topography, geology, soil, and surface vegetation, as well as the records of ground motion and precipitation before the disaster are collected from different sources, and used to analyze the characteristics of conditioning factors in landslides. Previous studies and reports on the landslide mechanism and field survey were also referred and combined to facilitate a better understanding of the landslide event.

Chapter 4 executes a landslide susceptibility analysis using the collected data by a GIS-based statistical approach to facilitate pre-event landslide disaster management in the future. The landslide inventory is used as dependent variable and the conditioning factors are used as independent variables, respectively. All collected data, in either raster types or vector types, are converted into the same format for analysis. The effectiveness and correlation among the indicators of the conditioning factors are analyzed to select the relatively effective indicators and to exclude the correlated indicators for analysis. The dataset of the dependent variable and selected independent variables are then divided into two groups with one group used for model training and

another used for model validating. A landslide susceptibility model was finally constructed and validated by the training and validating dataset using a logistic regression.

Chapter 5 explores rapid landslide detection approaches by the use of different features and information in SAR data to benefit post-event landslide disaster management in the future. Potential parameters and features that have the capabilities to measure ground changes and can be derived from the captured SAR products are first selected, calculated, and derived. Qualitative and quantitative analyses of these selected features are then carried out by visual observation and receiver operating characteristic (ROC) analysis, to compare their performances for landslide detection and to find the favorable ones. Landslides detected by the favorable SAR parameters are compared with actual landslide inventory to check the accuracy and reliability of the SAR-based landslide detection approaches.

Chapter 6 investigates an additional application of landslide susceptibility map or landslide conditioning factors to the SAR-based landslide detection. For areas with an available landslide susceptibility map, the additional application of it to the SAR-detected landslides can help draw attention to dangerous areas, improving the results and efficiency of landslide detection. For areas without such a map, the exterior conditioning factors of landslides (e.g., ground motion and precipitation) can be used to help narrow target areas for analysis and eliminate irrelevant areas. The interior conditioning factors of landslides (e.g., slope gradient and land use) can be applied to help exclude areas of no interest and areas where landslides are unlikely to occur.

Chapter 7 summarizes the main conclusions, recommendations, limitations, and possible directions for future study. In order to understand the landslide event caused by 2018 Hokkaido Eastern Iburi Earthquake, the spatial data and studies concerning the landslides are collected, analyzed, and studied. In order to learn from it, a GIS-based landslide susceptibility analysis and a SAR-based landslide detection are investigated for the application before and after a disaster, respectively. A combinational application of landslide susceptibility map and SAR-detected landslides is also simply explored and recommended for landslide disaster management in the future. Due to data availability and limitation in time and ability, there are some limitations in this work that can be further investigated. For instance,

polarimetry information in SAR data that should also have good performance for landslide detection has not been studied and compared in this case due to the data availability.

1.6. References

Bai, S., Wang, J., Lü, G., Zhou, P., Hou, S., Xu, S. (2010). GIS-based logistic regression for landslide susceptibility mapping of the Zhongxian segment in the Three Gorges area, China. Geomorphology, 115(1-2), 23-31.

Bui, D. T., Tuan, T. A., Klempe, H., Pradhan, B., Revhaug, I. (2015). Spatial prediction models for shallow landslide hazards: a comparative assessment of the efficacy of support vector machines, artificial neural networks, kernel logistic regression, and logistic model tree. Landslides, 13(2), 361-378.

Burrows, K., Walters, R. J., Milledge, D., Spaans, K., Densmore, A. L. (2019). A new method for large-scale landslide classification from satellite radar. Remote Sensing, 11(3), 237-241.

Chau, K. T., Sze, Y. L., Fung, M. K., Wong, W. Y., Fong, E. L., Chan, L. C. P. (2004). Landslide hazard analysis for Hong Kong using landslide inventory and GIS. Computer & Geoscience, 30 (4), 429-443.

Chau, K. T., Sze, Y. L., Fung, M. K., Wong, W. Y., Fong, E. L., Chan, L. C. P. (2004). Landslide hazard analysis for Hong Kong using landslide inventory and GIS. Computers & Geosciences, 30(4), 429-443.

Colesanti, C., Wasowski, J. (2006). Investigating landslides with space-borne Synthetic Aperture Radar (SAR) interferometry. Engineering Geology, 88(3-4), 173-199.

Confuorto, P., Martire, D. D., Centolanza, G., Iglesias, R., Mallorqui, J. J., Novellino, A., Plank, S., Ramondini, M., Thuro, K., Calcaterra, D. (2017). Post-failure evolution analysis of a rainfall-triggered landslide by multi-temporal interferometry SAR approaches integrated with geotechnical analysis. Remote Sensing of Environment, 188, 51-72.

Hong, H., Pradhan, B., Jebur, M. N., Bui, D. T., Xu, C., Akgun, A. (2015). Spatial

prediction of landslide hazard at the Luxi area (China) using support vector machines. Environmental Earth Sciences, 75(1), 40.

Hong, H., Pradhan, B., Xu, C., Bui, D. T. (2015). Spatial prediction of landslide hazard at the Yihuang area (China) using two-class kernal logistic regression, alternating decision tree and support vector machines. Catena, 133, 266-281.

JGS. (2019). 平成 30 年北海道胆振東部地震による地盤災害調査団最終報告書. 公益社団法人地盤工学会平成 30 年北海道胆振東部地震による地盤災害調査団. https://www.jiban.or.jp/file/saigai/H30_Hokkaido_EQ_FinalReport.pdf

JMA. https://www.jma.go.jp/en/doshamesh/index.html

Konishi, T., Suga, Y. (2018). Landslide detection using COSMO-SkyMed images: A case study of a landslide event on Kii Peninsula, Japan. European Journal of Remote Sensing, 51(1), 205-221.

Lee, C. (2014). Statistical seismic landslide hazard analysis: an example from Taiwan. Engineering Geology, 182, 201-212.

Lee, C. (2015). Review and perspective on methodology for landslide hazard analysis. 10th Asian Regional Conference of IAEG, Kyoto, JP, 26-29 September 2015.

Lee, C. (2015). Review and perspectives on methodology for landslide hazard analysis. 10th Asian Regional Conference of IAEG, Kyoto, Japan.

Lee, C., Huang, C., Lee, J., Pan, K., Lin, M., Dong, J. (2008). Statistical approach to earthquake-induced landslide susceptibility. Engineering Geology, 100(1-2), 43-58.

Lee, C., Huang, C., Lee, J., Pan, K., Lin, M., Dong, J. (2008). Statistical approach to storm-induced landslide susceptibility. Natural Hazards and Earth System Sciences, 8, 941-960.

Mainichi Shimbun. (2018). Damage from deadly Hokkaido quake estimated at over 367.5 billion yen. 4 October 2018. Retrieved 21 December 2018.

MLIT. (2018). The total area of landslides caused by the 2018 Hokkaido eastern Iburi earthquake is the largest for the first time after Meiji era. http://www.mlit.go.jp/river/sabo/h30_iburitobu/181005_sediment_volume.pdf.

Mondini, A. C. (2017). Measures of spatial autocorrelation changes in multitemporal SAR images for event landslides detection. Remote Sensing, 9(6), 554-569.

Osanai, N., Yamada, T., Hayashi, S., Kastura, S., Furuichi, T., Yanai, S., Murakami, Y., Miyazaki, T., Tanioka, Y., Takiguchi, S., Miyazaki, M. (2019). Characteristics of landslides caused by the 2018 Hokkaido Eastern Iburi Earthquake. Landslides, 16 (8), 1517–1528.

Pardeshi, S. D., Autade, S. E., Pardeshi, S. S. (2013). Landslide hazard assessment: recent trends and techniques. SpringerPlus, 2(1), 523.

Raspini, F., Ciampalini, A., Conte, S. D., Lombardi, L., Nocentini, M., Gigli, G., Ferretti, A., Casagli, N. (2015). Exploitation of amplitude and phase of satellite SAR images for landslide mapping: The case of Montescaglioso (South Italy). Remote Sensing, 7(11), 14576-14596.

Strozzi, T., Farina, P., Corsini, A., Ambrosi, C., Thüring, M., Zilger, J., Wiesmann, A., Wegmüller, U., Wegmüller, C. (2005). Survey and monitoring of landslide displacements by means of L-band satellite SAR interferometry. Landslides, 2(3), 193-201.

Tofani, V., Raspini, F., Catani, F., Casagli, N. (2013). Persistent scatterer interferometry (PSI) technique for landslide characterization and monitoring. Remote Sensing, 5(3), 1045-1065.

USGS.https://earthquake.usgs.gov/earthquakes/eventpage/us2000h8ty/executive#executive

Wang, F., Fan, X., Yunus, A. P., Subramanian, S. S., Rodriguez, A. F. A., Dai, L., Xu, Q., Huang, R. (2019). Coseismic landslides triggered by the 2018 Hokkaido, Japan (Mw 6.6), earthquake: Spatial distribution, controlling factors, and possible failure mechanism. Landslides, 16, 1551–1566.

Wang, H., Liu, G., Xu, W., Wang, G. (2005). GIS-based landslide hazard assessment: an overview. Progress in Physical Geography, 29(4), 548-567.

Xue, D., Yu, X., Jia, S., Chen, F., Li, X. (2018). Study on landslide disaster extraction method based on spaceborne SAR remote sensing images-take ALOS PALSAR

for an example. Int. Arch. Photogramm. Remote Sensing and Spatial Information Science, XLII-3, 2023-2027.

Yamagishi, H., Yamazaki, F. (2018). Landslides by the 2018 Hokkaido Iburi-Tobu earthquake on September 6. Landslides, 15 (12), 2521–2524.

Yun, S. H., Hudnut, K., Owen, S., Webb, F., Simons, M., Sacco, P., Gurrola, E., Manipon, G., Liang, C., Fielding, E., et al. (2015). Rapid Damage Mapping for the 2015 Mw 7.8 Gorkha Earthquake Using Synthetic Aperture Radar Data from COSMO-SkyMed and ALOS-2 Satellites. Seismology Research Letters, 86(6), 1549-1556.

Zhao, C., Lu, Z., Zhang, Q., Fuente, J. D. L. (2012). Large-area landslide detection and monitoring with ALOS/PALSAR imagery data over Northern California and Southern Oregon, USA. Remote Sensing of Environment, 124, 348-359.

Zhao, F., Mallorqui, J. J., Iglesias, R., Gili, J. A., Corominas, J. (2018). Landslide monitoring using multi-temporal SAR interferometry with advanced persistent scatterers identification methods and super high-spatial resolution TerraSAR-X images. Remote Sensing, 10(6), 921.

CHAPTER 2

LANDSLIDE, GEOGRAPHIC INFORMATION SYSTEM (GIS), REMOTE SENSING (RS), DISASTER, AND DISASTER MANAGEMENT

2.1. Introduction

This chapter introduced the significant concepts and terminologies applied in this thesis, to facilitate the understanding of the entire research. The defination, causes, types, and impacts of landslides were first introduced to provide a general understanding of the research subject. The important concepts and terms in geographic information system (GIS), remote sensing (RS), and synthetic aperture radar (SAR) mentioned in the research were then explained to facilitate understanding the research tools and methodologies used in this work. The basic knowledge and general concepts of disaster and disaster management were finally presented to help understand the research in a big picture of disaster research.

2.2. Landslide

2.2.1. Definition and Causes of Landslides

Landslides can be defined as the movement of a mass of rock, debris, or earth down a slope (Cruden, 1991). They are a type of "mass wasting," which denotes any down-slope movement of soil and rock under the direct influence of gravity, and occurs when forces acting down-slope (mainly due to gravity) exceed the strength of earth materials that compose the slope (USGS).

Factors that can increase down-slope forces and factors that can decrease earth strength are both able to cause landslides, including natural phenomenon (e.g., earthquake, rainfall, volcanic activity, snowmelt, weathering, and erosion) and human activities (e.g., blasting, underground mining, cutting, and draining of reservoirs). A specific landslide event usually has multiple causes and factors. Landslides due to earthquakes or other factors can also occur underwater, which are called as submarine landslides and sometimes cause tsunami. **Figure 2.1** shows several examples of landslides induced by different factors.

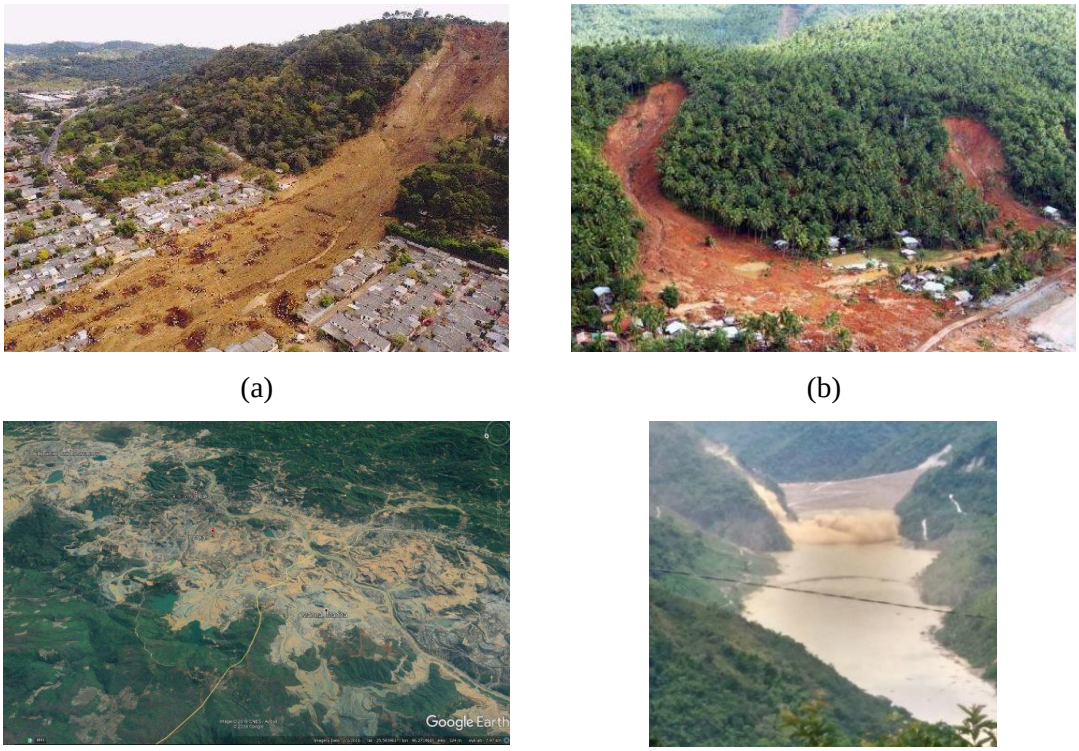

Figure 2.1. Examples of landslides induced by different factors: (a) Earthquake-triggered landslides in Las Colinas, Santa Tecla in 2001 (García-Rodríguez and Malpica, 2010); (b) Rainfall-induced landslides in Panaon Island, Southern Leyte in 2003 (PHIVOLCS); (c) Continued mining-induced landslides in Hpakant, Myanmar in 2018 (The Landslide Blog); (d) Dam landslides in Ituango, Colombia, 2018 (Global Forest Coalition).

2.2.2. Basic Types of Landslides

Landslide types are usually classified based on the type of involved materials and the type of movement (**Figure 2.2**). The type of materials involved in landslide mass includes rock, soil, or both of them. Soil is usually described as earth if its main composition is finer or sand-sized particles, and described as debris if its main composition is coarser fragments. The type of movement includes falls, topples, slides, spreads, and flows, which describes how the landslide mass is displaced due to internal failure mechanism. Rock falls and debris flows are the two most prevalent occurring landslides.

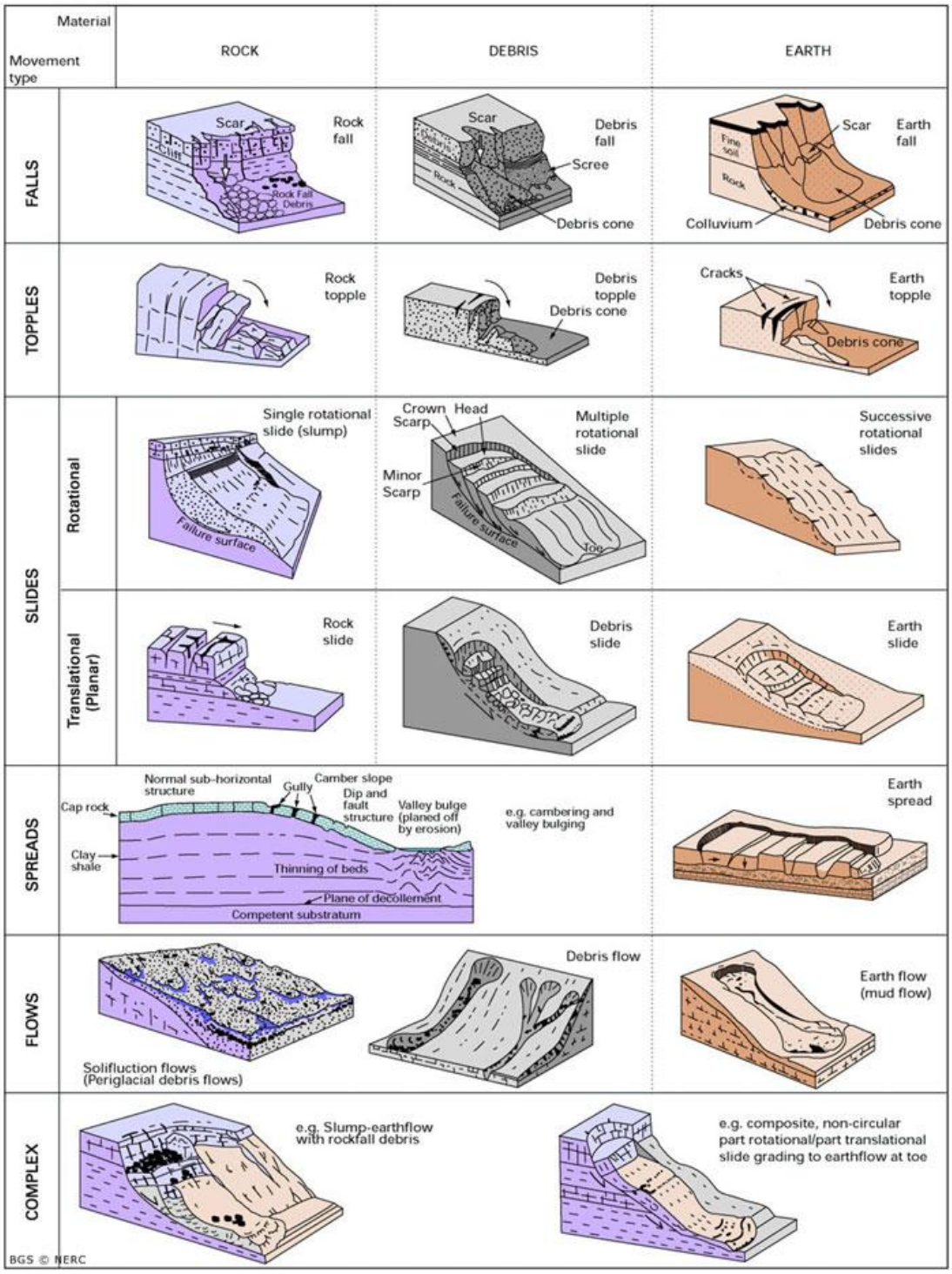

Figure 2.2. Basic landslide types (BGS).

Falls are sudden movements of debris, earth, or rock that separate from a cliff or slope. They usually take place because of gravity force, mechanical weathering, or earthquake. Topples are the forward spinning and movement of debris, earth, or rock

from a slope. They usually occur around an axis near or at the bottom of a rock block and generate a debris cone below the slope. Slides, including rotational and transitional ones, are moderate mass movement whereby the debris, earth, or rock breakaway from stable underlying materials. The material consistency can be maintained in slides. Spreads are lateral extension followed by tensile fractures that usually occur on gentle topography and include lateral spreads, block spreads, and liquefaction spreads. Flows are spatially continuous movements where the shear surfaces are closely spaced, short-lived, and usually not preserved. According to landslide materials, there are earth flows, debris flows, mudflows, debris avalanche, and creep. Moreover, landslides can also include more than one types of movements, forming the "complex landslides" (EARTH ECLIPSE; Highland and Bobrowsky, 2008). An example of each type of landslide was shown in **Figure 2.3** to provide an intuitive understanding.

(a)

(b)

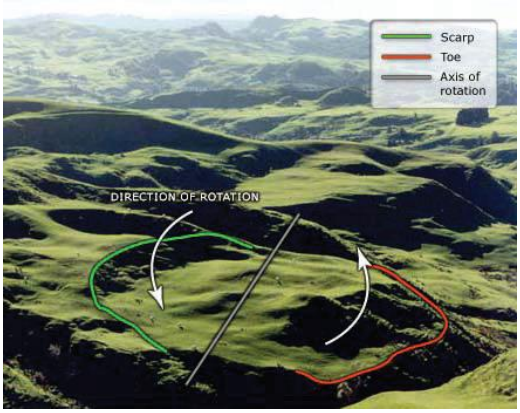

(c)

(d)

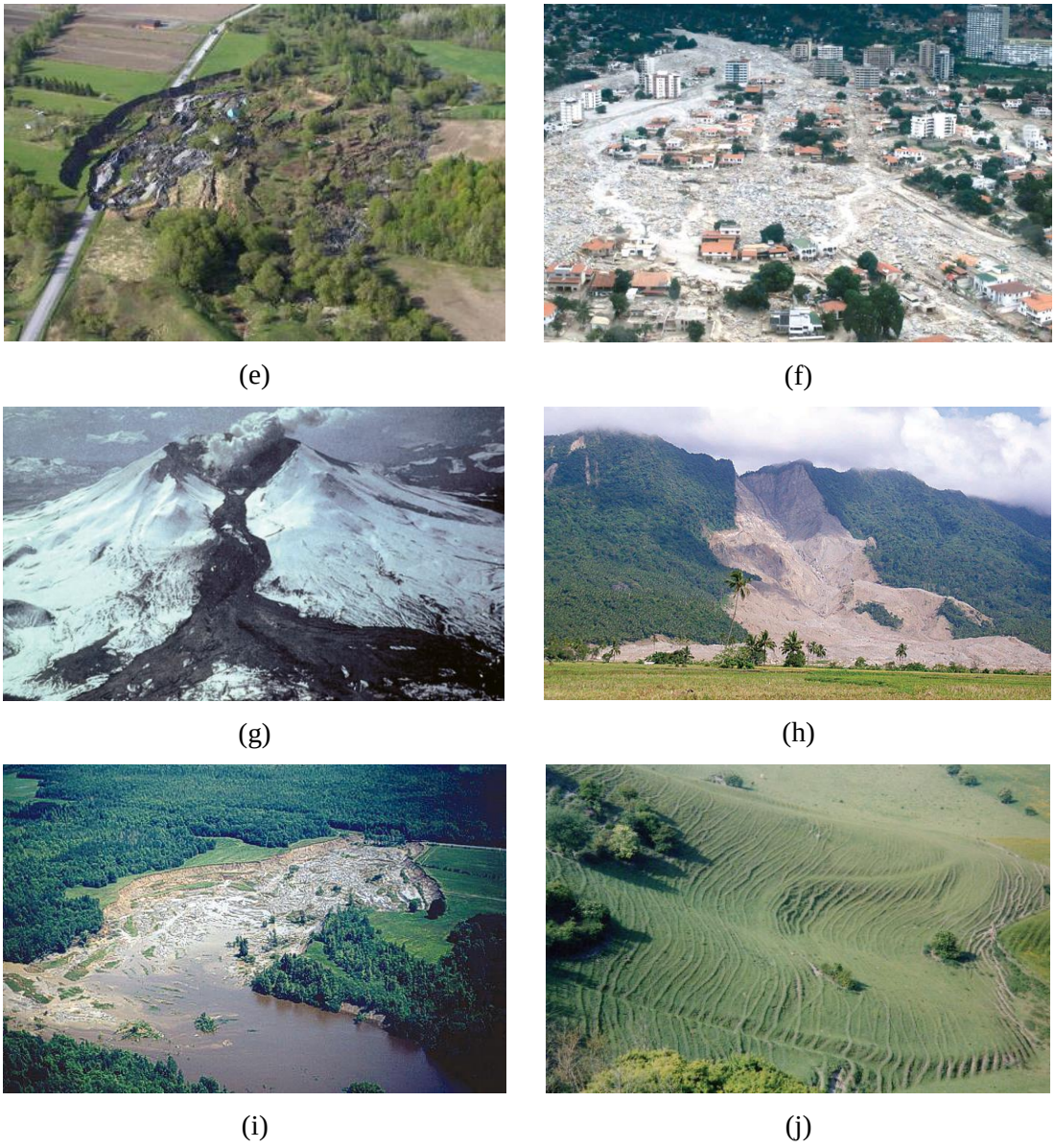

Figure 2.3. Examples of different types of landslides (Highland and Bobrowsky, 2008; Hungr et al., 2014): (a) Rock falls/slides; (b) Block topples; (c) Rotational slides; (d) Translational slides; (e) Lateral spreads; (f) Debris flows; (g) Volcanic mudflows; (h) Debris avalanche; (i) Earthflows; (j) Creep.

Associating with landslide types, the area of landslides can range from less than a few square meters (e.g., shallow soil slides) to hundreds even thousands of square kilometers (e.g., large submarine landslides). The displacement velocity of landslides can range from a few millimeters per year to several meters per second. Depending on landslide displacement velocity, risk of landslides can range from class one (mitigation works can reduce the risk from slow-moving slides) to class seven (there

is an expectation for the loss of life) (Cruden and Varnes, 1996; Schlogel, 2015).

2.2.3. Impacts of Landslides

Landslides represent problematic and widespread geo-hazards worldwide, causing casualties, property damages, and economic losses in mountainous areas globally (Zhao and Lu, 2018). Communities at the foot of mountains and hills are at a greater risk for destruction by landslides. A substantial landslide carries large amounts of rocks, heavy debris or earth, having the capacity to kill many people, cause serious damage to infrastructures (e.g., communication, transportation, power, electricity service, and buildings), and isolate remote communities for emergency rescue. The property value loss, transportation disruption, and cost used to rescue casualties and to repair infrastructures can all cause adverse impacts to enconomy development in local area. A major landslide event could even drain the economy of a local area. Moreover, lots of indirect costs can also be generated by landslides. For instance, the mass of rock, earth, and debris carried by the landslides can cover the downhill of mountain areas, influencing original land use (e.g., agricultural land or social land). If they find a way to the waters, such as rivers and lakes, the availability, quantity, and quality of domestic and irrigation water and fisheries in local area might also be influenced.

Globally, approximately 17% of the fatalities occurred due to landslides with around 66 million people living within high-risk landslide areas worldwide (Hong et al., 2015). Moreover, landslides were said to result in about 1,000 deaths and US 4 billion property damages per year worldwide (Lee and Pradhan, 2007). Earthquake-induced landslides are considered as one of the most important second hazard induced by earthquakes. Approximately 70% of all earthquake-related casualties not caused by shaking were caused by triggered landslides (Marano et al., 2010; Tanyas et al., 2017). From 2004 to 2010, 47,736 causalities caused by earthquake-triggered landslides were reported (Petley, 2012; Kennedy et al., 2015; Tanyas et al., 2017). Consequently, it is considered to be an important issue to assess, manage, or stabilize the potential danger areas by engineering projects or geotechnical studies, such as strengthening slopes, building retaining walls, and making landslide hazard map.

2.3. Geographic Information System (GIS) and Remote Sensing (RS)

2.3.1. Geographic Information System (GIS)

Geographic information system (GIS) is a computer system designed to analyze and manage all kinds of spatial and geographic data. The word geographic in it indicates that some portions of the data are spatial. The concept of GIS was first applied in 1854, when British physician John Snow started to map the breakout of cholera by adding the disease, water lines, roads, and property boundaries into one map, and found that the cholera cases were only along one water line. Then in 1968, the "father of GIS" Roger Tomlinson started to fuse modern computing with maps, raised the term GIS firstly, and made GIS become a true computer-based tool for storing map data (GISGeography; Tomlinson, 1969).

GIS can be used to show various types of data on one map, enabling to observe, analyze, and undestand patterns, trends, and relatinships more easily and clearly. The four main ideas of GIS are to create geographic data, manage it in a database, analyze it to find patterns, and visualize it on a map. Owing to various advantages, GIS has already been extensively applied by people from all walks of life for various purposes, such as scientific investigation, resource management, and development planning (GISGeography). It has also become a popular technology in calculating and managing natural hazards, including landslides, since the middle of 1980s (Chau et al., 2004).

At present, ArcGIS and QGIS are two main and important GIS softwares that specialize in spatial analyses by math in maps and combine geography and modern technologies to quantify, measure, and understand our world. Vector and raster are two common and major formats used in GIS to store data. Vector formats apply points, lines, or polygons to store information and data in thematic layers. Raster formats store data in rows and columns in the form of grids of cells or pixels. The data of them can be either discrete or countinuous (**Figure 2.4**) (GISGeography).

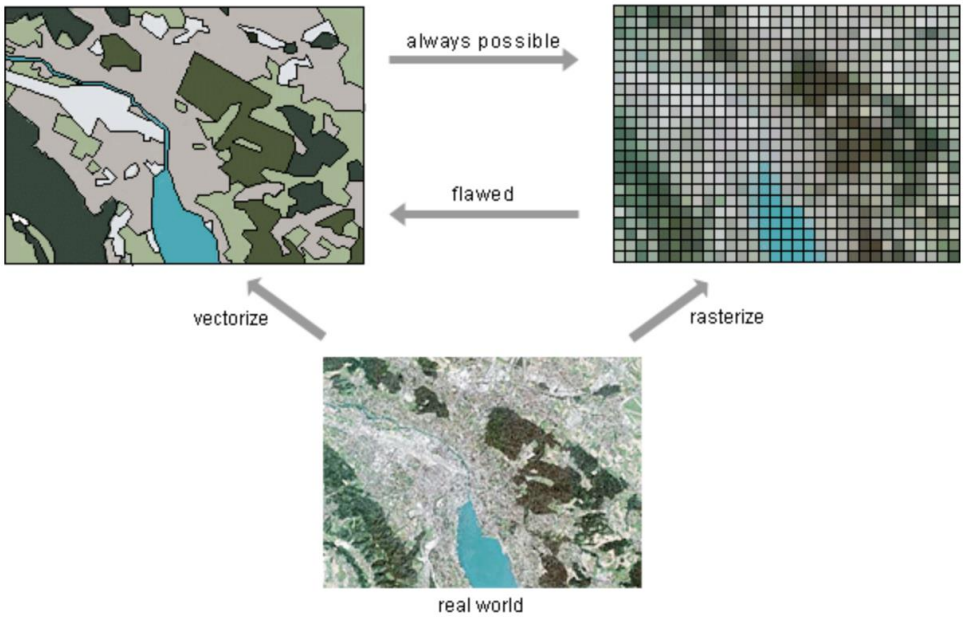

Figure 2.4. Two major types of data formats in geographic information system (GIS).

2.3.2. Remote Sensing (RS)

Remote sensing (RS) is able to collect data for dangerous and inaccessible areas. It is a science of acquiring information about an object or phenomenon from a distance without physical contact, usually via aircrafts or satellites. Satellites of RS can either operate in polar orbits, non-polar orbits, or geostationary orbits. Satellites of polar orbit travel in a plane that is inclined at nearly 90 degrees to the equatorial plane, which can sense the entire globe and capture the regions that are diffcult to reach via the ground. Polar orbits can be either ascending (from south to north) or descending (from north to south). Satellites of non-polar orbit usually operate at an altitude of less than 2,000km above the Earth's surface, which can only cover partial latitudes of the earth. Satellites of geostationary orbit travel at the same rate of the earth following the Earth's rotation, and are able to observe the same place continuously (NASA).

There are two types of sensors in RS: passive sensor and active sensor. Passive sensors use the naturally avaliable energy, which usually refers to the sun's energy (e.g., visible wavelength and thermal infrared wavelength), and measure the energy (radiation) reflected or re-emitted from the objects (**Figure 2.5**). Most of them operate in the visible, infrared, thermal infrared, or microwave portions of the electromagnetic

spectrum (**Figure 2.6**), and usually cannot penetrate dense clouds. Radiometers and spectrometers of different types are examples of passive sensors. Active sensors emit energy to the ground targets by itself and then measure the energy (radiation) backscattered or refelcted from these targets (**Figure 2.5**). They usually operate in the microwave band of the electromagnetic spectrum that has a longer wavelength (**Figure 2.6**), and are able to work at anytime regardless of the weather condition and light. Examples of active RS include light detection and ranging (LiDAR), synthetic aperture radar (SAR), and etc.

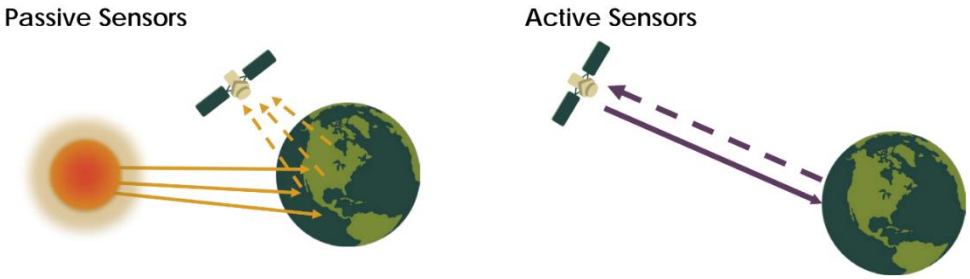

Figure 2.5. Two types of sensors used in remote sensing (RS) (NASA).

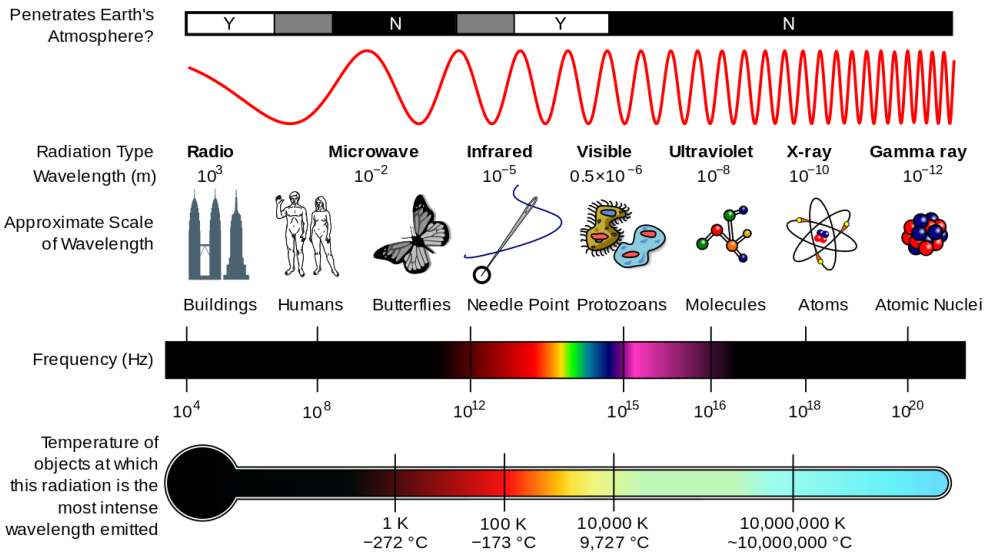

Figure 2.6. Electromagnetic spectrum (Wikiversity).

Resolution is an important factor in a RS image that influences how the image can

be applied. It varies with the orbit of the satellite and the design of the sensor. For any dataset, there are four kinds of resolution: spatial resolution, temporal resolution, spectral resolution, and radiometric resolution. Spatial resolution indicates the area on the Earth's ground represented by each pixel. The higher the spatial resolution, the more detailed information in the ground can be seen. Temporal resolution represents the time needed for a satellite to revisit a same location, which depends on the sensor's characteristics, the orbit, and the swath width. Satellites of geostationary orbit usually have a higher temporal resolution of around 30s to 1min, whereas satellites of polar orbits generally have a temporal resolution between 1 day and 16 days. Spectral resolution means the ability of a sensor to discern wavelengths. For a given band, the narrower the wavelength range, the higher spectral resolution. Radiometric resolution indicates the information amount in each pixel, that is, the bit number used to represent the recorded energy. The higher the radiometric resolution, the more values used to store information, and therefore the better discrimination between energy differences. In specific applications, trade-offs between these four kinds of resolution are usually needed according to demand, as it is hard to assemble all of these desirable features into one remote sensing sensor (NASA).

2.3.3. Synthetic Aperture Radar (SAR)

Synthetic aperture radar (SAR) was first invented in the early 1950s, and was an important and typical kind of active RS. It transmits energies in a side looking to the ground targets and then receives the reflected or backscattered energies. Both amplitude and phase information of the backscattered signal can be recorded by the radar sensor. Amplitude means the intensity or strength of the received signal. It can be influenced by both radar parameters, such as the wavelength (or frequency), polarization, and incidence angle, and surface parameters, such as the roughness, dielectric constant, and structure of objects. Phase indicates the position of a point in time on a waveform cycle. Its value depends on the distance between the radar sensor and the measured ground target.

Wavelength or frequency (the product of frequency and wavelength is the speed of light) of the applied microwave is an important parameter influencing the

application of the generated radar images. According to the frequency or wavelength, the microwaves have been classified into different bands as shown in **Table 2.1**. Among them, the L-band, C-band, and X-band are the predominate wavelenghs applied in present SAR satellites (**Figure 2.7**). In general, the longer the wavelength, the stronger the penetration ability of the microwave.

Table 2.1. Microwave frequency bands.

Band	Frequncy range	Wavelength
HF	3-30 MHz	10-100 m
VHF[3]	30-300 MHz	1-10 m
UHF[3]	300-1000 MHz	30-100 cm
L	1-2 GHz	15-30 cm
S	2-4 GHz	7.5-15 cm
C	4-8 GHz	3.75-7.5 cm
X	8-12 GHz	2.5-3.75 cm
Ku	12-18 GHz	16.7-25 mm
K	18-27 GHz	11.1-16.7 mm
Ka	27-40 GHz	7.5-11.1 mm
V	40-75 GHz	4.0-7.5 mm
W	75-110 GHz	2.7-4.0 mm
mm	110-170 GHz	1.8-2.7 mm

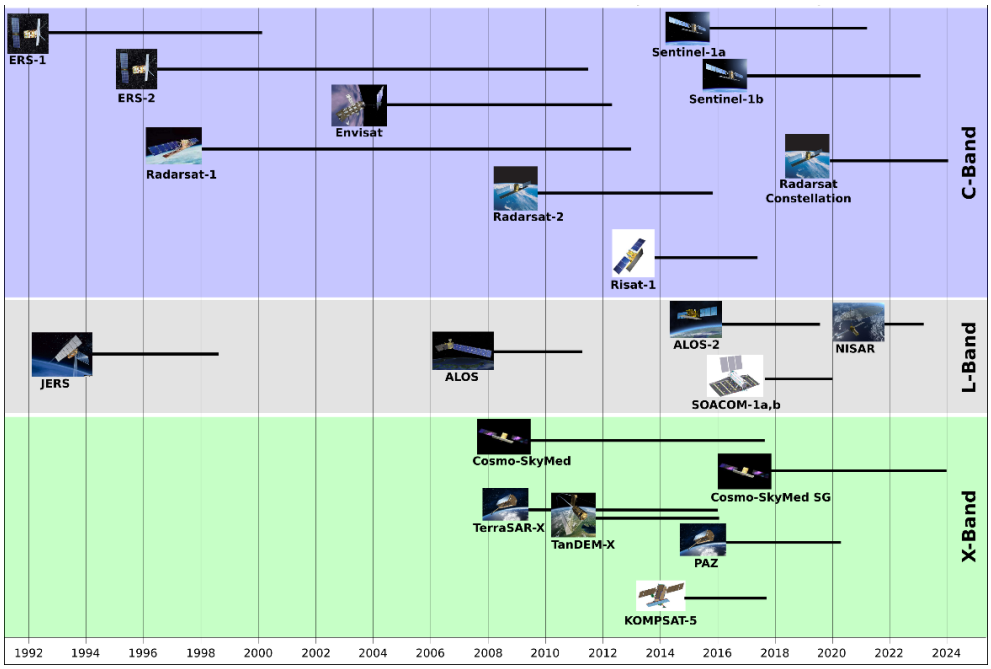

Figure 2.7. Main synthetic aperture radar (SAR) satellites in the world (UNAVCO).

Polarization is also a radar parameter that can influence the condition of the generated radar images. It is another essential property of electromagnetic waves, in addition to amplitude, phase, and frequency. Regardless of wavelength, a SAR platform can transmit horizontally polarized and/or vertically polarized electric field vectors, and then receive horizontally and/or vertically polarized return signals. Therefore, totally, there can be four kinds of polarization images, including horizontal transmit and horizontal receive (HH), horizontal transmit and vertical receive (HV), vertical transmit and horizontal receive (VH), and vertical transmit and vertical receive (VV). Radar images generated under different polarizations can show obvious differences for a specific ground target. For instance, the cross-polarization (HV or VH) measures the part of waves which are polarized at one direction when emitting and polarized at another direction when returning to the sensor, which doesn't happen to a large degree. Accordingly, the intensity of cross-polarization is usually lower than that of co-polarization (HH or VV) in most cases. Surfaces which are likely to cause change in polarization are often characterized by volume scattering (e.g., forest). Usually, a SAR system is designed to operate in either a single polarization mode (HH or VV), a dual-polarization mode (HH and HV or VV and VH), or a quad-polarization (or full-polarization) mode (HH, HV, VH, and VV).

2.4. Disaster and Disaster Management

2.4.1. Disaster

Disasters are defined as serious disruptions of the functioning of a community or a society, owing to the interactions between hazard events and exposure, vulnerability, and capacity conditions of the community or society, resulting in human, material, economic, or environmental losses and impacts (UNDRR, 2017). Hazard means a dangerous condition or event that threats or has the potential to cause casualties, environment damage, or property losses. Vulnerability indicates the extent to which a community or a society is likely to be disrupted by a particular hazard, owing to its nature, construction, and proximity to hazardous terrains or disaster prone areas. Capacity demonstrates the strengths, resources, and means existed in households and communities that enable them to prevent, mitigate, prepare, withstand, cope with, or

rapidly recover from a disaster (Khan et al., 2008).

Disasters can be divided into natural ones and man-made ones. Natural disasters are natural phenomenons or processes that cause casualities or property, environment, economic, or social impacts and damage. Earthquake, landslide, flood, and tsunami are all examples of natural disasters. Human-made disasters are the consequence of human hazards or human negligence, such as transportation accidences, wars, and toxic waste leakage. Moreover, depending on the size of the impacted area, there are small-scale disasters that only impact local communities and large-scale disasters that may influence a society and demand national or international assistance. According to the occurrence probability and return period, there are frequent disasters and infrequent disasters, or slow-onset disasters (e.g., desertification, drought, and epidemic disease) and sudden-onset disasters (e.g., earthquake, flood, and tranport accident) (UNDRR).

Disasters are usually able to cause big physical (buildings, roads, bridges, and etc.), environmental (water, landuse, atmosphere, and etc.), social (life, health, security, and etc.), and enconomic (assets, income, insurance, etc) impacts to a community or society. These impacts can either be direct (e.g., property damage) or indirect (e.g., stress and psychological damage), tangible (that are able to be measured by a financial value) or intangible (e.g., the damage of an artwork). They are usually widespread and can last for a long period of time, even though some are also localized and immediate. When the impacts of a disaster exceed the capabilities of the community or society to response and recover using its own resources, external sources and assistance are needed.

2.4.2. Disaster Management

Disaster management means the organization and management of resources and responsibilities before, during, and after the disaster to reduce or avoid the potential losses from hazards, to assure prompt and appropriate assistance to victims of disaster, and to achieve rapid and effective recovery (Warfield, 2008). Following the course of a disaster, a comprehensive disater management cycle has been proposed to minimize the losses and impacts caused by the disaster. This cycle includes three pre-event

countermeasures of mitigation, preparedness, prediction and early warning before the disaster, and four post-event countermeasures of damage assessment, disater response, recovery, and reconstruction after the disaster (**Figure 2.8**).

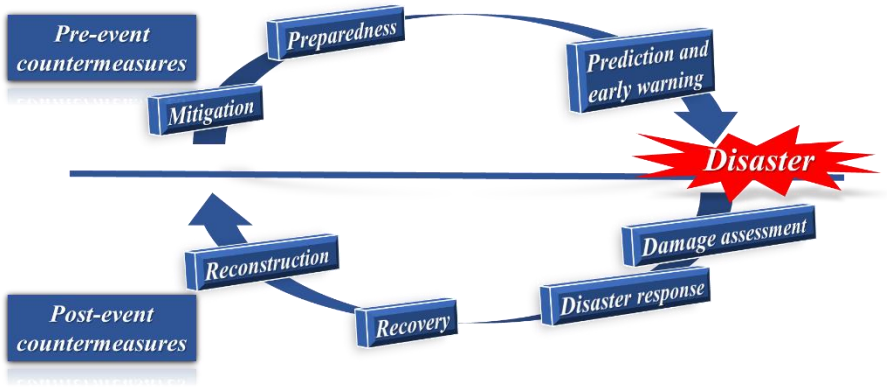

Figure 2.8. Comprehensive disaster management cycle.

Appropriate actions at each step of this disaster management cycle can lead to better preparedness, more favorable warning, reduced damage, and even the prevention from next cycle of the disaster. For instance, in the mitigation step, actions like implementing building codes strictly, performing vulnerability analyses, and conducting public education can be carried out. In the preparedness step, measures such as planning how to respond by making preparedess plans and carrying out emergency exercises and training can be executed. In the assessment and response step, actions like mapping the disaster quickly and carrying out emergency relief and rescue rapidly can be implemented. In the recovery step, measures such as returning the community to normal by temporary housing and good medical care can be applied.

GIS and RS are useful tools in the comprehensive disaster management system, which can provide effective and efficient information at each stage of the system, assisting in understanding the spatial phenomena, and providing authorities and scientists with objective data sources for decision making (Joyce et al., 2009). For instance, in the pre-event countermeasures before a disaster, they can be used for hazard map making, land use planning, hazardous area monitoring, and disaster forecasting. In the post-event countermeasures after the disaster, they can be applied to understand the magnitude and location of the disaster, form a quick damage map, and guide and monitor the recovery and reconstruction process.

2.5. References

BGS. https://www.bgs.ac.uk/landslides/How_does_BGS_classify_landslides.html

Chau, K. T., Sze, Y. L., Fung, M. K., Wong, W. Y., Fong, E. L., Chan, L. C. P. (2004). Landslide hazard analysis for Hong Kong using landslide inventory and GIS. Computer & Geoscience, 30 (4), 429-443.

Cruden, D. M. (1991). A simple definition of a landslide. Bull. Int. Assoc. Eng. Geol. 43(1), 27-29.

Cruden, D. M., Varnes, D. J. (1996). Landslide types and processes, in: Turner, A.K., Schuster, R.L., Landslides Investigation and Mitigation. Washington D.C., pp.36-75.

Disaster Center. http://disastercenter.com/New%20Guide/Landslides.html

EARTH ECLIPSE. https://www.eartheclipse.com/natural-disaster/causes-effects-and-types-of-landslides.html

García-Rodríguez, M. J., Malpica, J. A. (2010). Assessment of earthquake-triggered landslide susceptibility in El Salvador based on an Artificial Neural Network model. Natural Hazards and Earth System Sciences, 10, 1307-1315.

GISGeography. https://gisgeography.com/what-gis-geographic-information-systems/

Global Forest Coalition. https://globalforestcoalition.org/urgent-help-needed-for-those-affected-by-the-dam-tragedy-in-colombia/

Highland, L. M., Bobrowsky, P. (2008). The landslide handbook-a guide to understanding landslides: Reston, Virginia, U.S. Geological Survey Circular 1325, 129.

Hong, H., Pradhan, B., Xu, C., Bui, D. T. (2015). Spatial prediction of landslide hazard at the Yihuang area (China) using two-class kernel logistic regression, alternating decision tree and support vector machines. Catena, 133, 266-281.

Hungr, O., Leroueil, S., Picarelli, L. (2014). The Varnes classification of landslide types, an update. Landslides, 11(2), 167-194.

Joyce, K. E., Wright, K. C., Samsonov, S. V., Ambrosia, V. G. (2009). Remote sensing and the disaster management cycle. In: Jedlovec G (ed) Advances in geoscience and remote sensing, vol 48(7). INTECH, pp 317-346.

Kennedy, I. T. R., Petley, D. N., Williams, R., Murray, V. (2015). A systematic review of the health impacts of mass earth movements (landslides). Plos Currents. doi:10.1371/currents.dis.1d49e84c8bbe678b0e70cf7fc35d0b77

Khan, H., Vasilescu, L. G., Khan, A. (2008). Disaster management cycle - a theoretical approach. Management and Marketing Journal, 6 (1), 43-50.

Lee, S., Pradhan, B. (2007). Landslide hazard mapping at Selangor, Malaysia using frequency ratio and logistic regression models. Landslides, 4(1), 33-41.

Marano, K. D., Wald, D. J., Allen, T. I. (2010). Global earthquake casualties due to secondary effects: A quantitative analysis for improving rapid loss analyses. Natural Hazards, 52(2), 319-328.

NASA. https://earthdata.nasa.gov/learn/remote-sensing

Petley, D. (2012). Global patterns of loss of life from landslides. Geology, 40(10), 927-930.

PHIVOLCS. https://www.phivolcs.dost.gov.ph/index.php

Schlögel, R. (2015). Quantitative landslide hazard assessment with remote sensing observations and statistical modelling. Doctoral Dissertation, University of Strasbourg.

Tanyas, H., Westen, C. J. V., Allstadt, K., Jessee, A. N., Gorum, T., Jibson, R. W., Godt, J. W., Sato, H. P., Schmitt, R. G., Marc, O., et al. (2017). Presentation and analysis of a worldwide database of earthquake-induced landslide inventories. JGR Earth Surface, 122(10), 1991-2015.

The Landslide Blog. https://blogs.agu.org/landslideblog/2018/09/28/hpakant-1/

Tomlinson, R. F. (1969). A geographic information system for regional planning. Department of Forestry and Rural Development, Government of Canada, 200-210.

UNAVCO. https://www.unavco.org/instrumentation/geophysical/imaging/sar-satellites/sar-satellites.html

UNDRR. https://www.preventionweb.net/terminology/view/475

USGS. https://www.usgs.gov/faqs/what-a-landslide-and-what-causes-one?qt-news_science_products=0#qt-news_science_products

Warfield, C. (2008). The disaster management cycle. http://www.gdrc.org/uem/disasters/1-dm_cycle.html

Wikiversity. https://en.wikiversity.org/wiki/Electromagnetic_radiation

Zhao, C., Lu, Z. (2018). Remote sensing of landslides-A review. Remote Sensing, 10(2), 279.

CHAPTER 3

CHARACTERISTICS OF THE LANDSLIDES TRIGGERED IN 2018 HOKKAIDO EASTERN IBURI EARTHQUAKE

3.1. Introduction

In order to have an overall understanding of the whole picture of the landslide event, spatial data of landslide inventory and conditioning factors as well as previous reports and research on the landslide event were collected and studied. A vector map of landslide inventory created by Zhang et al. (2019) was applied to understand the basic condition of the landslides such as sizes and distribution. The maps of digital elevation model (DEM), geology, soil, surface vegetation, and the records of ground motion and precipitation before the disaster were collected from Geospatial Information Authority of Japan (GSI), Geological Survey of Japan (GSJ), National Agriculture and Food Research Organization (NARO), Biodiversity Center of Japan, U.S. Geology Survey (USGS), and Japan Meteorological Agency (JMA), respectively, and used to analyze the distribution and characteristics of the landslide conditioning factors in landslide areas. Previous reports and research concerning field survey and mechanism study of the landslides were also refered and studied to improve the understanding of the landslide event.

3.2. Basic Condition of the Landslides

GSI published a first-hand landslide database several days after the disaster with many landslide sites composed of several or dozens of landslides. Regarding the unreasonable landslide units in this database, Zhang et al. (2019) carried out a manual segmentation and combination according to ridge lines, valley lines, slope aspect, and hillshade derived from a DEM and high-resolution aerial images, creating a detailed landslide inventory map. In this chapter, this detailed landslide inventory map was applied to study the basic condition of the landslides, combing with previous reports and studies.

According to the landslide inventory, the total number and area of the landslides are 5,625 and 46.3 km^2, respectively. The area of single landslide ranges from smaller

than 100 m^2 to larger than 500,000 m^2, with an average value of around 8,000 m^2. There are only 5 landslides with an area smaller than 100 m^2 and 8 landslides with an area larger than 100,000 m^2. The overall distribution of the landslide size is shown in **Figure 3.1**, from which it can be seen that more than half of the landslides have an area smaller than 5,000 m^2 and around 80% of the landslides have an area smaller than 12,000 m^2. The landslides are basically small- to medium-sized. The average size of most landslides was said to be smaller than what is commonly observed for other earthquakes (Wang et al., 2019).

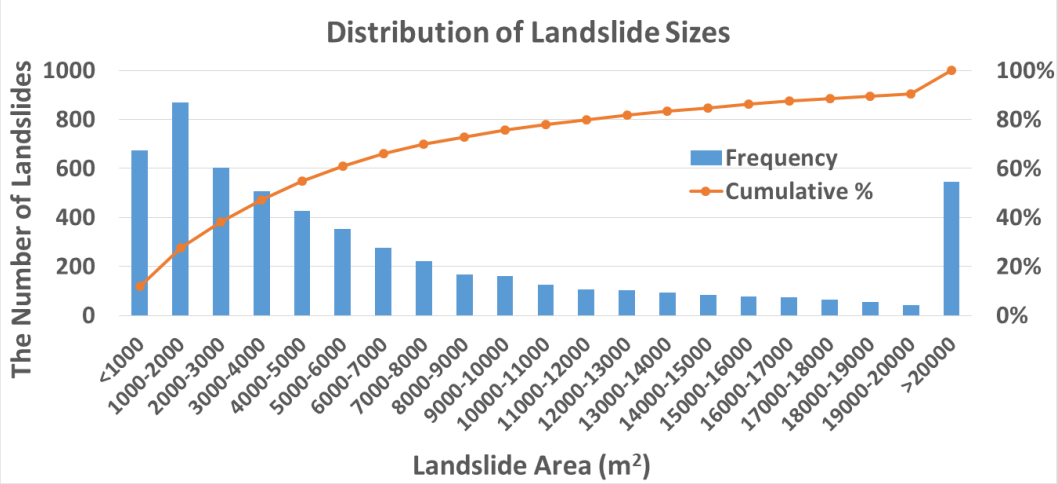

Figure 3.1. Distribution of the landslide size.

Moreover, these landslides are densely distributed in an area of the transition zone from Hidaka Mountains to Ishikari Depression. They are basically in the north of the earthquake epicenter and are approximately within 25km from the epicenter, with most in Atsuma town and some in Mukawa town and Abira town. The density of the landslides was said to be higher than what is observed for landslides triggered by other earthquakes with a similar focus depth (Wang et al., 2019). Most landslides are shallow with a slip surface above the basement complex and have a depth of several meters, moving down the volcano activity related soils with a high water content. Rare deep-seated landslides whose slip surface is within the basement complex also exist, with a large one even formed a landslide dam in the Hidaka-Horonai river (Kuwamura et al., 2019).

These landslides mainly occurred in valley terrain and planar slopes with high mobility and long run-out. Those occurred in vally terrain usually had a longer flow length than those occured in planar slopes. The upper slip surface of most landslides is exposed without overlapping slide mass, showing brownish patches over hill areas. Several types of landslides exist, such as translational earth slide, translational earth block slide, earth flow, and translational rock slide as shown in **Figure 1.2** (Osanai et al., 2019). The characteristics of the landslides are more like those of the rainfall-induced landslides, even though the direct trigger is earthquake, which might be due to the accumulation of previous precipitation in the special light porous soil types here.

3.3. Conditioning Factors of the Landslides

3.3.1. Topography

Topography factors such as elevation, slope gradient, slope aspect, and slope curvature are considered to be associated with landslide occurrence, and have already been widely used as conditioning factors to evaluate landslide hazards and risks.

Elevation is the height of the slope, which can be derived from a DEM directly. It can influence the condition of a slope such as local climate, temperature, soil type, and vegetation type, and therefore influences the stability condition of the slope.

Slope gradient is the first derivative of surface elevation, which represents the change rate of elevation. It is an important parameter influencing the balance between the force and the capability of a slope. Generally, the larger the slope gradient value, the steeper the slope, and the higher the landslide occurrence probability.

Slope aspect identifies the downslope direction of the maximum change rate from a point to its neighbors, and can be understood as the orientation of a slope. It can affect the exposure of the slope to sunlight, precipitation, and wind, which indirectly influce other factors that contribute to landslide occurrence such as rock weathering, soil moisture, and vegetation cover. The aspect of a slope can be north, northeast, east, southeast, south, southwest, west, northwest, and flat.

Slope curvature is the second derivative of surface elevation, and displays the shape of the slope, either concave or convex. There are generally three types of curvature

(planform curvature, profile curvature, and standard curvature), which highlight different aspects of the slope shape. Planform curvature is the curvature in a horizontal plane, perpendicular to the direction of the maximum slope, which influences the convergence and divergence of flow across a surface. Its values are positive for convex areas and negative for concave areas, and can be used to distinguish valleys and ridges (**Figure 3.2a**). Profile curvature indicates the curvature in the maximum slope direction and is parallel to the slope. It affects the acceleration and deceleration of flow across the surface, and hence impacts the erosion and deposition. Its values are positive for concave areas and negative for convex areas (**Figure 3.2b**). Standard curvature is the derivative of the slope surface instead of the line formed by the intersection of the slope surface with a plane like the planform curvature and profile curvature. Its values are positive for convex areas or peaks, negative for concave areas or valleys, and zero for flat areas or saddles (**Figure 3.2c**).

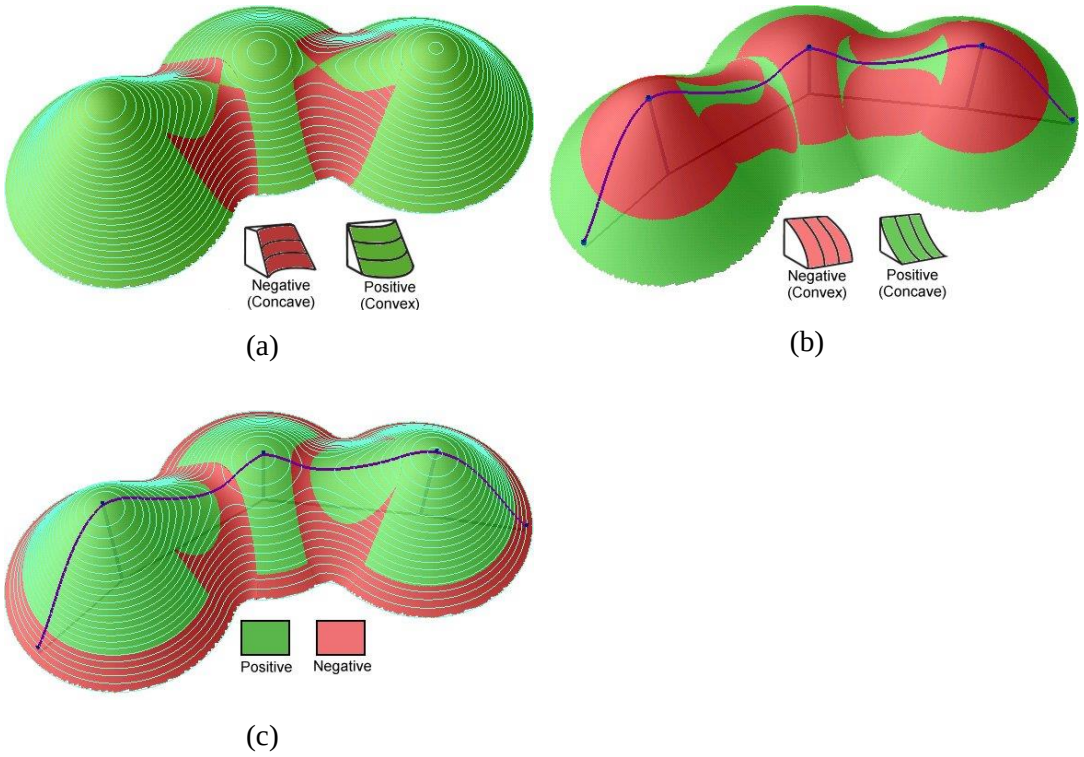

Figure 3.2. Three types of curvature: (a) Planform curvature; (b) Profile curvature; (c) Standard curvature (Raster Curvature).

In this case, most landslides were in mountainous areas of the east from Atsuma town and some were in relatively flat hills of the west from Atsuma town. In order to

have a intuitive and quantitative understanding of the topography characteristics in the landslide areas, a 10m resolution DEM acquired from GSI was applied to derive and calculate the slope characteristics mentioned above. The elevation values were obtained directly from the DEM. The slope gradient, slope aspect, and slope curvature including planform curvature, profile curvature, and standard curvature were derived by calculating the first and second derivatives of the DEM.

After these topography characteristics were calculated, the histograms of them were drawn to get a clear understanding of the topography characteristics in the landslide areas (**Figures 3.4-3.7**). As the landslide sizes varied a lot according to **Section 3.2**, histograms for both landslide number and landslide area were both displayed. Moreover, the general topography condition within the rough overall landslide region (ellipse area in **Figure 3.3**) and the ratio between the landslide area and total area within this region for each group were also drawn. What should be noted is that these two kinds of figures might change with the selection of general landslide region, the ellipse area in this case is just as an example to provide a better understanding of the relationship between landslide occurrence and topography characteristics in this case.

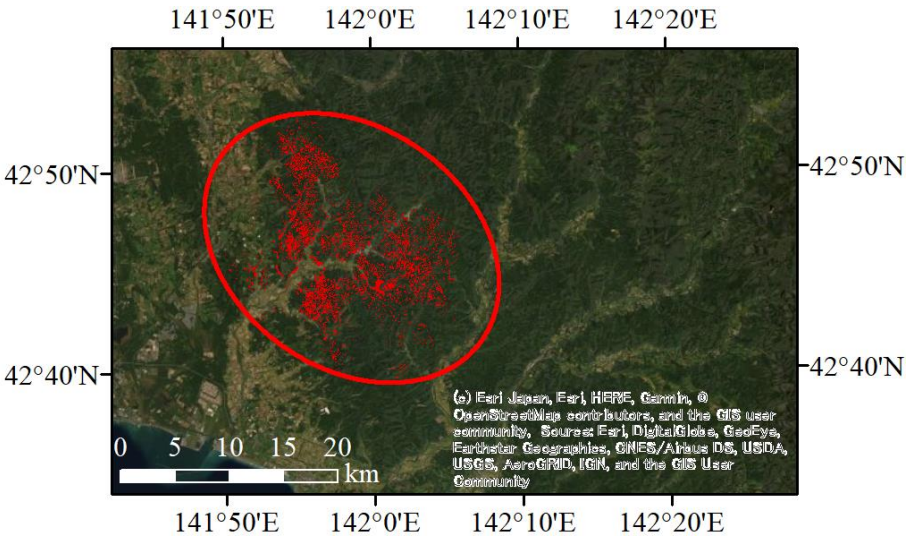

Figure 3.3. Landslide area.

As it can be seen from **Figure 3.4**, most of the areas in this region have an elevation of lower than 300m, and the majority of landslide occurred in areas with an

elevation of 100m-200m. The general elevation of the collapsed slopes was lower than the mean value obtained from a worldwide database of coseismic landslides (534m) (Tanyas et al., 2017), due to local topograpgy characteristics.

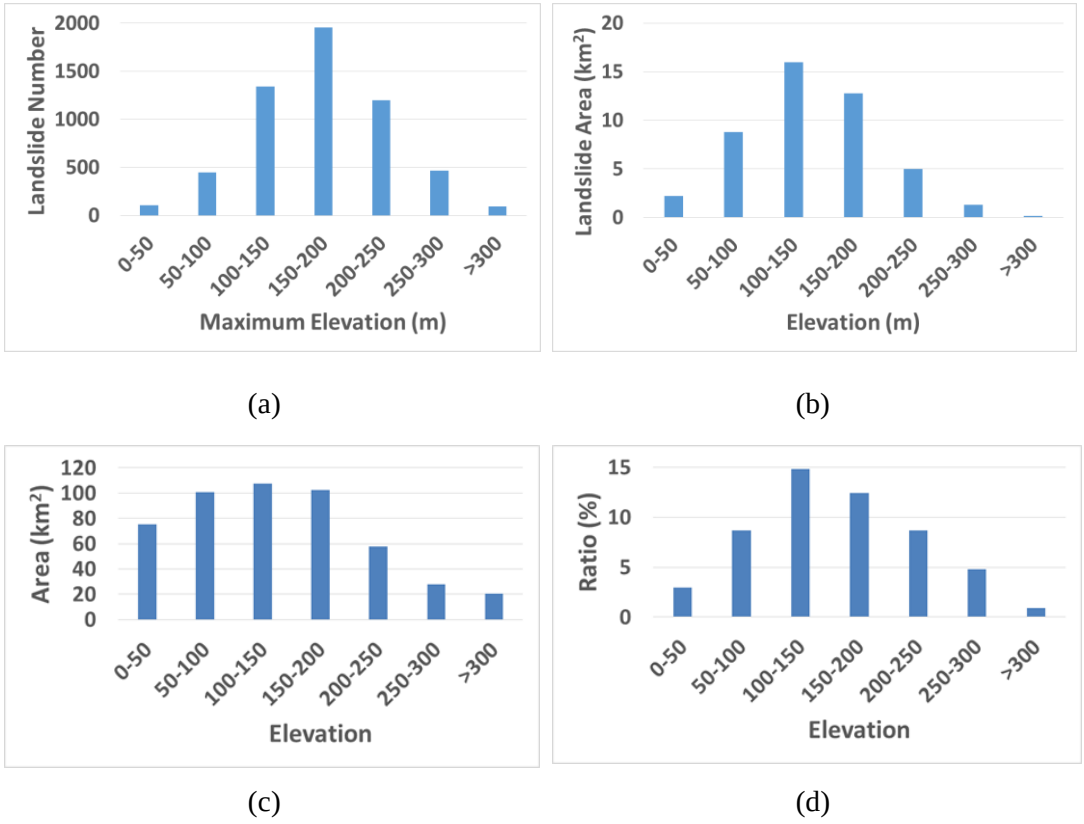

Figure 3.4. Histogram of elevation distribution: (a) Landslide number; (b) Landslide area; (c) Overall landslide region; (d) Ratio between landslide area and total area within the overall landslide region.

From **Figure 3.5** it can be seen that the majority of landslides occurred in regions with a slope gradient of around 15°-35°. The general slope gradient of the collapsed slopes is smaller comparing with other landslides. For instance, in previous studies, Okamoto and Murata (2016) indicated that rainfall-induced landslides and earthquake-induced landslides frequently occurred in slopes with an slope gradient of 30°-40° and 35°-55°, respectively, in the study of past landslides in Japan. Evan et al., (1999) demonstrated that, in general, the most susceptibility slopes are those with angles of around 35°-40° in the study of natural terrain landslides in Hong Kong. Tseng et al., (2015) showed that the rainfall-induced landslides by 2011 Typhoon Nanmadol in Taiwan mainly distributed in slopes with an slope gradient of 30°-55°.

Guo et al., (2017) indicated that 1,315 of 1,418 landslides triggered by 2015 Gorkha earthquake in Nepal distributed in slopes with an slope gradient of 20°-50°. Zhang et al., (2019) found that 79% of slope collapse cases had a slope of 30°-50° among the 1,610 collapse data in the past 15 years studied by them.

In this case, besides the majority gradient of the collapsed slope is 15°-35°, some landslides even occurred in slopes with a gradient gentler than 15°, such as those in Horosato area of Atsuma town and those in Hayakitamizuho area of Abira town. This might be owing to local topography characetristics (most areas in this region have a slope gradient smaller than 40° as can be seen from **Figure 3.5 (c)**) and also the types (mainly shallow earth flows and earth slides) and special mechanism (the combinational impact of the special porous soil, precipitation, and earthquake) of the landslides.

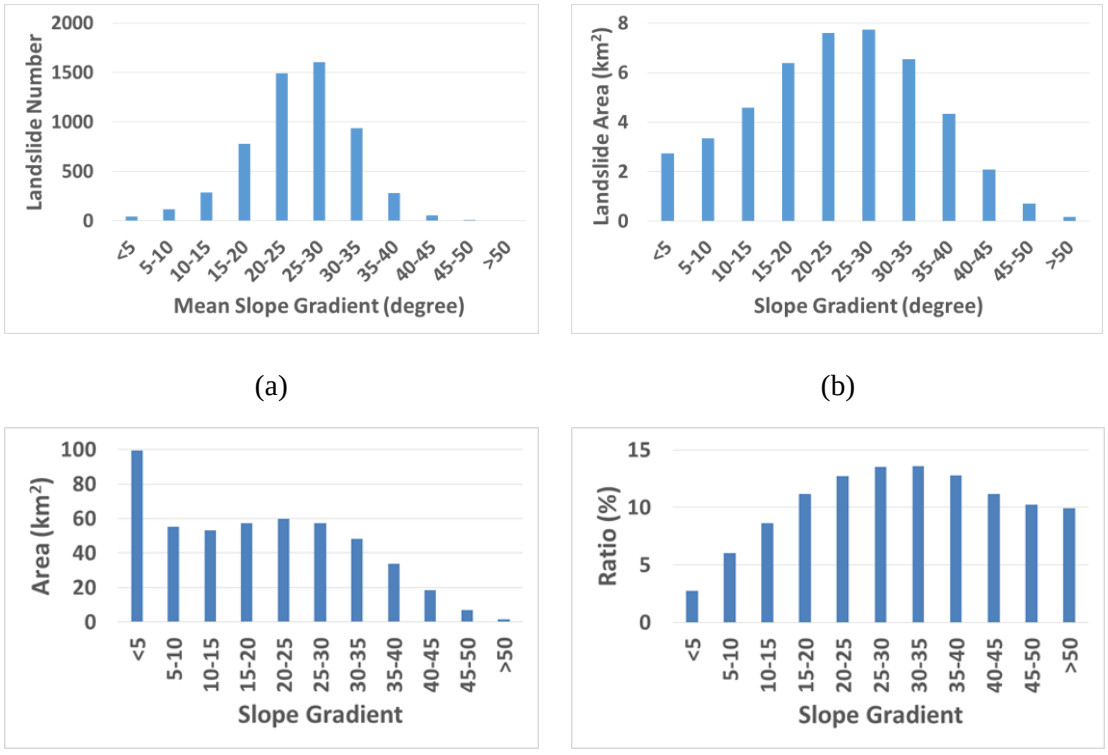

Figure 3.5. Histogram of slope gradient distribution: (a) Landslide number; (b) Landslide area; (c) Overall landslide region; (d) Ratio between landslide area and total area within the overall landslide region.

Figure 3.6 shows that, generally, the relatively preferred slope aspect of the landslides was south, facing the earthquake epicenter, which might relate to ground motion characteristics or local climate conditions of south-faced slopes, such as sunlight exposure condition, precipitation condition, and wind erosion condition.

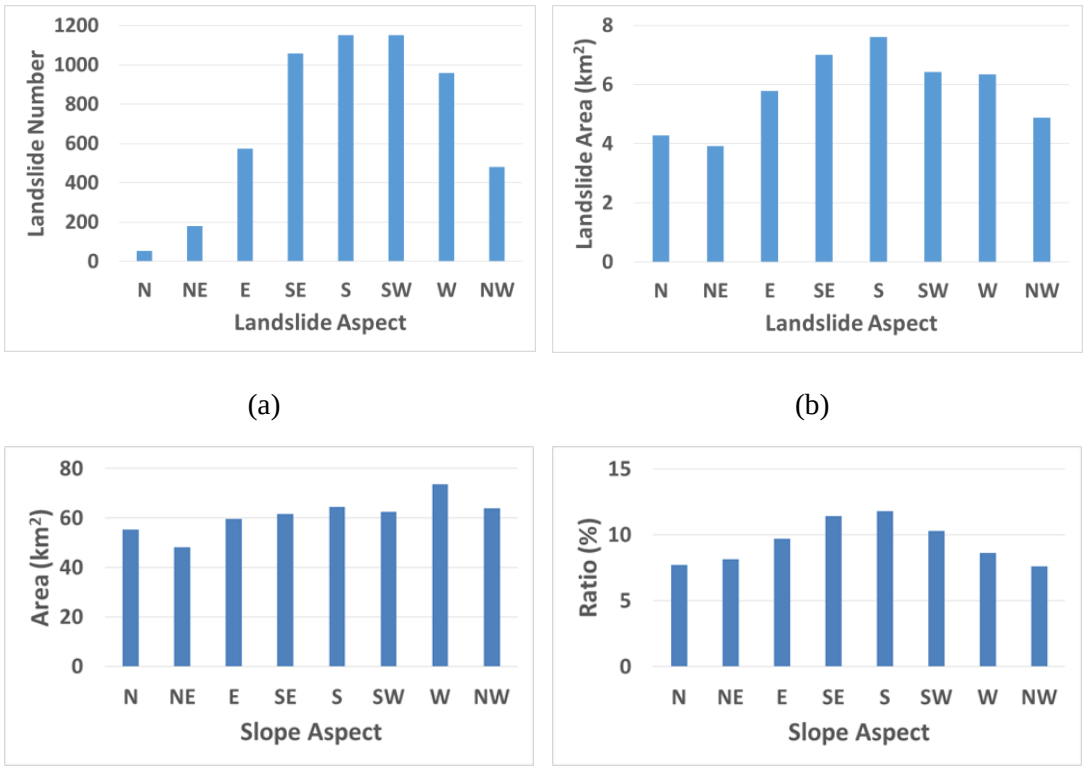

Figure 3.6. Histogram of slope aspect distribution: (a) Landslide number; (b) Landslide area; (c) Overall landslide region; (d) Ratio between landslide area and total area within the overall landslide region (N: North; NE: Northeast; E: East; SE: Southeast; S: South; SW: Southwest; W: West; NW: Northwest).

Figure 3.7 shows that the relatively preferred types of slope curvature were concave profile curvature, concave planform curvature, and concave standard curvature, respectively, even though the overall region have more areas with convex topography. This may be due to the hydrological characteristics of these kinds of terrains.

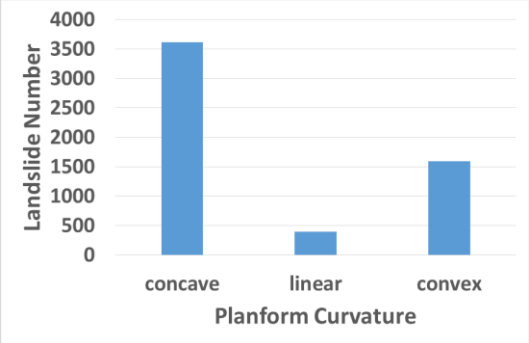
Landslide Number
4000
3500
3000
2500
2000
1500
1000
500
0
concave
linear
convex
Planform Curvature

(a)

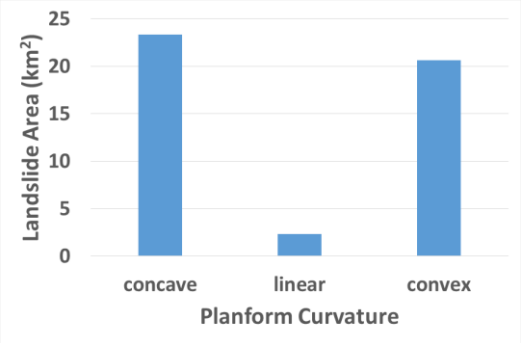
Landslide Area (km²)
25
20
15
10
5
0
concave
linear
convex
Planform Curvature

(b)

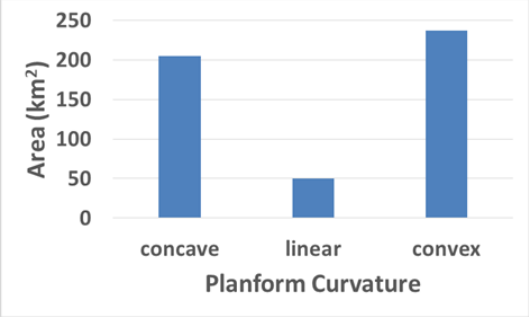
Area (km²)
250
200
150
100
50
0
concave
linear
convex
Planform Curvature

(c)

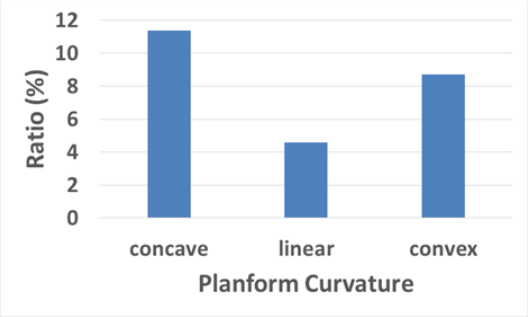
Ratio (%)
12
10
8
6
4
2
0
concave
linear
convex
Planform Curvature

(d)

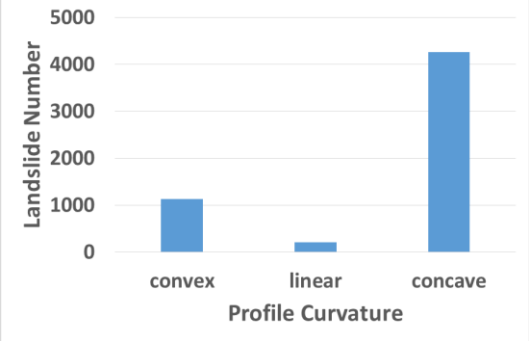
Landslide Number
5000
4000
3000
2000
1000
0
convex
linear
concave
Profile Curvature

(e)

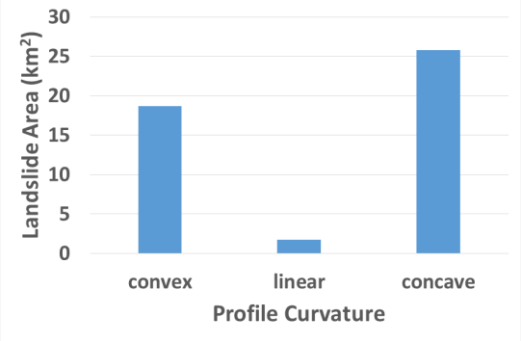
Landslide Area (km²)
30
25
20
15
10
5
0
convex
linear
concave
Profile Curvature

(f)

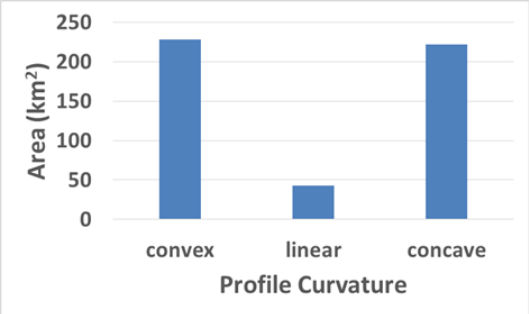
Area (km²)
250
200
150
100
50
0
convex
linear
concave
Profile Curvature

(g)

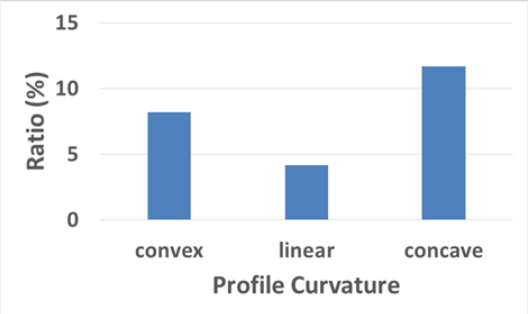
Ratio (%)
15
10
5
0
convex
linear
concave
Profile Curvature

(h)

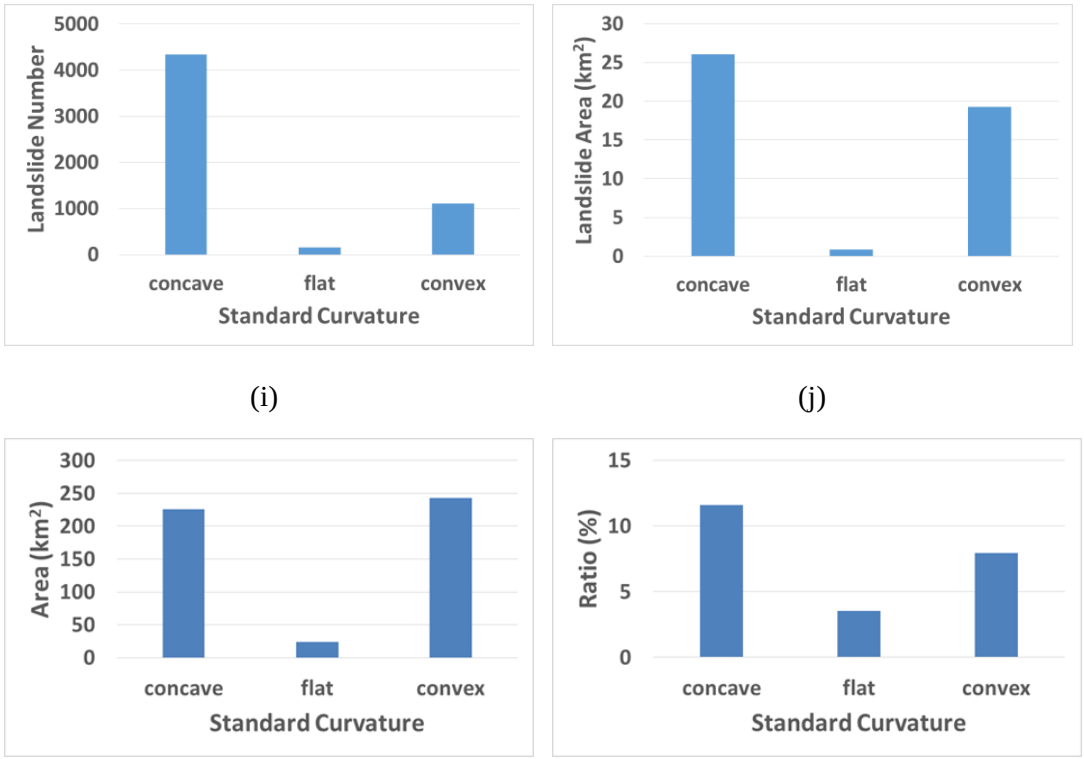

Figure 3.7. Histogram of slope curvature distribution: (a), (b), (c), and (d) are landslide number, landslide area, overall landslide region, and ratio between landslide area and total area within the overall landslide region for planform curvature, respectively; (e), (f), (g), and (h) are these figures for profile curvature; (i), (j), (k), and (l) are these figures for standard curvature.

Moreover, the geomorphologic and hydrologic features of a slope, such as topographic wetness index (TWI), stream power index (SPI), and sediment transport index (STI) can also be derived by the topography information. They can affect the drainage network and hydrological processes of the slope, and hence might also influence the slope stability. TWI, SPI, and STI are all functions of slope gradient and upstream contributing area (flow accumulation), which can be calculated by **Equations 3.1-3.3**, respectively. In all of the three equations, β indicates the slope gradient and A_s means the upstream area (number of upstream elements multiplied by the area of the grid cell).

TWI is a steady state wetness, which can reflect the soil moisture and is commonly used to quantify topographic control on hydrological process. Areas with high TWI

values (e.g., flats and channels) are not prone to slope failures whereas areas with low TWI values usually have low saturation capacity (e.g., ridges). SPI is a measure for the erosion power of land flow. The larger the slope gradient and upstream area, the larger the SPI value. STI is an indicator measuring the process of erosion and deposition, which weights the upstream area stronger than the slope gradient as is shown in **Equation 3.3**. The calcualtion shows that the majority values of TWI, SPI, and STI in landslide areas were around 3-6, 0-60, and 0-20, respectively.

$$TWI = \ln(A_s/\tan\beta) \tag{3.1}$$

$$SPI = A_s * \tan\beta \tag{3.2}$$

$$STI = (A_s/22.13)^{0.6} * (\sin\beta/0.0896)^{1.3} \tag{3.3}$$

3.3.2. Geology and Soil

Geology condition of an area also influences the stability of slopes there, even though the slope failures are controlled by surface soil, as the soil thickness and hillslope sediment supply is usually impacted by the bedrock (Wang et al., 2019). In order to understand the distribution of geology in the landslide areas, a geology map was collected from GSJ. It was a polygon vector map with a scale of 1:200,000. Using this map, the geology types in the landslide areas were summarized and shown in **Figure 3.8**. As it can be seen from this figure, most of the landslides distributed in areas with the bedrock of N2sn (Middle to Late Miocene marine and non-marine sediments). Some distributed in areas with the bedrock of N3sn (Late Miocene to Pliocene marine and non-marine sediments). According to GSJ, both of these two kinds of bedrock were mainly conglomerate, sandstone, and mudstone.

Above these bedrocks, there were several meters' volcano activity related soil layers, as the volcanoes located around 40km-70km west of this area around Lake Shikotsu distributed tephra throughout there. In an ascending order, these volcanic soil layers mainly included Spfa1 layer erupted from Shikotsu caldera (42.771°N, 141.358°E) in Late Pleistocene period, En-a layer erupted from Eniwa volcano (42.793°N, 141.285°E) in Late Pleistocene to Holocene period, and Ta-d and Ta-b

layers erupted Tarumae volcano (42.690°N, 141.377°E) in Holocene period. These volcanic soils seemed to be porous, soft, and have a high water storage capability according to the field survey and test of JGS (2019).

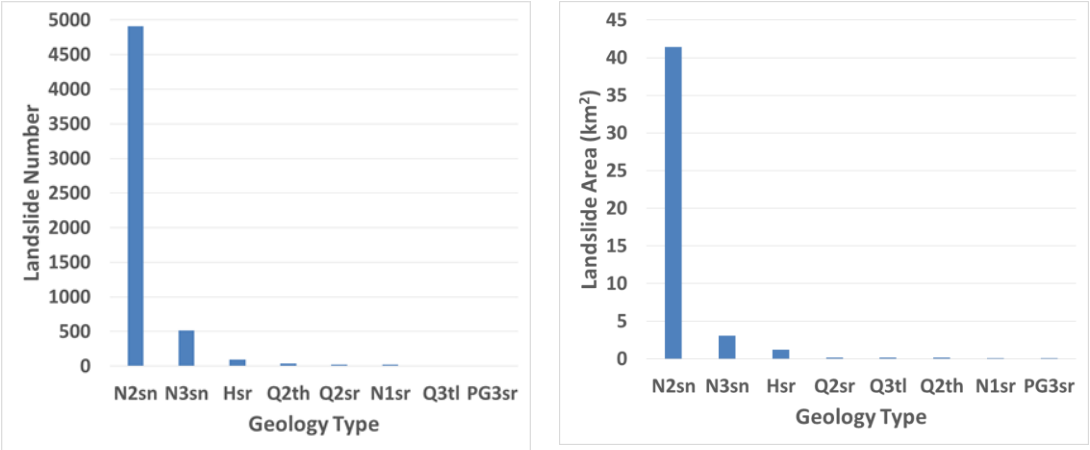

(a) (b)

Figure 3.8. Geology distribution: (a) Landslide number; (b) Landslide area (N2sn: Middle to Late Miocene marine and non-marine sediments; N3sn: Late Miocene to Pliocene marine and non-marine sediments; Hsr: Late Pleistocene to Holocene marine and non-marine sediments; Q2th: Middle Pleistocene higher terrace; Q2sr: Middle Pleistocene marine and non-marine sediments; N1sr: Early Miocene to Middle Miocene marine and non-marine sediments; Q3tl: Late Pleistocene lower terrace; PG3sr: Late Eocene to Early Olligocene marine and non-marine sediments).

Spfa1 was erupted around 46,000 years ago from Shikotsu caldera, and was a white fine-grained pumice fall deposit layer with a maximum thickness of around 4m in the landslide areas. En-a was erupted around 19,000~21,000 years ago from Mount Eniwa, and was a yellow-white pumice fall deposit layer with a maximum thickness of 1m there. Ta-d was erupted about 9,000 years ago from Tarumae volcano, and was reddish brown to yellowish brown pumice fall deposit layer with a maximum thickness of 1m there. It could be easily crushed with fingers according to JGS (2019). Ta-b was erupted around 1667 from Tarumae volcano, and was a white pumice fall deposit layer with a maximum thickness of 0.64m there (**Figure 3.9**) (Hirose at al., 2018; JGS, 2019; Ito et al., 2020). Moreover, between these layers, there were also other layers that were thinner than 0.5m, such as humus layer, weathered layer of the

previous layer, Ta-a and Ta-c erupted from Tarumea volcano 1739 and 2500 years ago, and other volcanic soils disrupted from volcanos in south Hokkaido (JGS, 2019).

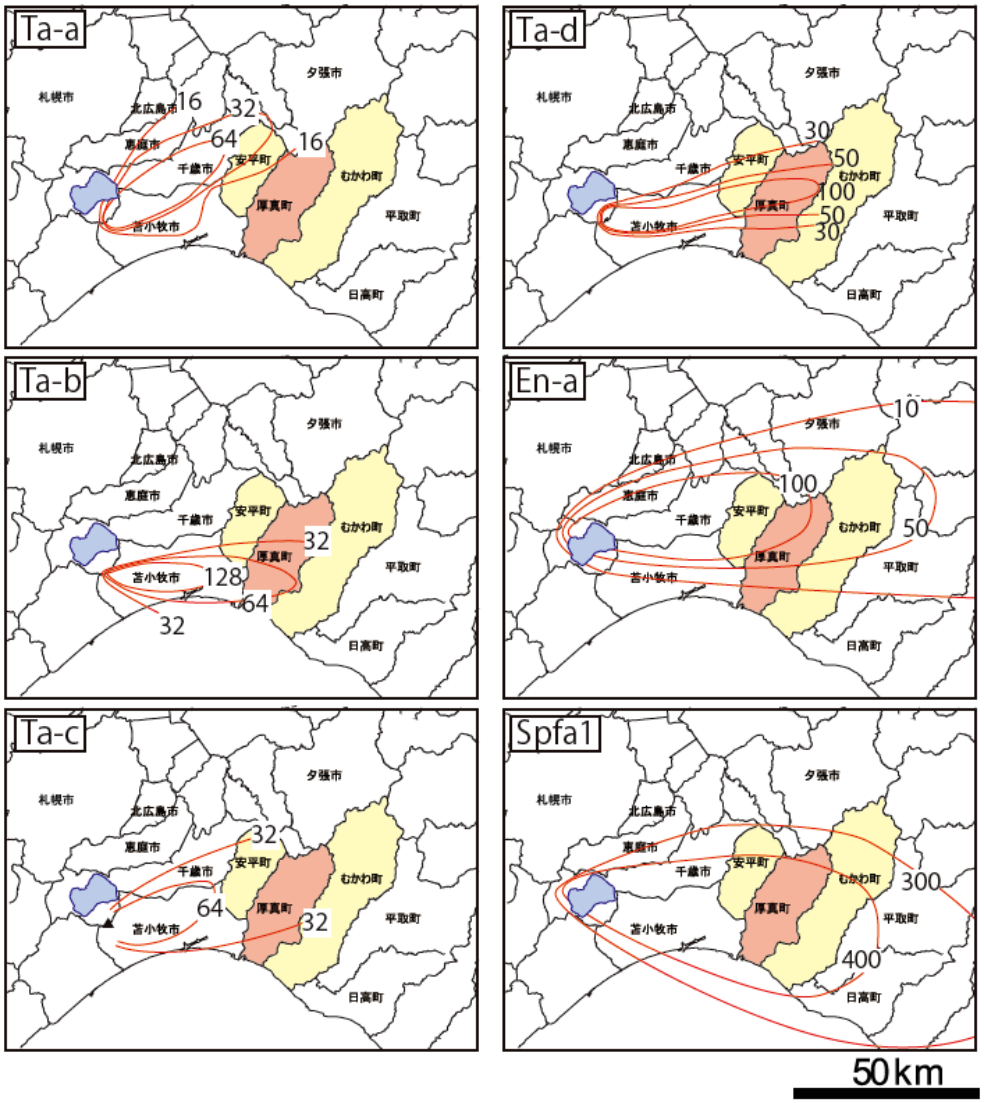

Figure 3.9. Distribution of late Pleistocene and Holocene volcanic soils for Atsuma Town and surrounding area (Hirose at al., 2018).

These volcanic soil layers covered the bedrock or a weathered layer of the bedrock directly. Depending on original thickness, slope gradient, slope aspect, and erosion process, the thickness and completeness of each layer varied from area to area. In gentle and flat areas, all of these layers might be preserved well, while in steep slopes or in areas near to rivers, some layers might have already been lost due to river erosion and solifluction (**Figure 3.10**). For instance, in Atsuma town, the layers older than Ta-

d were found to be lost, while in areas from Atsuma town to Abira town, the layers older than En-a or Spfa-1 were also observed (Kuwamura et al., 2019).

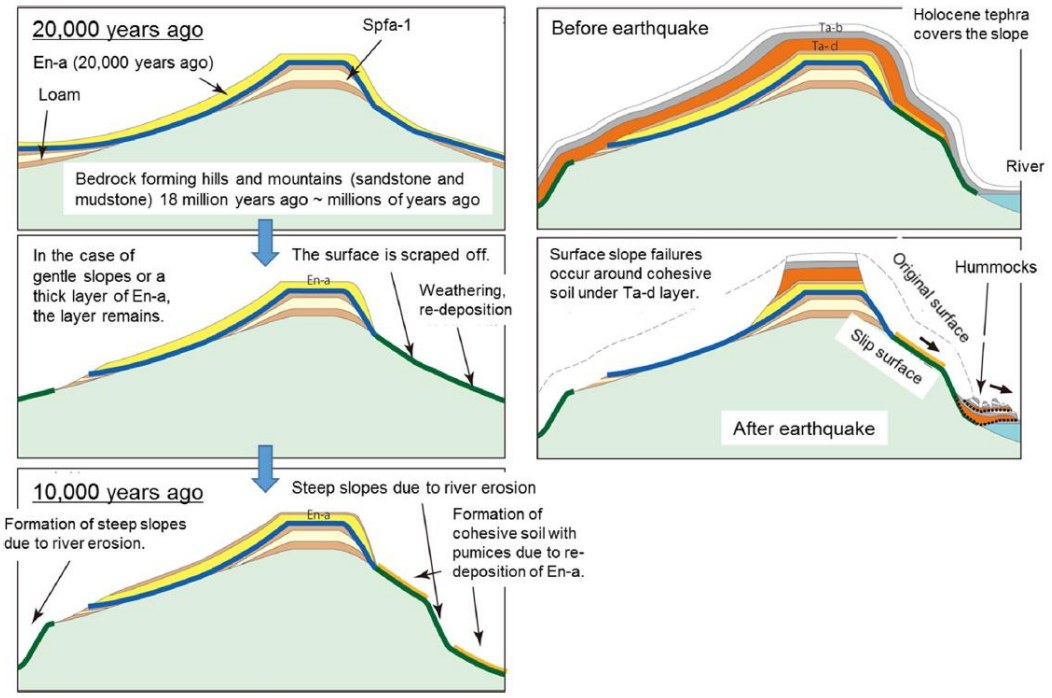

Figure 3.10. An example of slope evolution and movement process (Kuwamura at al., 2019).

The slipe surface of most landslides were in these volcanic soil layers. According to the report of JGS (2019), it is highly possible that the slip surface of the landslides in Yoshino area, Tomisato area, and Uryu area of Astuma town was at the boundary of Ta-d layer, and the slipe surface of landslides in Hayakitamizuho area of Abira town was in the weathered layer of mudstone or the loam layer below the En-a or Spfa1 layer (**Table 3.1**). These light porous volcano materials above the hard bedrock inundated by accumulated precipitation before the earthquake slided away after the shear force of the earthquake ruptured the strata, which was thought as the possible mechanism of most landslides in this case.

Moreover, according to a 1:200,000 scale soil map from NARO, the main types of surface soil in the landslide areas were D1(未熟黒ボク土) and J1 (火山放出物未熟土) (**Figure 3.11**). Both of these two types of soil are mainly composed of light porous volcanic soil that are unconsolidated, less cohesive, highly compressible, and easy to absorb and store water. According to NARO, D (黒ボク土) is the light soil

mainly composed of volcanic ash, which displays black due to the accumulation of organics and has high phosphoric acid absorption coefficient. It has a good capability of water retention and permeability, and can reflect the distribution of active volcanoes and volcanoes that had been active 20,000~30,000 years ago. Around 31% of the national land in Japan is coverd by D soil. D1 is one type of the D soil that has been subjected to certain amount of soil action and has shown the property of fixing phosphoric acid and the accumulation of organics. J1 is the immature soil consisting of unweathered volcanic ash and pumice. It generally includes few organics and clay.

Table 3.1. Possible slip surface of the surveyed landslides in different areas according to the report of JGS (2019).

Area	Slipe surface
Yoshino, Tomisato, and Uryu area of Astuma town	Ta-d layer
Horonai area	Bedrock for the deep-seated landslide and boundary between the weathered layer of the bedrock and Ta-d layer for other landslides
Hayakitamizuho area of Abira town	The weathered layer of mudstone or the loam layer below the En-a or Spfa1 layer

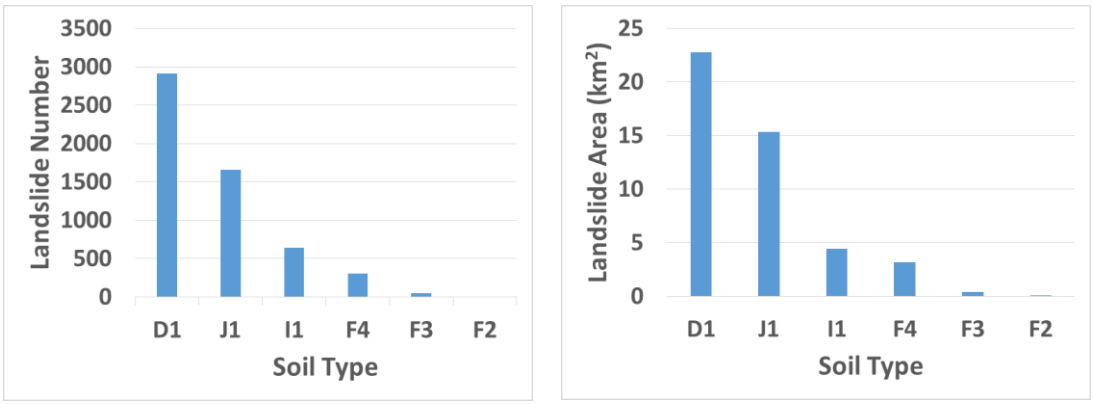

(a) (b)

Figure 3.11. Soil distribution: (a) Landslide number; (b) Landslide area (D1: 未熟黒ボク土; J1: 火山放出物未熟土; I1: 褐色森林土; F4: 褐色低地土; F3: 灰色低地土; F2: グライ低地土).

3.3.3. Surface Vegetation

Surface vegetation can either promote or hinder the stability of a slope, due to the complex combination among soil types, plant species, rainfall, slope aspect, and etc. It can affect the slope stability by means of wind throwing, water removal, mass of vegetation, or mechanical reinforcement of roots.

In the case, the landslides were mainly occurred in areas covered by trees. In order to understand the vegetation types in the landslide areas, a surface vegetation map was collected from the Biodiversity Center of Japan. This map was a polygon vector map with a scale of 1:50,000. Applying this map, the vegetation types in the landslide areas were summarized and shown in **Figure 3.12**. As it can be seen from this figure , the predominated vegetation types in the landslide areas were エゾイタヤーシナノキ (around 52%), 落葉針葉樹植林 (around 24%), and ミズナラーカシワーコナラ群落 (around 8%).

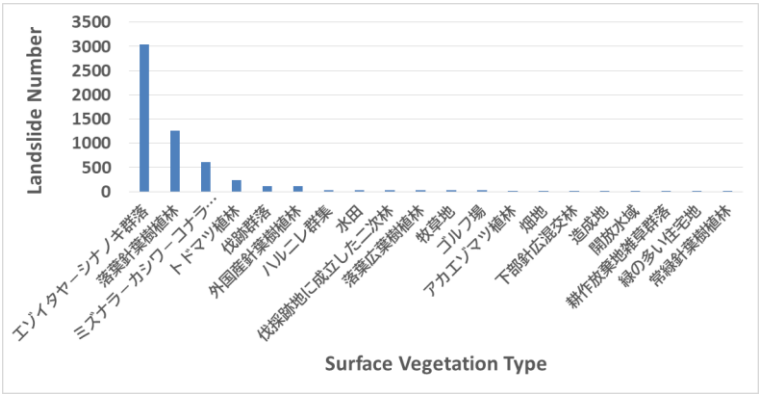

(a)

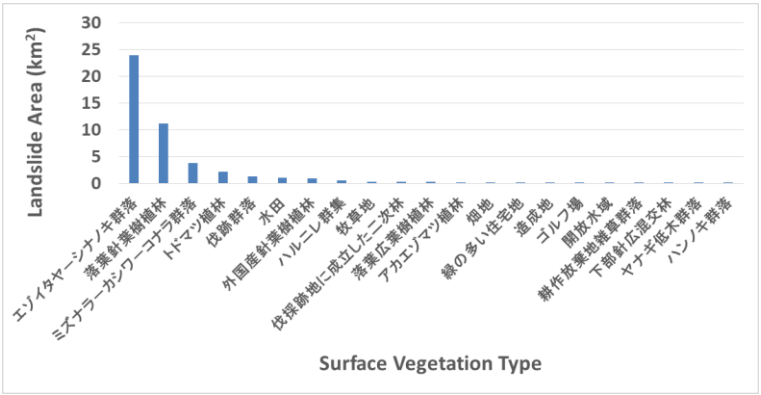

(b)

Figure 3.12. Surface vegetation distribution: (a) Landslide number; (b) Landslide area.

3.3.4. Precipitation

Prolonged precipitation and intense heavy rainfall are frequent and widespread triggers of landslides. They may add additional water loading to the slope, reduce the strength of soil on the slope, remove soil particles from the slope, or change the materials in the slope, which are all able to influence the stability of the slope and cause landslides. Rainfall-caused landslides are usually small, shallow (less than a few meters deep), run rapidly, and sometimes transform into debris flows. Even in an earthquake-induced landslides, the antecedent precipitation can also affect the number, distribution, and style of the landslides.

In order to understand the precipitation condition of the landslide area before the disaster, precipitation records within one month before the landslides were collected from JMA. There were totally 14 valid rainfall stations in Iburi, Hokkaido, Japan with four around the landslide areas (**Figure 3.13**) that recorded past precipitation data. Using these data, the precipitation condition in this area before the disaster were analyzed and shown in **Figures 3.14** and **3.15**.

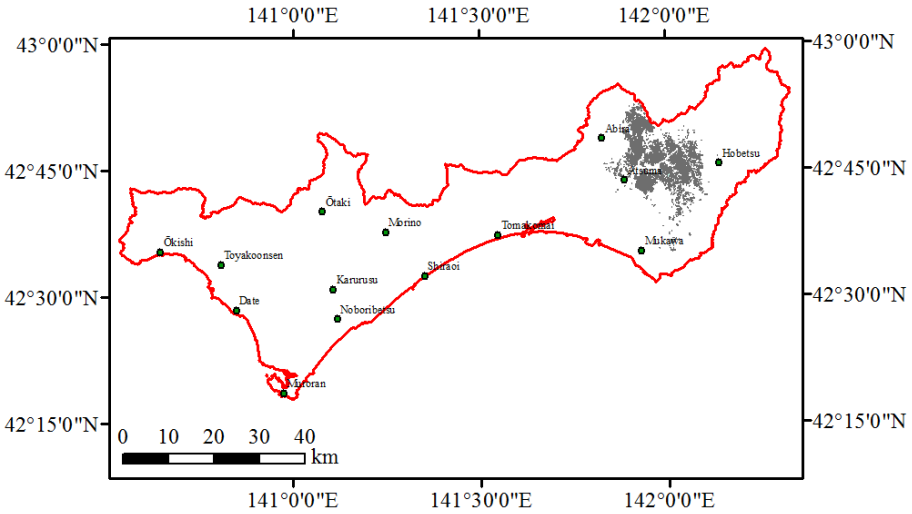

Figure 3.13. Rainfall stations in Iburi, Hokkaido, Japan.

Figure 3.14 showed that there was no more rainfall in the east of Iburi (landslide areas) than in the midwest of it. **Figure 3.15** indicated that there was totally around 200mm-300mm precipitation within one month before the disaster in the landslide areas. Around mid-August, several relatively heavy rains occured, with the heaviest

one bringing approximately 50mm precipitation. The powerful typhoon Jebi (Typhoon No.21 of 2018 in Japan), which occurred two days before the disater, brought heavy rainfall around Lake Shikotsu (around 50km west from Atsuma town), and was usually considered as an important factor for the extensive landslides, brought around 15mm of the precipitition in the landslide areas. The previous accumulated rainfall might be more important for the landslide occurrence.

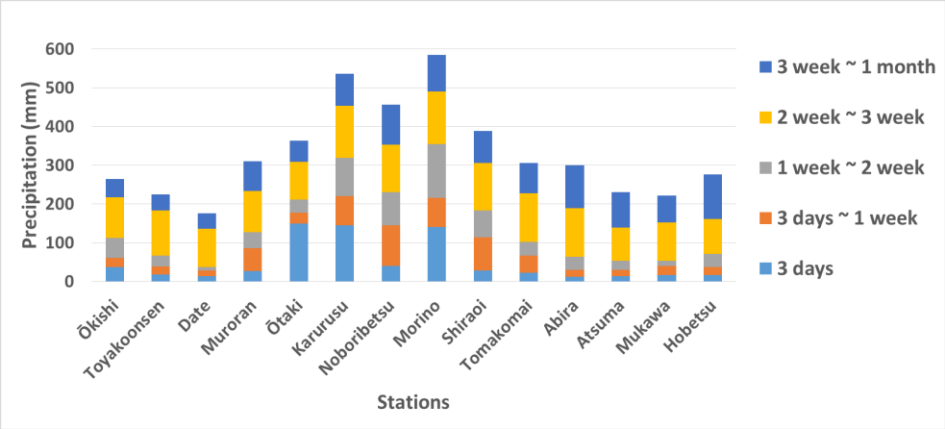

Figure 3.14. Accumulative precipitation before the disaster in Iburi.

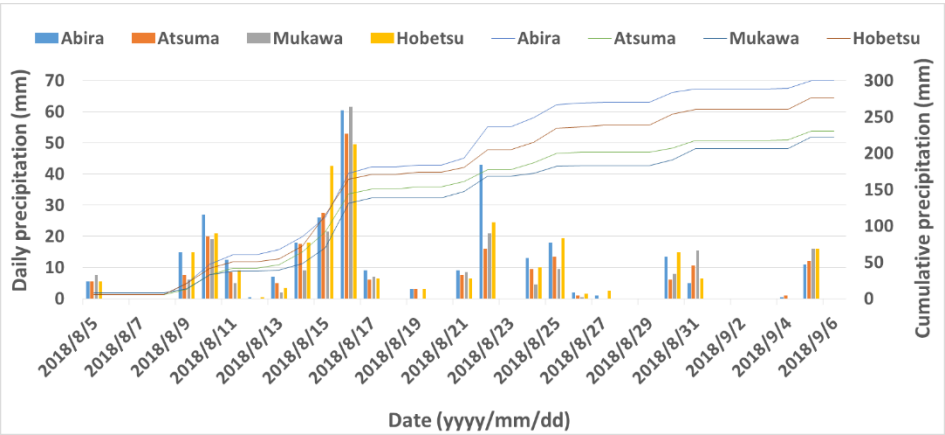

Figure 3.15. Precipitation around landslide areas before the disaster.

3.3.5. Ground Motion

Seismic activities have always been a main cause of landslides all around the world. In this case, the earthquake is the direct trigger of the extensive densely distributed landslides. The landslides were mainly distributed in the north of the

epicenter and within a distance of 25km from the epicenter. In order to understand the ground motion characteristics of the earthquake in landslide areas, the ShakeMaps of Modified Mercalli Intensity (MMI), peak ground acceleration (PGA), peak ground velocity (PGV), and peak spectral acceleration for 0.3s (PSA03), 1.0s (PSA10), and 3.0s (PSA30) were collected from USGS and analyzed.

MMI is a kind of earthquake intensity proposed by Wood and Neumann (1931), which permits seismologists to represent the ground shaking severity by a number. Its scales and levels were determined by considering the impacts of the earthquake on human beings, structures, and landscape. Lower scales were generally associated with how people felt about the shaking and higher scales were mainly based on observed structure damages. The descriptions of each scale in MMI are shown in **Table 3.2**.

Table 3.2. Description of the scales in MMI (USGS).

Intensity	Shaking	Description/Damage
I	Not felt	Not felt except by a very few under especially favorable conditions.
II	Weak	Felt only by a few persons at rest,especially on upper floors of buildings.
III	Weak	Felt quite noticeably by persons indoors, especially on upper floors of buildings. Many people do not recognize it as an earthquake. Standing motor cars may rock slightly. Vibrations similar to the passing of a truck. Duration estimated.
IV	Light	Felt indoors by many, outdoors by few during the day. At night, some awakened. Dishes, windows, doors disturbed; walls make cracking sound. Sensation like heavy truck striking building. Standing motor cars rocked noticeably.
V	Moderate	Felt by nearly everyone; many awakened. Some dishes, windows broken. Unstable objects overturned. Pendulum clocks may stop.
VI	Strong	Felt by all, many frightened. Some heavy furniture moved; a few instances of fallen plaster. Damage slight.
VII	Very strong	Damage negligible in buildings of good design and construction; slight to moderate in well-built ordinary structures; considerable damage in poorly built or badly designed structures; some chimneys broken.
VIII	Severe	Damage slight in specially designed structures; considerable damage in ordinary substantial buildings with partial collapse. Damage great in poorly built structures. Fall of chimneys, factory stacks, columns, monuments, walls. Heavy furniture overturned.
IX	Violent	Damage considerable in specially designed structures; well-designed frame structures thrown out of plumb. Damage great in substantial buildings, with partial collapse. Buildings shifted off foundations.
X	Extreme	Some well-built wooden structures destroyed; most masonry and frame structures destroyed with foundations. Rails bent.

Based on these ShakeMaps, the histograms of MMI, PGA, PGV, PSA03, PSA10, and PSA30 in the landslide areas was analyzed and shown in **Figures 3.16-3.21**. From these figures, it can be seen that, the majority of ground motions in the landslides have an MMI value of around 7.4-8.2, a PGA value of around 0.48g-0.68g, a PGV value of around 14cm/s-18cm/s, a PSA03 value of around 0.92g-1.52g, a PSA10 value of

around 0.20g-0.24g and 0.40g-0.56g, and a PSA30 value of around 0.08g -0.12g, relating to ground shaking condition and topography condition in local region.

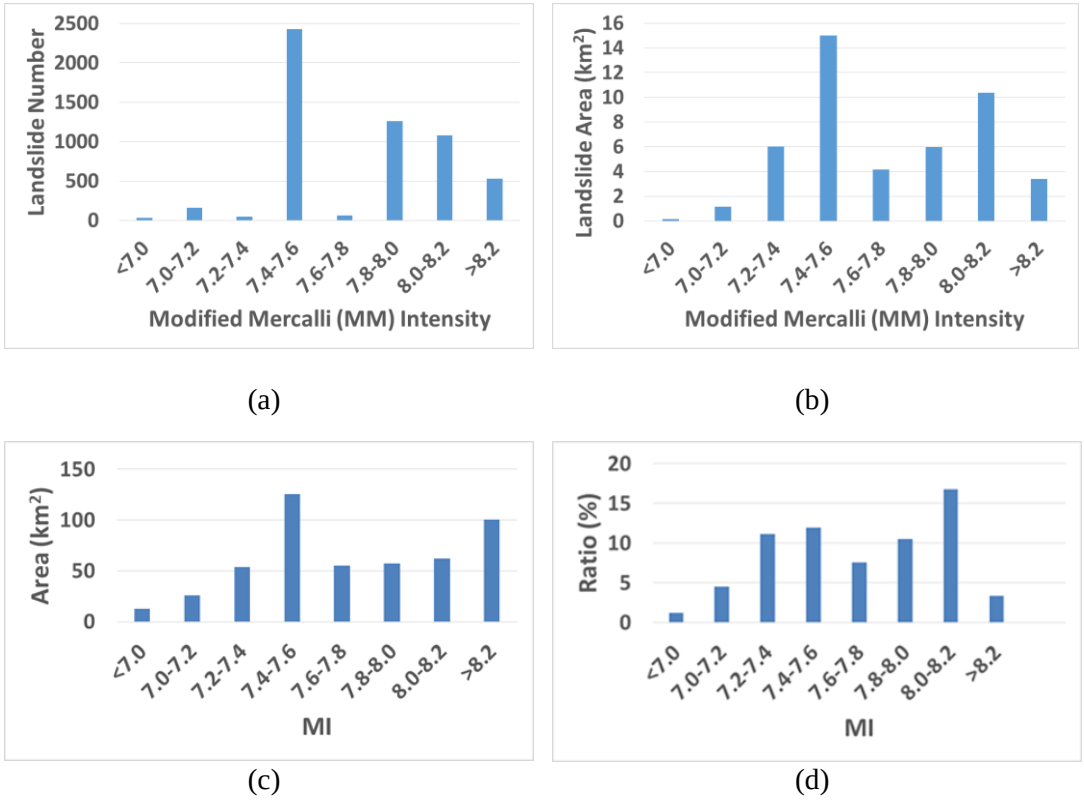

Figure 3.16. Histogram of Modified Mercalli Intensity (MMI) distribution: (a) Landslide number; (b) Landslide area; (c) Overall landslide region; (d) Ratio between landslide area and total area within the overall landslide region.

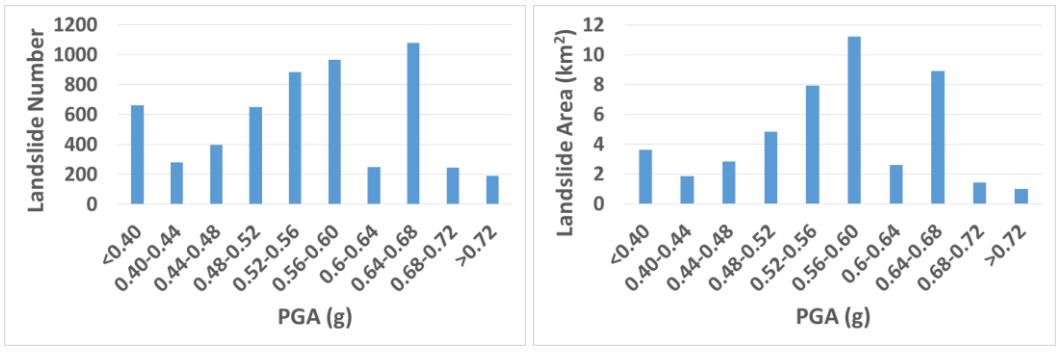

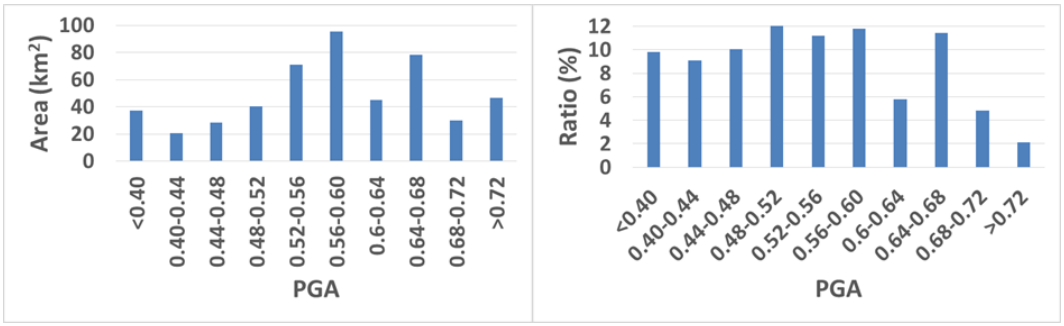

(c) (d)

Figure 3.17. Histogram of peak ground acceleration (PGA) distribution: (a) Landslide number; (b) Landslide area; (c) Overall landslide region; (d) Ratio between landslide area and total area within the overall landslide region.

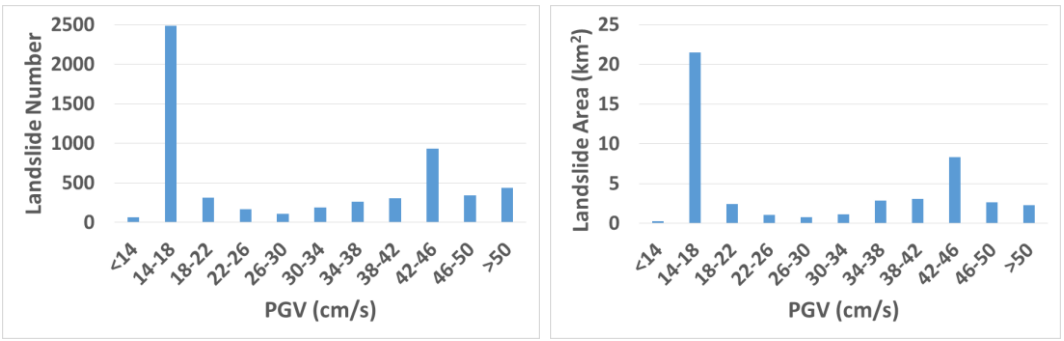

(a) (b)

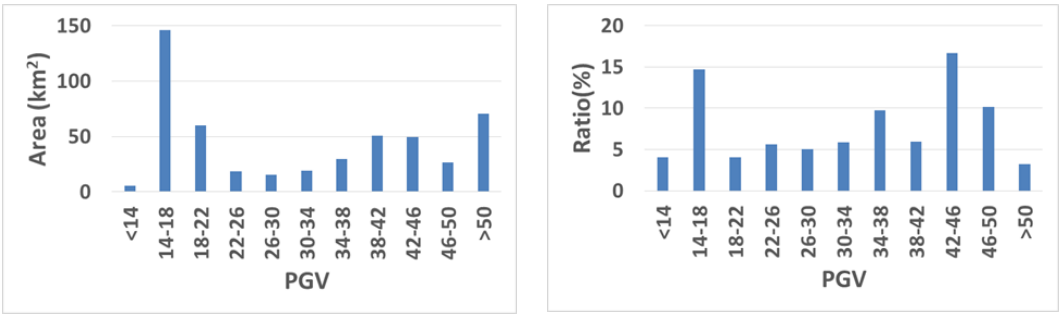

(c) (d)

Figure 3.18. Histogram of peak ground velocity (PGV) distribution: (a) Landslide number; (b) Landslide area; (c) Overall landslide region; (d) Ratio between landslide area and total area within the overall landslide region.

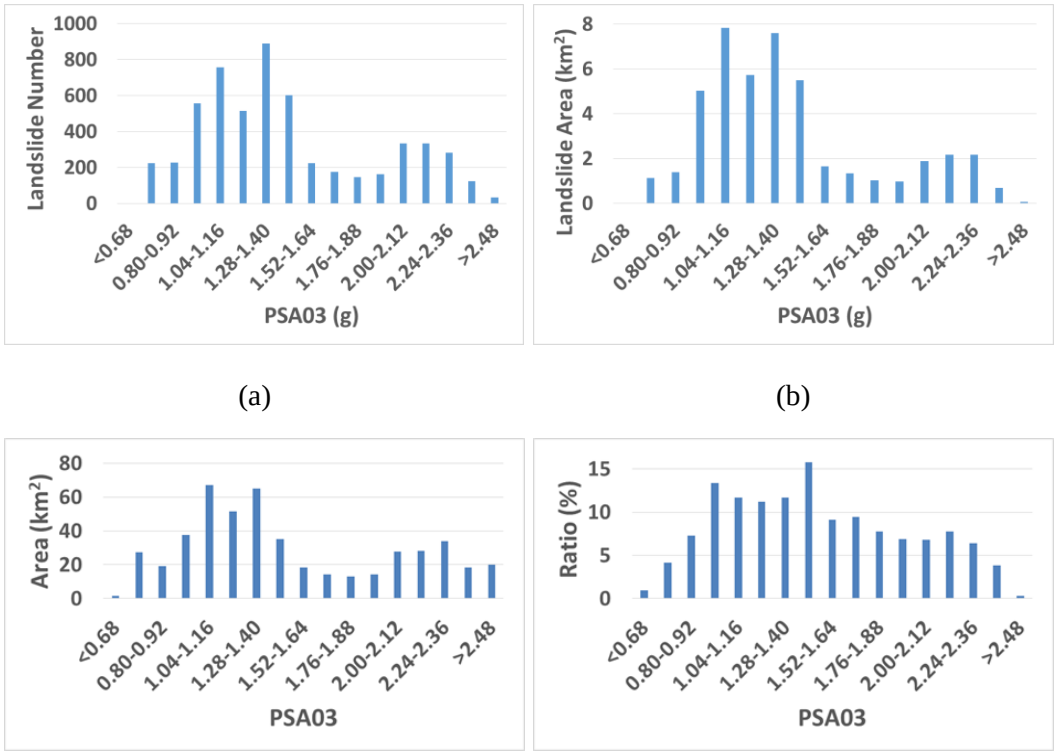

(a) (b)

(c) (d)

Figure 3.19. Histogram of peak spectral acceleration for 0.3s (PSA03) distribution: (a) Landslide number; (b) Landslide area; (c) Overall landslide region; (d) Ratio between landslide area and total area within the overall landslide region.

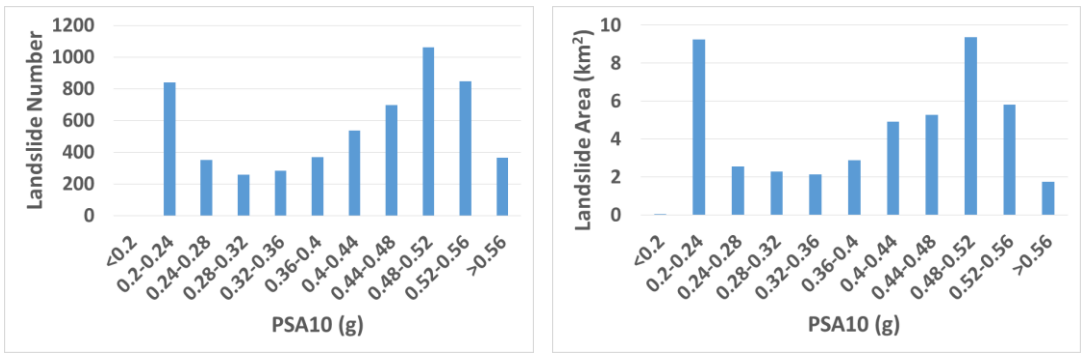

(a) (b)

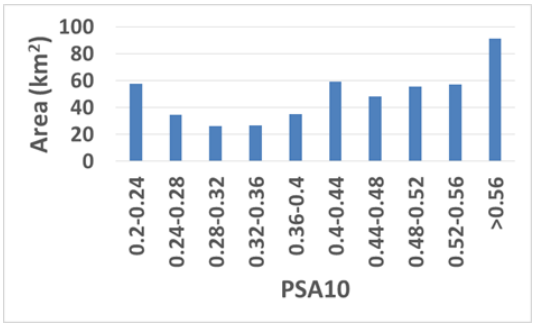

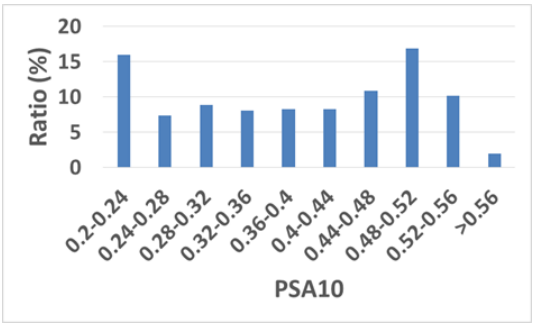

(c) (d)

Figure 3.20. Histogram of peak spectral acceleration for 1.0s (PSA10) distribution: (a) Landslide number; (b) Landslide area; (c) Overall landslide region; (d) Ratio between landslide area and total area within the overall landslide region.

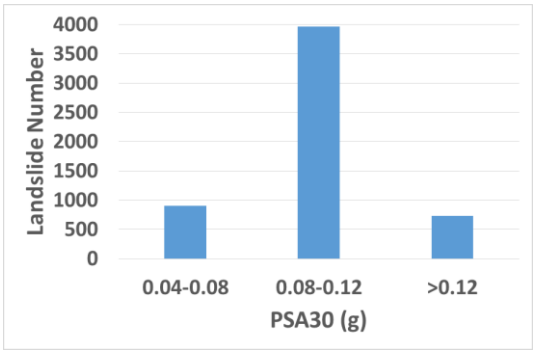

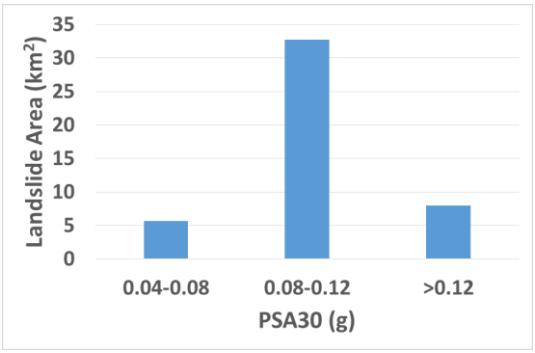

(a) (b)

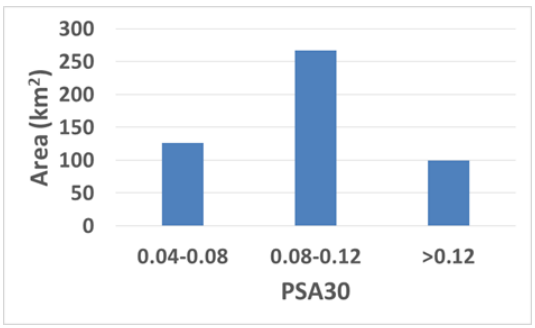

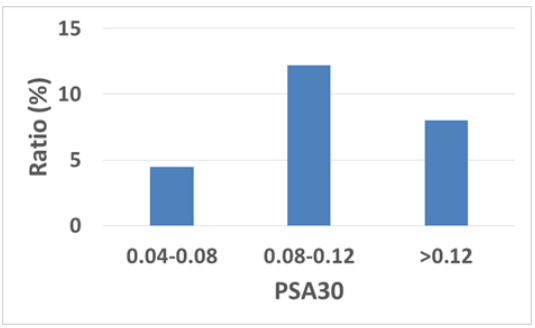

(c) (d)

Figure 3.21. Histogram of peak spectral acceleration for 3.0s (PSA30) distribution: (a) Landslide number; (b) Landslide area; (c) Overall landslide region; (d) Ratio between landslide area and total area within the overall landslide region.

3.4. Conclusions

Landslide inventory and conditioning factors were collected from different sources to understand the characteristics of the landslide event triggered in 2018 Hokkaido Eastern Iburi Earthquake, combining with previous studies and reports from other scholars concerning the mechanism and field survey of the landslides.

A detailed landslide inventory created by Zhang et al. (2019) based on a first-hand landslide database released by GSI was mainly applied to analyze the basic condition of the landslides, combining previous field survey reports and mechanism studies. Results showed that there were mainly small-sized shallow landslides, which densely distributed in an area of the transition zone from Hiddaka Mountains to Ishikari Depression in the north of the earthquake epicenter and within a distance of 25km to the epicenter. Most landslides had a slip surface above the basement complex and moved down the soft porous volcanic soil layers with high mobility and long run-out, leaving the landslide surface exposed as brownish patches. These landslides mainly occurred in valley terrain and planar slopes with several types. The characteristics of the landslides are more like those of the rainfall-induced landslides, even though the direct trigger is earthquake. The shear force of the ground motion ruptured the strata of the soft porous volcanic soil layers above the hard basement complex that have already been inundated by the precipitation before the earthquake, which might be the mechanism of most landslides.

The maps and records of topography, geology, soil, surface vegetation, precipitation, and ground motion in the landslide areas were collected from different official websites and used to analyze the characteristics of conditioning factors in landslide areas. A raster map of DEM was collected from GSI, and used to derive and analyze the topography and hydrological characteristics, including elevation, slope gradient, slope aspect, slope curvature, TWI, SPI, and STI. Maps of geology, soil, and surface vegetation were acquired from GSJ, NARO, Biodiversity Center of Japan, respectively, to understand the distribution of the bedrock, soil, and vegetation in the landslide areas. They were all polygon vector maps with a scale of 1:200,000, 1:200,000, and 1:50,000, respectivly. Precipitation records were collected from JMA, which recorded past preciptation data in 14 valid stations of Iburi, Hokkaido. One-month precipitation data before the disaster was analyzed to have an overall

undestanding of the precipitation condition before the disaster. Ground motion records were obtained from USGS, including ShakeMaps of MMI, PGA, PGV, PSA03, PSA10, and PSA30.

Analyses of the landslide conditioning factors showed that majority of the landslides occurred in areas with an elevation of around 100m-200m, a slope gradient of around 15°-35°, a geology type of N2sn (Middle to Late Miocene marine and non-marine sediments), soil types of D1 (未熟黒ボク土) and J1 (火山放出物未熟土), and and surface vegetation types of エゾイタヤーシナノキ and 落葉針葉樹植林. The elevation and slope gradient of the collpased slopes were lower, comparing with general values of other landslides, due to local topography and soil characteristics. The relatively preferred slope aspect was south, facing the earthquake epicenter. The relatively preferred slope curvature was concave, which may relate to raifall accumulation ability of these kind of topography. One month before the disaster, there were around 200mm-300mm precipitation, with several heavy rains in the mid of August. The powerful type Jebi, which occurred two days before the disater and was thought as an important factor of the landslides, brought approximately 15mm of the precipitation. The majority values of ground motion PGA and PGV in the landslide areas were 0.48g-0.68g and 14cm/s-18cm/s, respectively.

The earthquake was the direct trigger of the landslide event, and the combinationl impact of different conditioning factors, especially the porous soil, accumulated rainfall, and ground motion, were the real cause of these extensive densely distributed landslides. The soft porous volcano activity related soil here originally had a low shear strength and a high water storage capacity, while the hard bedrock below the soil had a poor water permeability. Due to these characteristics, water from previous rainfall could accumulate in the soil and made the water content in the soil very high, which not only reduced the soil shear strength but also lubricated the interface between soil and bedrock. Then when the earthquake occurred, the shaking from the ground motion not only produced shear force to the soil but also reduced the soil shear strength by increasing pore water pressure and decreasing soil effectiveness stress, causing the shear stress larger than the shear strength and leading to slope failures. In some areas, the soil effectiveness stress might even become zero, causing liquefaction.

3.5. References

Biodiversity Center of Japan. http://gis.biodic.go.jp/webgis/

Evans, N. C., Huang, S. W., King, J.P. (1999). The Natural Terrain Landslide Study - Phases I and II (Special Project Report SPR 5/97). GEO Report No. 73, GEO, CED, Hong Kong SAR Government, 128pp.

GSI. https://fgd.gsi.go.jp/download/menu.php

GSJ. https://gbank.gsj.jp/seamless/index_en.html

Guo, C., Huang, Y, Yao, L., Alradi, H. (2017). Size and spatial distribution of landslides induced by the 2015 Gorkha earthquake in the Bhote Koshi river watershed. Journal of Mountain Science, 14(10), 1938-1950.

Hirose, W., Kawakami, G., Kase, Y., Ishimaru, S., Koshimizu, K., Koyasu, H., Takahashi, R. (2019). Preliminary report of slope movements at Atsuma Town and its surrounding areas caused by the 2018 Hokkaido Eastern Iburi Earthquake. Hokkaido Geological Research Institute Report, (90), 33-44.

Ito, Y., Yamazaki, S., Kurahashi, T. (2020). Geological features of landslides caused by the 2018 Hokkaido Eastern Iburi Earthquake in Japan. Geological Society of London, Special Publications.

JGS. (2019). 平成 30 年北海道胆振東部地震による地盤災害調査団最終報告書. 公益社団法人地盤工学会平成 30 年北海道胆振東部地震による地盤災害調査団. https://www.jiban.or.jp/file/saigai/H30_Hokkaido_EQ_FinalReport.pdf

JMA. https://www.data.jma.go.jp/gmd/risk/obsdl/index.php#

Kuwamura, S., Kawajiri, S., Hirose, W., Watanabe, T. (2019). Slope failures/landslides over a wide area in the 2018 Hokkaido Eastern Iburi earthquake. Soils and Foundations, 59, 2376-2395.

NARO. https://soil-inventory.dc.affrc.go.jp/offer.html

Okamoto, A., Murata, I. (2016). Slope Failure Disasters and Countermeasures. http://www.nilim.go.jp/english/hottopics/pdf/sabo2.pdf

Raster Curvature. http://www.etst.com/et_surface/userguide/Raster/ETG_RasterCurvature.htm

Tanyas, H., van Westen, C. J., Allstadt, K. E., Anna Nowicki Jessee, M., Gorum, T., Jibson, R. W., Godt, J. W., Sato, H. P., Schmitt, R. J., Marc, O., Hovius, N. (2017). Presentation and analysis of a worldwide database of earthquake-induced landslide inventories. Journal of Geophysical Research F: Earth Surface, 122, 1991-2015.

Tseng, C. M., Chen, Y. R., Wu, S. M. (2015). Scale and spatial distribution assessment of rainfall-induced landslides in a catchment with mountain roads. Natural Hazards and Earth System Sciences, 18, 687-708.

USGS. https://www.usgs.gov/natural-hazards/earthquake-hazards/science/modified-mercalli-intensity-scale?qt-science_center_objects=0#qt-science_center_objects

USGS.https://earthquake.usgs.gov/earthquakes/eventpage/us2000h8ty/shakemap/intensity

Wang, F., Fan, X., Yunus, A. P., Subramanian, S. S., Alonso-Rodriguez, A., Dai, L., Xu, Q., Huang, R. (2019). Coseismic landslides triggered by the 2018 Hokkaido, Japan (Mw6.6), earthquake: spatial distribution, controlling factors, and possible failure mechanism. Landslides, 21, 1551-1566.

Wood, H. O., Neumann, F. (1931). Modified Mercalli intensity scale of 1931. Bulletin of the Seismological Society of America, 21(4), 277-283.

Zhang, S., Li, R., Wang, F., Iio, A. (2019). Characteristics of landslides triggered by the 2018 Hokkaido Eastern Iburi earthquake, Northern Japan. Landslides, 16 (9), 1691-1708.

Zhang, Y., Ding, J. (2019). Stability Analysis of Slopes on Both Sides of Highway in Geotechnical Area under Rainfall Conditions. 2019 International Conference on Oil & Gas Engineering and Geological Sciences, Dalian, CN, 28-29 September 2019.

CHAPTER 4

GIS-BASED STATISTICAL LANDSLIDE SUSCEPTIBILITY ANALYSIS FOR PRE-EVENT LANDSLIDE DISASTER MANAGEMENT

4.1. Introduction

As is said, present and past are keys to the future. Understanding and learning from past landslide event can provide useful and valuable information and experience for future landslide disaster management. In order to take advantage of the data and information brought by this landslide event to benefit pre-event landslide disater management in the future, a landslide susceptibility analysis was carried out in this chapter using a GIS-based statistical approach. Comparing with deterministic approaches that explore the slope failure mechanism by physical models, statistical approaches does not require detailed physical parameters of the slopes, such as soil strength, soil depth, and hydrological parameters, which are difficult to collect in a large area (Lee, 2015).

Both qualitative and quantitative approaches can be used for landslide susceptibility analysis. Qualitative approaches are subjective approaches, in which the experience of experts is of vital importance. In this kind of approaches, usually, the experts assign weights to each landslide conditioning factor indicators to estimate the potential of landslide occurrence in different areas. Quantitative approaches are data-dependent approaches and therefore are considered to be more objective. In this kind of approaches, the weights of different landslide conditioning factor indicators are generally estimated based on past landslide data. Statistical analysis, such as discriminant analysis and logistic regression, and advanced machine learning approaches, such as support vector machine (SVM) and neural network, can both be used for quantitative landslide susceptibility analysis.

In this chapter, the GIS-based logistic regression of quantitative approaches was applied for the landslide susceptibility analysis, to make full use of the dataset brought by the landslide event and to be objective. GIS is a system designed to deal with various types of spatial and geographic data, and has become a popular technology for the management of natural hazards including landslides (Chau et al., 2004).

Logistic regression can construct a model by analyzing the relationship between a binary dependent variable (landslide presence and absencein this case) and multiple independent variables either of numeric types or nominal types (landslide conditioning factors in this case). It is efficient, highly interpretable, does not require too much computational resources, and has already shown favorable performance in landslide susceptibility, hazard, and risk analysis.

To perform the GIS-based statistical landslide susceptibility analysis, spatial dataset of landslide inventory and conditioning factor indicators collected and derived in chapter 3 were preprocessed and constructed into a database on the ArcGIS platform as dependent and independent variables. All of the data, either in raster formats or vector formats, were converted into a unified format-10m raster cells for further calculation and analyses. As the raster cells tagged as landslides were much fewer than those tagged as non-landslides, a certain number of non-landslide cells was selected randomly from the non-landslide raster cell library for analysis, in order to avoid the underestimation of landslide occurrence. Effectiveness and multicollinearity problems of the conditioning factor indicators were analyzed and checked by several mathematical indicators to eliminate noneffective and related independent variables for logistic regression. A landslide susceptility model was finally constructed using these selected and checked data, and a landslide susceptibility map was generated in the study area applying this model.

4.2. Dataset

To carry out the statistical landslide susceptibility analysis in the study area, the spatial dataset of dependent and independent variables need to be prepared first. In this case, the landslide inventory and conditioning factor indicators collected and derived in chapter 3 were applied as dependent and independent variables in the analysis, respectively.

As has been mentioned, the landslide inventory was created by Zhang et al. (2019) based on a first-hand landslide database published by GSI. The considered conditioning factor indicators of landslides included the topography characteristics derived from a DEM provided by GSI (**Figure 4.1**), geology information obtained

from GSJ (**Figure 4.2**), soil information acquired from NARO (**Figure 4.3**), surface vegetation information obtained from Biodiversity Center of Japan (**Figure 4.4**), ground motion information collected from USGS (**Figure 4.5**), and precipitation information calculated through the past precipitation records in 14 stations of JMA (**Figure 4.6**). Interpolation has been carried out for the point precipitation data by inverse distance weighted (IDW) technique to supplement data in areas without stations. Three-day, one-week, two-week, three-week, and one-month cumulative precipitation before the disaster were all calculated and will be compared to choose a relatively effective one for final landslide susceptibility model construction.

As there is no widely accepted standard for the selection of landslide conditioning factors (Yalcin, 2008), these indicators were mainly determined based on the characteristics of the landslide event and local area, landslide mechanism, literature review, and data availibility. For instance, the understanding of the landslide characteristics and mechanism in chapter 3 showed that the soil, previous precipitation, and ground motion were important factors for the landslide occurrence. The slope gradient is always an important factor influencing the balance between the shear force and the slope capability. The slope aspect and elevation might influence local climate of the slope, which futher impacts the stability of the slope. The slope curvature might influence the hydrological characteristics of the slope that affects the slope stability.

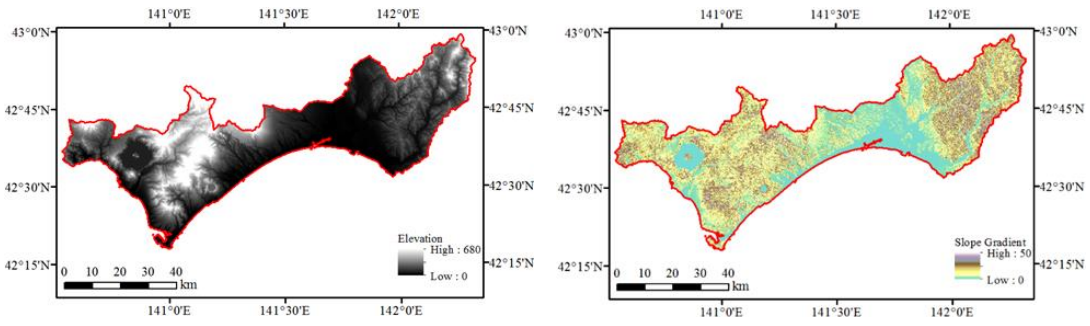

(a) (b)

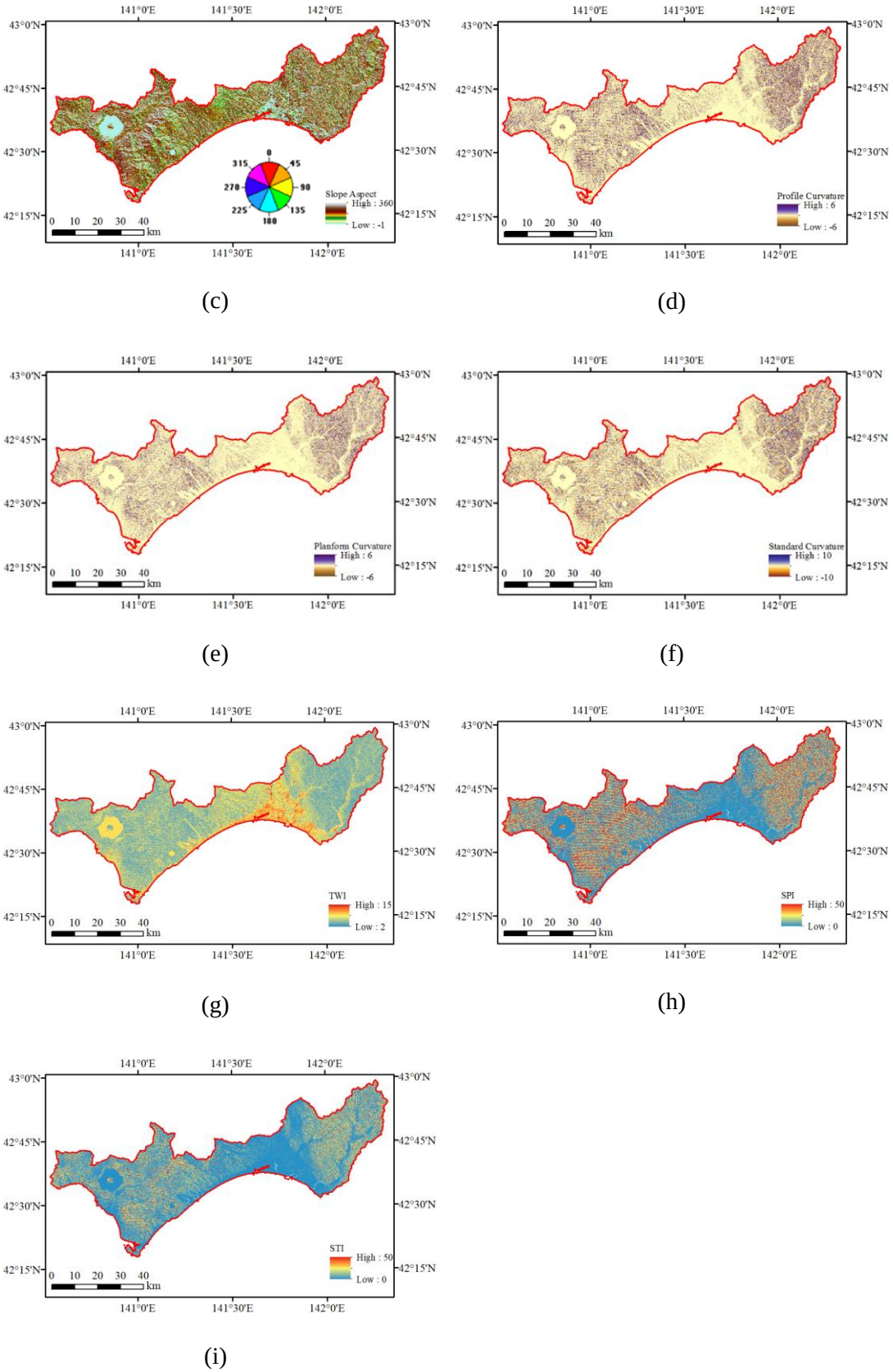

Figure 4.1. Topography maps: (a) Elevation; (b) Slope gradient; (c) Slope aspect; (d) Profile curvature; (e) Planform curvature; (f) Standard curvature; (g) Topographic wetness index

(TWI); (h) Stream power index (SPI); (i) Sediment transport index (STI).

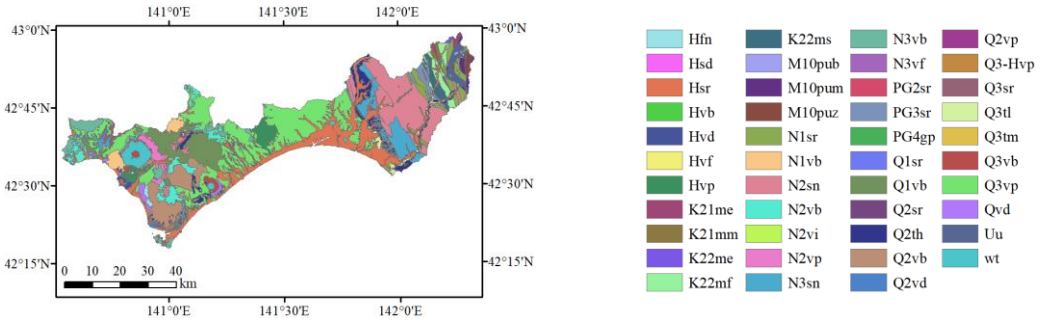

Figure 4.2. Geology map.

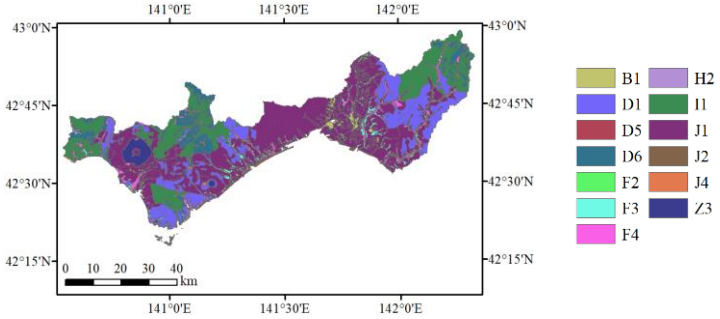

Figure 4.3. Soil map (B1: 泥炭土; D1: 未熟黒ボク土; D5: 非アロフェン質黒ボク土; D6: アロフェン質黒ボク土; F2: グライ低地土; F3: 灰色低地土; F4: 褐色低地土; H2: 疑似グライ土; I1: 褐色森林土; J1 火山放出物未熟土; J2: 砂質未熟土; J4: 陸成未熟土; Z3:その他.).

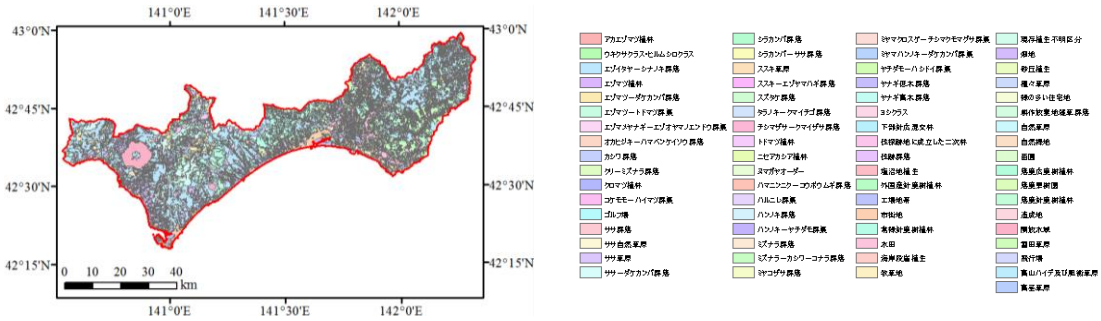

Figure 4.4. Surface vegetation map.

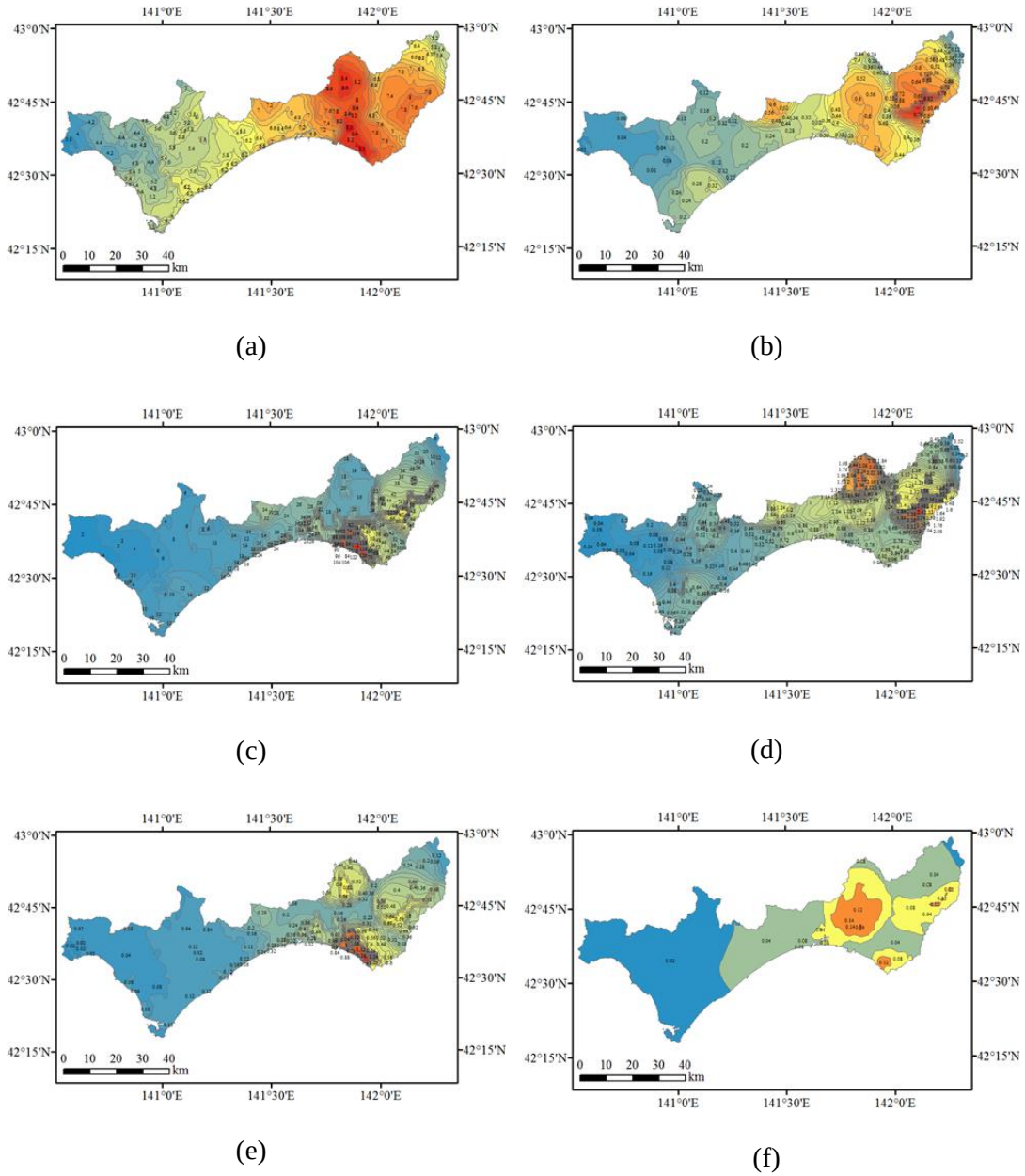

Figure 4.5. Ground motion maps: (a) Modified Mercalli intensity (MMI); (b) Peak ground acceleration (PGA); (c) Peak ground velocity (PGV); (d) Peak spectral acceleration for 0.3s (PSA03); (e) Peak spectral acceleration for 1.0s (PSA10); (f) Peak spectral acceleration for 3.0s (PSA30).

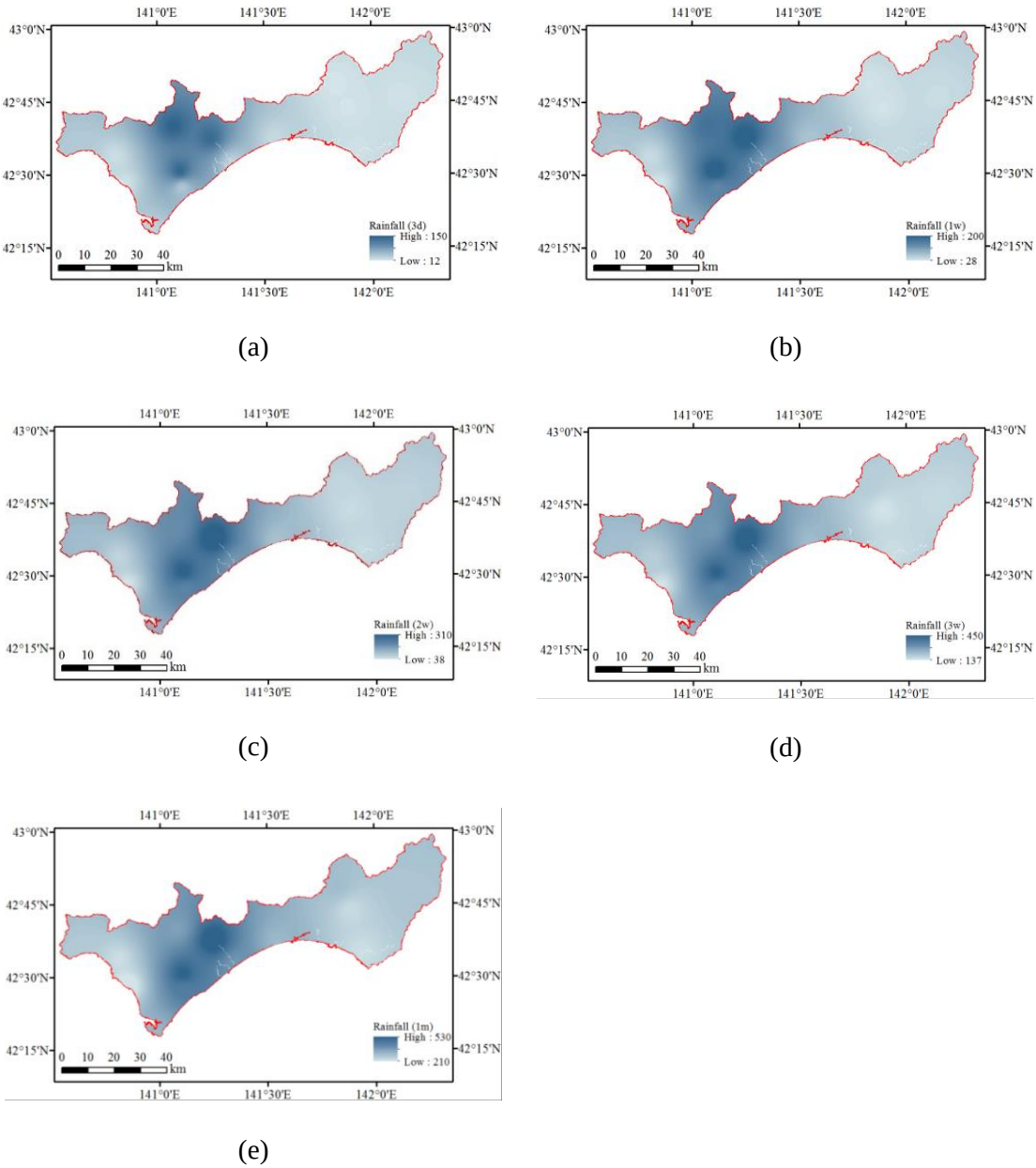

Figure 4.6. Precipitation maps: (a) Three-day cumulative precipitation before the disaster; (b) One-week cumulative precipitation before the disaster; (c) Two-week cumulative precipitation before the disaster; (d) Three-week cumulative precipitation before the disaster; (e) One-month cumulative precipitation before the disaster.

4.3. Methodology

As there were both raster and vector types in the collected data, first, they were converted into a unified format-10m×10m raster cells for further analysis. The total number of raster cells is more than 30 million, and the number of cells tagged as

landslides is around 400 thousand. Landslide presence only represents 1.26% of the study area, and therefore is considered as a rare event data (King and Zeng, 2001; Van Den Eeckhaut et al., 2006; Bai et al., 2010). The term "rare event data" was induced in political science, which described the binary dependent variables with dozens to thousands of times fewer 1s (landslide cells in this case) than 0s (non-landslide cells in this case). When applying popular statistical procedures (e.g., logistic regression) to model such conditions, the occurrence probability of the rare event can be sharply underestimated (King and Zeng, 2000, 2001). It is generally suggested to use the same number of landslide and non-landslide cells for model training (Süzen and Doyuran, 2004; Nefeslioglu et al., 2008; Bai et al., 2010), even though there are also studies applying unequal proportions of them (Ayalew and Yamagishi, 2005; Dominguez-Cuesta et al., 2007). In this study, referring to previous studies, the ratio of 1:1 to 1:5 between the landslide and non-landslide cells were tested and explored. While all landslide cells were applied, a certain number of non-landslide cells were randomly selected to make the ratio between landslide presence and absence to be 1:1, 1:2, 1:3, 1:4, and 1:5.

After that, as there were several indicators for curvature-related conditioning factors (i.e., planform curvatre, profile crvature, and standard curvature), earthquake-related conditioning factors (i.e., MMI, PGA, PGV, PSA03, PSA10, and PSA30), and precipitation-related conditioning factors (i.e., three-day, one-week, two-week, three-week, and one-month cumulative precipitation before the disaster), respectively, effectiveness of them was first carried out by receiver operating characteristic (ROC) analyses to select the relatively effective indicators for susceptibility model construction (Lee, 2014). The larger the area under the ROC curve (AUC) value, the more effective the indicator.

Then, the correlation and multicollinearity problems of the remaining numerical independent variables were analzyed by the pearson's correlation coefficient, tolerance (TOL), and variance inflation factor (VIF), to exclude related indicators for model construction. Pearson's correlation coefficient means the covariance of two variables divided by the product of their standard deviations. Its values are between -1 and 1. -1 means completely negative linear correlation, 1 means completely positive linear correlation, and 0 means no linear correlation. An absolute value of pearson's

correlation coefficient greater than 0.7 indicates a high collinearity (Bui et al., 2016; Booth et al., 2004). VIF is the quotient of the variance in a model with multiple terms by the variance of a model with one term alone. It is the reciprocal of TOL, and measures how much the variance of the estimated coefficient is inflated by multicollinearity (**Equation 4.1**). A large VIF value indicates that the associated independent variable is highly collinear with other independent variables. A TOL value smaller than 0.1 and a VIF value greater than 10 indicates that the multicollinearity is problematic.

$$VIF_i = \frac{1}{1 - R_i^2} = \frac{1}{Tolerance} \tag{4.1}$$

After these analyses, the five different ratios (1:1, 1:2, 1:3, 1:4, and 1:5) between landslide and non-landslide cells were compared to determine a better one for model construction, by the use of landslide inventory and remaining landslide conditioning factor indicators. The dataset under the determined ratio were then randomly divided into two groups with a ratio of 7:3. Logistic regression was carried out using 70% of the data for training and 30% of data for validation, to construct and check the final landslide susceptibility model. Logistic regression is a multivariate analysis approach that can be used to model the relationship between a dichotomous dependent variable and a set of independent variables. It is efficient, highly interpretable, can be implemented relatively easily and quickly, and does not require the independent variables to have a normal distribution. The independent variables used for logistic regression can be either continuous, discrete, or any combinations of them. A logistic function can be written as **Equation 4.2** (Allison, 2001), with $\hat{p}$ representing the probability of event occurring (the probability of landslide occurrence in this case), $\hat{\alpha}$ representing the intercept, and β_i representing the coefficient for the independent variable x_i. It applies a maximum likelihood estimation in the algorithm after transforming the dependent variable into a logit variable. Logistic regression has already been applied for landslide susceptibility, hazard, and risk analysis, and shown favorable performance comparing with other statistical approaches such as discriminant analysis and the weight of evidence.

$$P(Y=1)=\hat{p}=\frac{1}{1+e^{-(\hat{\alpha}+\widehat{\beta_1}x_1+\widehat{\beta_2}x_2+\cdots+\widehat{\beta_n}x_n)}} \quad (4.2)$$

4.4. Results and Discussions

The AUC values of ROC analyses for the three curvature-related, six earthquake-related, and five precipitation-related conditioning factor indicators were listed in **Tables 4.1-4.3**. As can be seen from these tables, no matter under what kinds of landslide and non-landslide cell ratios, the standard curvature, PSA03, and one-week cumulative precipitation before the disaster showed relatively better performance. This might be due to the parameter comprehensiveness of standard curvature comparing with planform and profile curvature, local soil water storage capability and evaporation conditon, and predominated period of local area. In the subsequent analysis, these three parameters will be used as the indicators for slope curvature, ground motion, and precipitation conditioning factors, respectively. Moreover, these tables also indicated that, for a specific indicator, there is no big difference among the AUC values under different ratios of landslide and non-landslide cells.

Table 4.1. AUC values of curvature-related conditioning factor indicators under different ratios of landslide and non-landslide cells.

Ratios	Planform curvature	Profile curvature	Standard curvature
1:1	0.54124	0.56543	0.56784
1:2	0.54096	0.56526	0.56757
1:3	0.54100	0.56523	0.56772
1:4	0.54113	0.56531	0.56781
1:5	0.54106	0.56546	0.56775

Table 4.2. AUC values of earthquake-related conditioning factor indicators under different ratios of landslide and non-landslide cells.

Ratios	MI	PGA	PGV	PSA03	PSA10	PSA30
1:1	0.81698	0.81247	0.70087	0.84492	0.77340	0.83532
1:2	0.81717	0.81257	0.70099	0.84472	0.77336	0.83533
1:3	0.81725	0.81269	0.70127	0.84476	0.77354	0.83526
1:4	0.81731	0.81250	0.70120	0.84474	0.77353	0.83532
1:5	0.81724	0.81250	0.70114	0.84472	0.77343	0.83528

Table 4.3. AUC values of precipitation-related conditioning factor indicators under different ratios of landslide and non-landslide cells.

Ratios	Three-day cumulative precipitation	One-week cumulative Precipitation	Two-week cumulative Precipitation	Three-week cumulative Precipitation	One-month cumulative Precipitation
1:1	0.89578	0.90505	0.87141	0.85990	0.78674
1:2	0.89587	0.90513	0.87173	0.86014	0.78711
1:3	0.89603	0.90528	0.87207	0.86041	0.78738
1:4	0.89610	0.90538	0.87216	0.86042	0.78743
1:5	0.89610	0.90539	0.87212	0.86043	0.78744

The calculated correlation coefficient, TOL, and VIF values for the remaining numerical conditioning factors (i.e., elevation, slope gradient, slope aspect, standard curvature, TWI, SPI, STI, PSA03, one-week cumulative precipitation before the disaster) under different ratios of landslide and non-landslide cells are listed in **Tables 4.4-4.9**. From these tables it can be seen that the correlation coefficient values between SPI and STI are higher than 0.7, which indicates that there may be some correlation between these two indicators. This might relate to the existence of many gentle slopes here, causing the sine and tangent value of the slope gradient for the calculation of STI and SPI, respectively, near to each other. In order to avoid the unnecessary problems caused by collinearity, SPI is excluded from the conditioning factor indicators, as it is not as effective as STI in this case.

Table 4.4. Correlation coefficient values between each two conditioning factor indicators (ratio of landslide and non-landslide cells=1:1).

	Elevation	Slope gradient	Slope aspect	Standard curvature	PSA03	One-week cumulative precipitation	TWI	SPI	STI
Elevation	1.000	0.168	0.058	0.057	-0.323	0.568	-0.203	0.033	0.074
Slope gradient	--	1.000	0.088	0.006	0.196	-0.175	-0.632	-0.017	0.240
Slope aspect	--	--	1.000	-0.007	0.048	-0.046	-0.104	0.010	0.031
Standard curvature	--	--	--	1.000	-0.064	0.065	-0.336	-0.163	-0.386
PSA03	--	--	--	--	1.000	-0.565	-0.105	-0.019	0.048
One-week cumulative precipitation	--	--	--	--	--	1.000	0.055	0.027	-0.040
TWI	--	--	--	--	--	--	1.000	0.247	0.249
SPI	--	--	--	--	--	--	--	1.000	0.753
STI	--	--	--	--	--	--	--	--	1.000

Table 4.5. Correlation coefficient values between each two conditioning factor indicators (ratio of landslide and non-landslide cells=1:2).

	Elevation	Slope gradient	Slope aspect	Standard curvature	PSA03	One-week cumulative precipitation	TWI	SPI	STI
Elevation	1.000	0.210	0.070	0.050	-0.335	0.560	-0.236	0.036	0.097
Slope gradient	--	1.000	0.096	-0.001	0.166	-0.124	-0.635	-0.005	0.252
Slope aspect	--	--	1.000	-0.006	0.047	-0.041	-0.124	0.010	0.034
Standard curvature	--	--	--	1.000	-0.060	0.057	-0.307	-0.144	-0.357
PSA03	--	--	--	--	1.000	-0.559	-0.082	-0.022	0.030
One-week cumulative precipitation	--	--	--	--	--	1.000	0.017	0.030	-0.014
TWI	--	--	--	--	--	--	1.000	0.214	0.204
SPI	--	--	--	--	--	--	--	1.000	0.761
STI	--	--	--	--	--	--	--	--	1.000

Table 4.6. Correlation coefficient values between each two conditioning factor indicators (ratio of landslide and non-landslide cells=1:3).

	Elevation	Slope gradient	Slope aspect	Standard curvature	PSA03	One-week cumulative precipitation	TWI	SPI	STI
Elevation	1.000	0.237	0.077	0.045	-0.335	0.554	-0.253	0.036	0.108
Slope gradient	--	1.000	0.099	-0.002	0.136	-0.088	-0.636	-0.001	0.253
Slope aspect	--	--	1.000	-0.005	0.044	-0.039	-0.132	0.009	0.035
Standard curvature	--	--	--	1.000	-0.051	0.048	-0.295	-0.135	-0.341
PSA03	--	--	--	--	1.000	-0.548	-0.063	-0.024	0.015
One-week cumulative precipitation	--	--	--	--	--	1.000	-0.007	0.031	0.003
TWI	--	--	--	--	--	--	1.000	0.199	0.187
SPI	--	--	--	--	--	--	--	1.000	0.767
STI	--	--	--	--	--	--	--	--	1.000

Table 4.7. Correlation coefficient values between each two conditioning factor indicators (ratio of landslide and non-landslide cells =1:4).

	Elevation	Slope gradient	Slope aspect	Standard curvature	PSA03	One-week cumulative precipitation	TWI	SPI	STI
Elevation	1.000	0.256	0.082	0.042	-0.335	0.551	-0.265	0.037	0.117
Slope gradient	--	1.000	0.101	-0.001	0.113	-0.061	-0.635	0.001	0.255
Slope aspect	--	--	1.000	-0.005	0.041	-0.035	-0.137	0.010	0.035
Standard curvature	--	--	--	1.000	-0.044	0.041	-0.289	-0.133	-0.333
PSA03	--	--	--	--	1.000	-0.538	-0.049	-0.025	0.005
One-week cumulative precipitation	--	--	--	--	--	1.000	-0.024	0.032	0.014
TWI	--	--	--	--	--	--	1.000	0.195	0.178
SPI	--	--	--	--	--	--	--	1.000	0.771
STI	--	--	--	--	--	--	--	--	1.000

Table 4.8. Correlation coefficient values between each two conditioning factor indicators (ratio of landslide and non-landslide cells =1:5).

	Elevation	Slope gradient	Slope aspect	Standard curvature	PSA03	One-week cumulative precipitation	TWI	SPI	STI
Elevation	1.000	0.270	0.085	0.039	-0.334	0.548	-0.273	0.038	0.123
Slope gradient	--	1.000	0.101	0.001	0.094	-0.042	-0.634	0.003	0.256
Slope aspect	--	--	1.000	-0.004	0.039	-0.033	-0.140	0.010	0.035
Standard curvature	--	--	--	1.000	-0.039	0.035	-0.286	-0.132	-0.328
PSA03	--	--	--	--	1.000	-0.530	-0.038	-0.026	-0.003
One-week cumulative precipitation	--	--	--	--	--	1.000	-0.036	0.033	0.023
TWI	--	--	--	--	--	--	1.000	0.193	0.174
SPI	--	--	--	--	--	--	--	1.000	0.773
STI	--	--	--	--	--	--	--	--	1.000

Table 4.9. TOL and VIF values for the conditioning factor indicators under different ratios of landslide and non-landslide cells.

Items	Ratios	Elevation	Slope gradient	Slope aspect	Standard curvature	PSA03	One-week cumulative precipitation	TWI	SPI	STI
TOL	1:1	0.826	0.595	1.000	0.930	0.889	0.732	0.611	0.587	0.439
	1:2	0.827	0.607	0.999	0.943	0.892	0.755	0.636	0.573	0.441
	1:3	0.828	0.616	0.999	0.950	0.901	0.773	0.648	0.562	0.438
	1:4	0.829	0.622	0.999	0.953	0.908	0.785	0.655	0.556	0.437
	1:5	0.830	0.626	0.999	0.956	0.913	0.794	0.659	0.554	0.438
VIF	1:1	1.210	1.680	1.000	1.075	1.124	1.365	1.637	1.704	2.279
	1:2	1.210	1.646	1.001	1.060	1.121	1.324	1.571	1.745	2.266
	1:3	1.207	1.624	1.001	1.053	1.110	1.294	1.544	1.780	2.281
	1:4	1.206	1.609	1.001	1.049	1.102	1.274	1.528	1.800	2.289
	1:5	1.205	1.597	1.001	1.046	1.095	1.260	1.517	1.804	2.283

In order to find the favorable ratio of landslide and non-landslide cells for model construction, the classification accuracy of logistic regression under different ratios were all calculated and listed in **Table 4.10**, including accuracy, recall, precision, and

F1 score. All data in the dataset were applied for training in the logistic regression analysis. Accuracy is an intuitive performance measure, indicating the ratio of correctly predicted observations to total observations (**Equation 4.3**). Recall is defined as the correctly predicted positive observations divided by all observations in actual class (**Equation 4.4**). Precision is defined as the correctly predicted positive observations divided by the total predicted positive observations (**Equation 4.5**). F1 score is a weighted average of recall and precision (Powers, 2011) calculated based on **Equation 4.6** to achieve a balance between the recall and precision measure.

As it can be seen from the values in **Table 4.10**, among all of the five different ratios between landslide and non-landslide cells, the classification results obtained under the ratio of 1:1 is relatively better in general. Moreover, the recall values under different ratios indicated that the more non-landslide cells involved in analysis, the more landslide cells would be classified as non-landslide cells. Therefore, in this study, the dataset with the same number of landslide and non-landslide raster cells would be applied for constructing the final landslide susceptibility model.

Table 4.10. Classification accuracy under different ratios of landsldie and non-landslide cells.

Ratios	Accuracy	Recall	Precision	F1 score
1:1	92.91%	97.06%	89.65%	93.20%
1:2	92.00%	94.38%	83.71%	88.73%
1:3	91.84%	90.72%	79.54%	84.76%
1:4	91.89%	86.09%	76.36%	80.84%
1:5	92.04%	81.28%	73.69%	77.30%

$$\text{Accuracy} = (TP+TN)/(TP+TN+FP+FN) \tag{4.3}$$

$$\text{Recall} = TP/(TP+FN) \tag{4.4}$$

$$\text{Precision} = TP/(TP+FP) \tag{4.5}$$

$$\text{F1 score} = 2\times(\text{Recall}\times\text{Precision})/(\text{Recall}+\text{Precision}) \tag{4.6}$$

Here TP, TN, FP, and FN are the true positive, true negative, false positive, and false negative in a confusion matrix shown in **Table 4.11**.

Table 4.11. Confusion matrix.

Actual \ Predict	Positive	Negative
Positive	True Positive (TP)	False Negative (FP)
Negative	False Positive (FP)	True Negative (TN)

In order to construct and check the final model, the dataset with a ratios of 1:1 between landslide presence and absence were randomly divided into two groups, with one including 70% of the data and used for model construction and another including 30% of the data and used for model validation. The final constructed model achieved a favorable accuracy for both training and validating dataset (**Table 4.12**). Using this model, a landslide susceptibility map in the study area was generated and shown in **Figure 4.7**, which seems to have a good consistency with the actual landslide distribution. In future application, by updating the changed conditioning factor indicators in the logistic regression function (i.e., the precipitation and ground motion indicators) according to actual situation, the landslide susceptibility model is expected to provide some useful information for landslide prediction, monitoring, and management in the study area.

Table 4.12. Classification accuracy of the logistic regression.

	Accuracy	Recall	Precision	F1 score
Training	93.92%	96.41%	89.72%	92.95%
Validation	90.61%	97.09%	90.21%	93.53%

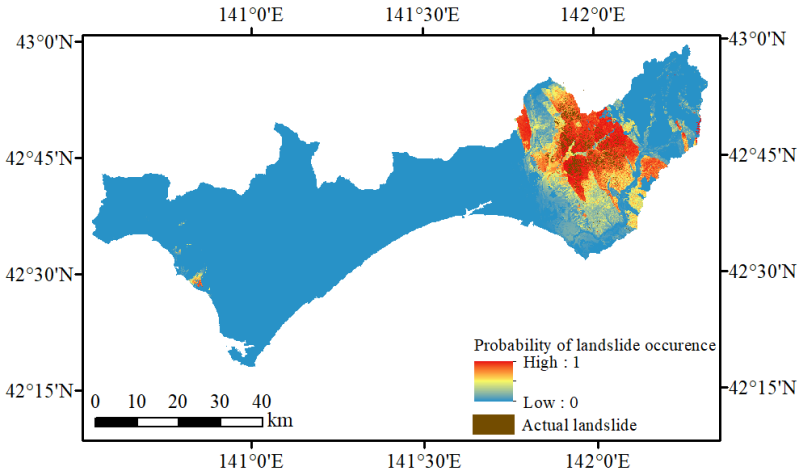

Figure 4.7. Landslide susceptibility map.

As there is no earthquake after the 2018 Hokkaido Eastern Iburi Earthquake in the study area, to test and explain the application of the model in a future disaster, the information of a past earthquake, i.e., 2003 Tokachi-Oki Earthquake, was applied. The 2003 Tokachi-Oki Earthquake was an undersea earthquake occurred at the epicenter of 41.815°N, 143.910°E with a depth of 27km, at 04: 50: 06 am on 26 September 2003 local time (JST) (UTC: 19:50:06 on 25 September 2003). The moment magnitude of the earthquake was 8.3Mw, and the maximum intensity of the earthquake was IX on a USGS scale (**Figure 4.8**) (USGS). It was said that, basically, no landslides were triggered in the study area by this earthquake.

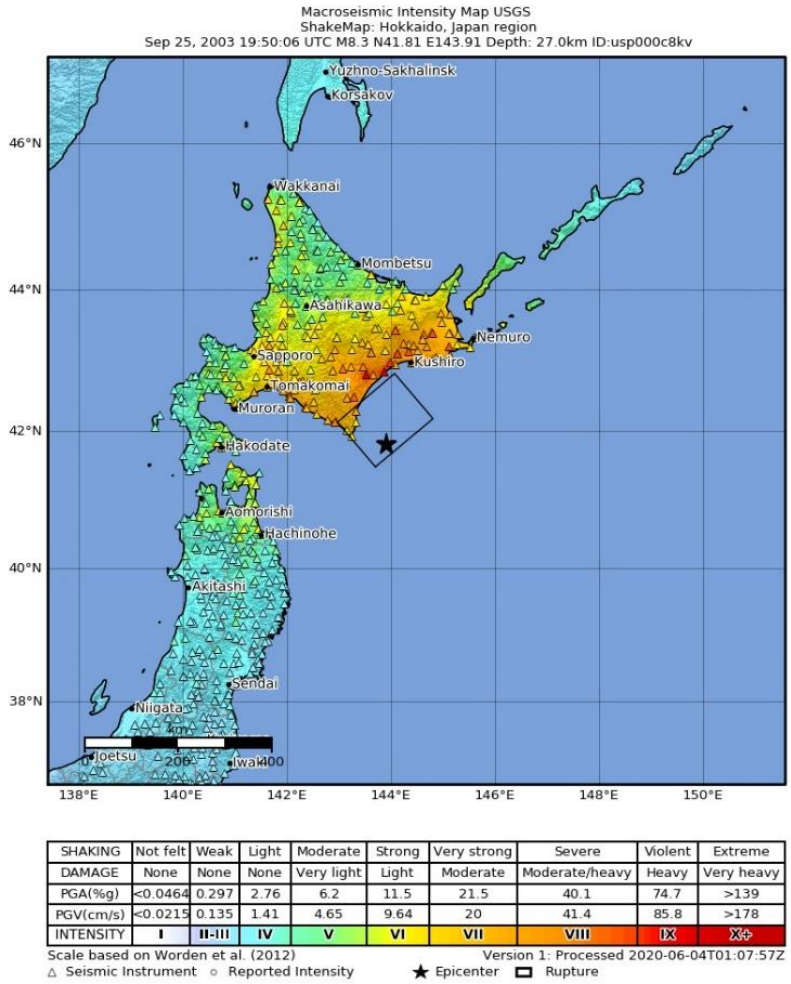

Figure 4.8. Shakemap for the 2003 Tokachi-Oki Earthquake (USGS).

The ground motion information of the earthquake and the previous precipitation information before the earthquake were collected from USGS and JMA, respectively.

After some preprocessing (e.g., interpolation for the point precipitation data and conversion from vector format to raster format), the PSA03 map and one-week cumulative precipitation map used in landslide susceptibility analysis were obtained (**Figure 4.9**). Updating these two dynamic terms in the previously constructed landslide susceptibility model and map, a new landslide susceptibility map was generated (**Figure 4.10**). As can be seen from this figure, there was only a small area with a relatively high landslide occurrence probability in the updated landslide susceptibility map, which had certain consistency with the actual situation. The small area of inconsistency might be due to the misclassification of the model or the changes in other conditioning factors such as soil and vegetation between these two earthquakes.

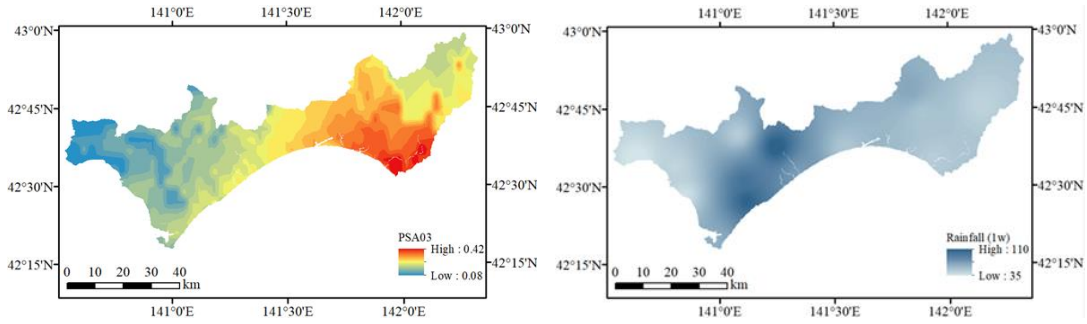

(a) (b)

Figure 4.9. PSA03 map and one-week cumulative precipitation map for the 2003 Tokachi-Oki Earthquake: (a) PSA03 map; (b) One-week cumulative precipitation map.

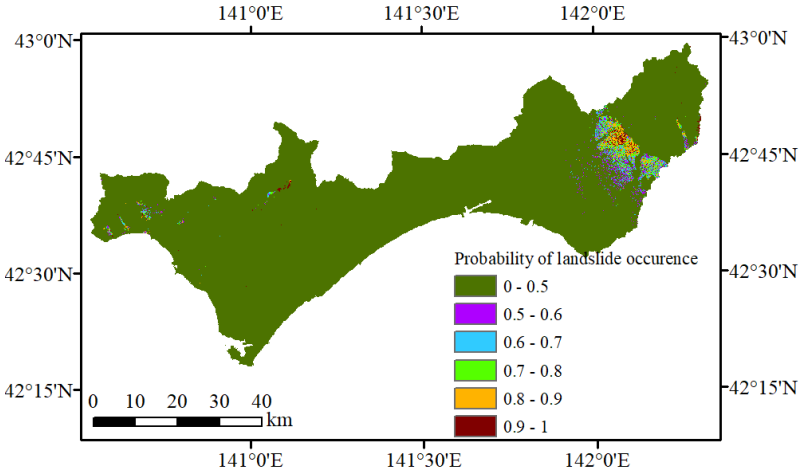

Figure 4.10. Landslide susceptibility after changing the ground motion and precipitation

information of 2003 Tokachi-Oki Earthquake.

4.5. Conclusions

Taking advantage of the data and information brought by the landslide event in 2018 Hokkaido Estern Iburi Earthquake, a landslide susceptibility analysis was carried out using a GIS-based statistical approach. Spatial data of landslide inventory and conditioning factors collected from different sources were preprocessed, analyzed, and constructed into a database in the ArcGIS platform, as dependent and independent variables for analysis. Considered independent variables (i.e., landslide conditioning factors) included topography, geology, soil, surface vegetation, precipitation, and ground motion. Representative indicators of these conditioning factors were calculated and derived in the ArcGIS platform for analysis.

The effectiveness and multicollineary problems of these conditioning factor indicators were analyzed and checked by the values of AUC, correlation coefficient, TOL, and VIF. Standard curvature, PSA03, and one-week cumulative precipitation before the disaster were found to be relatively effective among the three curvature-related (planform curvature, profile curvature, and standard curvature), six earthquake-related (MMI, PGA, PGV, PSA03, PSA10, PSA30), and five precipitation-related (three-day, one-week, two-week, three-week, and one-month cumulative precipitation before the disaster) conditioning factor indicators, respectively. SPI and STI seems to have some correlation with correlation coefficient values slightly larger than 0.7. After these analyses, eleven indicators were finally determined for the landslide susceptibility model construction, including elevation, slope gradient, slope aspect, standard curvature, TWI, STI, geology, soil, surface vegetation, PSA03, and one-week cumulative precipitation before the disaster.

All data, either in a raster format or vector format, were converted and resampled into 10m raster cells for raster calculation to incorporate various layers of information. The cells tagged as landslides occupied only 1.26% of the total raster cells, indicating a rare event of the landslide presence. Therefore, in order to avoid the underestimation of landslide occurrence, the non-landslide cells with the same number of landslide cells were randomly selected from the non-landslide cell library for susceptibility

analysis, as the testing results of different ratios between landslide and non-landslide cells (1:1, 1:2, 1:3, 1:4, and 1:5) showed that 1:1 was relatively favorable.

A landslide susceptibility model was finally constructed using the selected indicators under the determined ratio by a logistic regressiom. 70% of the data were used for training while 30% of data were used for validation. This model achieved an overall accuracy of over 90% for both training and validation dataset. Applying this model, a landslide susceptibility map was generated for the study area, which showed certain consistency with the actual landslides. It is expected to provide some useful information for the prediction, monitoring, and management of future landslide occurrence in the study area, by updating the changed causative factors such as precipitation indicator according to actual situation.

4.6. References

Allison, P. D. (2001). Logistic regression using the SAS system: theory and application. Wiley Interscience, New York. 288.

Ayalew, L., Yamagishi, H., Ugawa, N. (2004). Landslide susceptibility mapping using GIS-based weighted linear combination, the case in Tsugawa area of Agano River, Niigata Prefecture, Japan. Landslides, 1, 73-81.

Bai, S., Wang, J., Lü, G., Zhou, P., Hou, S., Xu, S. (2010). GIS-based logistic regression for landslide susceptibility mapping of the Zhongxian segment in the Three Gorges area, China. Geomorphology, 115 (1-2), 23-31.

Booth, G. D., Niccolucci, M. J., Schuste, E. G. (1994). Identifying proxy sets in multiple linear regression: an aid to better coefficient interpretation. U.S. Dept. of Agriculture, Forest Service, Ogden.

Bui, D. T., Tuan, T. A., Klempe, H., Pradhan, B., Revhaug, I. (2016). Spatial prediction models for shallow landslide hazards: a comparative assessment of the efficacy of support vector machines, artificial neural networks, kernel logistic regression, and logistic model tree. Landslides, 13, 361-378.

Chau, K. T., Sze, Y. L., Fung, M. K., Wong, W. Y., Fong, E. L., Chan, L. C. P. (2004). Landslide hazard analysis for Hong Kong using landslide inventory and GIS. Computer & Geoscience, 30 (4), 429-443.

Domínguez-Cuesta, M. J., Jiménez-Sánchez, M., Berrezueta, E. (2007). Landslides in the Central Coalfield (Cantabrian Mountains, NW Spain): geomorphological features, conditioning factors and methodological implications in susceptibility assessment. Geomorphology, 89 (3-4), 358-369.

JMA. https://www.data.jma.go.jp/gmd/risk/obsdl/index.php

King, G., Zeng, L. (2000). Explaining rare events in international relations. International Organisation, 55 (3), 693–715.

King, G., Zeng, L. (2001). Logistic regression in rare events data. Political Analysis, 9 (2), 137-163

Lee, C. (2015). Review and perspectives on methodology for landslide hazard analysis. 10th Asian Regional Conference of IAEG, Kyoto, Japan.

Lee, C. T. (2007). Statistical seismic landslide hazard analysis: An example from Taiwan. Engineering Geology, 182, 201-212.

Nefeslioglu, H. A., Duman, T. Y., Durmaz, S. (2008). Landslide susceptibility mapping for a part of tectonic Kelkit Valley (Eastern Black Sea region of Turkey). Geomorphology, 94 (3-4), 401-418.

Powers, D. M. W. (2011). Evaluation: from precision, recall and F-measure to ROC, informedness, markedness and correlation. Journal of Machine Learning Technologies. 2 (1), 37-63.

Süzen, M. L., Doyuran, V. (2004). Data driven bivariate landslide susceptibility assessment using geographical information systems: a method and application to Asarsuyu catchment. Turkey. Engineering Geology, 71 (3-4), 303-321.

USGS.https://earthquake.usgs.gov/earthquakes/eventpage/usp000c8kv/shakemap/intensity.

Van Den Eeckhaut, M., Vanwalleghem, T., Poesen, P., Govers, G., Verstraeten, G., Vandekerckhove, G. (2006). Prediction of landslide susceptibility using rare

events logistic regression: a case-study in the Flemish Ardennes (Belgium). Geomorphology, 76 (3-4), 392-410.

Yalcin, A. (2008). A. GIS-based landslide susceptibility mapping using analytical hierarchy process and bivariate statistics in Ardesen (Turkey): comparisons of results and confirmations. Catena, 72, 1-12.

Zhang, S., Li, R., Wang, F., Iio, A. (2019). Characteristics of landslides triggered by the 2018 Hokkaido Eastern Iburi earthquake, Northern Japan. Landslides, 16 (9), 1691-1708.

CHAPTER 5

SYNTHETIC APERTURE RADAR (SAR)-BASED LANDSLIDE DETECTION FOR POST-EVENT LANDSLIDE DISASTER MANAGEMENT

5.1. Introduction

Following a landslide event that impacted residents, a rapid detection and understanding of the landslides is of importance for coordinating emergency response efforts and limiting rescue arrangement delays. RS, especially optical sensors and SAR, can provide a valuable data source for rapid landslide detection, owing to their large coverage, non-contact, and rapid response. Making full use of the landslide inventory and RS products captured during this disaster, a SAR-based landslide detection was explored in this chapter to benefit post-event landslide disaster management in the future.

As has mentioned, optical sensors and SAR are two important and major remote sensing technologies that can be used for quick landslide detection and mapping after a disaster. Optical sensors can provide optical images like human eyes view the Earth, which are easy to interpret. Over the years, various optical images have been explored for landslide research through various means, either at an object level or at a pixel level. For instance, Sun et al. (2017) developed an algorithm for recognizing and mapping loess landslides, based on an object-oriented approach, by combining spectral, textural, and morphometric information with auxiliary topographic parameters, in high-resolution multispectral CF-1 satellite data and a high-precision DEM. The multi-scale segmentation and merging in object-oriented analysis were executed to obtain favorable landslide candidate objects. Chen et al. (2017) proposed an object-oriented landslide mapping framework, based on random forests and mathematical morphology, using ZY-3 satellite imagery. Random forest was first employed as a feature reduction tool, to identify significant features for landslide description. Mathematical morphology was then combined with the random forest to map the landslides. Bivic et al. (2017) applied two image correlator software packages (MicMac and Cosi-Corr) to ortho-rectified SPOT-5 images, in order to evaluate the possibility of measuring the displacement occurred between two image acquisitions

of a landslide located in a mountainous highly vegetated areas. In their study, the scale invariant feature transform method was employed to select image control points.

Nevertheless, optical sensors are passive RS using visible light, which rely heavily on sunlight for imaging, and cannot penetrate clouds. That may cause time delay in acquiring favorable images, hampering their application as an emergency tool for landslide detection, as landslide event usually occur in bad weather condition (especially rainfall-induced landslides) and sometimes at night such as the one in this case. In the 2015 Nepal earthquake, Burrows et al. (2019) indicated that there was almost no cloud-free imagery available for landslide detection in the first week following the disaster. SAR data, conversely, are relatively difficult to interpret, but can be acquired at night and in any weather condition, owing to the active characteristics of the radar sensors and long wavelengths of the applied microwaves. Therefore, they are deemed to be promising tools for quick response following a disaster even in harsh weather and at night. Actually, since the 1995 Kobe earthquake, SAR data have been widely investigated for building damage assessment in urban areas following a disaster (e.g., Matsuoka and Yamazaki, 2004; Dong and Shan, 2013; Plank, 2014).

As an active remote sensing, SAR sends electromagnetic microwaves to ground targets in a slanted way and then receives corresponding backscattering echoes. Under certain modes, it has the ability to obtain both intensity and phase information of the backscattering waves. Intensity refers to the amplitude information of the backscattering waves that can be influenced by both parameters of radar systems and characteristics of ground targets. Phase indicates the relative position of the backscattering waves within a full period, which is largely dependent on the distance between the radar sensor and ground targets. The path length of an electromagnetic signal to the ground and back usually contains a number of whole wavelength plus some fraction of a wavelength.

Over the years, SAR has been widely employed for the monitoring of specific slow-moving landslide through various interferometry techniques by the use of phase information (e.g., Strozzi et al., 2005, Colesanti and Wasowski, 2006, Zhao et al., 2012, Tofani et al., 2013, Confuorto et al., 2017, and Zhao et al., 2018). Nevertheless, the feasibility of interferometry technique depends on many observation

characteristics such as the spatial baseline, temporal baseline, coherence, and wavelength (Konishi and Suga, 2018), and is restricted by many actual conditions such as the steepness and orientation of the slope as well as the amount of vegetation (Lazecký et al., 2015). For instance, a favorable interferogram cannot be generated by the pre-event and post-event Advanced Land Observing Satellite-2 (ALOS-2) images applied in this case owing to the low coherence between them.

For the application of SAR images in landslide detection, there have not been many investigations. Several conducted studies were only concentrated on large individual landslides, catchments (Raspini et al., 2015; Yun et al., 2015; Xue et al., 2018), or dozens of landslides (Konishi and Suga, 2018). A couple of studies (Mondini, 2017; Burrows et al., 2019) focusing on large-scale landslide detection were also not for small-sized shallow landslides. Xue et al. (2018) synthesized a color image using SAR interference correlation value (red), backscattered intensity (green), and the difference between the backscattered intensities (blue), for the interpretation of the Daguanbao-Hongdongzigou giant landslide. Raspini et al. (2015) exploited both amplitude (through speckle tracking) and phase (through multi-image SAR interferometry) information of SAR images, for the displacement mapping of a single large landslide in Montescaglioso, Italy. Yun et al. (2015) found their damage proxy map, which was generated using the coherence difference calculated by a pre-event coherence map and a histogram-matched co-event coherence map, could roughly delineate the extent of debris from reported landslide/avalanche in Langtang valley. Konishi and Suga (2018) investigated the potential of backscattering coefficient difference and intensity correlation calculated by pre-event and post-event Constellation of Small Satellites for Mediterranean basin Observation (COSMO-SkyMed) images, for the detection of dozens of deep-seated landslides. Burrows et al. (2019) tested three potential SAR-coherence-based landslide methods (i.e., the absolute coherence method using one pre-event and one post-event SAR images, the Advanced Rapid Imaging and Analysis (ARIA) method applying two pre-event and one post-event images (Xue et al., 2018), and the newly proposed sibling-based coherence method employing a series of SAR images) for large-scale landslide classification, in the 2015 Gorkha, Nepal earthquake, using Sentinel-1 images. Mondini (2017) measured pixel-based changes between consecutive couples of

sixteen Sentinel-1 SAR intensity images using Log-Ratio index, for rainfall-triggered landslide detection in Tozang area, Myanmar. Moran's I index and semivariance were used to measure spatial autocorrelation evolution in the Log-Ratio index layers, and employed for landslide identification.

From these previous studies, the applicability of SAR data for the detection of the densely distrubuted small-sized shallow landslides is not very clear. Moreover, several information and features in SAR data can be used to measure ground changes, but there were no studies to compare them and tell which one is better or cost-effective for the application in landslide detection. Therefore, this chapter aimed to take advantage of the SAR products captured during this disaster to explore and compare different SAR features for the detecion of such densely distrubuted small-sized shallow landslides landslides. Two pre-event and one post-event ALOS-2 L-band single look complex (SLC) SAR products were applied. All potential parameters that have the capability to measure ground changes and can be derived relatively easily from these products were selected and calculated to facilitate a rapid detection. Qualitative and quantitative analyses were performed to compare the capability of these potential candidate parameters for landslide detection so as to provide a reference. A combinational use of these parameters and features was also investigated. A simple exploration and comparison between Sentinel-1 C-band SAR data and ALOS-2 L-band SAR data was also carried out to provide some reference for future application.

5.2. Study Area and Dataset

Before and after the disaster, the Japanese ALOS-2 satellite captured the affected area in the Level 1.1 single look complex (SLC) format at August 9, 2018, August 23, 2018, and September 6, 2018, respectively. All of the three products were captured from the left looking ascending track with an off-nadir angle of 37.8° and covered the same region with an area of 55 km×70 km (**Figure 5.1a**). SLC products means that the images were represented by complex I and Q channels to preserve amplitude and phase information, from which intensity and coherence can be derived. The acquisition mode of these images was stripmap ultra-fine mode single polarization

(UBS), with a polarization mode of HH. A summary of the data information was listed in **Table 5.1**.

A rectangular region in the landslide area covered by the three SAR images was used to explore the SAR information and features for landslide detection (**Figure 5.1a**). The two pre-event and one post-event ALOS-2 products were all used to calculate and derive potential features and parameters. The detailed landslide inventory created by Zhang et al., (2019), which has been introduced and used in chapters 3 and 4, was applied as the ground truth landslide data for result comparison and evaluation in this chapter. The distribution of actual landslides in the study area can be seen in **Figure 5.1b**.

Table 5.1. Information of the applied ALOS-2/PALSAR-2 data.

Date (UTC) (yyyy/mm/dd)	Format	Level	Mode	Polarization	Sample Spacing (Range × Azimuth)	Orbit Direction	Off-nadir Angle
2018/08/09	CEOS	L1.1 (SLC)	UBS	HH	1.43m × 1.95m	Left Looking/ Ascending	37.8 °
2018/08/23	CEOS	L1.1 (SLC)	UBS	HH	1.43m × 1.95m	Left Looking/ Ascending	37.8 °
2018/09/06 (13:37)	CEOS	L1.1 (SLC)	UBS	HH	1.43m × 1.95m	Left Looking/ Ascending	37.8 °

ALOS-2: Advanced Land Observing Satellite-2; PALSAR-2: Phased Array type L-band Synthetic Aperture Radar-2; CEOS: Committee on Earth Observation Satellites; SLC: single look complex; UBS: ultra-fine mode single polarization; HH: horizontal transmit and horizontal receive.

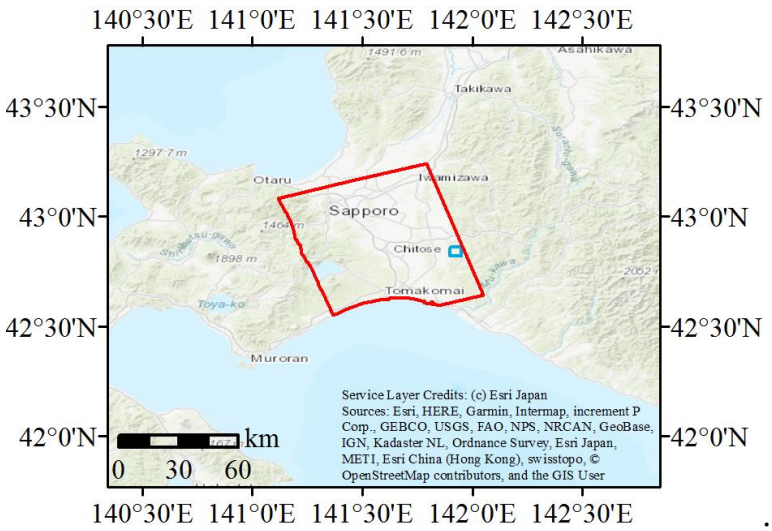

(a)

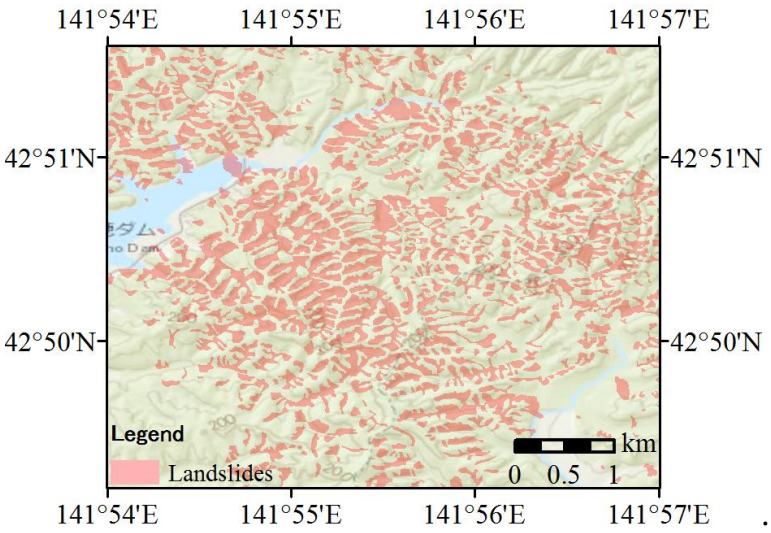

(b)

Figure 5.1. Location of captured synthetic aperture radar (SAR) products and study area as well as the landslide distribution in the study area: (a) Location of captured Advanced Land Observing Satellite-2 (ALOS-2) SAR products (red polygon) and study area (blue rectangle); (b) Landslide distribution in the study area.

5.3. Methodology

5.3.1. Principle and Parameter Calculation

As has been introduced in section 5.2, the applied ALOS-2 SLC products included both intensity and phase information of microwave echoes backscattered from ground targets. Intensity indicates the amplitude information of backscattering microwaves received by the SAR sensor after emitting microwaves to ground targets. It is influenced by not only radar system parameters (e.g., frequency, polarization, and incidence angles) but also ground target characteristics (e.g., roughness and material dielectric characteristics). Therefore, intensity changes in SAR images over a period of time can indicate the ground target changes during this time. As landslides usually cause land surface changes such as de-vegetation and slope smoothing, SAR image intensity changes are deemed to have the potential for landslide identification. Intensity difference and co-event correlation coefficient calculated by pre-event and post-event SAR images can be used to quantify SAR image intensity changes caused by a disaster event, and hence are selected as candidate parameters for landslide detection in this case.

Intensity difference, *d*, can be easily calculated by **Equation 5.1**. Regions with higher absolute values of *d* experienced larger ground changes, whereas regions with lower absolute values of *d* experienced smaller changes.

$$d = \frac{\sum_{i=1}^{N}(Ib_i - Ia_i)}{N} \tag{5.1}$$

where *N* is the total number of pixels within a certain window, and Ia_i and Ib_i are intensity values of pixel *i* in the two SAR images (hereafter).

Correlation coefficient, *r*, can be calculated according to **Equation 5.2**. Its values range from -1 to 1, with lower values indicating larger ground changes, and a 1 value representing no ground changes.

$$r = \frac{N\sum_{i=1}^{N} Ia_i Ib_i - \sum_{i=1}^{N} Ia_i \sum_{i=1}^{N} Ib_i}{\sqrt{(N\sum_{i=1}^{N} Ia_i^2 - (\sum_{i=1}^{N} Ia_i)^2) \cdot (N\sum_{i=1}^{N} Ib_i^2 - (\sum_{i=1}^{N} Ib_i)^2)}} \tag{5.2}$$

Moreover, to differentiate areas where the correlation coefficient value is always low and where it has decreased, the difference of pre-event and co-event correlation coefficient, Δr, was also calculated (**Equation 5.3**) and taken into account. This parameter has shown favorable performance for building damage detection in un-urbanized areas (Matsuoka and Yamazaki, 2006), and might have favorable performance for landslide detection in this case.

$$\Delta r = r_{co} - r_{pre} \tag{5.3}$$

where r_{co} is the co-event correlation coefficient calculated by one pre-event and one post-event SAR images, and r_{pre} is the pre-event correlation coefficient calculated by two pre-event SAR images.

Phase is a property of periodic phenomenon, referring to the relative value of the received backscattering wave within a whole period. It is very sensitive to the distance between the satellite sensor and ground target, and hence also has the ability to measure ground target changes. Phase difference has already been applied through

SAR interferometry techniques to measure earth's surface changes, such as the deformation caused by landslides, volcanoes, glaciers or anthropogenic activities (Massonnet and Feigl, 1998). Nevertheless, as has been mentioned, the feasibility of interferometry technique depends on many observation characteristics (e.g., spatial baseline, temporal baseline, coherence, and wavelength) (Konishi and Suga, 2018), and is restricted by many actual conditions when applied for landslide detection and monitoring (e.g., the steepness and orientation of the slope and the amount of vegetation) (Lazecký et al., 2015). In this case, a favorable interferogram cannot be generated by the pre-event and post-event SAR images due to the high decorrelation between them.

Coherence, γ, means the cross-correlation of phase information in two images (**Equation 5.4**), which is often used to prejudge whether a good interferogram can be generated. Its values range from 0 to 1, and can also be applied to measure ground changes, with a lower value indicating larger ground changes. In this case, the co-event coherence calculated by one pre-event and one post-event SAR image was also selected as a candidate parameter for landslide detection. Moreover, similar to the correlation coefficient, to distinguish areas where the coherence value is always low and where it has reduced, the difference of pre-event and co-event coherence, Δγ, was also calculated (**Equation 5.5**) and explored.

$$\gamma = \frac{E\langle c_1 c_2^* \rangle}{E\langle c_1 c_1^* \rangle E\langle c_2 c_2^* \rangle} \tag{5.4}$$

where c_1 and c_2 are corresponding complex pixel values in images of two acquisition dates, c^* means the complex conjugate of c, and E means the expected value.

$$\Delta\gamma = \gamma_{co} - \gamma_{pre} \tag{5.5}$$

where γ_{co} is the co-event coherence calculated by one pre-event and one post-event SAR images, and γ_{pre} is the pre-event coherence calculated by two pre-event SAR images.

To sum up, all of the parameters mentioned above, including intensity difference d, co-event correlation coefficient r, correlation coefficient difference Δr, co-event coherence γ, and coherence difference $\Delta\gamma$, have certain potential for landslide detection and were selected as candidate parameters in this case. In order to obtain

images of these parameters, the Sentinel Application Platform (SNAP) 6.0 of the European Space Agency (ESA) and ArcGIS 10.5 software of the Environmental Systems Research Institute (ESRI) were applied to process the three original SAR SLC products. SNAP 6.0 was primarily applied to derive the basic intensity and coherence information from the original complex images (Veci, 2016). ArcGIS 10.5 was mainly employed for the final calculation of these potential parameters.

5.3.2. Qualitative and Quantitative Analyses of the Potential Parameters

After obtaining images of these potential parameters, qualitative and quantitative analyses were carried out to investigate and compare their performance for landslide detection. Qualitative analyses were carried out by overlapping the landslide ground truth data (Zhang et al., 2019) upon the calculated parameter images, and observing the parameter characteristics in actual landslide and non-landslide areas intuitively.

Quantitative analyses were executed by ROC curves. ROC curves are graphical plots generated by true positive rate (TPR) values against false positive rate (FPR) values, and can be used to illustrate the diagnostic ability of binary classifiers (Metz, 1978; Zweig and Campbell, 1993; Tom, 2006). In a binary classification problem, under a certain threshold, there is a confusion matrix composed of four elements: true positive (TP), true negative (TN), false positive (FP), and false negative (FN), according to actual and predicted classification results (**Table 4.11**). Based on these four elements in the confusion matrix, TPR and FPR can be calculated easily by **Equations 5.6** and **5.7**, respectively. Moving the classification threshold from lower values to higher values, a series of TPR and FPR can be obtained, by which a ROC curve is able to be generated. On one hand, the ROC curve can be applied to measure and compare the performance of binary classifiers through calculating the area under the curve (AUC). Values of AUC range from 0.5 to 1, with a larger value representing a model with higher performance (Hanley and McNeil, 1982). On the other hand, for a specific binary model, the ROC curve can be employed to find the optimal classification threshold by seeking the point with highest Youden index (Youden, 1950) in the top left of the curve.

$$TPR = TP/(TP+FN) \quad (5.6)$$

$$FPR = FP/(FP+TN) \quad (5.7)$$

where TPR and FPR means true positive rate and false positive rate; TP, FN, FP, and TN means true positive, false negative, false positive, and true negative as shown in **Table 4.11**.

Parameter calculation window sizes influence characteristics of calculated parameter images (e.g., ground target boundary), and will also affect the performance of the parameters as landslide classifiers. In order to understand the influence of window sizes as well as to find the optimal window size for calculation, the equal step and hunt&fill scaling method in incremental dynamic analysis (Vamvatsikos and Cornell, 2001; 2002; Vamvatsikos, 2011) were referred in order to save computational efforts. First, calculation window sizes of 5×5, 15×15, 25×25, 35×35, 45×45, 55×55, 65×65, 75×75, and 85×85 were applied to understand the overall trend of window size impacts, as the pixel size of the applied SAR images is around three square meters, and the landslide sizes in the study areas vary from hundreds to tens of thousands square meters. Then, if big difference exists between the results of two adjacent calculation window sizes, interpolation will be carried out to fill the gap and hunt for the specific optimal window size.

5.4. Results

5.4.1. Parameter Qualitative Interpretation

The calculated parameter images overlapped by ground truth landslides are shown in **Figure 5.2**. As can be seen from this figure, more or less, all potential parameters show some different characteristics in landslide and non-landslide areas.

The intensity difference image (**Figure 5.2a**) displays some obvious higher-value and lower-value pixels in landslide areas. That means both increase and decrease of intensity have been caused by the earthquake-induced landslides. On one hand, triggered landslides wiped away many elements on the hillsides (e.g., trees and big stones) and smoothed the slopes, reducing the backscattering from these areas to the

radar sensor and causing the intensity decrease. On the other hand, the alluviums washed away by landslides deposited in some foot regions of the slope, increasing the backscattering from these areas to the radar sensor and inducing the intensity increase.

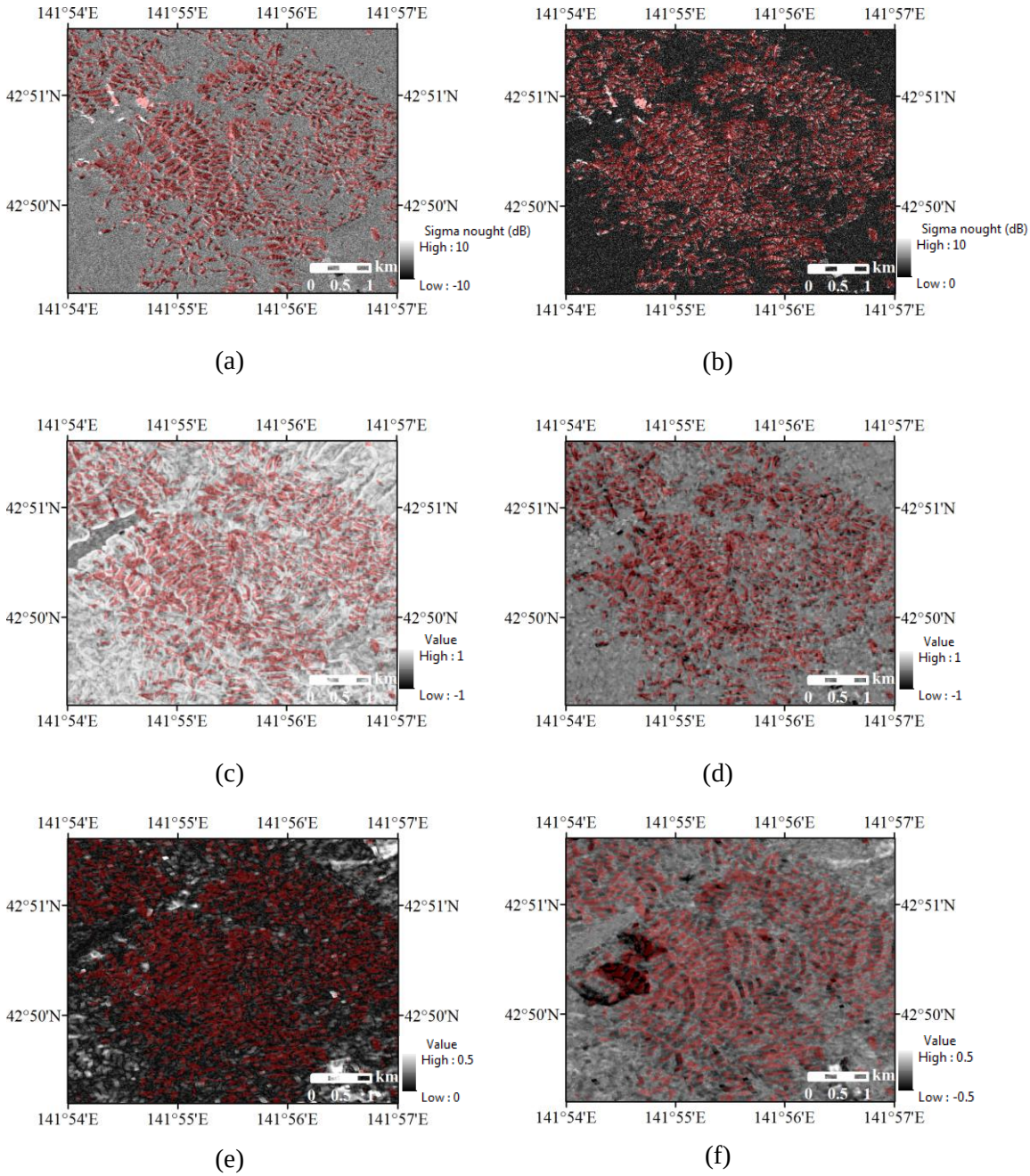

Figure 5.2. Images of calculated parameters overlapped by ground truth landslides (red color: ground truth landslides): (a) Intensity difference d; (b) Absolute value of intensity difference d_{abs1}; (c) Co-event correlation coefficient r; (d) Correlation coefficient difference Δr; (e) Co-event coherence γ; (f) Coherence difference $\Delta\gamma$.

As both intensity increase and decrease occurred in landslide areas, the absolute value of the intensity difference, d_{abs1}, was calculated (**Equation 5.8**) and would be applied to facilitate further analysis for landslide pixel identification. In the image of this parameter, landslide areas will only display higher-value pixels (**Figure 5.2b**). Besides, information loss may occur when calculating d and d_{abs1} according to **Equation 5.1**, as the increased and decreased intensity pixel values within the calculation window could be averaged and neutralized. Therefore, a new intensity difference absolute value, d_{abs2}, was created (**Equation 5.9**) to avoid information loss in intensity difference calculation, and would also be explored as a landslide classifier.

$$d_{abs1} = |d| \tag{5.8}$$

where d is the intensity difference calculated by Equation 5.1.

$$d_{abs2} = \frac{\sum_{i=1}^{N} |Ib_i - Ia_i|}{N} \tag{5.9}$$

Moreover, in both co-event correlation coefficient (**Figure 5.2c**) and correlation coefficient difference (**Figure 5.2d**) images, landslide areas display some lower-value pixels, indicating larger ground changes comparing with non-landslide areas. Due to larger backscattering changes in the post-event SAR image caused by landslide-induced ground changes, the co-event correlation coefficient in the landslide areas became relatively smaller, leading to these lower-value pixels. Besides, by subtracting a pre-event correlation coefficient, some areas where pixel values were always low seem to be excluded as expected in the correlation coefficient difference image. For instance, the water area at the top left of the study region (blue polygon in **Figure 5.3**), which showed relatively lower pixel values in the correlation coefficient image (**Figure 5.2c**), did not show clear lower pixel values in the correlation coefficient difference image (**Figure 5.2d**) anymore.

Furthermore, the co-event coherence (**Figure 5.2e**) and coherence difference (**Figure 5.2f**) images also display some lower-value pixels in some landslide areas, owing to the relatively larger decorrelation caused by landslide-involved ground changes. Nevertheless, the difference between landslide and non-landslide areas in these two images seems to be not as clear as that in other images. This may be due to

the fact that most study areas were covered by trees where the coherence is originally very low even no landslides occurred. A clear lower-value region can be seen in the darker area of the coherence difference image (**Figure 5.2f**). This area was initially covered by grass (green polygon in **Figure 5.3**), which had higher pre-event coherence values comparing with areas covered by trees. Therefore, when pre-event coherence was subtracted from the co-event coherence, a lower-value area region appears. This may indicate that the coherence difference is favorable for landslide detection in slopes covered by grass.

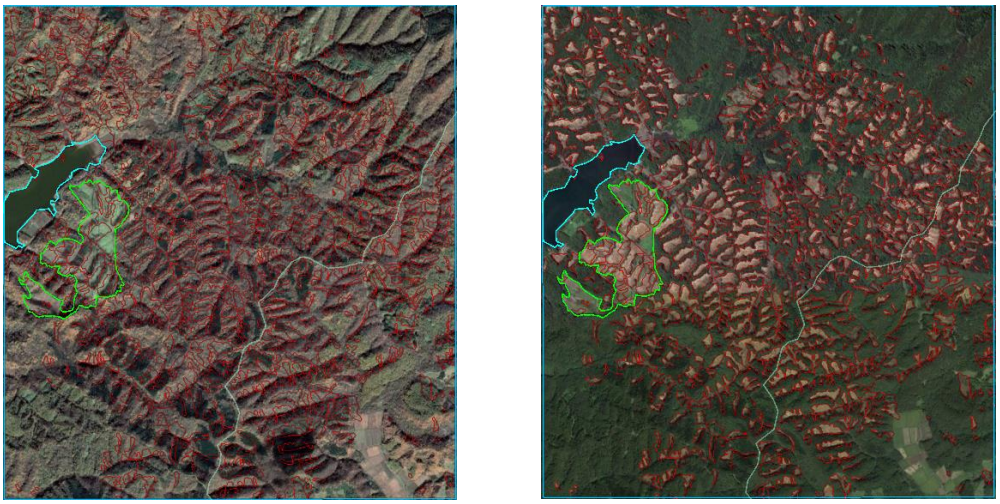

(a) (b)

Figure 5.3. Pre-event and post-event optical images in the study area from Google Earth: (a) Pre-event image (2017/10/24); (b) Post-event image (2018/09/11) (red polygon: ground truth landslides made by Zhang et al. (2019)). (The different shape of images in Figure 5.3 is due to the different coordinate system in Google Earth).

5.4.2. Parameter Quantitative Analyses

ROC analyses of the six parameters mentioned above (d_{abs1}, d_{abs2}, r, Δr, γ, and $\Delta\gamma$) calculated under different window sizes were carried out one by one. Obtained AUC values are listed in **Table 5.2** and then plotted in **Figure 5.4** for easy visual observation. As can be seen from the table and figure, the newly proposed parameter d_{abs2} shows the largest AUC values among all parameters, indicating its best performance as landslide classifiers in this case. The correlation coefficient difference Δr also shows good performance, whose AUC values are higher than the other four

parameters when the calculation window size is larger than 25. Besides, the largest AUC values of d_{abs2} and Δr are around 0.82 and 0.75 respectively, demonstrating their favorable performance in classifying landslide and non-landslide pixels.

Table 5.2. AUC values of the six parameters calculated under different window sizes.

	5×5	15×15	25×25	35×35	45×45	55×55	65×65	75×75	85×85
d_{abs1}	0.6385	0.6763	0.6856	0.6833	0.6745	0.6639	0.6551	0.6504	0.6483
d_{abs2}	0.6601	0.7552	0.7998	0.8153	0.8148	0.8063	0.7954	0.7851	0.7768
r	0.5537	0.6203	0.6525	0.6672	0.6729	0.6745	0.6742	0.6739	0.6741
Δr	0.5519	0.6437	0.7050	0.7388	0.7523	0.7540	0.7503	0.7447	0.7392
γ	0.5406	0.5794	0.6042	0.6217	0.6352	0.6482	0.6580	0.6648	0.6690
Δγ	0.5436	0.5842	0.6070	0.6242	0.6356	0.6435	0.6482	0.6511	0.6521

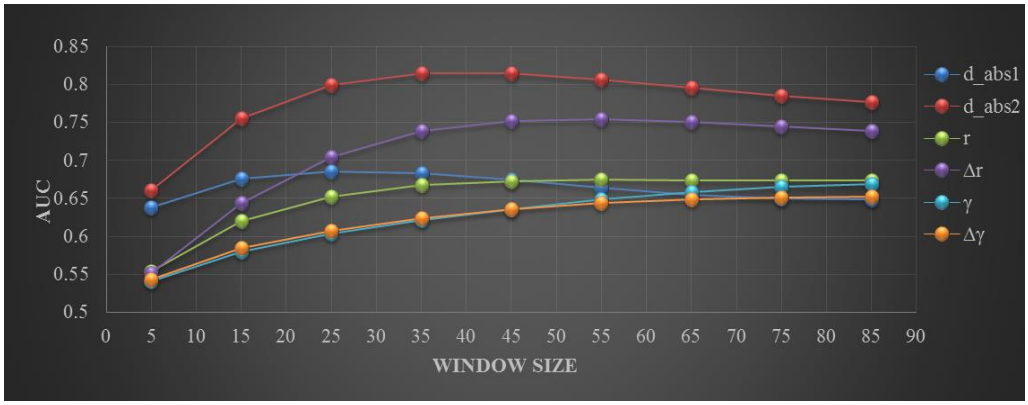

Figure 5.4. AUC values of the six parameters calculated under different window sizes.

Moreover, in general, the intensity-related parameters (d_{abs1}, d_{abs2}, r, and Δr) have better performance than the coherence-related parameters (γ and Δγ). This is considered to be associated with the sensitivity of these two kinds of information to ground changes and the land use here. Coherence information is more sensitive to minor changes (e.g., vegetation growth and movement of leaves and stalk induced by wind), and usually has low values in forests even if no disaster occurred. The study area was mainly covered by trees. The sensitivity of coherence information to the minor vegetation changes here interfered with their detection of landslides, which

might be the reason for the overall poorer performance of the coherence-related parameters.

In addition, between the two intensity difference parameters (d_{abs1} and d_{abs2}), d_{abs2} shows much better performance than d_{abs1}, demonstrating the advantage of **Equation 5.9**, which tried to avoid information loss in calculation. In addition, as the window size increases, the gap between the AUC values of d_{abs1} and d_{abs2} is growing increasingly larger. This also proves that information loss occurred in the calculation of d_{abs1}, which was caused by the average of increased and decreased intensity pixel values within the calculation window. As for the two correlation coefficient parameters (i.e., r and Δr), Δr shows much better performance than r, as some pixels whose values were always low were excluded by subtracting one pre-event correlation coefficient image. However, this approach dose not achieve the same good effect on coherence parameters, as most of the study area was covered by trees that along can cause large coherence decorrelation. The classification performance of $\Delta\gamma$ is as unsatisfactory as that of γ.

As for the influence of calculation window sizes, the general trend for the intensity-related parameters is that, as the window size increases, the classification accuracy first increases and then tends decrease. Favorable window sizes are around 25 to 55, with the optimal being 25, 35, 55, and 55 for d_{abs1}, d_{abs2}, r, and Δr, respectively. Comparing with other parameters, d_{abs1} achieves the optimal performance in a smaller window size, as the bigger the window size, the more increased and decreased pixels will be averaged. For the coherence-related parameters, within the calculation window sizes that have been applied, the parameter performance is becoming better and better with the increase of the calculation window size. Nevertheless, the improvement is very slight.

Furthermore, as can be seen from **Table 5.2**, there is no big difference between the AUC values of parameters calculated under two adjacent optimal window sizes. Therefore, interpolation between the calculation window sizes was not carried out. The highest AUC values for the six parameters, i.e., d_{abs1}, d_{abs2}, r, Δr, γ, and $\Delta\gamma$, are around 0.69, 0.82, 0.67, 0.75, 0.67, and 0.65, respectively. That means, individually, d_{abs1}, r, γ, and $\Delta\gamma$ are not very appropriate as binary classifiers for distinguishing landslide and non-landslide pixels in this case, while d_{abs2} and Δr have favorable

performances. What should be noted is that this conclusion is obtained based on only this specific case: detection of densely distributed shallow landslides with a small size in slopes covered by trees, using high-resolution L-band ALOS-2 products. For images of other bands or other resolution conditions, or for landslides in bare slopes or of deep-seated or large-sized types, there may be some differences. For instance, the coherence parameters may have better performances for landslide detection in bare slopes due to there being no vegetation interference.

5.4.3. Landslide Detection by the Favorable Parameters

In order to specifically understand the performances of the two favorable parameters (d_{abs2} and Δr) found in quantitative analyses, detailed analyses were carried out. ROC curves of the two parameters calculated under the optimal window sizes were shown in **Figure 5.5**. Optimum thresholds were then determined by seeking the point with highest Youden index at the top left of the curves. Corresponding threshold values for d_{abs2} and Δr were 2.08 and -0.11, respectively. Classification results under the optimal thresholds were shown in **Figure 5.6** to compare with the ground truth landslides. A summary of the classification accuracy was listed in **Table 5.3**, including accuracy, recall, precision, and F1 score (**Equations 4.3-4.6**), to provide a quantitative understanding.

The shape of the ROC curves in **Figure 5.5** can give an intuitive impression of the parameter performance as binary landslide classifiers. As *x* and *y* axis represent TPR and FPR respectively, the closer the curve to y axis, the better the parameter performance. The accuracy and recall values in **Table 5.3** can provide a quantitative understanding of the parameter capabilities for landslide and non-landslide pixel classification. When using d_{abs2} as a landslide classifier, 69.36% landslide and non-landslide pixels can be correctly classified, and 87.76% landslide pixels can be correctly identified. When using Δr as a landslide classifier, 64.57% landslide and non-landslide pixels can be correctly classified, and 81.68% landslide pixels can be correctly identified. Since the key point of landslide detection is to identify all landslide areas correctly, the higher recall values indicate that the two parameters have certain values for the landslide detection.

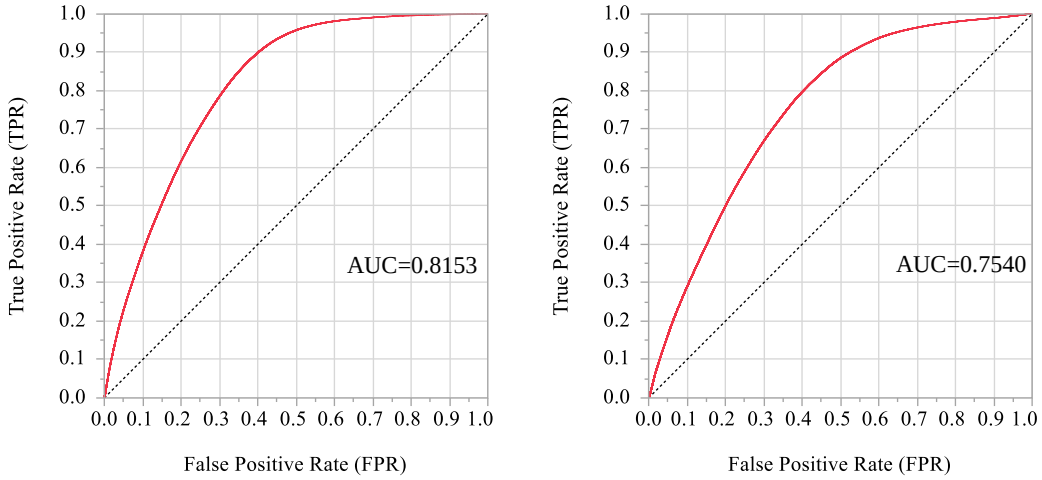

(a) (b)

Figure 5.5. Receiver operating characteristic (ROC) curves of d_{abs2} and Δr calculated under the optimal window sizes: (a) d_{abs2}; (b) Δr.

Table 5.3. Landslide detection accuracy of d_{abs2} and Δr calculated under the optimum window sizes.

Parameter	Accuracy	Recall	Precision	F1 score
d_{abs2}	69.36%	87.76%	47.04 %	61.25%
Δr	64.57%	81.68 %	42.59%	55.99%

The low precision values of the classification results (**Table 5.3**) demonstrate that many non-landslide pixels were classified as landslide pixels. This can been seen more clearly from **Figure 5.6**, which shows that many non-landslide areas around the ground truth landslides were classified as landslides by the two parameters. To some extent, this phenomenon is due to the imprecise boundary of the ground truth landslides and the principal of the two SAR intensity parameters. The landslide boundaries in the ground truth landslide inventory were generally curves roughly consistent with visible ground changes caused by landslides, such as de-vegetation, as shown in **Figure 5.3**. They were not very precise. Moreover, surrounding areas of the landslide boundaries where there seems to be no clear visible changes may also experience implicated changes, for instance, vegetation tilt caused by the erosion or lashing of surrounding soils. These implicated changes may also cause significant

SAR backscattering changes, making these areas detected as landslides by the SAR intensity parameters. F1 score, which balanced the recall and precision measures, has a value of 61.25% for d_{abs2} and a value of 55.99% for Δr, indicating a relatively better performance of d_{abs2} compared with Δr on the whole.

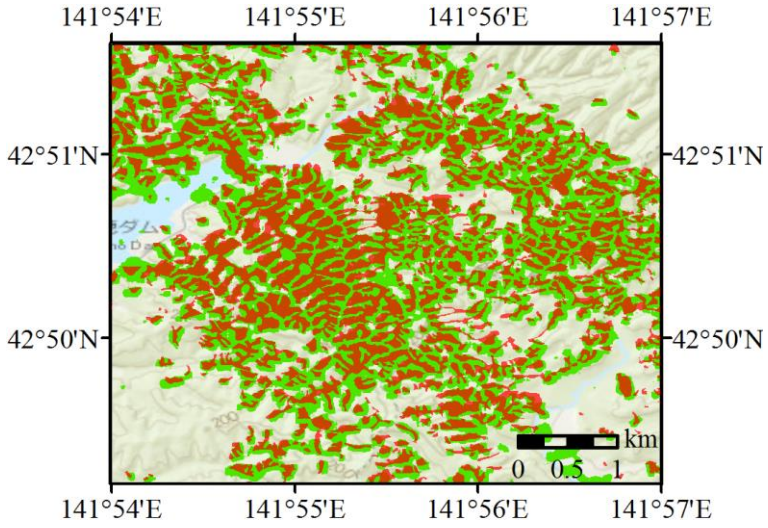

(a)

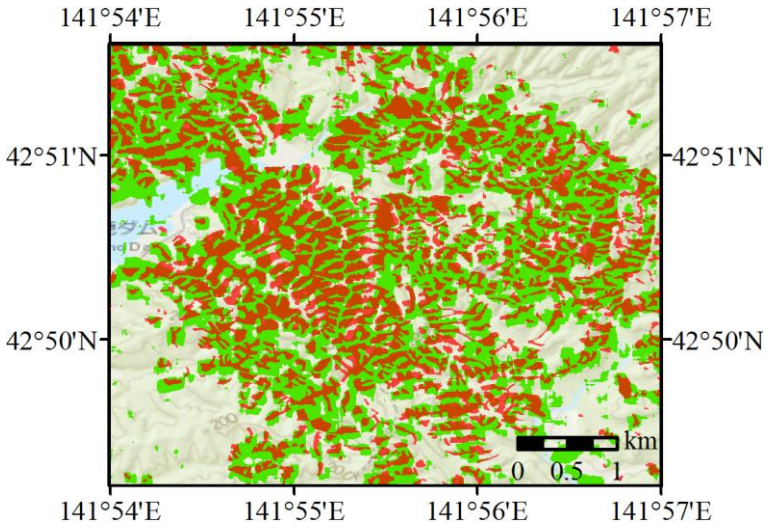

(b)

Figure 5.6. Landslides detected by d_{abs2} and Δr (green: landslides detected by d_{abs2} and Δr; red: ground truth landslides made by Zhang et al. (2019)): (a) d_{abs2}; (b) Δr.

5.4.4. Landslide Detection by Jointly Applying Three Types of Parameters

As the sensitivities of the three types of parameters (i.e., intensity difference, correlation coefficient, and coherence) to ground changes are different, a combinational application of them may provide complementary information to each other, and improve the landslide detection accuracy. To explore the combinational use of the three types of parameters, linear discriminant analysis (Balakrishnama and Ganapathiraju, 1998) was carried out using three relatively favorable parameters with one in each type.

Linear discriminant analysis is a mathematical process that employs functions to separately analyze multiple object or item classes. It has been applied for SAR-based building damage assessments since the 1995 Kobe Earthquake, and has shown favorable performances, e.g., Matsuoka and Yamazaki, 2004 and 2010. d_{abs2}, Δr, and $\Delta\gamma$ were applied as the intensity difference, correlation coefficient, and coherence parameters, respectively, as they have shown relatively favorable performances in parameter analyses, and/or are able to distinguish areas where parameter values were always low and have decreased.

A discriminant function combining d_{abs2}, Δr, and $\Delta\gamma$ was obtained from the linear discriminant analysis and is shown in **Equation 5.10**. Landslides detected by this discriminant function are shown in **Figure 5.7**, to provide an intuitive observation. Pixels with positive discriminant scores (z values) were assigned as landslides, whereas pixels with negative discriminant scores were assigned as non-landslides. The accuracy, recall, and precision values of the mapping results are 74.31%, 70.13%, and 52.58%, respectively. Compared with the landslides detected by d_{abs2} and Δr mentioned in the previous section, the accuracy and precision values are higher, and the recall value is lower. Misclassifications owing to the fact that surrounding non-landslide pixels were classified as landslide pixels seem to be reduced, even though some still exist. Some misclassified landslide pixels seemed to be excluded (e.g., water area in **Figure 5.6**) by this method, while some landslide pixels in some areas were not identified (**Figure 5.7**). Overall, the combinational application of these three parameters did not improve the landslide detection significantly. This may because that these parameters could not provide much effective supplementary information to

each other and the coherence information is originally not good for the landslide detection in this case.

What should be noted is that this discriminant function was also obtained based on only this case study. For the application to other SAR images and other ground conditions, a further check is still needed, as the parameter coefficients in the function may vary with the conditions of SAR images and actual sites. Moreover, the combination application of these parameters may improve the results to a greater exent for other cases, such as those with many types of landslides.

$$z = 1.069\, d_{abs2} - 1.822\, \Delta r - 2.986\, \Delta\gamma - 3.406 \qquad (5.10)$$

where z is the discriminant score.

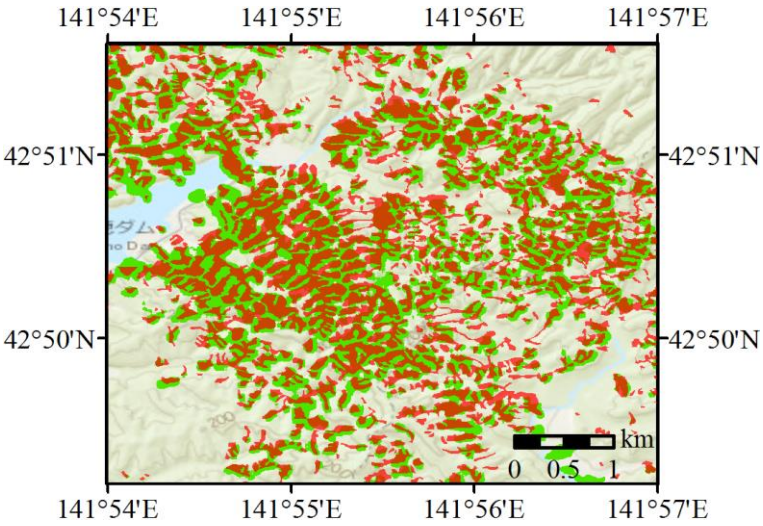

Figure 5.7. Landslides detected by the discriminant analysis (green: landslides detected by the discriminant analysis; red: ground truth landslides made by Zhang et al. (2019)).

5.5. Discussions

In the previous work, a relatively comprehensive study was conducted concerning the application of intensity and coherence information in two pre-event and one post-event L-band ALOS-2 SAR products for rapid landslide detection at a pixel level. Qualitative interpretation, quantitative analyses, and a combinational application of

the potential parameters were carried out, to obtain some results and conclusions for future reference.

What should be noted is that these results and conclusions were obtained based on only this one specific case: detection of densely distributed shallow landslides with a small size in slopes covered by trees, using high-resolution L-band ALOS-2 products. For other types of landslides or other kinds of SAR images, there may be some differences, and further verifications are still needed. The coherence difference may be a good parameter for identifying landslides in slopes covered by grass (as shown in the darker area of **Figure 5.2f**). The coefficients of different parameters in the discriminant function shall vary with the landslide situations and SAR image conditions. Nevertheless, the two favorable parameters (d_{abs2} and Δr) shall also have favorable performances for the detection of other types of landslides, especially deep-seated and large-sized landslides, as the principal of them for landslide detection is that they can detect the ground changes caused by landslides and such landslides can cause more conspicuous ground changes. The combinational use of the three types of parameters shall lead to more obvious accuracy improvement for areas with landslides of more types or more sizes, owing to the different sensitivities of different parameters to ground changes of different degrees.

Moreover, in this study, the linear discriminant analysis was applied to jointly use several different parameters, as it is relatively simple, intuitive, and has shown favorable performance for SAR-based building damage assessment. Other machine learning classifiers, such as the decision tree, random forest, and support vector machine, also have good capabilities for classification problems based on a series of variables, and can be explored to jointly use these intensity and coherence information for landslide detection. Yet, no matter which kind of classification method is applied, the trained models and parameters (e.g., coefficients of parameters in the discriminant function) shall vary with the conditions of landslides and SAR images. For an emergency application in a specific event, if such trained models are not available, an intuitive observation of the favorable parameters would be a good way, as these parameters can be calculated very easily, and have shown favorable performance even in the qualitative analyses. Furthermore, to make full use of different parameters' advantages, the intuitive observation can also be conducted by compositing several

calculated parameter images into a color image (e.g., red: intensity difference, green: correlation coefficient difference, blue: coherence difference). Besides, a sample area in the images of the parameters can be extracted and the histogram of pixel values in the sample area can be analyzed, or the unsupervised classification can be carried out to find a suitable value or model to extract these areas, if the specific ones in this study are not suitable.

In addition, it seems that a reasonable inference can be obtained concerning the parameter calculation window sizes: the more sensitive the parameter to other minor ground changes, the bigger window sizes are needed to blur parameter changes caused by these minor changes in order to reduce their interference, and therefore the bigger the optimal window size. In this case, the sensitivity of these three kinds of parameters to other minor ground changes was: coherence parameters > correlation coefficient parameters > intensity difference parameters, and the optimal calculation window size for them was generally: coherence parameters > correlation coefficient parameters > intensity difference parameters. Besides, the favorable window sizes for the intensity-related parameters seem to be associated with image pixel sizes and landslide area distribution. In this case, the favorable window sizes for the intensity-related parameters were about 25 to 55. The size of each pixel is approximately $3m^2$. The landslide areas in the study region range from $100m^2$ to $50{,}000m^2$, with an average value of approximately 7,000 m^2 (between the window size of 45 and 55). Landslides with an area of less than 2,000 m^2 (around the window size of 25) account for around 25% of the total number of landslides, and landslides with an area of less than $9{,}000m^2$ (around the window size of 55) account for around 75% of the total number of landslides. Further verification of this phenomenon is still needed, yet it seems to be rational, as the performance of parameters increases first and then decreases with the increasing of calculation window sizes. Therefore, in a specific case, if possible, it is suggested to consider both the distribution of landslide areas (or at least the rough scale of most landslides) and image pixel sizes when selecting an appropriate window size for parameter calculation.

Furthermore, this study applied only SAR intensity and coherence information for rapid detection of massive landslides. Nevertheless, when available, the polarimetry information of SAR data should also have favorable performances for landslide

detection, as the changes of different scattering mechanisms (e.g., surface scattering, double-bounce scattering, and volume scattering) can be clearly understood by decomposing the polarimetry data using model-based and/or eigenvalue-eigenvector-based decompositions. The fusion of other information, such as slope characteristics, pre-event optical images, geology information, and landslide triggering factors, should also be able to improve the landslide detection accuracy, and improve the performance of some unfavorable parameters. For instance, as coherence changes are very sensitive to minor ground variations, small ground changes unrelated to landslides, such as the area change of river band caused by flood, also influence the performance of coherence information as landslide classifiers. If ancillary information, such as optical images and landuse maps can be obtained and applied to eliminate irrelevant areas (e.g., flats and waters) first, the landslides mapped by coherence will be much more accurate.

5.6. A Simple Exploration and Comparison of Sentinel-1 C-band SAR Data for the Landslide Detection

Previous sections of this chapter explored two pre-event and one post-event ALOS-2 SAR products for the rapid detection of the densely distributed small-sized shallow landslides. These three ALOS-2 products had a high resolution and were generated by L-band microwave, which has a relatively long wavelength (23.5cm). The high resolution allows the images to contain more detailed information about the ground target, benefiting the identification of small-sized landslides. The long wavelength makes the microwave have a favorable penetration ability, facilitating the study in areas covered by vegetation.

Nevertheless, the ALOS-2 products are not free data that can be obtained and applied by everyone. Moreover, as has been mentioned in the discussion section, for different SAR data, there may be some differences in the conditions and results for the application in landslide detection. Therefore, in this section, a simple exploration and comparision of the Sentinel-1 C-band (5.5cm) SAR products, which can be downloaded from the official website freely and easily, for the detection of these landslides were carried out, in order to provide a reference for future application.

5.6.1. Dataset

The study area is the same to the one used for ALOS-2 SAR products, in order to have a simple comparison between these two products. As coherence information did not show favorable performances in the previous studies, only intensity-related information and parameters were explored in this section to simplify the analysis.

Applied dataset included two pre-event and one post-event Sentinel-1 Level 1 Ground Range Detected (GRD) products captured at August 12, 2018, August 24, 2018, and September 5, 2018 (UTC), respectively. GRD products means that the focused SAR data have been detected, multi-looked and projected to ground range using an earth ellipsoid model, in which phase information has been lost (ESA). All of these three products were captured from path 46, covering the same area from a right looking descending track, including two kinds of polarization: VV and VH. A summary of the data information is listed in **Table 5.4**.

Table 5.4. Information of the applied Sentinel-1 data.

Date (UTC) (yyyy/mm/dd)	Level	Mode	Polarization	Sample Spacing (Range × Azimuth)	Orbit Direction	Incidence Angle
2018/08/12	L1.1 (GRD)	IW	VV/VH	10m × 10m	Right Looking/ Descending	38.3 °
2018/08/24	L1.1 (GRD)	IW	VV/VH	10m × 10m	Right Looking/ Descending	38.3 °
2018/09/05 (20:41)	L1.1 (GRD)	IW	VV/VH	10m × 10m	Right Looking/ Descending	38.3 °

GRD: ground range detected; IW: interferometric wide swath; VV: vertical transmit and vertical receive; VH: vertical transmit and horizontal receive.

Comparing **Table 5.1** and **Table 5.4** it can be found that, besides the difference in wavelength of the applied microwaves, there are several other differences between these two kinds of products. Sentinel-1 SAR products have a lower spatial resolution and a higher temporal resolution than the ALOS-2 SAR products. The capture time of the post-event Sentinel-1 product is earlier than that of the post-event ALOS-2 product, owing their different temporal resolution. Moreover, the polarization and orbit direction of the ALOS-2 products are HH and left looking/ascending, whereas those

of the Sentinel-1 products are VV/VH and right looking/descending. Furthermore, there are also slight differences in the incidence angle of these two dataset.

5.6.2. Results and Discussions

Similar to the study of ALOS-2 SAR products, potential intensity parameters were first calculated from the two pre-event and one post-event Sentinel-1 SAR products, including the intensity difference (d_{abs1} and d_{abs2}), correlation coefficient (r), and correlation coefficient difference (Δr). Applied window sizes for the parameter calculation included 3×3, 5×5, 7×7, 9×9, 11×11, 13×13, and 15×15, taking into account the landslide size and image pixel size. All parameters were calculated by three cases: VV polarization image, VH polarization image, and the average of VV and VH polarization images, to make full use of the obtained information and to compare their performances. After that, ROC analyses of these calculated parameters were carried out to quantitatively understand and compare the performance of them for the landslide detection. The analysis results are listed and drawn in **Table 5.5** and **Figure 5.8** for interpretation.

Table 5.5. AUC values of the parameters calculated under different window sizes by the Sentinel-1 SAR products.

		3×3	5×5	7×7	9×9	11×11	13×13	15×15
d_{abs1}	VV	0.6304	0.6289	0.6149	0.5944	0.5733	0.5528	0.5364
	VH	0.6356	0.6468	0.6481	0.6434	0.6342	0.6263	0.6219
	(VV+VH)/2	0.6708	0.6715	0.6586	0.6373	0.6167	0.5999	0.5887
d_{abs2}	VV	0.6612	0.6863	0.6957	0.6969	0.6954	0.6937	0.6933
	VH	0.6592	0.6890	0.7027	0.7056	0.7043	0.7023	0.7012
	(VV+VH)/2	0.7065	0.7340	0.7425	0.7413	0.7368	0.7318	0.7283
r	VV	0.5473	0.5571	0.5635	0.5669	0.5698	0.5734	0.5776
	VH	0.5532	0.5702	0.5842	0.5950	0.6022	0.6068	0.6116
	(VV+VH)/2	0.5729	0.5877	0.5965	0.6010	0.6038	0.6064	0.6092
Δr	VV	0.5510	0.5632	0.5695	0.5710	0.5714	0.5716	0.5725
	VH	0.5540	0.5727	0.5840	0.5892	0.5904	0.5910	0.5921
	(VV+VH)/2	0.5796	0.6060	0.6261	0.6370	0.6416	0.6438	0.6459

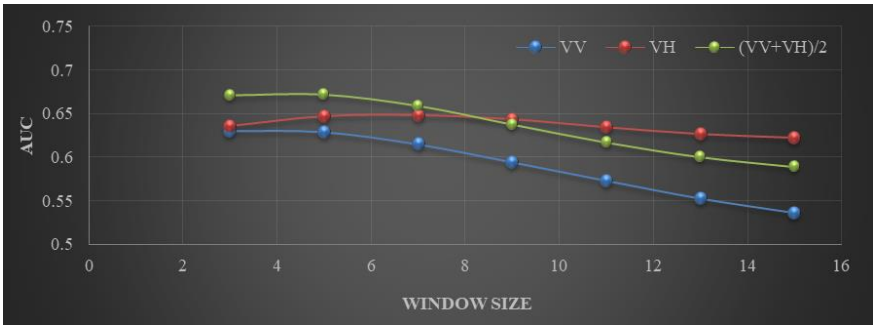

(a)

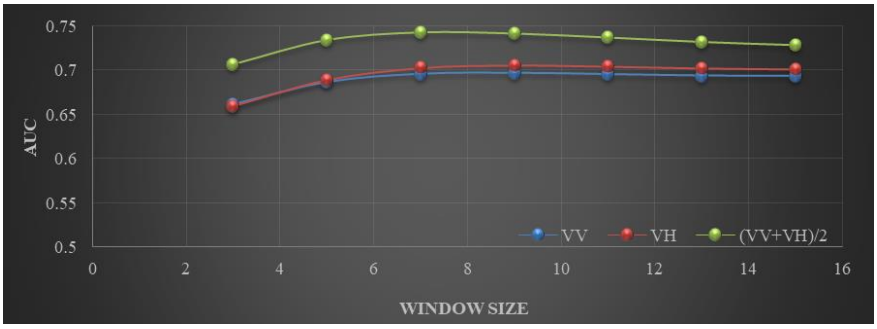

(b)

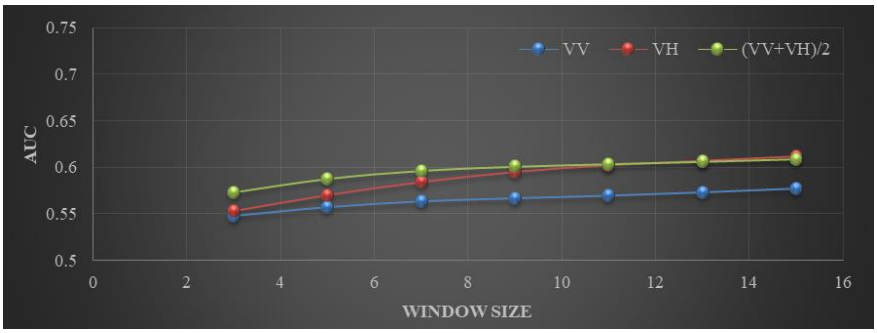

(c)

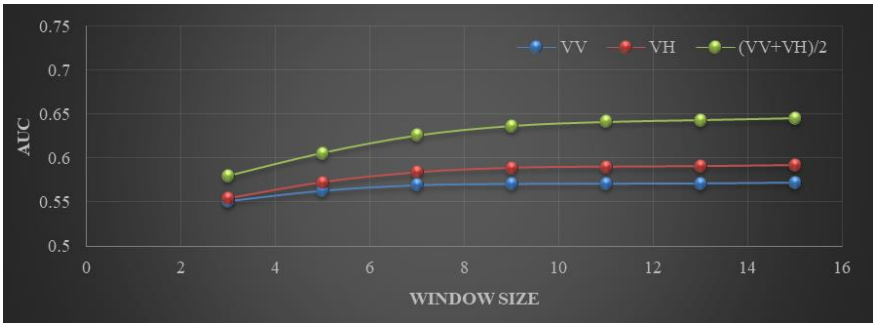

(d)

Figure 5.8. AUC values of the parameters calculated under different window sizes by the Sentinel-1 SAR products: (a) d_{abs1}; (b) d_{abs2}; (c) r; (d) Δr.

Comparing AUC values of the parameters calculated by ALOS-2 SAR products (**Table 5.2** and **Figure 5.4**) and by Sentinel-1 SAR products (**Table 5.5** and **Figure 5.8**), it can been seen that, generally, the ALOS-2 products showed better performance than Sentinel-1 products for the landslide detection in this case. Actually, according to **Table 5.5**, expect the d_{abs2} calculated by the VH polarization image and the average of VV and VH polarization images, other parameters calculated by the Sentinel-1 products are not suitable for landslide and non-landslide pixel classification in this case anymore. This phenomenon may relate to the low spatial resolution of the Sentinel-1 SAR products and the small size of the landslides in this case. The pixel size of the applied ALOS-2 products is around $3m^2$, while the pixel size of the applied Sentinel-1 products is $100m^2$. The higher resolution made the ALOS-2 products contain more detailed information about the ground targets, facilitating the detection of small-sized shallow landslides. Even though the area of the calculation window were near for the two kinds of products, the high-resolution can still contain more information due to the pixel size of the calculated parameter image, the SAR imaging principal, and the parameter calculation method, especially d_{abs2}. Besides, the difference in the imaging microwave, looking direction, and polarization might also have some influence to the different performance of the two kinds of products. For instance, microwaves of different lengths have different penetration ability, which might cause image differences. If possible, a further study by controlling different variables might be better to understand and compare these influences.

Moreover, **Table 5.5** and **Figure 5.8** also showed that, in general, the parameters calculated by the average of VV and VH polarization images have the best performance among all of the three cases (VV polarization image, VH polarization image, and the average of VV and VH polarization images), as they included more information. The parameters calculated by the cross-polarization VH image displayed relatively better performace than those calculated by the co-polarization VV image, because, comparing with co-polarization, cross-polarization is more sensitive to the backscattering changes caused by the landslides, i.e., mainly from volume scattering generated by the forests to surface scattering generated by the bare soil.

Furthermore, among all parameters, the favorable parameter d_{abs2} proposed for ALOS-2 products still showed the best performance for the Sentinel-1 products,

indicating its advantages. The optimal calculation window size of the parameters suitable for landslide detection in this case (d_{abs2} calculated by the VH polarization image and the average of VV and VH polarization images) is around 7×7 (4900 m^2) to 9×9 (8100m^2), which also seems to be related to the distribution of the landslide sizes (landslides with an area of less than 2,000m^2 , 7,000m^2, and 9,000m^2 account for around 25%, 50%, and 75% of the total number of landslides, respectively) as has been discussed in section 5.5.

In order to have a more specific understanding of the Sentinel-1 SAR products for the landslide detection in this case, the optimal threshold of the favorable parameter (d_{abs2} calculated by the average of VV and VH polarization images) calculated under the optimal window size (7×7) was found and then used for the classification of landslide and non-landslide pixels. The classified results are shown in **Figure 5.9**. As it can be seen, comparing with the results achieved by d_{abs2} calculated using ALOS-2 SAR products (**Figure 5.6a**), there seems to be more misclassifications in the results achieved by d_{abs2} calculated using the Sentinel-1 SAR products.

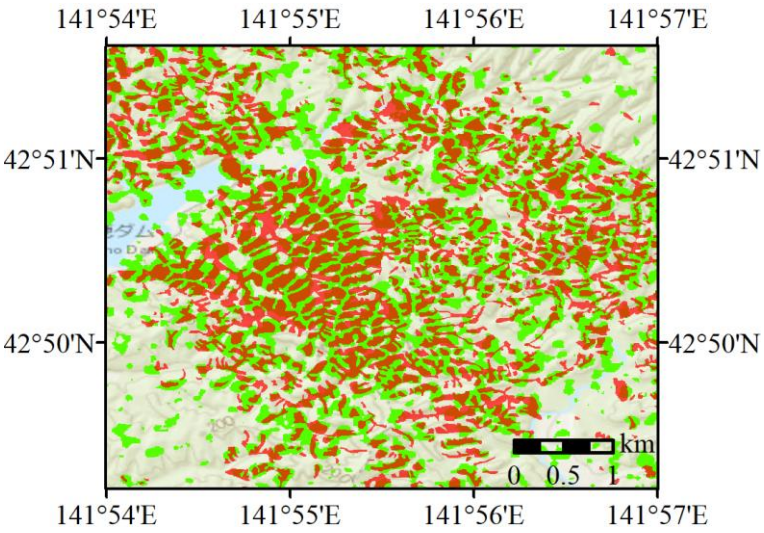

Figure 5.9. Landslides detected by d_{abs2} calculated using the average of VV and VH polarization Sentinel-1 products (green: landslides detected by d_{abs2}; red: ground truth landslides made by Zhang et al. (2019)).

As has been analyzed above, in general, the Sentinel-1 SAR products did not achieve as good results as the ALOS-2 SAR products for landslide detection in this case. Nevertheless, they are free data that can be downloaded and applied by everyone conveniently. Moreover, Sentinel-1 satellite has a repeat cycle of six days for European area and twelve days for other areas (combining Sentinel-1A satellite and Sentinel-1B satellite), which is more available for emergency response than the ALOS-2 satellite that has a temporal resolution of fourteen days. In this case, the capture time of the post-event Sentinel-1 product is earlier than that of the post-event ALOS-2 product. In addition, in the visual and intuitive observation, the intensity difference calculated by the pre-event and post-event Sentinel-1 SAR products also displayed clear different characteristics in the landslide areas (**Figure 5.10**), which is able to provide useful information for the understanding of the general landslide condition following a disaster, although not as precise as that calculated by the high-resolution ALOS-2 SAR products. Furthermore, the Sentinel-1 SAR products may have favorable performance for the detection of larger-sized landslides, which is worth further investigation.

As has been mentioned in section 2.3.2, in a specific application, trade-offs among the different kinds of resolution (e.g., temporal resolution and spatial resolution) are usually needed, as it is hard to assemble all desirable features into one remote sensing sensor (NASA). Moreover, there might also be a compromise between the image covarage and spatial resolution. High-resolution images are able to provide more detailed information regarding ground targets, but may have a smaller spatial coverage and be limited by satellite storage and processing capacities (Joyce et al., 2009). In a real application, all of these factors (e.g., spatial resolution, temporal resolution, and image coverage) should be considered comprehensively so that appropriate products can be applied to achieve the study or application purpose properly.

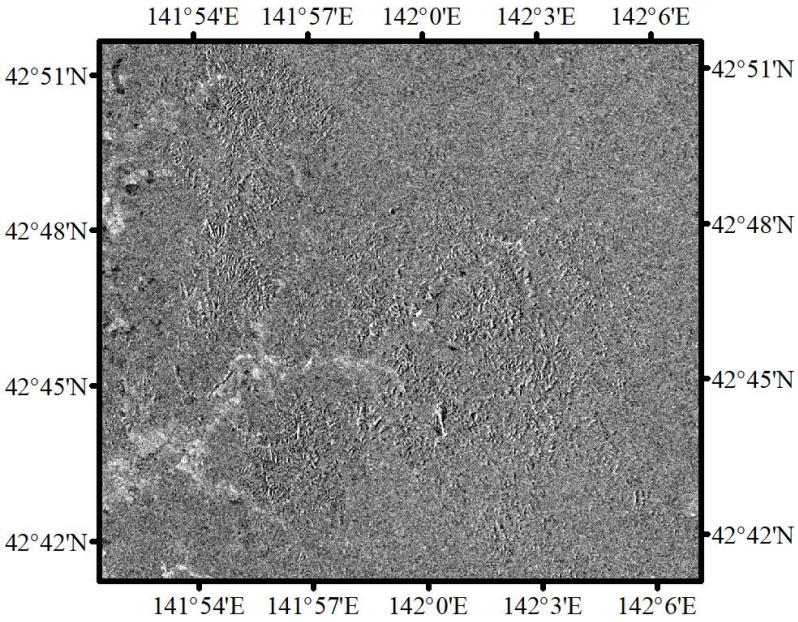

(a)

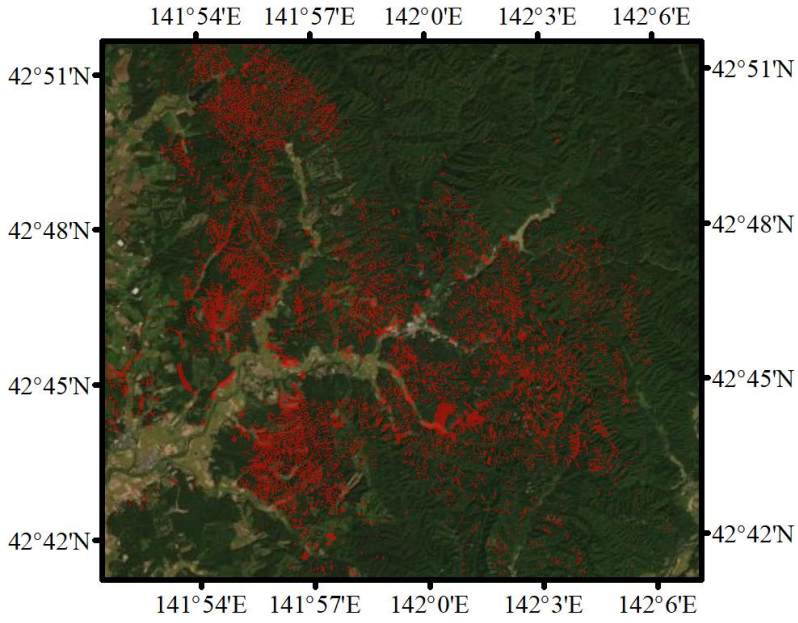

(b)

Figure 5.10. Intensity difference calculated by pre-event and post-event Sentinel-1 SAR products and ground truth landslides: (a) Intensity difference; (b) Ground truth landslides made by Zhang et al. (2019).

5.7. Conclusions

This chapter provided an exploration on the intensity and coherence information of three ALOS-2 SAR images for rapid detection of densely distributed shallow landslides with a small size. Two pre-event and one post-event high-resolution ALOS-2 SLC products were processed and applied. Four intensity-related (d_{abs1}, d_{abs2}, r, and Δr) and two coherence-related (γ and $\Delta\gamma$) potential parameters that can be derived from the three products relatively easily were selected and calculated based on SAR imaging principal, including a new parameter (d_{abs2}) proposed to avoid information loss in the calculation. Visual interpretation and ROC analyses were performed to analyze and compare these parameters for landslide detection qualitatively and quantitatively, in order to provide a reference for future application. The new intensity difference parameter d_{abs2} and correlation coefficient difference Δr showed favorable performance in these analyses, and therefore were further explored for classifying landslide and non-landslide pixels by suitable thresholds. A discriminant analysis was also carried out to explore the combinational application of these two types of information by combining three relatively favorable parameters (d_{abs2}, Δr, and $\Delta\gamma$) with one in each type. A simple exploration and comparison of the free Sentinel-1 C-band SAR data for the landslide detection was also carried out to provide some reference for future application. Several conclusions obtained from this study are summarized as follows.

Qualitatively, intensity difference showed clear lower-value and higher-value pixels in landslide areas, as triggered landslides smoothed hillsides, causing backscattering decrease, and roughened foothill areas, inducing backscattering increase. Co-event correlation coefficient and correlation coefficient difference displayed lower-value pixels in landslide regions due to the relatively larger ground changes induced by landslides. Co-event coherence and coherence difference also more or less showed some lower-value pixels in landslide areas owing to the relatively larger decorrelation caused by the landslide-involved ground changes.

Quantitatively, intensity-related parameters showed better performance than coherence-related parameters for landslide detection in these vegetation areas, as coherence information is very sensitive to minor changes in vegetation (e.g., vegetation growth and leave movement). The new intensity difference parameter d_{abs2} and correlation coefficient difference Δr showed favorable performance and

are recommended for future application. In particular, d_{abs2} can achieve an AUC value of around 0.82 under the optimal window size, and can be derived easily from only one pre-event and one post-event SAR intensity images. Nevertheless, the largest AUC values of other four parameters (d_{abs1}, r, γ, and $\Delta\gamma$) were around 0.65-0.69, indicating that, individually, they are not very appropriate binary classifiers for distinguishing landslide and non-landslide pixels in this case. Furthermore, between the two intensity difference parameters (d_{abs1} and d_{abs2}), d_{abs2} showed better performance than d_{abs1}, demonstrating the advantage of considering avoiding information loss in parameter calculation. Between the two correlation coefficient parameters (r and Δr), Δr showed improved performance, as some pixels whose values were always low can be excluded by subtracting one pre-event correlation coefficient image.

Moreover, the landslide detection results demonstrated that, individually, the two favorable parameters (d_{abs2} and Δr) correctly classified around 64%-70% landslide and non-landslide pixels and properly identified 81%-88% landslide pixels by suitable thresholds. The combinational application of the intensity difference, correlation coefficient, and coherence parameters (d_{abs2}, Δr, and $\Delta\gamma$) through linear discriminant analysis achieved an overall accuracy of around 74%. Misclassification is mainly due to the fact that some non-landslide pixels around the ground truth landslides were classified as landslide pixels, as landslide surroundings where there seems to be no clear visible changes might have experienced implicated backscattering changes (e.g., tree tilt caused by alluvium erosion or lashing). The rough or imprecise boundary of the ground truth landslides is also a reason of the relatively low accuracy and precision values.

Furthermore, the simple investigation of Sentinel-1 SAR products showed that, generally, they did not achieve as good results as ALOS-2 products for the detection of these small-sized shallow landslides in this case, which might relate to the relatively coarser resolution of them. Nevertheless, the Sentinel-1 products also have their own advantages. They are free data that can be downloaded and applied by everyone. They can be obtained every twelve days globally (every six days in Europea), which is more frequent the ALOS-2 products (every fourteen days). As the pre- and post-event intensity difference calculated by them also showed clear different characteristics in

landslide areas, they are also considered as valuable data for a general understanding of a landslide event following a disaster. In a real application, a comprehensive consideration is needed for the application of different products according to the purpose, as a trade-off among different kinds of resolution and a compromise between image resolution and image coverage are usually needed.

5.8. References

Balakrishnama, S., Ganapathiraju, A. (1998). Linear discriminant analysis—A brief tutorial. Institude for Signal Information Processing, 18, 1-8.

Bivic, R. L., Allemand, P., Quiquerez, A., Delacourt, C. (2017). Potential and limitation of SPOT-5 ortho-image correlation to investigate the cinematics of landslides: The example of “Mare à Poule d’Eau” (Réunion, France). Remote Sensing, 9(2), 106-111.

Burrows, K., Walters, R. J., Milledge, D., Spaans, K., Densmore, A. L. (2019). A new method for large-scale landslide classification from satellite radar. Remote Sensing, 11(3), 237-241.

Chen, T., Trinder, J. C., Niu, R. (2017). Object-oriented landslide mapping using ZY-3 satellite imagery, random forest and mathematical morphology, for the Three-Gorges reservoir, China. Remote Sensing, 9(4), 333-347.

Colesanti, C., Wasowski, J. (2006). Investigating landslides with space-borne Synthetic Aperture Radar (SAR) interferometry. Engineering Geology, 88(3-4), 173-199.

Confuorto, P., Martire, D. D., Centolanza, G., Iglesias, R., Mallorqui, J. J., Novellino, A., Plank, S., Ramondini, M., Thuro, K., Calcaterra, D. (2017). Post-failure evolution analysis of a rainfall-triggered landslide by multi-temporal interferometry SAR approaches integrated with geotechnical analysis. Remote Sensing of Environment, 188, 51-72.

Dong, L., Shan, J. (2013). A comprehensive review of earthquake-induced building damage detection with remote sensing techniques. ISPRS Journal of Photogrammetry and Remote Sensing, 84, 85-99.

ESA. https://sentinel.esa.int/web/sentinel/missions/sentinel-1/data-products

Hanley, J. A., McNeil, B. J. (1982). The meaning and use of the area under a receiver operating characteristic (ROC) curve. Radiology, 143(1), 29-36.

Joyce, K. E., Belliss, S. E., Samsonov, S. V., Mcneill, S. J., Glassey, P. J. (2009). A review of the status of satellite remote sensing and image processing techniques for mapping natural hazards and disasters. Progress in Physical Geography, 33(2), 183-207.

Konishi, T., Suga, Y. (2018). Landslide detection using COSMO-SkyMed images: A case study of a landslide event on Kii Peninsula, Japan. European Journal of Remote Sensing, 51(1), 205-221.

Lazecký, M., Çomut, F. C., Hlaváčová, I., Gürboğa, Ş. (2015). Practical application of satellite-based SAR interferometry for the detection of landslide activity. Procedia Earth Planetary Science, 15, 613-618.

Massonnet, D., Feigl, K. L. (1998). Radar interferometry and its application to changes in the earth's surface. Reviews of Geophysics, 36(4), 441-500.

Matsuoka, M., Yamazaki, F. (2004). Use of satellite SAR intensity imagery for detecting building areas damaged due to earthquakes. Earthquake Spectra, 20(3), 975-994.

Matsuoka, M., Yamazaki, F. (2006). Use of SAR imagery for monitoring areas damaged due to the 2006 Mid Java, Indonesia earthquake. In Proceedings of the 4th International Workshop on Remote Sensing for Post-Disaster Response, Cambridge, UK, 25-26 September 2006.

Matsuoka, M., Yamazaki, F. (2010). Comparative analysis for detecting areas with building damage from several destructive earthquakes using satellite synthetic aperture radar images. Journal of Applied Remote Sensing, 4(1), 041867.

Metz, C. E. (1978). Basic principles of ROC analysis. Semin. Nucl. Med., 8(4), 283-298.

Mondini, A. C. (2017). Measures of spatial autocorrelation changes in multitemporal SAR images for event landslides detection. Remote Sensing, 9(6), 554-569.

NASA. https://earthdata.nasa.gov/learn/remote-sensing

Plank, S. (2014). Rapid damage assessment by means of multi-temporal SAR-a comprehensive review and outlook to Sentinel-1. Remote Sensing, 6(6), 4870-4906.

Raspini, F., Ciampalini, A., Conte, S. D., Lombardi, L., Nocentini, M., Gigli, G., Ferretti, A., Casagli, N. (2015). Exploitation of amplitude and phase of satellite SAR images for landslide mapping: The case of Montescaglioso (South Italy). Remote Sensing, 7(11), 14576-14596.

Strozzi, T., Farina, P., Corsini, A., Ambrosi, C., Thüring, M., Zilger, J., Wiesmann, A., Wegmüller, U., Wegmüller, C. (2005). Survey and monitoring of landslide displacements by means of L-band satellite SAR interferometry. Landslides, 2(3), 193-201.

Sun, W., Tian, Y., Mu, X., Zhai, J., Gao, P., Zhao, G. (2017). Loess landslide inventory map based on GF-1 satellite imagery. Remote Sensing, 9(4), 314-331.

Tofani, V., Raspini, F., Catani, F., Casagli, N. (2013). Persistent scatterer interferometry (PSI) technique for landslide characterization and monitoring. Remote Sensing, 5(3), 1045-1065.

Tom, F. (2006). An introduction to ROC analysis. Pattern Recognition Letters, 27(8), 861-874.

Vamvatsikos, D. (2011). Performing incremental dynamic analysis in parallel. Computer & Structures, 89(1-2), 170-180.

Vamvatsikos, D., Cornell, C. A. (2001). Tracing and Post-Processing of IDA Curves: Theory and Software Implementation, RMS Program Report No. RMS-44, Stanford University: Stanford, CA, USA, 2001.

Vamvatsikos, D., Cornell, C. A. (2002). Incremental dynamic analysis. Earthquake Engineering & Structure Dynamics, 31(3), 491-514.

Veci, L. (2016). ALOS PALSAR Orthorectification Tutorial, Array System Computing Inc.: North York, ON, Canada.

Xie, S., Duan, J., Liu, S., Dai, Q., Liu, W., Ma, Y., Guo, R., Ma, C. (2016). Crowdsourcing rapid assessment of collapsed buildings early after the earthquake based on aerial remote sensing image: A case study of Yushu earthquake. Remote Sensing, 8(9), 759-775.

Xue, D., Yu, X., Jia, S., Chen, F., Li, X. (2018). Study on landslide disaster extraction method based on spaceborne SAR remote sensing images-take ALOS PALSAR for an example. Int. Arch. Photogramm. Remote Sensing and Spatial Information Science, XLII-3, 2023-2027.

Youden, W. J. (1950). Index for rating diagnostic tests. Cancer, 3(1), 32-35.

Yun, S. H., Hudnut, K., Owen, S., Webb, F., Simons, M., Sacco, P., Gurrola, E., Manipon, G., Liang, C., Fielding, E., et al. (2015). Rapid Damage Mapping for the 2015 Mw 7.8 Gorkha Earthquake Using Synthetic Aperture Radar Data from COSMO-SkyMed and ALOS-2 Satellites. Seismology Research Letters, 86(6), 1549-1556.

Zhang, S., Li, R., Wang, F., Iio, A. (2019). Characteristics of landslides triggered by the 2018 Hokkaido Eastern Iburi earthquake, Northern Japan. Landslides, 16(9), 1691-1708.

Zhao, C., Lu, Z., Zhang, Q., Fuente, J. D. L. (2012). Large-area landslide detection and monitoring with ALOS/PALSAR imagery data over Northern California and Southern Oregon, USA. Remote Sensing of Environment, 124, 348-359.

Zhao, F., Mallorqui, J. J., Iglesias, R., Gili, J. A., Corominas, J. (2018). Landslide monitoring using multi-temporal SAR interferometry with advanced persistent scatterers identification methods and super high-spatial resolution TerraSAR-X images. Remote Sensing, 10(6), 921.

Zweig, M. H., Campbell, G. (1993). Receiver-operating characteristic (ROC) plots: A fundamental evaluation tool in clinical medicine. Clinical Chemistry, 39(4), 561-577.

CHAPTER 6

ADDITIONAL APPLICATION OF LANDSLIDE SUSCEPTIBILITY MAP OR LANDSLIDE CONDITIONING FACTORS TO THE SAR-BASED LANDSLIDE DETECTION

6.1. Introduction

In order to explore and compare different SAR information and features for landslide and non-landslide pixel classification, a landslide region was used as the study area in chapter 5. Optimal thresholds of the favorable parameters were found and a discriminant function combining three different types of parameters was developed for the classification of landslide and non-landslide pixels. Relatively favorable results have been achieved by using these thresholds or function for the landslide detection in the study area. Nevertheless, when applying these thresholds or function to other areas, many misclassifcations occurred in other types of landuse, especially the crops, which may be due to the harvest of agriculture in the autumn (**Figure 6.1**). To exclude or reduce these misclassifications, the additional application of other information and/or data is a cost-effective option.

Therefore, in this chapter, an additional application of the generated landslide susceptibility map or landslide conditioning factors to the SAR-based landslide detection was explored to solve this issue, to improve landslide detection results, and to provide more reasonable information for guiding rescue and response operations following a landslide disaster.

On one hand, the landslide susceptibility map generated in chapter 4 includes rich information (combining a series of landslide conditioning factors) and provides the dangerous condition of landslide occurrence in different areas. It can help to draw attention to dangerous areas and to exclude areas of no interest for landslide detection analysis. When available, a combinational use of it and the SAR-detected landslides shall be able to improve landslide detection results and to provide more information for disaster response following a landslide event.

On the other hand, the conditioning factors of landslides can also provide useful information for narrowing down target area for analysis and excluding areas where

landslides are unlikely to occur. The exterior conditioning factors or the triggering factors of landslides (e.g., precipitation and ground motion) can provide information to narrow down the areas of interest and exclude areas that are not related to this event . The interior conditioning factors or the inherent properties of the slopes (e.g., slope gradient and geology condition) can help to exclude areas of no interest or areas where landslides are unlikely to occur (e.g., flats and waters).

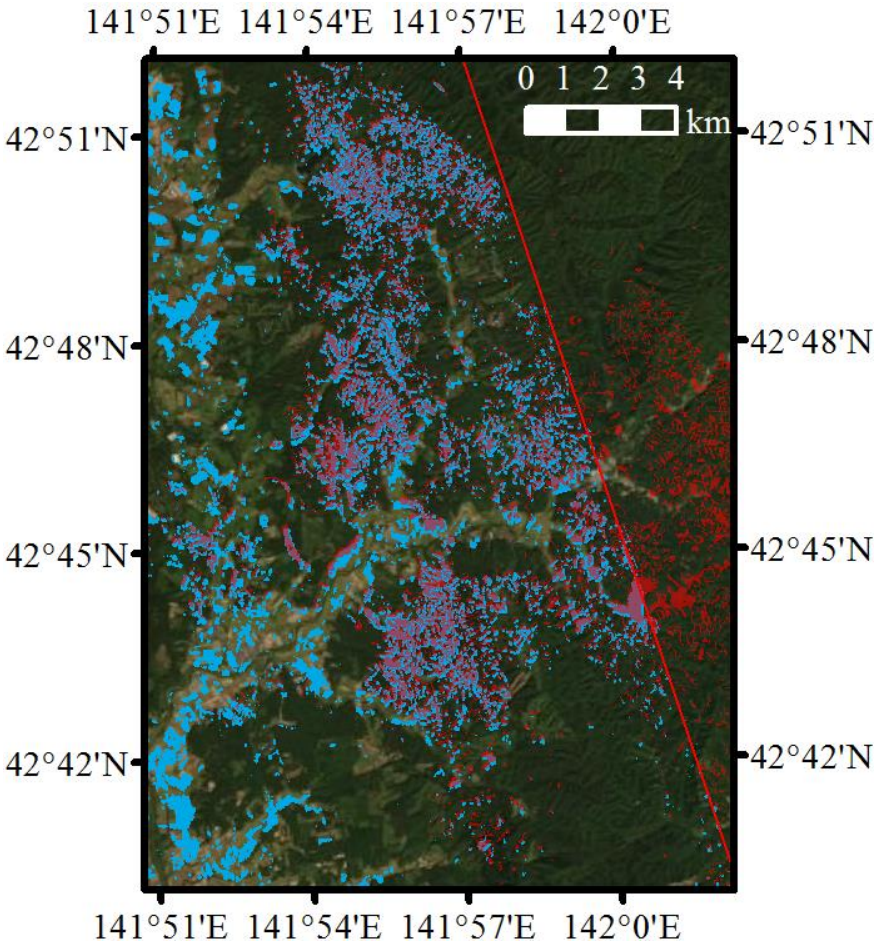

Figure 6.1. Landslides detected by the discriminate score developed in chapter 5 (blue: landslides detected by the discriminate score; red: ground truth landslides made by Zhang et al. (2019); red line: SAR image boundary).

6.2. The Additional Application of Landslide Susceptibility Map to the SAR-based Landslide Detection

As has been introduced in chapters 3 and 4, various conditioning factors related to the landslide occurrence need to be considered in order to generate a landslide susceptibility map. The generated landslide susceptibility map is able to provide information concerning the susceptibility or probability of landslide occurrence in a specific area. Therefore, an additional application of it to the SAR-based landslide detection is able to draw attention to the most dangerous areas and to exclude areas with a low probability of landslide occurrence, improving the accuracy of the landslide identification. For instance, in this case, when using the probability of landslide occurrence larger than 0.7 to restrict the area of concern, the landslides detected by the discriminate score derived using the SAR features can be improved to **Figure 6.2**.

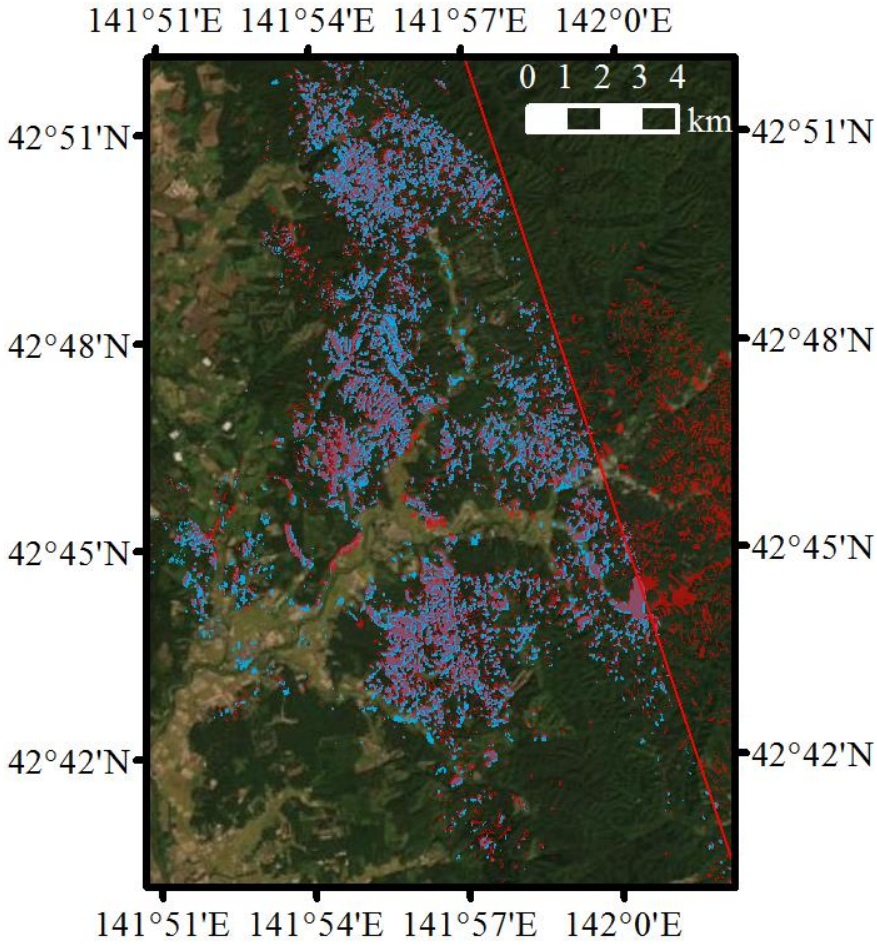

Figure 6.2. Landslides detected by the discriminate score developed in chapter 5 considering the landslide susceptibility map developed in chapter 4 (blue: landslides detected by the

discriminate score considering the landslide susceptibility map; red: ground truth landslides made by Zhang et al. (2019); red line: SAR image boundary).

Comparing **Figure 6.1** and **Figure 6.2**, it can be seen that most of the misclassifications in the agriculture area have been excluded, by using the landslide susceptibility map as an additional information. Moreover, a simple overlaying of the landslides detected by the SAR data to the landslide susceptibility map or a quick comparison between the landslides detected by SAR featrues and the landslide occurrence probabilities in different areas are able to provide more valuable and useful information for the rescue and recover processe following a landslide disaster event, for instance, arranging the prioty order of the rescue process.

6.3. The Additional Application of Landslide Conditioning Factors to the SAR-based Landslide Detection

A landslide susceptibility map combines various conditioning factors of landslides, and is very favorable information to supplement the SAR-based landslide detection. However, not all regions have an available landslide susceptibility map, and not all people who want to detect landslides following a disaster have an appropriate landslide susceptibility map. Under such circumstances, an additional application of the landslide conditioning factors to the SAR-based landslide detection may be a good alternative. The exterior conditioning factors (i.e., the triggering factors) of the landslides, such as the intensity of earthquake and the intensity or amount of precipitation, can be used to narrow down the target area for analysis and to exclude areas that have nothing to do with the disater event. The interior conditioning factors (i.e., the properties of the slopes) of the landslides, such as the slope gradient and landuse, can be applied to exclude areas of no interest or areas where landslides are unlikely to occur (e.g., flatlands and waters).

For instance, in this case, when applying the PSA03 value of the ground motions and the amount of one-week cumulative precipitation before the disater to narrow down the target area, and employing the slope gradient to exclude areas with level, nearly level, very gentle, and gentle slopes (**Table 6.1**), the landslides detected by the

discrinimant score in chapter 5 can be improved to **Figure 6.3**. As can be seen from this figure, although not as good as the one considering landslide susceptibility map (**Figure 6.2**), the results have been improved greatly comparing with the one applying only SAR data (**Figure 6.1**), with many misclassifications in the agriculture areas excluded. Similar to the landslide susceptibility map, even by a simple overlaying of the SAR-detected landslides, the slope gradient, and the landslide triggering factors, a better understanding of the landslide event can be obtained.

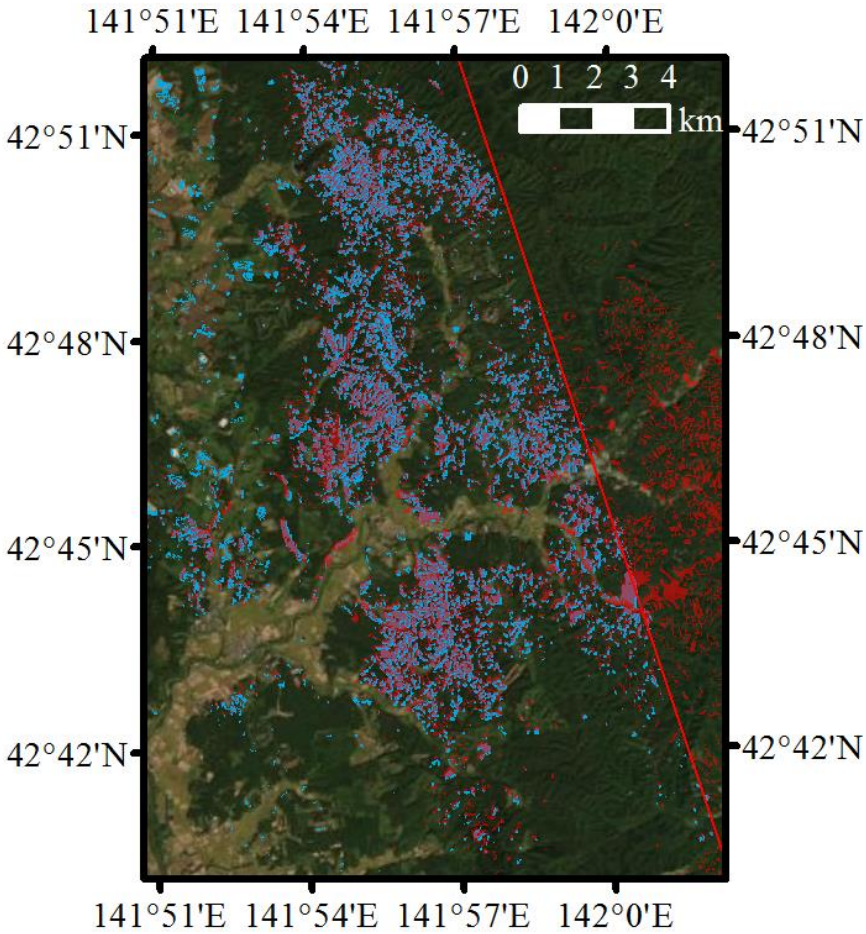

Figure 6.3. Landslides detected by the discriminate score developed in chapter 5 considering landslide conditioning factors (blue: landslides detected by the discriminate score considering landslide conditioning factors; red: ground truth landslides made by Zhang et al. (2019); red line: SAR image boundary).

Table 6.1. Standard slope descriptors (Barcelona Field Studies Centre).

Slope (%)	Approximate degrees	Terminology
0 - 0.5	0	Level
0.5 - 2	0.3 - 1.1	Nearly level
2 - 5	1.1 - 3	Very gentle slope
5 - 9	3 - 5	Gentle slope
9 - 15	5 - 8.5	Moderate slope
15 - 30	8.5 - 16.5	Strong slope
30 - 45	16.5 - 24	Very strong slope
45 - 70	24 - 35	Extreme slope
70 - 100	35 - 45	Steep slope
> 100	> 45	Very steep slope

6.4. Conclusions

An additional application of landslide susceptibility map or landslide conditioning factors to the SAR-based landslide detection was explored in this chapter. The landslide susceptibility map considers various conditioning factors of landslides including the exterior ones (e.g., earthquake and precipitation) and interior ones (e.g. topography and geology). When available, it is able to provide information concerning the dangerous degree of landslide occurrence in a specific area, helping to draw attention to areas with higher landslide occurrence susceptibility and to exclude areas where landslides are unlikely to occur. An additional application of it to the SAR-based landslide detection in this case showed an obvious improvement in the results, by excluding many miscalssifications in other types of landuse.

When there are no landslide susceptibility maps in the study area, an additional application of landslide conditioning factors can be a good alternative to help improve landslide detection results using only SAR data. The triggering factors of landslides, such as the intensity or amount of rainfall, can be used to narrow down the target area for analysis and to exclude areas having nothing to do with the disater event. The interior factors, such as the geology and slope gradient, can be used to exclude areas

where landslides are unlikely to occur or areas of no interest. In this case, the triggering factors and slope gradient were applied to improve the results of the landslides detected by using only SAR data. Many misclassifications were also excluded comparing with the results achieved by using only SAR data.

For a rapid application, even a simple overlaying of the SAR-detected landslides to the landslide susceptibility map or the landslide conditioning factors can provide a better understanding of the landslide event. Moreover, before landslide detection, the landslide susceptibility map can also be used to limit the scope of SAR images for processing to save time. After the landslide occurred, the combination of landslide susceptibility map and SAR-detected landslides can provide more reasonable information for efficient and effective rescue and response. For instance, referring to the combination of the landslide susceptibility map and the SAR-detected landslides, the prioty order of rescue process can be arranged more reasonably.

6.5. References

Barcelona Field Studies Centre. https://geographyfieldwork.com/SlopeSteepnessIndex.htm

Zhang, S., Li, R., Wang, F., Iio, A. (2019). Characteristics of landslides triggered by the 2018 Hokkaido Eastern Iburi earthquake, Northern Japan. Landslides, 16(9), 1691-1708.

CHAPTER 7

CONCLUSIONS AND RECOMMENDATIONS

The 2018 Hokkaido Eastern Iburi Earthquake induced a special landslide event, in which extensive densely distributed small-sized shallow landslides occurred in the towns of Atsuma, Mukawa, and Abira. This disaster brought valuable data, information, experience, and lessons, while causing big casualties and damage in Eastern Iburi area of Hokkaido prefecture, Japan. In order to make full use of these data and information to understand and learn from this landslide event for preferable landslide disaster management in the future, a systematic study on these landslides was carried out based on GIS and SAR remote sensing. The spatial data in GIS and remote sensing technologies are suitable and powerful for understanding and learning from these extensive and widespread landslides from a whole picture owing to its broad and wide coverage. The objectives of this study are to:

1. Understand the landslide event by collecting and analyzing the spatial data of landslide inventory and conditioning factors as well as previous reports and studies concerning the landslide event.
2. Develop a suitable landslide susceptibility model using the collected spatial data of landslide inventory and conditioning factors to facilitate pre-event landslide disaster management in the future.
3. Explore favorable SAR-based landslide detection approaches by analyzing different features in captured SAR data to benefit post-event landslide disaster management in the future.

7.1. Conclusions

To achieve these objectives, a series of studies has been implemented sequentially from chapters 3 to 6. Main conclusions obtained in these studies concerning the three objectives are summarized as follows.

Conclusions on understanding the landslide event (chapter 3)

The spatial data of landslide inventory and conditioning factors, including topograpphy, geology, soil, surface vegetation, precipitation, and ground motion, were collected from different sources and used to analyze the characteristics of the extensive earthquake-triggered landslides, combining with the understanding from previous field survey reports and mechanism studies of other scholars.

- Landslide inventory analyses and previous reports and studies showed that the landslides were densely distributed in a region of the transition zone from Hiddaka Mountains to Ishikari Depression in the north of the earthquake epicenter and within a distance of 25km from the epicenter. Most landslides were small-sized and shallow with a slip surface above the basement complex. These landslides mainly occurred in valley topography and planar slopes, moving down several meters' volcano activity related soil layers with long run-out and high mobility, as the moved materials seemed to have a high water content. The upper surface of most landslides were exposed, showing brownish patches over the hill areas. The characteristics of the landslides were more like those of the rainfall-induced landslides, even though the direct trigger was earthquake. The general mechanism of the lanslides might be that the shear force of the earthquake ruptured the strata of the light porous volcanic soil layers above the hard bedrock, which have already been inundated by the previous accumulated precipitation before the earthquake.
- Landslide conditioning factor analyses showed that the majority of landslides distributed in areas with an elevation of around 100m-200m, a slope gradient of around 15°-35°, a geology type of N2sn (Middle to Late Miocene marine and non-marine sediments), soil types of D1 (未熟黒ボク土) and J1 (火山放出物未熟土), and vegetation types of エゾイタヤーシナノキ and 落葉針葉樹植林. Above the bedrock, there were several meters' volcano activity related soil layers, which were the main materials of the landslides. Comparing with other landslides, the elevation and slope gradient of the collapsed slopes were relatively lower, which are mainly due to special terrain and soil types in local area. Especially, in some areas (e.g., Horosato area in Atsuma town), some landslides even occurred in very gentle slopes that had a gradient smaller than 15°. Moreover, the relatively preferred slope aspect of

the landslides was south, facing the earthquake epicenter. The relatively preferred slope curvature was concave, which might relate to the hydrological properties of such terrains. One month before the disaster, there were totally around 200mm-300mm precipitation around the landslide areas. Several heavy rains occurred in the mid of August, with a heaviest one bringing around 50mm precipitation. The powerful typhoon Jebi, which took place two days before the disaster and was usually thought as an important cause of the landslides, brought around 15mm of the precipitation in the landslide areas. The predominated MM intensity, PGA, and PGV values of the ground motion in landslide areas were around 7.4-8.2, 0.48g-0.68g, and 14cm/s-18cm/s, respectively.

- The earthquake was the direct trigger of the landslide event, and the combinational impact of several conditioning factors, especially the special porous soil type here, the accumulation of previous precipitation in the special soil, and the shaking of the ground motion, were the real cause of the landslide event. The soft porous volcano activity related soil here originally had a low shear strength and a high water storage capacity, while the hard bedrock below the soil had a poor water permeability. Due to these characteristics, water from previous rainfall accumulated in the soil and made the water content in the soil very high, which not only reduced the soil shear strength but also lubricated the interface between soil and bedrock. Then when the earthquake occurred, the shaking from the ground motion not only produced shear force to the soil but also reduced the soil shear strength by increasing pore water pressure and decreasing soil effectiveness stress, causing the shear stress larger than the shear strength and leading to slope failures. In some areas, the soil effectiveness stress might even become zero, causing liquefaction.

Conclusions on GIS-based landslide susceptibility analysis for pre-event landslide disaster management (chapter 4)

A landslide susceptibility analysis was carried out by a GIS-based statistical approach using the collected landslide inventory as dependent variable and landslide conditioning factors as independent variables. Effectiveness, correlation, and multicollinearity problems of the landslide conditioning factor indicators were analyzed by the area under the ROC curve, pearson's correlation, TOL, and VIF, to find the relatively effective indicators and to exclude the correlated indicators for model construction. Several different ratios of landslide presence and absence were tested to find a favorable one for statistical analysis, as there were much more non-landslide cells than landslide cells. A landslide susceptibility model was finally constructed using the selected indicators under the determined ratio by a logistic regression. Applying this model, a landslide susceptibility map was generated.

- The effectiveness analyses of landslide conditioning factor indicators showed that the standard curvature, one-week cumulative precipitation, and PSA03 were relatively more effective among curvature-, rainfall-, and earthquake-related indicators. It might relate to the parameter comprehensiveness, local soil water storage capacity and evaporation condition, and predominate period of local soil, respectively. The correlation and multicollinearity analyses indicated that SPI and STI seems to be correlated, as the correlation coefficient values between them were slightly larger than 0.7. In order to avoid the unnecessary problems caused by correlation, SPI was excluded because it was not as effective as STI in this case. After these analyses, there were totally eleven indicators left for final landslide susceptibility model construction, including elevation, slope gradient, slope aspect, standard curvature, TWI, STI, geology, soil, surface vegetation, PSA03, and one-week cumulative precipitation before the disaster.
- The study on different ratios of landslide presence and absence showed that, generally, the ratio of 1:1 achieved better results than other ratios tested (1:2, 1:3, 1:4, and 1:5). The more non-landslide cells involved in analysis, the lower recall value, that is, the more landslide cells would be classified as non-landslide cells. Therefore, the dataset with the same number of landslide raster cells and non-landsldie raster cells was determined for the final landslide susceptibility model construction.

- Using the selected landslide conditioning factor indicators under the determined ratio of landslide presence and absense, a landslide susceptibility model was finally constructed by a logistic regression. 70% of the data was used for training and 30% of the data was used for validation to construct and check the model. The constructed model achieved a good accuracy for both training and validation data. Applying this model, a landslide susceptibility map was generated in the study area, which showed a good consistency with the distribution of actual landslides. It is expected to provide some useful information for the prediction, monitoring, and management of future landslide occurrence, by updating the changed conditioning factors, that is, the precipitation and ground motion information.

Conclusions on SAR-based landslide detection for post-event landslide disaster management (chapter 5 and chapter 6)

Two pre-event and one post-event ALOS-2 SLC SAR products with a high resolution were applied to explore rapid landslide detection approaches. Potential parameters that can be derived from these products and have the ability to measure ground changes were selected and calculated based on radar reflection mechanism. Considered parameters included the absolute value of intensity difference (d_{abs1} and d_{abs2}), co-event correlation coefficient (r), correlation coefficient difference (Δr), co-event coherence (γ), and coherence difference ($\Delta\gamma$). Qualitative and quantitative analyses of these parameters were carried out to understand and compare their performance for landslide and non-landslide pixel distinguishment. Favorable parameters were explored for identifying landslide pixels by optimal thresholds. A joint application of several parameters for landslide detection was also investigated by a linear discriminant analysis, using three relatively favorable parameters with one in each type (d_{abs2}, Δr, and $\Delta\gamma$). A simple exploration of the free Sentinel-1 C-band SAR products for the landslide detection was also performed to provide some comparision and reference for future application. An additional application of landslide susceptibility map or conditioning factors to the SAR-based landslide detection was also investigated to exclude more misclassifications, improve detection

results, and provide more information for effective and efficient rescue and response operations.

- Parameter qualitative analyses indicated that all of the potential parameters showed some differences in landslide and non-landslide areas. The intensity difference showed clear lower-value and higher-value pixels in landslide areas, as triggered landslides smoothed hillsides, which caused backscattering decrease, and roughened foothill areas, which caused backscattering increase. The co-event correlation coefficient and correlation coefficient difference displayed some lower-value pixels in landslide regions due to the relatively larger ground changes induced by landslides. The co-event coherence and coherence difference also showed more or less some lower-value pixels in landslide areas owing to the relatively larger decorrelation caused by the landslide-involved ground changes.

- Parameter quantitative analyses showed that the intensity-related parameters had better performance than coherence-related parameters for the landslide detection in these vegetation areas. It might relate to the sensitivity of these two kinds of parameters to other minor ground changes. Coherence-related parameters are much more sensitive to minor changes in vegetation (e.g., the growing of plants and the movement of stalk and leaves caused by wind), which interfered with their performance for the landslide detection. The new intensity difference parameter d_{abs2} and the correlation coefficient difference Δr showed favorable performance and were recommended for future application. In particular, d_{abs2} achieved an AUC value of around 0.82 under the optimal window size, and could be derived easily from only one pre-event and one post-event SAR intensity images.

- The sensitivity of parameters to other minor changes not only influenced the performance of them for landslide detection in these vegetation areas but also impacted the optimal window size for parameter calculation. The more sensitive the parameter, the more inteference from other minor changes, and therefore the worse the performance and the larger the window size needed to filter and blur these inteference. In this case, the sensitivity of these three kinds of parameters to other minor ground changes was: coherence

parameters > correlation coefficient parameters > intensity difference parameters, the performance of them was generally: coherence parameters < correlation coefficient parameters < intensity difference parameters, and the optimal calculation window size for them was generally: coherence parameters > correlation coefficient parameters > intensity difference parameters.

- Moreover, as the calculation window size increased, the performance of the intensity parameters first increased and then decreased. A value around 25%~75% cumulative distribution curve of landslide sizes could achieve relatively favorable results. A relatively smaller value within this range was better for intensity difference, while a relatively larger value within this range was better for correlation coefficient parameters.
- Landslide detection results demonstrated that, individually, the two favorable parameters (d_{abs2} and Δr) correctly classified around 64%-69% landslide and non-landslide pixels and properly identified around 81%-88% landslide pixels by suitable thresholds. The combinational application of the intensity difference, correlation coefficient, and coherence parameters (d_{abs2}, Δr, and $\Delta\gamma$) through linear discriminant analysis achieved an overall accuracy of around 74%.
- Studies on Sentinel-1 products showed that they did not achieve as good results as ALOS-2 products for landslide detection in this case. This might relate to the lower spatial resolution of the Sentinel-1 products and also the difference between the looking direction, imaging micorwave, and polarization between these two products. If possible, a further study by controlling different variables might be better to understand and compare these influences. Nevertheless, Sentinel-1 products are free data that can be downloaded and applied by everyone and have a higher temporal resolution (six days for Europe and twelve days for other areas) than ALOS-2 products (fourteen days). As the intensity difference calculated by pre-event and post-event Sentinel-1 products also showed clear different characteristics in landslide and non-landslide areas, although not as accurate as that calculated

by ALOS-2 products, they are also considered as valuable data that can be used to understand the general landslide condition following a disaster.

- In a specific application, trade-offs among different kinds of resolution (e.g., temporal resolution, spatial resolution, and radiometric resolution) are usually needed, as it is hard to assemble all desirable features into one remote sensing sensor. Moreover, there might also be a compromise between the image covarage and spatial resolution. High-resolution images are able to provide more detailed information but may have a smaller spatial coverage and be limited by satellite storage and processing capacities. In a specific case, all of these factors (e.g., spatial resolution, temporal resolution, and image coverage) need to be considered comprehensively so that appropriate products can be applied to achieve the study or application purpose properly.
- The additional application of landslide susceptibility map or conditioning factors to SAR-based landslide detection could help improve landslide detection results by drawing attention to areas with high risk, narrowing down target area for analysis, and excluding areas of no interest or areas where landslides were unlikely to occur. Moreover, the combination application of them can provide more reasonable information for efficient and effective response and rescue operations following a landslide event. For instance, referring to the combination of the landslide susceptibility map and the SAR-detected landslides, the prioty order of rescue process can be arranged more reasonably.

7.2. Recommendations

Based on these studies and conclusions, several recommendations for landslide disaster management are listed as follows.

- The special characteristics of the landslide event remind us to pay attention to the dynamic characteristics of volcano activity related soil. Moreover, areas with special characteristics (in this case, areas covered by special soil types even with very gentle slope) should also be taken seriously, when landslide triggers such as rainfall and earthquake occur even with a low intensity, as the

combinational impact of several different conditioning factors that are not very significant might cause a severe landslide event.

- According to the GIS-based landslide susceptibility analysis and SAR-based landslide detection, corresponding to a disaster process, a following landslide disaster management procedure is suggested: before the disaster, updating the predicted or actual rainfall and/or earthquake term in the landslide susceptibility map according to actual situation, to understand the dangerous condition of landslide occurrence in different areas and to remind local people for better preparation; after the disaster, detecting the induced landslides rapidly by suggested SAR features and combining them with the updated landslide susceptibility map to provide more reasonal information for efficient and effective rescue and response operations; after that, when available and applicable, analyzing optical remote sensing images and carrying out field survey to obtain more detailed information of the landslide event from other aspects. The obtained information, data, experience, and lessons can then be used to improve the developed models and approaches in the previous two procedures or to develop more advanced and accurate models and approaches combining new technologies.
- The important landslide conditioning factors and the weights of different conditioning factors might vary from area to area. It is suggested to develop its own landslide susceptibility model for a specific area, based on local condition of landslide history and mechanism, according to the procedure and suggestions in this study, to be accurate and suitable, as there is usually much time before the disaster to prepare such data and to construct such models. The relatively effective conditioning factors in this case, such as the standard curvature and PSA03, can be referred, and the ratio of 1:1 between landslide presence and absence is suggested for analysis.
- SAR data with only intensity information can first be used to save the processing time following a landslide event. For instance, for Sentinel-1 Level 1.1 products, GRD products (include only intensity information) can first be downloaded instead of SLC products (include both intensity and phase information) to save the processing time. For products including different

types of information (e.g., phase and intensity), the intensity parameters can first be analyzed to understand the landslide condition, as they showed favorable performances and could be calculated quickly and easily. Intensity difference is suggested for a quick response, a combinational application of several different parameters can be carried out to make full use of different parameters' advantages to provide more information when there were more time. For instance, by compositing several calculated parameter images into a color image (e.g., red: intensity difference, green: correlation coefficient difference, blue: coherence difference), the different information provided by different parameters can be used in combination. Moreover, in a specific case, different factors (e.g., spatial resolution, temporal resolution, and image coverage) of SAR products need to be considered comprehensively so that appropriate products can be applied to achieve the study or application purpose properly.

7.3. Limitations and Future Research Directions

Several limitations and future research directions concerning this research are listed as follows.

- The GIS-based statistical analysis is very suitable and powerful to provide information about the extensive and widespread landslides in an overall aspect and a wide view. But it cannot provide as detailed information as physical analysis to understand the mechanism of the landslide occurrence (e.g., limit equilibrium state of the slope stability). The physical mechanism of the landslide occurrence and the dynamic characteristics of the volcano activity related soil can be studied further. Moreover, the important landslide conditioning factors and the weights of different conditioning factors might be different in different area. It is suggested to develop its own landslide susceptibility model for a specific area, based on local condition of landslide history and mechanism, according to the procedure and suggestions in this study, to be accurate and suitable. Furthermore, other advanced machine

learning approaches can also be explored for the landslide susceptibility analysis, especially when there are much more recored data in the future.

- Only SAR intensity and coherence features were investigated and compared for the detection of these densely distributed shallow landslides. The polarimetry information in SAR data should also have favorable performance for landslide detection, as the changes of different scattering mechanisms (e.g., surface scattering and volume scattering) caused by ground changes can be clearly understood by decomposing the polarimetry data using model-based and/or eigenvalue-eigenvector-based decompositions. When available, the application of SAR polarimetry information for landslide detection can also be investigated and compared. Moreover, this study explored SAR-based landslide detection in a pixel level, to merge similar pixels for analysis, approaches in an object level can also be investigated.
- Only the additional application of landslide susceptibility map and conditioning factors of ground motion, precipitation, and slope gradient to SAR-based landslide detection was explored in this case. Depending on actual situation, other data (e.g., pre-event optical image and landslide hazard map) and other landslide conditioning factors (e.g., geology and landuse) can also be applied as supplementary information to improve the reuslts. Moreover, different ways to fuse the different information can also be investigated further to get as much information as possible for landslide disaster management.

APPENDIX

A REVIEW ON SYNTHETIC APERTURE RADAR (SAR)-BASED BUILDING DAMAGE ASSESSMENTS IN DISASTERS

A prompt and overall understanding of building damages following a disaster is critical, as they are usually closely related to casualties. As an important active RS technology, SAR is also a valuable tool for assessing building damages in disasters, owing to its large coverage, quick response, non-contact, and independence of weather and light capabilities. Over the years, various approaches have already been proposed for SAR-based building damage assessment with the development of radar technology and interpretation techniques. While providing numerous choices, these multifarious approaches also make it burdensome to ponder the applicable approach in a specific case, and to reflect on potential fields for further research.

Therefore, instead of developing new approches for building damage assessment using SAR data, this chapter hierarchically classified and summarized the existing approaches to provide a structured understanding for assisting in approach decisions and promising field considerations. First, depending on the pre-event data availability, the numerous approaches were classified into change detections employing both pre- and post-event data, and assessments applying only post-event data. Then, determined by the data resolution level and acquisition mode, the plentiful change detection approaches were further distinguished into block-unit approaches analyzing intensity, coherence, or polarimetry features, and building-unit approaches that simply generalize the block-unit approaches, or that concretely explore the detailed individual building features. The post-event data-based assessments, with relatively fewer approaches, were further introduced as methods exploring polarimetry or/and texture features. In each classification category, the principle was first introduced to explain the basic concept and essence of the approaches. An approach review was then provided by organizing relevant studies in a logical or structured way, to facilitate a clear understanding of the overall research status. Favorable parameters in each category were also summarized for easy reference and application in the future.

1. Introduction

In the crisis management phase of the comprehensive disater management system (**Figure 2.6**), that is, the damage assessment and disaster response, a rapid and overall understanding of damage distribution is of vital importance for making reasonable and effective rescue decisions. Among them, building damage evaluation in an early stage is a crucial issue, as the distribution of damaged buildings is usually closely related to life saving in emergency response (Xie et al., 2016). Moreover, the time for information acquisition is of critical importance, as people trapped in collapsed buildings can generally survive for only approximately 48h (Karimzadeh et al., 2014, 2017; Karimzadeh and Matsuoka, 2018). Nevertheless, it is difficult and sometimes dangerous to conduct field surveys for the entire influenced areas in a short time after a disaster. In addition, transportation and communication systems may have been destroyed by the disaster, impeding the implementation of an on-site survey. RS can observe and respond quickly over a wide field, without physically being on site. When properly selected in terms of sensor type, spatial resolution, and return time, as well as the availability of pre-disaster data, ancillary maps, and the like, it can be efficiently and effectively applied in building damage assessment after a disaster (Yamazaki and Matsuoka, 2007; Dong and Shan, 2013).

Mainly, two types of RS technologies - optical sensors and SAR can be applied for building damage assessment in and after disasters. As has introduced in chapter 5, optical sensors can provide intuitive optical images, which show the earth's surface as human eyes view it, and are easy to interpret. However, they are passive RS, need sun illumination for imaging, and cannot penetrate clouds, which severely limits their application as an emergency tool. In contrast, SAR data are relatively difficult to interpret, and can be easily influenced by speckle noises. Nevertheless, they can be obtained both at night and in harsh weather conditions, owing to the active characteristics of SAR sensors and the long wavelength of the applied microwaves (Hanssen, 2001; Elachi and Zyl, 2006; Franceschetti and Lanari, 2016). Therefore, SAR is considered to be more flexible and reliable for damage assessment at an early time following a disaster.

Various approaches for SAR-based building damage assessment in disasters have been proposed, owing to the advantages of SAR technologies, together with the

development of microwave RS and interpretation techniques. Depending on the data availability, resolution level, and acquisition mode, these approaches vary from methods applying both pre-event and post-event data to methods employing only post-event data, from methods carrying out analysis in a block unit to methods executing analysis in a building unit, from methods based on intensity information to methods based on coherence or polarimetry information, and from methods exploring traditional physical relationships to methods exploiting machine learning technologies. These massive and multifarious approaches provide many choices for achieving expected results, yet they also make it burdensome to select the applicable one in a specific case, to understand the overall research status in this field, and to find promising fields for further study.

Therefore, this paper aimed to classify the various approaches and summarize the favorable parameters, to provide a clear and comprehensive understanding in this field. Even though it is impossible to recommend a single data type or processing solution that will work under all conditions (Joyce et al., 2009), the overall overview is an attempt to provide some references for considering the applicable methods and pondering future efforts, through a designed classification (**Figure 1**).

First, the massive set of SAR-based building damage assessment approaches was divided into two major categories: change detection (applying both pre- and post-event data), and assessment (applying only post-event data), according to the pre-event data availability. Then, the numerous change detection approaches were further classified into block-unit approaches analyzing the intensity, coherence, or polarimetry features in each regular or irregular block, and building-unit approaches that perform analysis in each original, modified, or buffered building footprint area, by simply generalizing the block-unit approaches or concretely exploring the clear individual building features. The post-event data-based assessments, with relatively fewer approaches, were further introduced as methods exploring polarimetry features by polarimetry indices, and methods exploiting texture features through SAR simulators or machine learning classifiers. In each classified category, the principle was first explained, in order to provide a basic understanding of the concept and essence of the approaches in this category. Relevant studies were then organized and introduced in a logical or structured way, to facilitate a clear and comprehensive

understanding of the research status. A summary of different approaches and favorable parameters in each category was also provided to facilitate future reference and application.

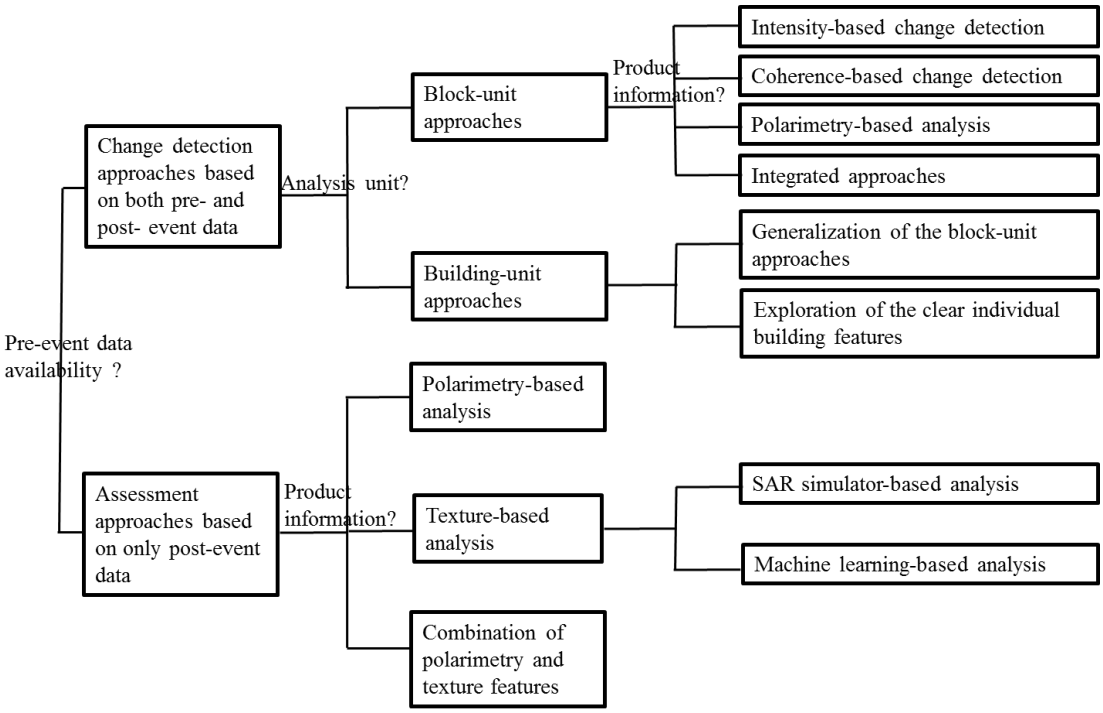

Figure 1. A classification of synthetic aperture radar (SAR)-based building damage assessment approaches.

2. Change Detection Approaches Based on Both Pre- and Post-event SAR Data

When appropriate pre-event SAR products are available, change detection can be carried out by applying both pre- and post-event data. It is based on variations of intensity, phase, or polarimetry features in the SAR images before and after a specific disaster. As different damage degrees cause different changes in these SAR features, the physical relationships between the image change characteristics and building damage conditions can be analyzed, constructed, and then applied to identify actual building damage levels.

Depending on the resolution level of the applied SAR images, change detection can either be carried out in a block unit, or in a building unit. On one hand, for low-resolution data such as the SAR images obtained by spaceborne satellite sensors before 2007 (e.g. ERS-1/2 and RADARSAT-1), several ground targets contribute to

one resolution cell, making it difficult to identify the features of one individual building. Therefore, only block-unit analyses are feasible. On the other hand, for high-resolution SAR images acquired from either airborne sensors or high-resolution spaceborne sensors, individual building information in the image such as edges can be observed, enabling approaches in a building unit.

2.1. Block-unit Approaches

Change detection in a block unit, dating back to the 1990s, was first developed in the field of SAR-based building damage assessment, owing to the limitations of image resolution in the initial stages. In this type of method, building damage conditions are usually represented by damage levels or damage ratios in each block. According to actual field conditions and study purposes, three types of blocks (**Figure 2**) have been applied, including tiles formed by one (Matsuoka and Yamazaki, 2004a) or several (Bai et al., 2017a) pixels, irregular blocks divided by the street or urban boundaries (Zhai and Huang, 2016), and irregular blocks segmented based on homogeneous features (Gokon et al., 2017a, 2017b).

(a)

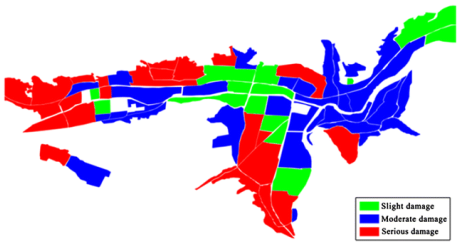

(b)

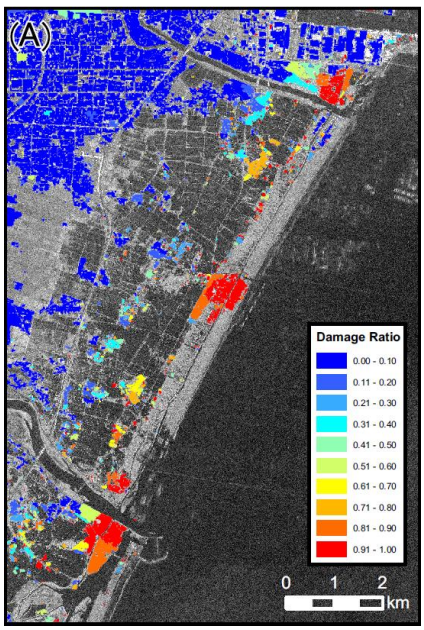

(c)

Figure 2. Three types of block units that have been applied: (a) Tiles formed by one pixel (the thick black grids indicate that the severe damage ratio equals to 100%) (Matsuoka and Yamazaki, 2004a); (b) Irregular blocks divided by street or urban boundaries (Zhai and Huang, 2016); (c) Irregular blocks segmented based on homogeneous features (Gokon et al., 2017a).

Various approaches for block-unit change detection have been proposed over the years. Depending on the applied satellite and its image acquisition mode, intensity, phase, and polarimetry features can be analyzed alone, or in combination for building damage assessment (**Table 1**). Intensity information is relatively easy to obtain, as it poses no requirement for the radar acquisition mode. Changes of intensity information are usually quantified by the intensity difference, correlation coefficient, correlation coefficient difference/ratio, highlight area ratio, texture features, etc. Coherence, which means the correlation coefficient of phase information, can be acquired when the satellite works in an interferometry mode. The ratio/difference of pre- and co-event coherence is commonly used in coherence-based change detection. Polarimetry features can facilitate the understanding of radar scattering mechanisms, and are available when a satellite works in a polarimetry mode. Favorable indicators for distinguishing damaged and undamaged urban areas include surface scattering, volume scattering, double bounce scattering decomposed through model-based decomposition, entropy decomposed through eigenvalue-eigenvector-based decomposition, and several additional polarimetric parameters, such as polarization coherence.

Table 1. A summary of block-unit change detection approaches.

Approaches	Classification	Commonly-used parameters	Image requirement (number/ acquisition mode)	Representative studies	Other descriptions
Intensity-based change detection	Classic discriminant analysis	Intensity difference and correlation coefficient	One pre-event and one post-event images/no mode requirement	Matsuoka and Yamazaki (2004a, 2004b, 2010); Matsuoka et al. (2010); An et al. (2016), etc.	Classic approaches with many references/ coefficients of parameters (i.e., intensity difference and correlation coefficient) vary with the applied images
	Improved discriminant analysis for densely built-up areas	Intensity difference and correlation coefficient	One pre-event and one post-event images/no mode requirement	Matsuoka and Yamazaki (2005)	Suitable for congested building areas as both intensity increases and decreases were considered

Approaches	Classification	Commonly-used parameters	Image requirement (number/ acquisition mode)	Representative studies	Other descriptions
	Improved analysis for low damage ratios in less density built-up areas	The ratio/difference of pre- and co-event correlation coefficient	Two pre-event and one post-event images/no mode requirement	Matsuoka et al. (2005); Matsuoka and Yamazaki (2006)	Suitable for small building damage ratios in less density built-up areas/can minimize impacts from signal noises and earth's surface changes/need two pre-event images
	Others	Intensity difference, correlation coefficient, the proportion of highlight areas, texture features, K-distribution and Getis statistics, etc.	One pre-event and one post-event images/no mode requirement	Liu and Yamazaki (2011); Liu and Yamazaki (2017); Gokon et al. (2017a, 2017b); Cui et al. (2018); Dell'Acqua et al. (2010, 2011); Wang and Jin (2009)	Other ways to explore the intensity changes/the correlation coefficient is more sensitive to minor changes than intensity difference
Coherence -based change detection	Approaches based on co-event coherence	Co-event coherence	One pre-event and one post-event images/ interferometry mode	Matsuoka and Yamazaki (2000); Chen et al. (2011); Liu and Yamazaki (2017)	Need only one pre-event image/can be influenced by other changes/impacts from other changes can be reduced by extracting built-up areas first to improve the assessment performance
	Approaches based on the ratio of pre- and co-event coherence	The ratio of pre-event and co-event coherence	Two pre-event and one post-event images/ interferometry mode	Ito and Hosokawa (2002); Ito et al. (2003); Hoffmann (2007); Liu and Yamazaki (2017)	Can reduce common coherence variations caused by other effects/ need two pre-event images/histogram matching between pre- and post-event coherence can mitigate bulk changes
	Approaches based on the difference of pre- and co-event coherence	The original, normalized, or histogram-matched difference of pre-event and co-event coherence	Two pre-event and one post-event images/ interferometry mode	Arciniegas et al. (2007); Fielding et al. (2005); Yun et al. (2011, 2015a, 2015b); Watanabe et al. (2016)	
	Earthquake damage visualization (EDV) technique	The normalized difference (both forward and backward) and average value of pre-event and co-event coherence	Two pre-event and one post-event images/ interferometry mode	Sharma et al. (2017)	More sensitive to damaged buildings
Polarimetry-based analysis	Approaches applying model-based decomposition	Surface scattering, double-bounce scattering, volume scattering, and additional parameters such as polarization orientation angle	One pre-event and one post-event images/full-polarization mode	Yamaguchi (2012); Singh et al. (2013); Chen and Sato (2013); Chen et al. (2016)	Have a clear physical meaning with respect to the backscattering mechanisms of damaged and intact buildings/ building damages usually cause the decreases of double bounce scattering and the increases of surface scattering and/or volume scattering
	Approaches applying eigenvalue-eigenvector-based decomposition	Entropy, anisotropy, average scattering angle, etc.	One pre-event and one post-event images/full-polarization mode		Have a clear mathematical background

Approaches	Classification	Commonly-used parameters	Image requirement (number/ acquisition mode)	Representative studies	Other descriptions
	Approaches based on both decomposition methods	Parameters derived from both decomposition methods mentioned above, four component parameters (HH, HV, VH, and VV), and additional parameters such as polarization orientation angle	One pre-event and one post-event images/full-polarization mode	Sato et al. (2012); Watanabe et al. (2012); Park et al. (2013)	Make full use of all polarimetry features
Integrated approaches	The combination of intensity and coherence information	Parameters in intensity- and coherence-based change detection approaches mentioned above	One pre-event and one post-event images/ interferometry mode	Arciniegas et al. (2007); Zhang et al. (2018)	Achieve higher accuracy than applying only one type of information/ intensity is stable and coherence is sensitive to minor changes
	The addition of dual-polarization information to coherence-based approaches	Parameters in coherence-based change detection approaches mentioned above considering dual-polarization information	One pre-event and one post-event images or a stack of repeated-pass images/dual-polarization and interferometry mode	Watanabe et al. (2016); Sharma et al. (2017); Oxoli et al. (2018)	Improve the accuracy of coherence-based approaches
	The addition of ancillary data to SAR data	Parameters in SAR-based change detection approaches mentioned above and parameters in ancillary data such as NDVI derived from optical images	SAR images and ancillary data such as optical images and GIS data	Stramondo et al. (2006); Gamba et al. (2007); Chini et al. (2009); Trianni et al. (2010); Karimzadeh and Mastuoka (2017), etc.	Ancillary data can be applied to provide complementary information or remove areas of no interest to improve detection accuracy

2.1.1 Intensity-based Change Detection

Principle

If the SAR satellite is not working in an interferometry or polarimetry mode when images are captured, only intensity information can be obtained and used for building damage assessment. Here, "intensity" means the amplitude information of the backscattering waves received by a SAR sensor after sending microwaves to the ground targets. It is not only influenced by the operating parameters of the radar system (e.g., incidence angle and wavelength), but is also dependent on the characteristics of ground targets (e.g., dielectric properties and roughness). Therefore, intensity changes in pre- and post-event SAR images can be used to measure ground changes caused by a disaster event.

The principle of building damage assessment based on SAR intensity changes is as follows: owing to the slanted view of the SAR satellite sensor, an intact building usually shows regular layover and shadow zones in a SAR image. In parts of areas facing the radar sensor, a bright zone emerges, owing to double bounce effects in corner areas and the overlying of reflection from the roof, wall, and ground. In most building footprint areas and parts of areas facing backward to the radar sensor, a shadow zone appears, owing to the occlusion of the building (**Figure 3**). When a building collapses in a disaster, however, the layover, double bounce, and even shadow characteristics may disappear or decrease in the SAR image, making the reflection around the building more random and averaged. Therefore, by identifying and quantifying the intensity changes mentioned above through favorable parameters such as intensity difference, correlation coefficient and textures, the building damage condition can be speculated. Examples of high-resolution SAR image intensity characteristics in intact and collapsed building areas (Cui et al., 2018) are shown in **Figure 4**, to provide an intuitive understanding.

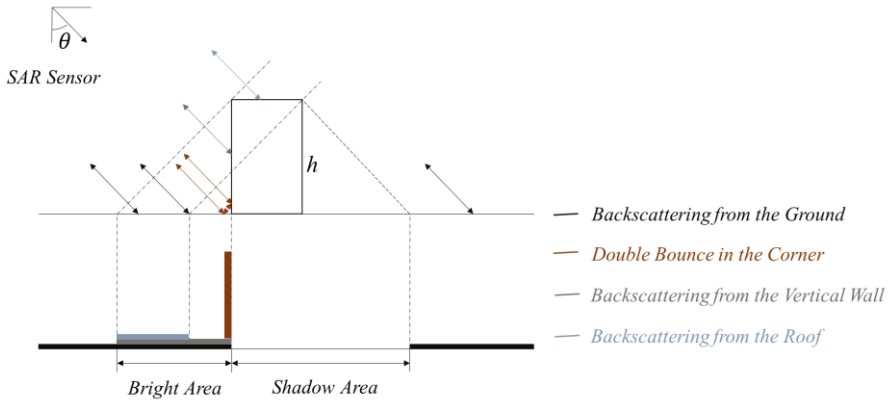

Figure 3. Schematic of intact building backscattering in synthetic aperture radar (SAR) images.

(a) (b) (c) (d) (e)

Figure 4. Examples of high resolution SAR image intensity characteristics in intact and collapsed building areas: (a) Post-event optical image of intact building areas; (b) Post-event SAR image of intact building areas; (c) Pre-event optical image of collapsed building areas; (d) Post-event optical image of collapsed building areas; (e) Post-event SAR image of collapsed building areas (Cui et al., 2018). As can be seen, the SAR intensity image shows regular shadow and layover zones in the intact building areas (b), and displays more random and averaged pixel distribution in the collapsed building areas (e).

Approach review

The classic and commonly-used method for intensity-based change detection is to calculate the intensity difference and correlation coefficient of the pre- and post-event images within a certain window, combine them together by a specific relationship, and then apply certain thresholds to discriminate building damages. This method dates back to the time when scholars (Aoki et al., 1998; Matsuoka and Yamazaki, 1999) found that in severely-damaged areas, the backscattering difference became high, and correlation coefficient became low. The damage levels tended to be related to SAR image characteristic changes. Subsequently, by utilizing discriminant analysis, a discriminant function combining backscattering difference and correlation coefficients (**Equation 1**) was proposed for building damage detection in 1995 Kobe Earthquake (Matsuoka and Yamazaki, 2004a), and later applied to damage assessment in 1999 Turkey Earthquake, 2001 India Earthquake, and 2003 Algeria Earthquake (Matsuoka and Yamazaki, 2004b, 2010). This function was developed based on the European Remote Sensing (ERS) satellite C-band images with a resolution of 30×30 m. The optimum window size was examined to be 21×21 pixels for the calculation of backscattering difference and correlation coefficient.

$$z = -2.140d - 12.465r + 4.183 \quad (1)$$

Here, z is the discriminant score, and d and r are the backscattering difference and correlation coefficient of the pre- and post-event SAR images (hereafter), respectively.

This discriminant analysis-based method achieved good agreement with field survey results, and is still employed by scholars nowadays for other SAR data and other disasters. To generalize this model from C-band images to L-band images, Matsuoka et al. (2010) carried out a regression discriminant analysis for the Japan Earth Resources Satellite (JERS)-1/SAR L-band images in the affected areas of the 1995 Kobe Earthquake. Intensity difference and correlation coefficient were calculated in a window size of 13×13 pixels. Discriminant scores were calculated by **Equation 2**, and then used to build a likelihood function for damage ratio estimation. This proposed function was then applied to Advanced Land Observing Satellite/Phased Array-Type L-band SAR (ALOS/PALSAR) L-band images with a resolution of 30 m in the 2007 Peru Earthquake, by rebuilding a likelihood function (Matsuoka and Nojima, 2010).

$$z_{Rj} = -1.277d - 2.729r \quad (2)$$

In addition, Matsuoka and Estrada (2013) developed a regression discriminant function for the 2007 Peru Earthquake based on field survey data and ALOS/PALSAR imagery, with a resolution of approximately 10 m. After an examination of window sizes, 13×13 pixels was adopted as the optimum one for the calculation of intensity difference and correlation coefficient. In this formula, the derived coefficients for the intensity difference and correlation coefficient were -0.089 and -2.576, respectively. An et al. (2016) deduced an analogous function (**Equation 3**) for the 2008 Wenchuan Earthquake and 2010 Yushu Earthquake using the ALSO/PALSAR satellite data. The window size used for parameter calculation was also 13×13 pixels.

$$Z_I = -1.145d_I - 2.562r_I + 0.997 \quad (3)$$

Nevertheless, an actual situation, such as the building distribution and damage condition, is usually protean. Sometimes exceptional cases occur, making the classic method unable to be used directly. On one hand, in a congested building area, the radar reflections of damaged areas may be stronger in the post-event image than in the corresponding pre-event image (Matsuoka and Yamazaki, 2005). To generalize this method in such conditions, Matsuoka and Yamazaki (2005) revised their discrimination function (**Equation 1**) to **Equations 4-6** for the 2003 Bam, Iran Earthquake damage assessment, by introducing another discriminant line (**Equation 6**).

$$z = \max(z_0, z_1) \tag{4}$$

$$z_0 = -2.140d - 12.465r + 4.183 \tag{5}$$

$$z_1 = 2.140d - 12.465r + 4.183 \tag{6}$$

On the other hand, for the identification of small building damage ratios in less densely built-up areas, the ratio and difference of the pre- and co-event correlation coefficient have been applied to minimize the impacts from other factors. Matsuoka et al. (2005) revealed that the correlation coefficient ratio were more suitable for damage detection in 2004 Niigate Earthquake, owing to the small distribution of severely damaged building areas. Matsuoka and Yamazaki (2006) applied the correlation coefficient difference (**Equation 7**) calculated by two pre- and one post-event ALSO/PALSAR images for damage assessment in the 2006 Mid Java Earthquake, in order to minimize impacts from signal noise and temporal changes of the earth's surface.

$$r_{dir} = r_{ab} - r_{bb} \tag{7}$$

In the above, r_{ab} is the correlation coefficient of one pre-event and one post-event image, and r_{bb} is the correlation coefficient of two pre-event images.

In addition to applying and modifying the classic approach mentioned above, some scholars also have proposed other methods in recent years. Liu and Yamazaki (2011) raised a change factor (**Equation 8**) that was calculated by the correlation

coefficient and the normalized absolute value of intensity difference for urban change monitoring. They thought that the correlation coefficient was sensitive to subtle changes, whereas the intensity difference was more stable. Therefore, they set a larger weight for the intensity difference. In their case, the data used were TerraSAR-X images with a resolution of 3 m, and the applied window size for parameter calculation was 9×9 pixels.

$$z = \left| \frac{d}{max|d|} \right| - c \cdot r \tag{8}$$

Here, c is the weight between the difference and correlation coefficient, and was determined as 0.25 in their research.

Gokon et al. (2017a, 2017b) regressed a damage function between the actual building damage ratio and correlation coefficient mean value in an object scope, to estimate the number of washed-away buildings in the 2011 Tohoku Earthquake and Tsunami. The correlation coefficient image was first calculated, and then segmented by region growing method to form homogeneous objects. The average value of the correlation coefficient at each object was then calculated to regress the relationship between its values and actual building damage ratios. The obtained functions for the TerraSAR-X data with a resolution of 3 m and ALOS/PALSAR data with a resolution of 10 m are shown in **Equation 9** and **Equation 10**, respectively.

Damage function for TerraSAR-X data:

$$F_X = 1.20 - \frac{1.20}{\left(1 + exp\left(-\frac{R_{mX} - 0.21}{0.08}\right)\right)} \tag{9}$$

Damage function for ALOS/PALSAR data:

$$F_L = 0.95 - \frac{0.95}{\left(1 + exp\left(-\frac{R_{mL} - 0.16}{0.03}\right)\right)} \tag{10}$$

In the above, F_X and F_L are the damage ratios of washed away buildings for the TerraSAR-X data and ALOS/PALSAR data, respectively, and R_{mX} and R_{mL} are the mean correlation coefficient at each object for the TerraSAR-X data and ALOS/PALSAR data, respectively.

Cui et al. (2018) proposed a SAR image damage index (SARDI) based on the proportion of highlight (layover and bright line) areas to quantify the seismic damage distribution of buildings in a street block (**Equation 11**). The highlighted area was first extracted by low-pass and high-pass filtering in a frequency domain. The damage index in **Equation 11** was then calculated and classified for building damage differentiation. The applied data for this study were high-resolution airborne SAR images with a resolution of 0.5 m.

$$D_{\mathrm{SAR}} = 1 - S_{\mathrm{HL}} / S_{\mathrm{SB}} \tag{11}$$

Here, D_{SAR} is the average seismic damage index based on a SAR image (SARDI) of a street block, S_{HL} is the highlighted area of the street block on the SAR image, and S_{SB} is the total area occupied by the buildings within a street block.

Moreover, texture features (Dell'Acqua et al., 2010a; Dell'Acqua et al., 2011), K-distribution and Getis statistics (Wang and Jin, 2009), as well as hyperboloid change index (Nakmuenwai et al., 2016) were also said to be valuable information for building damage assessment in disasters.

2.1.2 Coherence-based Change Detection

Principle

Interferometric synthetic aperture radar (InSAR) is a technique that exploits the interference of electromagnetic waves received from different times. It came into use at the end of the 1960s, when Rogers and Ingalls (1969) employed radar interferometry to study the Venus surface and moonscape. Then, Graham (1974) introduced the concept to terrain mapping. Massonnet et al. (1993) and Fruneau et al. (1996) introduced it to earthquake-induced displacement field mapping and landslide monitoring, respectively. When an InSAR system is operating, single-look complex (SLC) products, which preserve not only magnitude information but also phase

information, can be acquired (Monserrat et al., 2014). Therefore, in addition to intensity, phase can also be explored, to mine more information for ground change measurement. The "phase" in SAR data indicates the relative value of the returned backscattering waves in a whole period. It is very sensitive to the distance between the satellite sensor and ground target, and can therefore be applied for ground change detection. The path length of an SAR signal to ground and back usually contains a number of whole wavelengths, plus some fraction of a wavelength.

Over the years, InSAR technique has been widely investigated and applied for ground deformation monitoring or detection (Zhao et al., 2012; Barboux et al., 2015; Zhao et.al., 2018; Strozzi et. al., 2018; Zhang et al., 2019) and digital elevation model (DEM) generation (Lanari et al., 1996; Rosen at al., 2000; Stramondo et al., 2007; Neelmeijer et al., 2017), by exploring the phase information in two (or a series of) SAR images. Nevertheless, the feasibility of InSAR depends on many observation characteristics, such as the spatial baseline and temporal baseline (Konishi and Suga, 2018), and is restricted by many actual conditions, e.g., the amount of vegetation (Lazecký et al., 2015).

Coherence is a by-product of SAR interferometry, and indicates the cross-correlation of phase information (**Equation 12**) in two images. The decorrelation of coherence usually indicates ground changes (Zebker and Villasenor, 1992; Moreira et al., 2013; Milisavljevic et al., 2015), and can be explored for building damage assessment in disasters. Values of coherence range from 0 to 1, with a lower value indicating larger ground changes (Ram et al., 2017) (severe damage in building damage assessment field). As an example, **Figure 5** shows the co-event coherence image in Yushu County urban area influenced by the 2010 Yushu Earthquake (Chen et al., 2011).

$$\gamma = \frac{E\left\langle c_1 c_2^* \right\rangle}{E\left\langle c_1 c_1^* \right\rangle E\left\langle c_2 c_2^* \right\rangle} \tag{12}$$

In the above, γ is the calculated coherence, c_1 and c_2 are corresponding complex pixel values of two images, respectively, c^* represents the complex conjugate of c, and E represents the expected value.

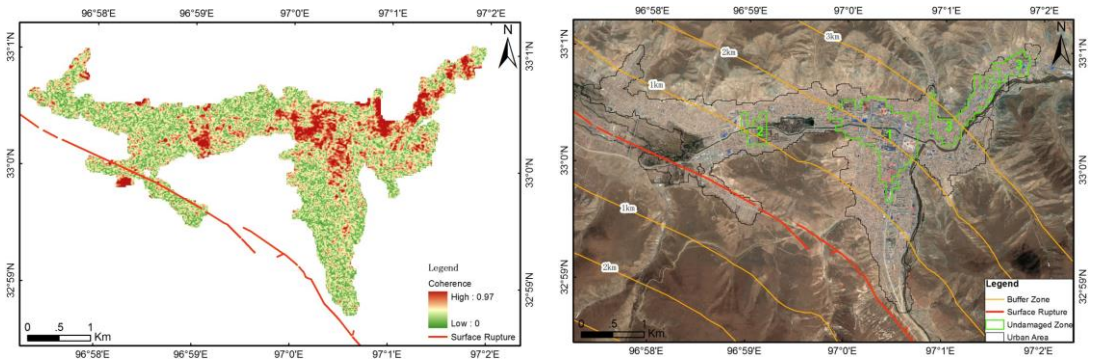

(a) (b)

Figure 5. An example of co-event SAR coherence image in Yushu County urban area influenced by 2010 Yushu Earthquake: (a) Co-event coherence map; (b) Optical image from Google Earth showing building damage conditions (Chen et al., 2011). As can be seen, the undamaged zones show clearly higher coherence as compared with the damaged urban areas.

Approach review

Coherence information is more sensitive to minor ground changes than intensity information. When interferometric SAR image pairs are available with suitable temporal and spatial baselines, coherence can provide valuable information for identifying building damages, especially minor damages. In the analysis of 1999 Kocaeli, Turkey Earthquake damages, Matsuoka and Yamazaki (2000) declared that the coherence degree was a good index for distinguishing slight to moderate damage levels. In a study of the 2003 Bam, Iran Earthquake building damage conditions, Arciniegas et al. (2007) demonstrated that coherence difference produced relatively better detection accuracy than the absolute amplitude change, and the combination of coherence and amplitude change could further increase analysis accuracy. In the 2016 Kumamoto Earthquake damage assessment, Liu and Yamazaki (2017) explored two representative coherence indices (i.e., the co-event coherence and the ratio of co- and pre-event coherence) and one representative intensity parameter (i.e., the *z*-factor in **Equation 8**) to extract areas with collapsed buildings. The results indicated that the coherence ratio yielded the highest accuracy among the three parameters.

Coherence-based change detection dates back to the time when scholars (Ito et al., 2000; Yonezawa and Takeuchi, 2001) found that the decorrelation of coherence in the 1995 Kobe Earthquake SAR images was related to damage conditions, and could be

used for building damage assessment. By setting reasonable thresholds, even a single co-event coherence image can be applied to assess building damages. In the 2010 Yushu Earthquake damage detection, Chen et al. (2011) set the mean value of co-event coherence as the breaking point for judging building damages in the built-up areas extracted by DEM and SAR intensity information. Nevertheless, more commonly-used approaches are based on two-pair coherence images (i.e., pre- and co-event coherences). In that way, common coherence variations caused by other effects can be reduced through calculating the ratio or difference of the pre- and co-coherence images.

On one hand, the coherence ratio has been explored for building damage assessments. Ito and Hosokawa (2002) proposed a damage estimation model according to the coherence ratio in the 1995 Kobe Earthquake applying ERS-1 C-band and JERS-1 L-band SAR data, and examined it in the 1999 Kocaeli Earthquake employing ERS-1/2 SAR images (Ito et al., 2003). Their coherence ratio, calculated by dividing a co-event coherence image using a pre-event coherence image, was said to have a linear relationship with the cumulative probability of the damage degree. Similarly, Hoffmann (2007) quantified coherence changes by their coherence change index-coherence ratio for damage condition interpretation in the 2003 Bam Earthquake, using environmental satellite advanced synthetic aperture radar (ENVISAT ASAR) images. Their coherence ratio was defined as an index calculated by diving a coherence image not spanning the earthquake, using a coherence image spanning the earthquake (**Equation 13**).

$$\rho = \frac{\gamma_{ref}}{\gamma_{eq}} \tag{13}$$

Here, ρ is the coherence change index, γ_{ref} is the coherence not spanning the time of the earthquake, and γ_{eq} is the coherence spanning the time of the earthquake.

On the other hand, the coherence difference, either calculated in the original way or in an improved way, has been exploited for discriminating between damaged and undamaged buildings. Arciniegas et al. (2007) demonstrated the favorable performance of the coherence difference in the building damage assessment of the

2003 Bam, Iran Earthquake using ENVISAT ASAR data. Fielding et al. (2005) also applied the coherence difference of ENVISAT ASAR data for building damage mapping in the 2003 Bam, Iran Earthquake, to separate the coherence reductions caused by vegetation and other effects. Yun et al. (2011, 2015a, 2015b) proposed a prototype algorithm based on the difference of histogram-matched pre- and co-event coherence for generating damage proxy maps in disasters. Pre- and co-event coherence maps were first calculated and spatially registered. Histogram matching (Coltuc et al., 2006) was then applied to the co-event coherence map, to modify its pixel values in order to make the pre- and co-event coherence maps statistically identical. After that, the coherence difference was calculated to generate a color damage proxy map. It was said that bulk changes in the two coherence maps could be mitigated by histogram matching before the calculation of the difference. Watanabe et al. (2016) applied the normalized difference (**Equation 14**) of two coherence image pairs as the parameter for discriminating building damages in disasters.

$$\Delta\gamma = \frac{\gamma_{pre} - \gamma_{int}}{\gamma_{pre} + \gamma_{int}} \tag{14}$$

Here, $\Delta\gamma$ is the normalized coherence difference, and γ_{pre} and γ_{int} are the pre- and co-event coherence, respectively.

In addition, by compositing several parameters calculated through pre- and co-event coherence images, Sharma et al. (2017) presented an earthquake damage visualization (EDV) technique for rapid earthquake damage assessment. Their EDV used RGB imagery, merged using three indicators calculated through pre- and post-event coherence images: forward change (**Equation 15**), backward change (**Equation 16**), and change-free (**Equation 17**). Moreover, Ito et al. (2000) applied multi-source and temporal coherence images and neural classifiers to extract damaged regions in the 1995 Kobe earthquake. Five coherence images were used, including one generated from L-band JERS-1 images, and four produced by C-band ERS-1 images. The results showed that the average coherence of JERS-1 data has a significantly higher contrast than that of ERS-1 data, and that the use of it achieved better results.

$$Red(R) = \frac{PC - CC}{PC + CC} \tag{15}$$

$$Green(G) = \frac{CC - PC}{PC + CC} \tag{16}$$

$$Blue(B) = \frac{PC + CC}{2.0} \tag{17}$$

In the above, *PC* and *CC* indicate the pre-seismic coherence (*PC*) and co-seismic coherence (*CC*), respectively. In that regard, *PC* and *CC* in **Equations 15-17** have the same meaning as γ_{ref} and γ_{eq} in **Equation 13**, and γ_{pre} and γ_{int} in **Equation 14**, even though the notations are different depending on the authors.

2.1.3 Polarimetry-based Analysis

Principle

Polarization is another essential property of electromagnetic waves, in addition to amplitude, phase, and frequency. It can be applied to investigate the propagation and scattering of the electromagnetic vector phenomenon. Electric field vectors of energy pulses emitted by a radar system can either be polarized in a horizontal (H) plane or in a vertical (V) plane. Regardless of wavelength, a SAR platform can transmit H and/or V electric field vectors, and then receive H and/or V return signals. Therefore, in total, four types of polarization exist: horizontal transmit and horizontal receive (HH), horizontal transmit and vertical receive (HV), vertical transmit and horizontal receive (VH), and vertical transmit and vertical receive (VV). Generally, a SAR system can operate in either a single polarization mode, a dual-polarization mode, or a full-polarization (or quad-polarization) mode. The single polarization mode denotes the application of only one type of polarization, which usually refers to HH or VV. The dual-polarization mode refers to the addition of another polarization form when one polarization form has been applied (e.g., HH and HV dual polarization). The full-polarization mode includes all four types of polarization forms, and requires the emission of H and V pulses, along with the simultaneous reception of H and V pulses under each type of emitted pulses.

The polarization features of multi-polarized SAR data are sensitive to dielectric constants, physical properties, geometry, and the orientation of ground targets. Therefore, they can greatly improve the ability of imaging radar to acquire various information of the targets. The first multi-polarized SAR data were obtained after the launches of the ENVISAT, ALOS-1, and RADARSAT-2 satellites (Karimzadeh and Mastuoka, 2017). From then on, they have been widely explored and applied in studies on subjects such as land classification and target detection (Boerner, 2003; Huang et. al., 2011; Dickinson et. al., 2013), and also have been proven to provide valuable information for facilitating building damage assessment in disasters (Watanabe et al., 2016; Karimzadeh and Mastuoka, 2017).

Approach review

The addition of another polarization when one polarization has been applied was shown to be favorable for improving the accuracy of building damage assessment. In the damage detection of the 2015 Gorkha Earthquake, Watanabe et al. (2016) demonstrated that the incorporation of HV polarization to HH polarization improved the accuracy of the interferometric SAR coherence change detection. In the 2016 Amatrice Earthquake damage assessment, Karimzadeh and Mastuoka (2017) revealed that, for Sentinel-1 satellite imagery, the accuracy of a VV and VH combination-based method was higher than that of a VV-based or VH-based method; similarly, for ALOS-2 satellite imagery, the HH and HV combination-based method achieved better accuracy than the HV-based or HH-based method. In the EDV technique for rapid earthquake damage assessment, Sharma et al. (2017) also considered the addition of HV polarization to the HH polarization as one of the reasons for accuracy improvement.

Whereas dual-polarization information can assist in accuracy improvement, full-polarization information is capable of providing more rich information for understanding the backscattering scattering mechanisms of ground targets. When full-polarization data are acquired, the polarized scattering, which was first proposed by Sinclair (1950), can be expressed as **Equation 18**. Subjected to a reciprocity condition, the Pauli scattering vector can be expressed as **Equation 19**, and the coherency matrix

T can be expressed as **Equation 20**. Through rational decomposition, the fully-polarized data can be decomposed into several different components, facilitating a specific and effective interpretation of ground changes.

$$S = \begin{bmatrix} S_{HH} & S_{HV} \\ S_{VH} & S_{VV} \end{bmatrix} \tag{18}$$

Here, S_{HH}, S_{HV}, S_{VH}, and S_{VV} indicate the backscattering coefficients of the HH, HV, VH, and VV polarizations, respectively.

$$k_P = \frac{1}{\sqrt{2}}[S_{HH} + S_{VV} \;\; S_{HH} - S_{VV} \;\; 2S_{HV}]^T \tag{19}$$

$$T = \langle k_P k_P^H \rangle = \begin{bmatrix} T_{11} & T_{12} & T_{13} \\ T_{21} & T_{22} & T_{23} \\ T_{31} & T_{32} & T_{33} \end{bmatrix} \tag{20}$$

In the above, <> denotes the ensemble average, k_P^H is the complex conjugation and transposition of k_P, and T_{ij} is the (i, j)th entry of T.

Polarimetry decomposition theorems date back to the 1970s, in Huynen's work (Huynen, 1970). So far, various decomposition approaches (Cloude and Pottier, 1996, 1997; Freeman and Durden, 1998; Yamaguchi et al., 2005, 2006, 2011; Chen et al., 2014a, 2014b, 2014c) have been proposed. Among these decomposition approaches, the coherency matrix (**Equation 20**)-based ones, including model-based and eigenvalue-eigenvector-based decompositions, have been commonly used for building damage assessment in disasters. On one hand, the model-based decomposition, especially the four-component scattering model (Yamaguchi et al., 2005, 2006, 2011) which can decompose the coherency matrix (T) into surface scattering, double-bounce scattering, volume scattering, and helix scattering contributions (**Equation 21**), has a clear physical meaning with respect to the backscattering mechanisms of damaged and intact buildings (Section 2.1.1). On the other hand, the eigenvalue-eigenvector-based decomposition (Cloude and Pottier, 1996, 1997) can decompose T into matrix-characterizing parameters such as entropy (H), anisotropy (A), and average scattering angle ($\bar{\alpha}$), having a clear mathematical background. The entropy can be used to measure the statistical disorder degrees in a scattering process, with a value close to 1 indicating a distributed target response. The anisotropy quantifies the relative contributions of the secondary and tertiary scattering

mechanisms. The average scattering angle denotes the average target scattering mechanism, and can be applied to distinguish between different scattering types.

$$\mathrm{T} = f_v\langle T_{vol}\rangle + f_d\langle T_{dbl}\rangle + f_s\langle T_{surf}\rangle + f_h\langle T_{hel}\rangle \quad (21)$$

Here, f_v, f_d, f_s, and f_h indicate model coefficients, and T_{vol}, T_{dbl}, T_{surf}, and T_{hel} represent volume scattering, double-bounce scattering, surface scattering, and helix scattering, respectively.

Many studies have been carried out concerning the application (Yamaguchi, 2012; Singh et al., 2013; Park et al., 2013) and mechanisms (Kimura et al., 2005; Iribe and Sato, 2007; Lee and Ainsworth, 2011; Chen et al., 2013) of SAR polarimetry features on buildings and building damages. Both model-based and eigenvalue-eigenvector-based decompositions are able to provide favorable polarimetry indicators for building damage assessment in disasters. Double-bounce scattering, surface scattering, and volume scattering derived from model-based decomposition, as well as H, A, and $\bar{\alpha}$ decomposed through eigenvalue-eigenvector-based decomposition have all been demonstrated to be valuable parameters for identifying damaged urban areas. Several additional polarimetry parameters, such as polarization coherence, which can be used to characterize surface roughness (Mattia et al., 1997), and the polarimetric orientation angle, which has a close relationship with building orientation (Lee et al., 2002), were also said to be favorable parameters for understanding damages in built-up areas. **Figure 6** shows an example of pre- and post-event polarimetry color images (Singh et al., 2013), from which the changes of several decomposition components before and after the disaster can be clearly seen.

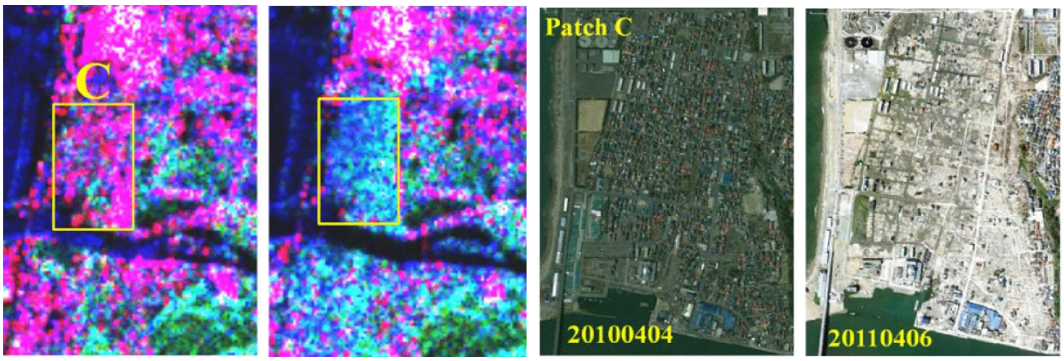

(a) (b) (c) (d)

Figure 6. An example of pre- and post-event SAR polarimetry images in the 2011 Tohoku Earthquake and Tsunami: (a) Pre-event SAR image for patch C and surrounding areas (2009/04/02); (b) Post-event SAR image for patch C and surrounding areas (2011/04/08); (c) Pre-event Google optical image for patch C (2010/04/04); (d) Post-event Google optical image for patch C (2011/04/06). Red, green, and blue color in SAR images represent double-bounce scattering, volume scattering, and surface scattering, respectively (Singh et al., 2013). Comparing patch C before and after the disaster, it can be seen clearly that after many buildings were damaged and collapsed in the disaster, the double-bounce scattering (red) decreased, and the volume scattering (green) and surface scattering (blue) increased.

Yamaguchi (2012) synthesized full color images for the straightforward recognition of changes applying model-based decomposition. The red, green, and blue colors in the composited full color images were merged by double-bounce scattering, volume scattering, and surface scattering respectively, with the brightness of each color corresponding to the magnitude of each scattering. The results demonstrated that most disaster areas showed increased surface scattering. Similarly, Singh et al. (2013) investigated damage assessment in urban areas by analyzing RGB color-coded images composited by components derived through model-based decomposition. They concluded that different scattering parameters showed different behaviors in influenced areas, and the double-bounce scattering is the most promising input parameter for automated detection of disaster-affected urban areas at a pixel level.

Based on model-based decomposition and polarimetric orientation angle, Chen and Sato (2013) proposed two polarimetry indicators - the ratio of dominant double-bounce scattering and the standard deviation of polarization orientation angle differences - for damage level discrimination in the 2011 Tohoku Earthquake and Tsunami. These two indicators can reflect the amount of destroyed ground-wall structures and the homogeneity reduction of polarization orientation angles, respectively. They (Chen et al., 2016) then confirmed and validated the linear relationship between the polarimetry damage index (the ratio of dominant double-bounce scattering mechanisms between the post- and pre-event cases) and the ground truth urban damage levels.

In addition, Sato et al. (2012) applied model-based decomposition to analyze damaged built-up areas and flooded river areas caused by the 2011 Tohoku Earthquake and Tsunami. The polarization orientation angle and eigenvalue-eigenvector-based decomposition were also applied to provide additional information for understanding built-up area damages, and to further confirm scattering changes in flooded areas. The results indicated that the dominant scattering of washed-away built-up areas changed from double-bounce scattering to surface scattering after the disaster. Moreover, the flooded river neighborhood was dominated by surface scattering after the tsunami. Watanabe et al. (2012) compared representative polarimetry parameters of full polarimetric SAR images acquired before and after the 2011 Tohoku Earthquake and Tsunami. They analyzed and discussed polarimetry coherence (HH-VV and RR-LL), four-component decomposition parameters (HH, HV, VH, and VV), and all parameters derived from model-based and eigenvalue-eigenvector-based decompositions. Results showed that the α angle reduced to 30° after the disaster, indicating that the targets were mainly composed of surface scattering components. The entropy showed a higher value both before and after the disaster, ranging from 0.6 to 0.8, indicating that a complex scattering mechanism is involved in this region. In addition, the polarimetry coherence parameters were said to be the most important factors for distinguishing disaster areas in this case. Park et al. (2013) also investigated earthquake-caused backscattering mechanism changes in the 2011 Tohoku Earthquake and Tsunami using polarimetric indicators. The parameters derived from model-based decompositions (surface, double-bounce, and volume scattering) and eigenvalue-eigenvector-based decompositions (H, A, and $\overline{\alpha}$), and additional parameters such as polarization coherence and polarimetric orientation angle were all studied. It was said that the swept urban areas were characterized by a significant decrease of double-bounce scattering, whereas the partly-damaged urban areas did not show a distinctive double-bounce scattering reduction. Nevertheless, minor changes can still be identified using the polarimetric parameters such as anisotropy and polarimetric coherence.

Despite the fact that full polarimetry data includes rich and effective information facilitating scattering mechanism interpretation, there are fewer opportunities for the observation of that type of data than for single/dual-polarization data (Watanabe et al.,

2016). Besides, all high-resolution SAR systems offer multi-polarization data, at the cost of reduced resolution (Balz and Liao, 2010). However, when assessing the Tohoku earthquake damage using full polarimetric SAR data, Sato et al. (2012) indicated that the scattering mechanism is adequate for discriminating damaged and flooded areas, even though the resolution of the applied data is not fine.

2.1.4 Integrated Approaches

Intensity, coherence, and polarimetry information of SAR data can all be used for building damage assessment in a block unit, with different pros and cons. Coherence information is sensitive to smaller changes, whereas intensity information is more suitable for larger ground change analysis. Coherence data are highly dependent on factors such as spatial and temporal baseline to give favorable results, whereas intensity data are influenced by acquisition duration, geometry, and wavelengths (Plank, 2014). Polarimetry information is sensitive to ground target characteristics such as dielectric constants and orientation. Imaging radars can acquire various information of the targets when operating in a multi-polarization mode, helping to understand the physical scattering mechanisms. Nevertheless, there are fewer opportunities to acquire full-polarization SAR data, and the acquired full-polarization data may have relatively lower resolution. When several types of information are available at the same time, integrated methods that combine several types of information or several types of data can be investigated and developed, to compensate for each other and achieve better assessment results.

The combination of intensity and coherence information

The intensity and coherence information can be combined to complement each other. In the analysis of the Bam, Iran Earthquake damage, Arciniegas et al. (2007) indicated that the combination of coherence change and intensity difference could lead to an improved accuracy, as compared with the use of each property separately. For urban change detection using SAR data, Zhang et al. (2018) presented a method combining intensity difference and coherence coefficient. The amplitude difference was initially used to determine suspected change areas, and then the coherence

coefficient was applied to analyze if the suspected change areas were genuinely changed areas. The results showed that this method can achieve a much higher accuracy than a single amplitude difference, as it was able to remove pseudo-changes attributed to vegetation, tree growth, and seasonal changes.

The addition of dual-polarization information to coherence-based approaches

The dual-polarization information, which is relatively easier to acquire than full-polarization information, can be integrated into coherence-based approaches for accuracy improvement. Watanabe et al. (2016) applied the coherence change detection technique to dual-polarization (HH and HV) images for assessing building damages in the 2015 Gorkha Earthquake. The incorporation of HV polarization to HH polarization was considered to marginally improve the detection accuracy. Sharma et al. (2017) indicated that calculating the average value of coherence (both pre- and co-event coherence) in HH and HV polarization images could contribute to accuracy improvement in their EDV technique. Oxoli et al. (2018) applied coherence change detection to automatic building damage assessment in the 2016 Central Italy Earthquake, using a set of 20 interferometry SAR images with different polarizations (VV, VH, VV+VH). The ratio between the probability of no-change and that of change occurring after the disaster was evaluated to perform change detections, and the generalized likelihood ratio test (Fan et al., 2001) was applied to infer the significance of detected changes.

The addition of ancillary data to SAR data

Ancillary data, such as optical images and GIS maps, when available, can be applied in SAR-based building damage assessments as a sort of complementary information. Stramondo et al. (2006) explored the combination use of optical images and SAR data for damage assessment. The results showed that the fusion of SAR and optical data improved correct classification of damaged areas, and the complex coherence achieved a higher classification accuracy when combined with the optical images. Arciniegas et al. (2007) employed a pre-event advanced spaceborne thermal emission and reflection radiometer image to mask out vegetated areas, to thereby

facilitate SAR-based building damage analyses. It was said that this method achieved slightly higher assessment accuracy as compared to only using SAR information. Chini et al. (2009) processed both QuickBird very high resolution (VHR) optical images and SAR data to extract features for damage-level estimation, and pointed out their possible synergy. Uprety and Yamazaki (2012) applied both correlation coefficient and backscattering difference calculated through SAR images, and normalized difference vegetation index (NDVI) derived from optical images for building damage detection in the 2010 Haiti Earthquake. Tamkuan and Nagai (2017) proposed an approach combining optical satellite imagery and interferometric SAR coherence for building damage assessment. The post-event optical imagery was employed to extract water bodies and highly-vegetated areas, the pre-event coherence was used to separate urban and non-urban areas, and the co-event coherence was applied to judge damage levels.

In addition, in the damage detection of the 2003 Bam Earthquake, Gamba et al. (2007) indicated that the combination of intensity and phase features enhanced damage extraction, and the use of ancillary data further improved the detection accuracy by discarding uninteresting parts and forcing homogeneous classification. Trianni et al. (2010) combined ancillary GIS information and statistical features of SAR images for building damage mapping, with the ancillary data used for urban block definition, and the SAR statistical features applied for damage discrimination. Karimzadeh and Mastuoka (2017) integrated all SAR image information including intensity, coherence, and polarimetry, as well as optical image features, for damage detection in the 2016 Italy Earthquake.

2.2. Building-unit Approaches

High-resolution images, when available, are able to provide more detailed information regarding ground targets, even though they may have smaller spatial coverage, and be limited by satellite storage and processing capacities (Joyce et al., 2009a). In high-resolution SAR images, building geometric features become evident (Stilla at al., 2005), providing the possibility for damage assessment in a building unit. Additionally, the high resolution ensures that there are sufficient pixels within each building footprint for analysis. Nowadays, most modern sensors are designed to

acquire data at various ground resolutions. Since the first launch of high-resolution SAR satellites (e.g., TerraSAR-X and CosmoSkyMed) in 2007, not only can airborne imagery provide a source of single building damage information (Simonetto et al., 2003, 2005; Stilla at al., 2005; Shi et al., 2015), but also the operative spaceborne platforms have reached a spatial resolution potentially allowing for change detection in a building scale (Plank, 2014; Nakmuenwai et al., 2016; Natsuaki et al., 2018). As a result, approaches for SAR-based change detection in a building unit have been gradually developed.

The principles of building-unit change detection approaches were basically similar to those of the block-unit ones, with some simply generalizing the block-unit methods into building-unit methods, and some making full use of the clear individual building features in the high-resolution images (**Table 2**). Nevertheless, different from block-unit approaches, building-unit approaches can provide more detailed and specific information regarding building damage conditions. Instead of showing rough damage levels and damage ratios in each block (**Figure 2**), they are able to provide the specific damage condition of each particular building (**Figure 7**). Besides, as higher resolution is the development trend of remote sensing technology, building-unit approaches may get more and more attention in the future to make full use of the rich information in the high-resolution images.

Table 2. A summary of building-unit change detection approaches.

Approaches	Commonly used parameters	Representative studies	Other descriptions
Approaches by generalizing block-unit change detection methods	Intensity difference, correlation coefficient, coherence, texture features, etc.	Uprety et al. (2013); Liu et al. (2013); Miura et al. (2016); Bai et al. (2017b); Natsuaki et al. (2018); Ge et al. (2019)	Need building footprint information /building footprints can be shifted or buffered to incorporate more valuable double-bounce, layover, and shadow characteristics owing to the side-looking of SAR sensors
Approaches by exploring the clear individual building features in high resolution images	Double bounce effect features	Guida et al. (2008, 2010a, 2010b, 2011); Brett (2013); Brett and Guida (2013); Chini et al. (2015)	Explore the characteristic changes of the double-bounce areas
	High and low backscattering areas caused by the double bounce, layover, and shadow effects	Liu et al. (2012); Gokon et al. (2015)	Explore the percentage/area/ statistical characteristic changes of the bright and/or shadow regions
Others	SAR image parameters mentioned above and ancillary data parameters	Brunner et al. (2010); Wang and Jin (2012)	Add ancillary data to provide complementary information and improve detection accuracy

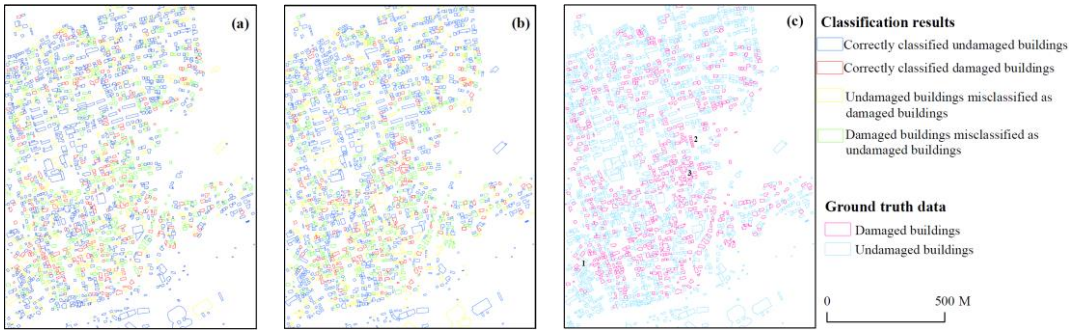

Figure 7. An example of building-unit damage assessment results (Bai et. al., 2017b): (a) Damage mapping results using only post-event SAR image; (b) Damage mapping results using multi-temporal SAR images; (c) Ground truth data.

2.2.1 Generalization of the Block-unit Approaches

By averaging or calculating relevant parameters in the block-unit approaches (e.g., discriminant scores and coherence) within each original, moved, or buffered building footprint area, the block-unit approaches can be directly generalized into building-unit change detection approaches. In this type of approaches, the building footprint information, which is not necessary in the block-unit approaches, is needed as an ancillary data to set boundaries for the calculation of mean parameter values. Owing to the side-looking nature of SAR sensors, building footprints have sometimes been shifted or buffered to incorporate the valuable double bounce, layover, and shadow characteristics. Uprety et al. (2013) calculated the averaged value of the correlation coefficient within each building footprint, and then set an appropriate threshold value for differentiating building damage conditions in the 2009 L'Aquila Earthquake. Liu et al. (2013) applied the average value of the change factor (**Equation 8**) within each shifted GIS map building outline to detect impacted buildings in the 2011 Tohoku Earthquake and Tsunami. Miura et al. (2016) calculated the mean value of the intensity difference and correlation coefficient inside each displaced building footprints, and then constructed a two-group discriminant function (**Equation 22**) for damage grade separation in the 2010 Haiti Earthquake.

$$z = 0.501|d|-2.568r+0.177 \tag{22}$$

Here, z indicates the discriminant score, d indicates the intensity difference, and r indicates the correlation coefficient.

Bai et al. (2017b) applied the differences of polarimetry features and texture features within each building footprint for damage mapping in the 2016 Kumamoto Earthquake. Natsuaki et al. (2018) evaluated the limitations and sensitivity of coherence for building damage detection at an individual building level. The coherence difference was applied in their study. Results indicated that, for damage detection of individual buildings by SAR coherence information, the damage levels should be larger than level-2 in the European macroseismic scale (EMS-98) (Grünthal, 1998), and the buildings should be larger than the window size of the coherence. Ge et al. (2019) calculated the difference of texture features within each buffered building footprint area for building damage assessment in the 2015 Nepal Earthquake.

2.2.2 Exploration of the Clear Individual Building Features

Features of individual buildings, especially double bounce, layover, and shadow effects in the intensity image (Section 2.1.1), become clear in high-resolution SAR images, and therefore, can be analyzed in detail for building damage condition identification in disasters. Different from block-unit approaches, which usually calculate the intensity difference or correlation coefficient to roughly measure the changes of these features, this type of approaches explores more detailed characteristics of them (e.g., characteristic changes of double bounce areas and percentage/area changes of layover regions). Guida et al. (2011) investigated the feasibility of deterministic feature extraction method, which was proposed by them based on the double bounce mechanism (Franceschetti et al., 2007; Guida et al., 2008, 2010a, 2010b) for identifying damaged and collapsed buildings in the 2009 L' Aquila Earthquake. Brett (2013) described two feature classification techniques based on a curvilinear feature detection algorithm, which was applied to extract bright lines in SAR images. Then, by integration of these techniques, an unsupervised tool for earthquake damage detection was developed and verified in the 2009 L' Aquila Earthquake and 2010 Haiti Earthquake (Brett, 2013; Brett and Guida, 2013). Chini et al. (2015) used four change indicators (intensity ratio, intensity correlation, Kullback-Leibler divergence and interferometric coherence) calculated from pixels within double bounce regions for earthquake damage mapping in the 2009 L'Aquila Earthquake. Liu et al. (2012) applied the percentage of pixels with decreased intensity

within walls, and those with increased intensity outside walls, to judge building damage conditions in the 2011 Tohoku Earthquake and Tsunami. Gokon et al. (2015) proposed a parameter-change ratio of areas with high backscattering (C_r) (**Equation 23**) in the buffered building region according to layover and double-bounce principles, for building damage assessment. In addition, Brunner et al. (2010) and Wang and Jin (2012) detected building damages at an individual level based on one pre-event optical image and one post-event SAR image. The pre-event optical image was first used to estimate building information. The SAR acquisition parameters were then applied to expect building signatures after the disaster, assuming no damage prior to combining with the building information estimated from the optical image. Finally, the similarity between the predicted image and an actual post-event SAR image was compared to judge the damage condition of each building.

$$C_r = 1 - \frac{\text{Areas}_{\text{intersect}}}{\text{Areas}_{\text{pre}}} \tag{23}$$

In the above, $\text{Areas}_{\text{intersect}}$ indicates the intersection of the pre- and post-event areas with high backscattering in each building and $\text{Areas}_{\text{pre}}$ refers to the pre-event areas with high backscattering in each building.

2.3. Summary

Various change detection approaches have been proposed for building damage assessment in disasters, either in a block unit or in a building unit. Block-unit methods, which have obtained extensive studies since the 1995 Kobe Earthquake, were first proposed because of the image resolution limitations in the initial stages. Damage conditions in block-unit approaches were usually illustrated by damage levels or damage ratios in irregular administrative division blocks, or regular artificial division blocks. The development of high-resolution SAR images, such as the first launch of high-resolution SAR satellites in 2007, promoted the development of building-unit assessment approaches. As the high resolution made individual building features observable and ensured enough pixels within each building footprint for analysis, change parameters and features can be calculated and analyzed within each original, modified, or buffered building footprint area for damage assessment.

As compared with block-unit methods, building-unit approaches are able to provide more specific and clearer damage information (e.g., the specific damage condition of a particular building). However, that does not mean that they are always the best choice under any circumstances. On one hand, high-resolution images used for building-unit analysis usually have smaller spatial coverage, and may be limited by satellite storage and processing capacities. When disasters affect wide areas, and a rapid even rough identification of major damage areas is needed, block-unit approaches may be more suitable. On the other hand, the damage of one building usually causes changes not only inside the building outline, but also in the surrounding areas. In densely built-up areas, some building-unit methods may be unable to take into account these factors, and therefore cannot perform very well. Hence, it is better to comprehensively consider the detection purpose, image information (e.g., resolution and coverage area), and actual field characteristics (e.g., building density and damage distribution) when selecting an appropriate analysis unit.

Intensity, coherence, and polarimetry information of SAR data are all applicable for building damage detection in a block or building unit, with different pros and cons. The intensity difference, correlation coefficient, correlation coefficient difference/ratio, texture features, double-bounce effects, layover, and shadow areas are commonly used to quantify intensity changes and establish relationships with actual damages. The co-event coherence, coherence ratio, and original, normalized, or histogram-matched coherence difference have been explored for target change measurement in coherence-based change detection approaches. The model-based and eigenvalue-eigenvector-based decompositions have both been exploited to derive favorable polarimetry features (e.g., double-bounce scattering, surface scattering, and entropy) for building damage assessments. When available, several types of information or data can be integrated together to compensate for each other, which usually can improve the accuracy of the assessment results.

Intensity information is relatively easy to obtain, as it has no requirement for the SAR acquisition mode. It is relatively stable for minor changes, and therefore is more suitable for the analysis of major damages. Moreover, between intensity difference and correlation coefficient, intensity difference is thought to be more stable to subtle changes (Liu et al., 2013). In intensity-based block-unit approaches, both intensity

decreases and increases may occur in congested building areas. Therefore, it is recommended to add another discriminant line (e.g., Equation 7.6) in the discriminant analysis, or to use the absolute value of intensity difference for parameter construction. For small building damage ratios in less densely built-up areas, the difference/ratio of pre- and co-event correlation coefficient is suggested in order to minimize impacts from signal noises and Earth's surface changes. Matsuoka et al. (2005) analyzed the differences between the *z* value (**Equation 1**), correlation coefficient ratio, and coherence ratio for damage mapping, and demonstrated that the correlation coefficient ratio is suitable for damage detection in situations where the areas and distribution of severely-damaged buildings were rather small. Matsuoka and Yamazaki (2006) indicated that the correlation coefficient difference was also a favorable parameter under similar conditions, in the 2006 Mid Java Earthquake.

Coherence information, which can be acquired when the SAR satellite works in an interferometry mode, is relatively sensitive to small changes, and hence is more suitable for minor damage analysis. Yet, it is also susceptible to vegetation, owing to its sensitivity. Therefore, if possible, built-up areas can be extracted first to reduce the impacts from other land uses and improve the assessment performance. Co-event coherence can be applied to classify building damage conditions when there are only one pre-event and one post-event products. The difference/ratio of pre- and co-event coherence can be calculated to reduce common coherence variations caused by other effects when another pre-event image exists. The histogram-matched coherence difference was thought to have better performance than simple coherence difference, as it can mitigate bulk changes in the two coherence images. The EDV technique was said to be more sensitive to building damages than the damage proxy map generated by the histogram-matched coherence difference, as it applied an additional polarization and more change parameters (Sharma et al., 2017). Liu and Yamazaki (2017) analyzed the intensity parameter *z*-factor (**Equation 8**), co-event coherence, and coherence ratio for building damage assessments in the 2016 Kumamoto Earthquake, and showed that the coherence ratio achieved higher accuracy (60.3%) than z-factor (52.6%) and co-event coherence (58.0%). Arciniegas et al. (2007) explored coherence difference and absolute amplitude change for mapping urban damages caused by the 2003 Bam, Iran Earthquake. The results indicated that

coherence difference led to a higher accuracy (44.5%) than absolute amplitude change (41.2%), and the combination of both resulted in a much higher accuracy (52.3%). In addition, masking out vegetated areas using a pre-event advanced spaceborne thermal emission and reflection radiometer image improved the accuracy by 4%.

There are relatively fewer opportunities to acquire polarimetry data, especially full-polarization data. Moreover, the acquired full-polarization data may have relatively lower resolution. Nevertheless, they can provide rich information for the understanding of scattering mechanisms. Building damages usually lead to a decrease of double-bounce scattering and an increase of surface scattering and/or volume scattering, which can be explored in detail by decomposing the full-polarization data through model-based decomposition. Additionally, the entropy, anisotropy, and average scattering angle (as decomposed from eigenvalue-eigenvector-based decomposition) can be used to measure the scattering disorder degrees, weigh the relative contributions of second and third scattering mechanisms, and distinguish between different scattering types, facilitating the interpretation of scattering mechanism changes. Several other polarimetry parameters, such as polarimetry coherence that can reflect surface roughness, and polarimetry orientation that relates to building orientations, can also provide useful additional information for distinguishing between damaged and undamaged urban areas. In the 2011 Tohoku Earthquake damage analysis, Park et al. (2013) indicated that the mapping accuracy for tsunami-swept urban areas can be improved from 30%–40% to 89%, by applying polarimetry features instead of a conventional single-channel backscattering measurement.

Change detection in a building unit can be carried out either by generalizing the block unit approaches, or by exploring clear individual building features in high-resolution SAR images. When building footprint information can be obtained, the mean values of change detection parameters in the block-unit approaches can be calculated to judge the damage condition of each building. The correlation coefficient, change factor and discriminant score calculated by the intensity difference and correlation coefficient, coherence difference, and texture features have been explored in that way. Miura et al. (2016) compared the correlation coefficient, z factor (**Equation 8**), and discriminant score (**Equation 22**) for building damage

classification in the 2010 Haiti Earthquake. The results showed that the overall accuracies achieved by these three parameters were almost the same (72.3%, 74.2%, and 74.3%), yet the discriminant score could achieve a much higher producer's accuracy for identifying collapsed buildings. Natsuaki et al. (2018) indicated that when applying coherence information for damage detection of individual buildings, the buildings should be larger than a window size of the coherence, and the damage levels should be larger than level-2 in EMS-98 (Grünthal, 1998). Individual building features in the second type of approach mainly refer to the double bounce, layover, and shadow features in SAR intensity images. By analyzing and comparing the characteristic, percentage, or area changes of these features in the pre-event and post-event SAR images, the damage condition of a particular building can be speculated.

3. Assessment Approaches Based on Only Post-event SAR Data

In many cases, especially in undeveloped areas, ideal archived pre-event SAR images are unavailable, rendering the classic change detection approaches infeasible. Therefore, approaches for building damage assessment based on only post-event SAR data have aroused the attention of many scholars. Without desired pre-event images, many commonly-used parameters for damage assessment, such as intensity difference and coherence, cannot be calculated. Therefore, in post-event SAR data-based assessment approaches, exploring new favorable features in one single post-event image for discriminating damaged buildings is a key issue. For one thing, polarimetry features can be potential indicators, as damaged and undamaged structures usually show different characteristics in different decomposition components. For instance, intact parallel buildings are usually characterized by double-bounce scattering, whereas collapsed buildings can be characterized by volume scattering (Zhai and Huang, 2016). For another, texture measures (e.g., entropy and homogeneity) in post-event SAR data also have shown some correlation to damage levels (Dell'Acqua and Polli, 2009; Dell'Acqua et al., 2010b), and can be employed through SAR simulators or machine learning classifiers for building damage assessment (**Table 3**).

Table 3. A summary of the assessment approaches based on only post-event SAR data.

Approaches	Commonly used methods or tools	Commonly used characteristics	Representative studies	Other descriptions
Polarimetry-based analysis	Model-based and eigenvalue-eigenvector-based decomposition	Polarimetry features (entropy, average scattering angle, double bounce scattering, polarization orientation angle, polarization coherence, etc.)	Guo et al. (2010); Li et al. (2012); Zhai and Huang (2016)	Need full-polarization post-event SAR products
Texture-based analysis	SAR simulators	First-order and second-order statistical characteristics (mean, variance, entropy, etc.)	Balz (2006); Balz and Liao (2010); Kuny et al. (2014, 2016)	Apply the texture features of SAR intensity images / only intensity information is enough
	Machine learning classifiers (random forest, support vector machine (SVM), K-nearest neighbor (KNN), etc.)	First-order (mean, variance, skewness, kurtosis, etc.) and second-order texture features (contrast, dissimilarity, homogeneity, mean, variance, correlation, entropy, etc.)	Wu et al. (2016); Gong et al. (2016); Bai et al. (2017b)	
Approaches combing both polarimetry and texture features	Machine learning classifiers (random forest, SVM, KNN, etc.)	Polarimetry features (entropy, anisotropy, total scattering power, cross-polarization ratio, etc.), texture features (first-order textures, second-order textures, speckle divergence, etc.), and color features (hue, saturation, value, and light)	Zhao et al. (2013); Bai et al. (2017a, 2017c)	For dual-polarization or full-polarization products
Deep learning-based approaches	Deep learning (e.g., SqueezeNet network and modified wide residual network)		Bai et al. (2018)	Split images into numerous tiles for training and learning

3.1. Polarimetry-based Analysis

Guo et al. (2010, 2012) and Li et al. (2012) proposed an H-α-ρ approach to extract collapsed buildings in the 2010 Yushu Earthquake, based on post-event polarimetry SAR data. H, α, and ρ indicated the polarimetry features of entropy, average scattering mechanism, and circular polarization correlation coefficient, respectively. In their approach, images of H, α, and ρ were first obtained via polarimetry decomposition, using PolSARpro software. Then the bare soil surface was removed from the ρ image by rational thresholds of H and α values. After that, the spatial distribution of collapsed buildings was extracted through an optimal threshold of the ρ value in the bare surface-removed ρ image. Zhai and Huang (2016) extracted building damages by a single post-event PolSAR image based on the principle that collapsed buildings are characterized by volume scattering, whereas undamaged parallel buildings are characterized by double-bounce scattering. Besides, in order to solve the scattering mechanism ambiguity problem of undamaged buildings in traditional model-based

decomposition, the scheme of polarization orientation angle compensation was applied to enhance the double-bounce scattering, and the difference in relative contribution change rate of scattering components was put forward to strengthen the difference between undamaged and collapsed buildings.

3.2. Texture-based Analysis

SAR simulators can be employed to exploit texture features for building damage assessment, based only on a post-event SAR image. Balz and Liao (2010) detected building damages caused by the 2008 Wenchuan Earthquake using a post-event SAR image and a SAR simulator called SARViz (Balz, 2006), as no suitable archived pre-event SAR images were available for the rather remote damaged areas. Kuny and Schulze (2014) applied simulated SAR textures of modelled debris to detect massive destruction regions in real SAR images. Texture features were analyzed by first-order and second-order statistical characteristics such as mean, variance, and entropy. Later, in order to improve the detection results, they also simulated high vegetation and gravel areas, to rule them out (Kuny et al., 2016).

Machine learning classifiers can also be applied to explore texture features in post-event SAR images for building damage level discrimination. Wu et al. (2016) used a random forest classifier to analyze destroyed buildings, based on two backscattering features (mean and variance of backscattering) and eight texture features (gray-level co-occurrence matrix (GLCM) mean, variance, homogeneity, contrast, dissimilarity, entropy, second moment, and correlation). The results showed that the GLCM second moment and homogeneity, as well as the variance of backscattering, were better features for distinguishing damage types. Gong et al. (2016) explored three machine learning classifiers and twelve statistical features for building damage detection using a sub-meter post-event SAR image and a building footprint map. The three machine learning classifiers were the random forest, support vector machine (SVM), and K-nearest neighbor (KNN). The twelve statistical features included four first-order features (mean, variance, skewness, and kurtosis) and eight second-order features (mean, variance, homogeneity, contrast, dissimilarity, entropy, second moment, and correlation). The results showed that the first-order and second-order statistics derived from the building footprints had a good ability to distinguish between collapsed and

standing buildings. Ge et al. (2019) applied a random forest classifier to distinguish damaged buildings in the 2015 Nepal Earthquake, based on texture features extracted from a post-event SAR image. They indicated that the data range value and standard deviation calculated within the buffered building footprints had favorable capabilities for building damage assessment.

3.3. Combination of Polarimetry and Texture Features

Zhao et al. (2013) proposed a new method combining polarimetry information and texture features in post-event high-resolution airborne PolSAR data for damage assessment. The normalized circular-pol correlation coefficient and GLCM homogeneity were applied as polarimetry and texture features, respectively. Bai et al. (2017b) applied a KNN classifier for damage assessment based on one polarimetry feature and thirty-two texture features derived from a post-event image. The backscattering coefficient of HH polarization was applied as the polarimetry feature. Four statistics derived from the gray-level histogram (data range, variance, skewness, and mean) and twenty-eight statistics obtained from the GLCM (contrast, dissimilarity, homogeneity, mean, variance, correlation, and entropy, calculated at 0°, 45°, 90°, and 135°) were employed as the texture features. They (Bai et al., 2017c) also explored one hundred and two features for building damage assessment, including fifteen polarimetry features, eighty-three texture features, and four color features, through random forest and KNN classifiers. It was demonstrated that the random scattering metric and reflection symmetry metric showed good performance in determining damage types, whereas color information only provided a small amount of complementary information. They (Bai et al., 2017a) also investigated an SVM classifier for exploiting ninety-one features (four polarimetry features, eighty-three texture features, and four color features) in a post-event SAR image for earthquake damage assessment. This study indicated that the texture features derived from cross-polarization intensity showed higher performance in distinguishing building damages, and feature reduction could improve classification accuracy.

In addition, deep learning algorithms, which have become popular again following a significant breakthrough in 2006 (Hinton and Salakhutdinov, 2006), can also assist

in SAR-based building damage assessment. Bai et al. (2018) proposed a deep learning-based framework for tsunami damage mapping using only post-event TerraSAR-X data. Tile-based image split analyses were used to generate a dataset. A selection algorithm with a SqueezeNet network was constructed to classify built-up and unbuilt-up areas. A recognition algorithm with a modified wide residual network was constructed to distinguish different damage levels in the classified built-up areas.

3.4. Summary

Polarimetry and texture features can be explored for building damage assessment when there are only post-event SAR data. For full-polarization SAR products, polarimetry features can be decomposed to distinguish between damaged and undamaged buildings, as intact and collapsed buildings usually show different scattering mechanisms. Polarimetry coherence, double-bounce scattering, and volume scattering have shown favorable performance in damage assessment with the assistance of entropy, average scattering mechanisms, and polarization orientation angles. For single/dual-polarization SAR products, texture features and/or polarimetry features that can be derived from the dual-polarization information can be exploited for damage detection, as undamaged areas usually show regular higher-value and lower-value pixel distribution (bright and shadow areas), whereas damaged areas usually have more random and averaged pixel distribution. The variance (or standard deviation), GLCM second moment, and homogeneity were said to be favorable texture features. Moreover, in the post-event data-based assessment, advanced computer and mathematical technologies can work as powerful tools to make full use of the limited SAR information, and ancillary data can provide more supplementary information for the limited SAR archives.

In addition, it has been said that feature reduction by selecting highly correlated features could improve classification accuracy. Bai et al., (2017a) compared the classification performance of ninety-one features and ten highest-correlated features (selected using Pearson's correlation coefficient) by machine learning classifiers. The results showed that, in the SVM and KNN classifiers, the ten features achieved accuracies of 80.5% and 73.3%, respectively, whereas the ninety-one features led to

accuracies of 70.6% and 62.7%, respectively. Moreover, assessments based on only post-event data may achieve as good results as change detections using both pre- and post-event data. Bai et al., (2017b) quantitatively compared the performance of building damage assessment by polarimetry and texture features calculated through only post-event images and both pre- and post-event SAR images, using the KNN classifier. It was demonstrated that an accuracy of 64.5% was achieved by using only the post-event image, which was 2.3% higher than the accuracy achieved by using both pre- and post-event images (**Figure 7**).

4. Conclusions

As an active RS technology independent of light and weather, SAR has the ability to play a role in crisis management of disasters for promptly identifying damaged buildings and reasonably arranging rescue forces. Multifarious approaches have been proposed for SAR-based building damage assessments in disasters, owing to the various advantages of this technology, together with the development of microwave RS and interpretation techniques. This paper classified these plentiful approaches, and summarized the favorable parameters in each category, according to the pre-event data availability, analysis unit, and applied image features. It aimed to provide a comprehensive and clear understanding of this research field, so as to facilitate ponderation on promising study areas and approach decisions in a specific case. Several conclusions and future efforts can be summarized as follows.

Depending on the data availability and affected areas, various SAR-based approaches have been explored to facilitate building damage assessment after a disaster. Both data conditions and local field situations will influence the approaches that can be applied. The existence of desired pre-event SAR images makes classic change detections feasible. The high-resolution data enables detection approaches in a building unit. The interferometry or polarimetry acquisition mode provides information for coherence- or polarimetry-based analysis. The correlation coefficient difference/ratio showed better performance in identifying small building damage ratios in less densely built-up areas. The coherence degree was said to be more suitable for distinguishing minor damage levels.

Despite the fact that there are substantial approaches, a quantitative comparison and evaluation of them to select an optimum one is challenging, as most of them were designed according to the specific characteristics of applied data and affected areas, and were difficult to be tested with one or more experimental data. Moreover, all approaches have different pros and cons, the optimal solution in one case may not work well in another. There is no absolute optimum approach for all cases. Therefore, for a specific case, if similar cases exist, they can be referred to; if no similar cases exist, it may be a good way to determine the general conditions of applicable methods (e.g., change detection or post-event data-based assessment, block- or building-unit method) first, according to the analysis purpose, image information, and actual field characteristics, and then explore corresponding favorable parameters (e.g., correlation coefficient, coherence difference, and double-bounce scattering) within the determined scope referring to the tables and summary sections in this paper.

When desired pre-event data are available, the intensity difference, correlation coefficient, correlation coefficient difference/ratio, texture features, and proportion of highlighted areas (double bounce and layover) can be calculated to quantify intensity changes. The co-event coherence, coherence ratio, and original, normalized, or histogram-matched coherence difference can be considered for observing coherence changes. The double-bounce scattering, surface scattering, volume scattering, entropy, polarimetry coherence, and polarimetry orientation can be derived from full polarimetry data to analyze scattering mechanism changes. When pre-event SAR data are unavailable, texture features and polarimetry features can be exploited alone or together for identifying damaged areas, depending on the data acquisition mode.

Several future efforts were noted as follows.

The advanced computer and mathematical technologies can work as powerful tools for achieving desired results with limited data archives. The application of these technologies to SAR-based building damage assessment is worth further research, as more innovative, effective, and efficient ways may be generated. For instance, if a training library can be established by the popular deep learning algorithm using existing SAR images, the damage condition of a new disaster can be identified easily and promptly, by simply putting the newly-acquired images into the library.

The integration of different SAR features and different ancillary data is able to provide complementary information for assessment improvement, and is a promising field of exploration. For instance, the combination of intensity and coherence features has been shown to be mutual complementary to each other, and the optical images have been indicated as valuable supplementary information for SAR images.

As compared with the comprehensive studies in block-unit change detection approaches, the post-event data-based approaches and building-unit approaches have not been adequately studied. As archived pre-event SAR images are usually not available in remote undeveloped areas, and higher resolution is the development trend of remote sensing technology, more attention can be paid to the investigation of these two types of approaches.

Time is of vital importance in damage detection and disaster response. The value of damage mapping reduces at an exponential rate following a disaster, and any delay will aggravate the situation. Thus, in order to map damages as soon as possible and save the time for rescue, the more automated the method, the better.

Even though substantial approaches for SAR-based building damage assessment have been developed, field survey remains the main method for many relevant departments. In order to promote these approaches from research to practical application, the validity and reliability of them should be verified more strictly in order to make them trustworthy, and detailed guidance and instructions should be compiled to make them accessible to the general public.

5. References

An, L., Zhang, J., Gong, L., Li, Q. (2016). Integration of SAR image and vulnerability data for building damage degree estimation. Geoscience and Remote Sensing Symposium. IEEE, 4263-4266.

Aoki, H., Matsuoka, M., Yamazaki, F. (1998). Characteristics of satellite SAR images in the damaged areas due to the Hyogoken-Nanbu earthquake. Proceedings of the 19th Asian Conference of Remote Sensing, C7, Asian Association on Remote Sensing, 1–6.

Arciniegas, G. A., Bijker, W., Kerle, N., Tolpekin, V. A. (2007). Coherence- and amplitude-based analysis of seismogenic damage in Bam, Iran, using ENVISAT ASAR data. IEEE Transactions on Geoscience & Remote Sensing, 45(6), 1571-1581. DOI: 10.1109/TGRS.2006.883149

Bai, Y., Adriano, B., Mas, E., Gokon, H., Koshimura, S. (2017c). Object-based building damage assessment methodology using only post event ALOS-2/PALSAR-2 dual polarimetric SAR intensity images. Journal of Disaster Research, 12(2), 259-271.

Bai, Y., Adriano, B., Mas, E., Koshimura, S. (2017a). Building damage assessment in the 2015 Gorkha, Nepal, earthquake using only post-event dual polarization synthetic aperture radar imagery. Earthquake Spectra, 33(S1), S185-S195.

Bai, Y., Adriano, B., Mas, E., Koshimura, S. (2017b). Machine learning based building damage mapping from the ALOS-2/PALSAR-2 SAR imagery: case study of 2016 Kumamoto earthquake. Journal of Disaster Research 12(sp), 646-655.

Bai, Y., Gao, C., Singh, S., Koch, M., Adriano, B., Mas., E Koshimura, S. (2018). A framework of rapid regional tsunami damage recognition from post-event TerraSAR-X imagery using deep neural networks. IEEE Geoscience and Remote Sensing Letters, 15(1), 43-47.

Balz, T. (2006). Real time SAR simulation on graphics processing units. In 6th European Conference on SAR, EUSAR 2006, Dresden, Germany.

Balz, T., Liao, M. (2010). Building-damage detection using post-seismic high-resolution SAR satellite data. International Journal of Remote Sensing, 31(13), 3369-3391. DOI: 10.1080/01431161003727671

Barboux, C., Strozzi, T., Delaloye, R., Wegmüller, U., Collet, C. (2015). Mapping slope movements in Alpine environments using TerraSAR-X interferometric methods. ISPRS Journal of Photogrammetry & Remote Sensing, 109, 178-192.

Boerner, W. M. (2003). Recent advances in extra-wide-band polarimetry, interferometry and polarimetric interferometry in synthetic aperture remote

sensing and its applications. IEEE Proceedings-Radar, Sonar and Navigation, 150(3), 113-124.

Brett, P. T. B. (2013). Urban damage detection in high resolution amplitude images. University of Surrey, Surrey Space Centre.

Brett, P. T. B., Guida, R. (2013). Earthquake damage detection in urban areas using curvilinear features. IEEE Transactions on Geoscience and Remote Sensing, 51(9), 4877-4884.

Brunner, D., Lemoine, G., Bruzzone, L. (2010). Earthquake damage assessment of buildings using VHR optical and SAR imagery. IEEE Transactions on Geoscience and Remote Sensing, 48(5), 2403-2420.

Chen, L., Shen, X., Hong, S., Shao, Y. (2011). Estimation of the building damages in Yushu earthquake based on ALOS SAR data. International Symposium on Multispectral Image Processing & Pattern Recognition, Proceedings of SPIE - International Society for Optics and Photonics. 8006(1), 420-430.

Chen, S. W., Li, Y. Z., Wang, X. S., Xiao, S. P., Sato, M. (2014a). Modeling and interpretation of scattering mechanisms in polarimetric synthetic aperture radar: advances and perspectives. IEEE Signal Processing Magazine, 31(4), 79-89.

Chen, S. W., Ohki, M., Shimada, M., Sato, M. (2013). Deorientation effect investigation for model-based decomposition over oriented built-up areas. IEEE Geoscience and Remote Sensing Letters, 10(2), 273-277. DOI:10.1109/LGRS.2012.2203577

Chen, S. W., Sato, M. (2013). Tsunami damage investigation of built-up areas using multitemporal spaceborne full polarimetric SAR images. IEEE Transactions on Geoscience and Remote Sensing, 51(4), 1985-1997. DOI: 10.1109/TGRS.2012.2210050

Chen, S. W., Wang, X. S., Li, Y. Z., Sato, M. (2014b). Adaptive model-based polarimetric decomposition using PolInSAR coherence. IEEE Transactions on Geoscience and Remote Sensing, 52(3), 1705-1718.

Chen, S. W., Wang, X. S., Sato, M. (2016). Urban damage level mapping based on scattering mechanism investigation using fully polarimetric SAR data for the 3.11

east japan earthquake. IEEE Transactions on Geoscience and Remote Sensing, 54(12), 6919-6929. DOI: 10.1109/TGRS.2016.2588325

Chen, S. W., Wang, X. S., Xiao, S. P., Sato, M. (2014c). General polarimetric model-based decomposition for coherency matrix. IEEE Transactions on Geoscience and Remote Sensing, 52(3):1843–1855. DOI:10.1109/TGRS.2013.2255615

Chini, M., Anniballe, R., Bignami, C., Pierdicca, N, Mori, S., Stramondo, S. (2015). Identification of building double-bounces feature in very high resolution SAR data for earthquake damage mapping. IEEE International Geoscience and Remote Sensing Symposium (IGARSS), 2723-2726. DOI: 10.1109/IGARSS.2015.7326376

Chini, M., Pierdicca, N., Emery, W. J. (2009). Exploiting SAR and VHR optical images to quantify damage caused by the 2003 Bam earthquake. IEEE Transactions on Geoscience and Remote Sensing, 47(1), 145-152. DOI: 10.1109/TGRS.2008.2002695

Cloude, S. R., Pottier, E. (1996). A review of target decomposition theorems in radar polarimetry. IEEE Transactions on Geoscience and Remote Sensing, 34(2), 498-518.

Cloude, S. R., Pottier, E. (1997). An entropy based classification scheme for land applications of polarimetric SAR. IEEE Transactions on Geoscience and Remote Sensing, 35(1), 68-78.

Coltuc, D., Bolon, P., Chassery, J. M. (2006). Exact histogram specification. IEEE Transactions on Image Processing, 15(5), 1143-1152. DOI: 10.1109/TIP.2005.864170

Cui, L., Wang, X, Dou, A, Ding, X. (2018). High resolution SAR imaging employing geometric features for extracting seismic damage of buildings. The International Archives of the Photogrammetry, Remote Sensing and Spatial Information Sciences XLII-3, 239-244.

Dell'Acqua, F., Bignami, C., Chini, M., Lisini, G., Polli, D., Stramondo, S. (2011). Earthquake rapid mapping by satellite remote sensing data: L'Aquila April 6th,

2009 event. IEEE Journal of Selected Topics in Applied Earth Observations & Remote Sensing, 4(4), 935-943.

Dell'Acqua, F., Gamba, P., Polli, D. (2010). Mapping earthquake damage in VHR radar images of human settlements: Preliminary results on the 6 TH April 2009, Italy case. 2010 IEEE International Geoscience and Remote Sensing Symposium (IGARSS), 1347–1350.

Dell'Acqua, F., Polli, D. (2010). Radar remote sensing for damage assessment: case study on L'Aquila, Italy, 6th April 2009 earthquake. 2009 International Symposium on Geo-information for Disaster Management (Gi4DM), Turin, Italy.

Dell'Acqua, F., Polli, D., Lisini, G. (2010). Automatic mapping of earthquake damage using post-event radar satellite data: the story goes on. Proceedings of the 30th EARSeL Symposium, Paris, France.

Dickinson, C., Siqueira, P., Clewley, D., Lucas, R. M. (2013). Classification of forest composition using polarimetric decomposition in multiple landscapes. Remote Sensing of Environment, 131(131), 206-214.

Dong, L., Shan, J. (2013). A comprehensive review of earthquake-induced building damage detection with remote sensing techniques. ISPRS Journal of Photogrammetry and Remote Sensing, 84, 85-99.

Elachi, C., Zyl, J. V. (2006). Introduction to the physics and techniques of remote sensing. JOHN WILEY & SONS, INC.

Fan, J., Zhang, C., Zhang, J. (2001). Generalized likelihood ratio statistics and Wilks phenomenon. The Annals of Statistics, 29(1), 153-193.

Fielding, E. J., Talebian, M., Rosen, P. A., Nazari, H., Jackson, J. A., Ghorashi, M., Walker, R. (2005). Surface ruptures and building damage of the 2003 Bam, Iran, earthquake mapped by satellite synthetic aperture radar interferometric correlation. Journal of Geophysical Research, 110(B3), B03302.

Franceschetti, G., Guida, R., Iodice, A., Riccio, D., Ruello, G., Stilla, U. (2007). Building feature extraction via a deterministic approach: application to real high resolution SAR images. Proceedings of the International Geoscience and Remote

Sensing Symposium, Barcelona, Spain, 2681-2684. DOI: 10.1109/IGARSS.2007.4423395

Franceschetti, G., Lanari, R. (2016). Synthetic Aperture Radar Processing, Second Edition. CRC Press, Inc.

Freeman, A., Durden, S. L. (1998). A three-component scattering model for polarimetric SAR data. IEEE Transactions on Geoscience and Remote Sensing, 36(3), 963-973.

Fruneau, B., Achache, J., Delacourt, C. (1996). Observation and modelling of the Saint-Étienne-de-Tinée landslide using SAR interferometry. Tectonophysics, 265(3-4), 181-190.

Gamba, P., Dell''Acqua, F., Trianni, G. (2007). Rapid damage detection in the Bam area using multitemporal SAR and exploiting ancillary data. IEEE Transactions on Geoscience and Remote Sensing, 45(6), 1582-1589. DOI: 10.1109/TGRS.2006.885392

Ge, P., Gokon, H., Meguro, K. (2019). Building damage assessment using intensity SAR data with different incidence angles and longtime interval. Journal of Disaster Research, 14(3), 456-465.

Gokon, H., Koshimura, S., Meguro, K. (2017a). Verification of a method for estimating building damage in extensive tsunami affected areas using L-band SAR data. Journal of Disaster Research, 12(2), 251-258.

Gokon, H., Koshimura, S., Meguro, K. (2017b). Towards a damage assessment in a tsunami affected area using L-band and X-band SAR data. 2017 Joint Urban Remote Sensing Event (JURSE), Dubai, United Arab Emirates. DOI: 10.1109/JURSE.2017.7924633

Gokon, H., Post, J., Stein, E., Martinis, S., Matsuoka, M. (2015). A method for detecting buildings destroyed by the 2011 Tohoku earthquake and tsunami using multitemporal TerraSAR-X data. IEEE Geoscience and Remote Sensing Letters, 12(6), 1277-1281.

Gong, L., Wang, C., Wu, F., Zhang, J., Zhang, H., Li, Q. (2016). Earthquake-induced building damage detection with post-event sub-meter VHR TerraSAR-X staring spotlight imagery. Remote Sensing, 8(11), 887.

Graham, L. C. (1974). Synthetic interferometer radar for topographic mapping. Proceedings of the IEEE, 62(6), 763-768.

Grünthal, G. (1998). European Macroseismic Scale 1998 (EMS-98). Centre Europèen de Géodynamique et de Séismologie, Luxembourg.

Guida, R., Iodice, A., Riccio, D. (2010a). Assessment of TerraSAR-X products with a new feature extraction application: monitoring of cylindrical tanks. IEEE Transactions on Geoscience and Remote Sensing, 48(2), 930-938. DOI: 10.1109/tgrs.2009.2029233

Guida, R., Iodice, A., Riccio, D. (2010b). Monitoring of collapsed built-up areas with high resolution SAR images. Geoscience & Remote Sensing Symposium, Honolulu, HI, USA. DOI: 10.1109/IGARSS.2010.5650083

Guida, R., Iodice, A., Riccio, D. (2011). An application of the deterministic feature extraction approach to COSMO-SKyMed data. European Conference on Synthetic Aperture Radar, Aachen, Germany. DOI: 10.1103/PhysRevA.92.032113

Guida, R., Iodice, A., Riccio, D., Stilla, U. (2008). Model-based interpretation of high-resolution SAR images of buildings. IEEE Journal of Selected Topics in Applied Earth Observations and Remote Sensing, 1(2), 107-119. DOI: 10.1109/jstars.2008.2001155

Guo, H., Liu, L., Fan, X., Li, X., Zhang, L. (2012) Earth observation for earthquake disaster monitoring and assessment. Earthquake research and analysis-statistical studies, observations and planning. INTECH Open Access Publisher, Croatia, 293–312. DOI: 10.5772/28055

Guo, H., Wang, X, Li, X., Liu, G., Zhang, L., Yan, S. (2010). Yushu earthquake synergic analysis using multimodal SAR datasets. Chinese Science Bulletin, 55(31), 3499-3503. DOI: 10.1007/s11434-010-4078-3

Hanssen, R.F. (2001). Radar interferometry: data interpretation and error analysis. R.F. Hanssen.

Hinton, G.E., Salakhutdinov, R. R. (2006). Reducing the dimensionality of data with neural networks. Science, 313(5786), 504-507.

Hoffmann, J. (2007). Mapping damage during the Bam (Iran) earthquake using interferometric coherence. International Journal of Remote Sensing, 28(6), 1199-1216.

Huang, L., Li, Z., Tian, B. S., Chen, Q., Liu, J. L., Zhang, R. (2011). Classification and snow line detection for glacial areas using the polarimetric SAR image. Remote Sensing of Environment, 115(7), 1721-1732.

Huynen, J. R. (1970). Phenomenological theory of radar targets. Ph.D. Dissertation, Delft University of Technology, The Netherlands.

Iribe, K., Sato, M. (2007). Analysis of polarization orientation angle shifts by artificial structures. IEEE Transactions on Geoscience and Remote Sensing, 45(11), 3417-3425.DOI:10.1109/TGRS.2007.905973

Ito, Y., Hosokawa, M. (2002). Damage estimation model using temporal coherence ratio. IEEE International Geoscience & Remote Sensing Symposium (IGARSS), Toronto, Canada, 2859–2861.

Ito, Y., Hosokawa, M., Lee, H., Liu, J. (2000). Extraction of damaged regions using SAR data and neural networks. Proc. 19th ISPRS Congr., Amsterdam, The Netherlands, 33, 156–163.

Ito, Y., Hosokawa, M., Matsuoka, M. (2003). A degree estimation model of earthquake damage using temporal coherence ratio. IEEE International Geoscience & Remote Sensing Symposium (IGARSS), Toulouse, France, 2410–2412.

Joyce, K. E., Belliss, S. E., Samsonov, S. V., Mcneill, S. J., Glassey, P. J. (2009b). A review of the status of satellite remote sensing and image processing techniques for mapping natural hazards and disasters. Progress in Physical Geography, 33(2), 183-207.

Karimzadeh, S., Feizizadeh, B., Matsuoka, M. (2017). From a GIS-based hybrid site condition map to an earthquake damage assessment in Iran: methods and trends. International Journal of Disaster Risk Reduction, 22, 23-36.

Karimzadeh, S., Mastuoka, M. (2017). Building damage assessment using multisensor dual-polarized synthetic aperture radar data for the 2016 M6.2 Amatrice earthquake, Italy. Remote Sensing, 9(4), 330.

Karimzadeh, S., Matsuoka, M. (2018). Building damage characterization for the 2016 Amatrice earthquake using ascending–descending COSMO-SkyMed data and topographic position index. IEEE Journal of Selected Topics in Applied Earth Observations & Remote Sensing, 11(8), 2668-2682.

Karimzadeh, S., Miyajima, M., Hassanzadeh, R., Amiraslanzadeh, R., Kamel, B. (2014). A GIS-based seismic hazard, building vulnerability and human loss assessment for the earthquake scenario in Tabriz. Soil Dynamics and Earthquake Engineering, 66, 263-280.

Kimura, H., Papathanassiou, K., Hajnsek, I. (2005). Polarization orientation effects in urban areas on SAR data. IEEE International Geoscience & Remote Sensing Symposium (IGARSS), Seoul, Korea, 7, 4863–4867. DOI:10.1109/IGARSS.2005.1526763

Konishi, T., Suga, Y. (2018). Landslide detection using COSMO-SkyMed images: a case study of a landslide event on Kii Peninsula, Japan. European Journal of Remote Sensing, 51(1), 205-221.

Kuny, S., Hammer, H., Schulz, K. (2016). Assessing the suitability of simulated SAR signatures of debris for the usage in damage detection. ISPRS-International Archives of the Photogrammetry, Remote Sensing and Spatial Information Sciences, XLI-B3, 877-881. DOI: 10.5194/isprs-archives-XLI-B3-877-2016

Kuny, S., Schulz, K. (2014). Debris detection in SAR imagery using statistics of simulated texture. 8th Workshop on Pattern Recognition in Remote Sensing PRRS, Stockholm, Sweden. DOI: 10.1109/PRRS.2014. 6914289

Lanari, R., Fornaro, G., Riccio, D., Migliaccio, M., Coltelli, M. (1996). Generation of digital elevation models by using SIR-C/X-SAR multifrequency two-pass

interferometry: the Etna case study. IEEE Transactions on Geoscience and Remote Sensing, 34(5), 1097-1114.

Lazecký, M., Çomut, F. C., Hlaváčová, I., Gürboğa, Ş. (2015). Practical application of satellite-based SAR interferometry for the detection of landslide activity. Procedia Earth and Planetary Science, 15, 613-618.

Lee, J. S., Ainsworth, T. L. (2011). The effect of orientation angle compensation on coherency matrix and polarimetric target decompositions. IEEE Transactions on Geoscience and Remote Sensing, 49(1), 53-64. DOI:10.1109/TGRS.2010.2048333

Lee, J. S., Schuler, D. L., Ainsworth, T. L., Krogager, E., Kasilingam, D., Boerner, W. M. (2002). On the estimation of radar polarization orientation shifts induced by terrain slopes. IEEE Transactions on Geoscience and Remote Sensing, 40(1), 30-41. DOI: 10.1109/36.981347

Li, X., Guo, H., Zhang, L., Chen, X., Liang, L. (2012). A new approach to collapsed building extraction using radarsat-2 polarimetric SAR imagery. IEEE Geoscience and Remote Sensing Letters, 9(4), 677-681. DOI: 10.1109/LGRS.2011.2178392

Liu, W., Yamazaki, F. (2011). Urban change monitoring from multi-temporal TerraSAR-X images. In: Stilla U, Gamba P, Juergens C, Maktav D (Eds) JURSE 2011 - Joint Urban Remote Sensing Event --- Munich, Germany, April 11-13.

Liu, W., Yamazaki, F. (2017). Extraction of collapsed buildings in the 2016 Kumamoto earthquake using multi-temporal PALSAR-2 Data. Journal of Disaster Research, 12 (2).

Liu, W., Yamazaki, F., Gokon, H., Koshimura, S. (2012). Extraction of damaged buildings due to the 2011 Tohoku, Japan earthquake tsunami. IEEE International Geoscience and Remote Sensing Symposium (IGARSS), 4038-4041. DOI: 10.1109/IGARSS.2012.6350523

Liu, W., Yamazaki, F., Gokon, H., Koshimura, S. (2013). Extraction of tsunami-flooded areas and damaged buildings in the 2011 Tohoku-Oki earthquake from TerraSAR-X intensity images. Earthquake Spectra, 28(S1), S183–S200.

Massonnet, D., Rossi, M., Carmona, C., Adragna, F., Peltzer, G., Feigl, K., Rabaute, T. (1993). The displacement field of the Landers earthquake mapped by radar interferometry. Natural, 364, 138–142.

Matsuoka, M., Estrada, M. (2013). Development of earthquake-induced building damage estimation model based on ALOS/PALSAR observing the 2007 Peru earthquake. Journal of Disaster Research, 8(2), 346–355.

Matsuoka, M., Horie, K., Ohkura, H., Yamazaki, F. (2005). Characteristics of remote sensing images for the 2004 Niigata-ken Chuetsu earthquake. Third International Workshop on Remote Sensing for Post-Disaster Response, Chiba, Japan.

Matsuoka, M., Koshimura, S., Nojima, N. (2010). Estimation of building damage ratio due to earthquakes and tsunamis using satellite SAR imagery. IEEE International Geoscience & Remote Sensing Symposium, IGARSS 2010, July 25-30, 2010, Honolulu, Hawaii, USA.

Matsuoka, M., Nojima, N. (2010). Building damage estimation by integration of seismic intensity information and satellite L-band SAR imagery. Remote Sensing, 2(9), 2111-2126.

Matsuoka, M., Yamazaki, F. (1999). Characteristics of satellite images of damaged areas due to the 1995 Kobe earthquake. Proc. of 2nd Conference on the Applications of Remote Sensing and GIS for Disaster Management, The George Washington University.

Matsuoka, M., Yamazaki, F. (2000). Use of interferometric satellite SAR for earthquake damage detection. Sat, 2, z1.

Matsuoka, M., Yamazaki, F. (2004a). Use of satellite SAR intensity imagery for detecting building areas damaged due to earthquakes. Earthquake Spectra, 20(3), 975-994.

Matsuoka, M., Yamazaki, F. (2004b). Damage detection for the 2003 Algeria earthquake using SAR intensity images. Processing of 1st Asia Conference on Earthquake Engineering.

Matsuoka, M., Yamazaki, F. (2005). Building damage mapping of the 2003 Bam, Iran, earthquake using Envisat/ASAR intensity imagery. Earthquake Spectra, 21(S1), 285-294.

Matsuoka, M., Yamazaki, F. (2006). Use of SAR imagery for monitoring areas damaged due to the 2006 Mid Java, Indonesia earthquake. Proceedings of 4th International workshop on Remote Sensing for Post-Disaster Response, Cambridge, United Kingdom.

Matsuoka, M., Yamazaki, F. (2010). Comparative analysis for detecting areas with building damage from several destructive earthquakes using satellite synthetic aperture radar images. Journal of Applied Remote Sensing, 4(1), 041867.

Mattia, F., Toan, T. L., Souyris, J. C., Carolis, G. D., Floury, N., Posa, F., Pasquariello, G. (1997). The effect of surface roughness on multifrequency polarimetric SAR data. IEEE Transactions on Geoscience and Remote Sensing, 35(4), 954–965. DOI: 10.1109/36.602537

Milisavljevic, N., Closson, D., Holecz, F., Collivignarelli, F., Pasquali, P. (2015). An approach for detecting changes related to natural disasters using synthetic aperture radar data. International Archives of the Photogrammetry Remote Sensing & S, XL-7/W3(7), 819-826.

Miura, H., Midorikawa, S., Matsuoka, M. (2016). Building damage assessment using high-resolution satellite SAR images of the 2010 Haiti earthquake. Earthquake Spectra, 32(1), 591-610.

Monserrat, O., Crosetto, M., Luzi, G. (2014). A review of ground-based SAR interferometry for deformation measurement. ISPRS Journal of Photogrammetry and Remote Sensing, 93(7), 40-48.

Moreira, A., Prats-Iraola, P., Younis, M., Krieger, G., Papathanassiou, K. P. (2013). A tutorial on synthetic aperture radar. IEEE Geoscience and Remote Sensing Magazine, 1(1), 6-43.

Nakmuenwai, P., Yamazaki, F., Liu, W. (2016). Multi-temporal correlation method for damage assessment of buildings from high-resolution SAR images of the 2013 Typhoon Haiyan. Journal of Disaster Research, 11(3), 577–592.

Natsuaki, R., Nagai, H., Tomii, N., Tadono, T. (2018). Sensitivity and limitation in damage detection for individual buildings using InSAR coherence—a case study in 2016 Kumamoto earthquakes. Remote Sensing, 10(2), 245.

Neelmeijer, J., Motagh, M., Bookhagen, B. (2017). High-resolution digital elevation models from single-pass TanDEM-X interferometry over mountainous regions: A case study of Inylchek Glacier, Central Asia. ISPRS Journal of Photogrammetry and Remote Sensing, 130, 108-121.

Oxoli, D., Boccardo, P., Brovelli, M. A., Molinari, M. E., Guarnieri, A. M. (2018). Coherent change detecting for repeated-pass interferometric SAR images: an application to earthquake damage assessment on buildings, The International Archives of the Photogrammetry, Remote Sensing and Spatial Information Sciences, Istanbul, Turkey, XLII-3/W4, 383-388.

Park, S. E., Yamaguchi, Y., Kim, D. J. (2013). Polarimetric SAR remote sensing of the 2011 Tohoku earthquake using ALOS/PALSAR. Remote Sensing of Environment, 132(6), 212-220.

Plank, S. (2014). Rapid damage assessment by means of multi-temporal SAR — a comprehensive review and outlook to sentinel-1. Remote Sensing, 6(6), 4870-4906. DOI: 10.3390/rs6064870

Ram, S., Ryutaro, T., Keitarou, H., Hoan, N., Saeid, G., Luong, N. (2017). Earthquake damage visualization (EDV) technique for the rapid detection of earthquake-induced damages using SAR data. Sensors, 17(2), 235-246.

Rogers, A. E. E., Ingalls, R. P. (1969). Venus: mapping the surface reflectivity by radar interferometry. Science, 165 (3895),797-799. DOI: 10.1126/science.165.3895.797

Rosen, P. A., Hensley, S., Joughin, I. R., Li, F. K., Madsen, S. N., Rodriguez, E., et al. (2000). Synthetic aperture radar interferometry. Proceedings of the IEEE, 88(3), 333-382.

Sato, M., Chen, S. W., Satake, M. (2012). Polarimetric SAR analysis of tsunami damage following the March 11, 2011 east japan earthquake. Proceedings of the IEEE, 100(10), 2861-2875. DOI: 10.1109/JPROC.2012.2200649

Sharma R. C., Tateishi R., Hara K., Nguyen, H. T., Gharechelou, S., Nguyen, L. V. (2017). Earthquake damage visualization (EDV) technique for the rapid detection of earthquake-induced damages using SAR data. Sensors, 17(2), 235.

Shi, L., Sun, W., Yang, J., Li, P., Lu, L. (2015). Building collapse assessment by the use of postearthquake Chinese VHR airborne SAR. IEEE Geoscience and Remote Sensing Letters, 12(10), 2021-2025.

Simonetto, E., Oriot, H., Garello, R. (2003). Radargrammetric processing for 3-D building extraction from high-resolution airborne SAR data. Proceedings of IGARSS, Toulouse, France. 780–782.

Simonetto, E., Oriot, H., Garello, R. (2005). Rectangular building extraction from stereoscopic airborne radar images. IEEE Transactions on Geoscience and Remote Sensing, 43(10), 2386-2395.

Sinclair, G. (1950). The transmission and reception of elliptically polarized waves. Proceedings of the IRE, 38(2), 148-151.

Singh, G., Yamaguchi, Y., Boerner, W. M., Park, S. E. (2013). Monitoring of the March 11, 2011, off-Tohoku 9.0 earthquake with super-tsunami disaster by implementing fully polarimetric high-resolution POLSAR techniques. Proceedings of the IEEE, 101(3), 831-846.

Stilla, U., Soergel, U., Thoennessen, U., Brenner, A. (2005). Potential and limit for reconstruction of buildings from high resolution SAR data of urban areas.

Stramondo, S., Arturi, A., Del Frate, F. (2007). Digital elevation model generation of the Alban hills area from SAR interferometry technique. Molecular Biology & Evolution, 24(11), 2535-2545.

Stramondo, S., Bignami, C., Chini, M., Pierdicca, N., Tertulliani, A. (2006). Satellite radar and optical remote sensing for earthquake damage detection: results from different case studies. International Journal of Remote Sensing, 27(20), 4433-4447. DOI: 10.1080/01431160600675895

Strozzi, T., Klimeš, J., Frey, H., Caduff, R., Huggel, C., Wegmüller, U., Rapre, A. C. (2018). Satellite SAR interferometry for the improved assessment of the state of

activity of landslides: a case study from the cordilleras of Peru. Remote Sensing of Environment, 217, 111-125.

Tamkuan, N., Nagai, M. (2017). Fusion of multi-temporal interferometric coherence and optical image data for the 2016 Kumamoto earthquake damage assessment. SPRS International Journal of Geo-Information, 6(7), 188.

Trianni, G., Lisini, G., dell'Acqua, F., Gamba, P. (2010). Fusion of GIS and statistical features of satellite SAR images for earthquake damage mapping at the block scale. In Machine Interpretation of Patterns, Image Analysis and Data Mining, Singapore, 195–206.

Uprety, P., Yamazaki, F. (2012). Building damage detection using SAR images in the 2010 Haiti earthquake. 15th World Conference on Earthquake Engineering 2012, Lisbon, Portugal.

Uprety, P., Yamazaki, F., Dell'Acqua, F. (2013). Damage Detection Using High-Resolution SAR Imagery in the 2009 L'Aquila, Italy, Earthquake. Earthquake Spectra, 29(4), 1521-1535.

Wang, H., Jin, Y. Q. (2009). Statistical analysis to assess building damage in 2008 Wechuan earthquake from multi-temporal SAR Images. 2009 2nd Asian-Pacific Conference on Synthetic Aperture Radar, Shanxi, China.

Wang, T. L., Jin, Y. Q. (2012). Post-earthquake building damage assessment using multi-mutual information from pre-event optical image and post-event SAR image. IEEE Geoscience and Remote Sensing Letters, 9(3), 452-456. DOI: 10.1109/lgrs.2011.2170657

Watanabe, M., Motohka, T., Miyagi, Y., Yonezawa, C., Shimada, M. (2012). Analysis of urban areas affected by the 2011 off the pacific coast of Tohoku earthquake and tsunami with L-band SAR full-polarimetric mode. IEEE Geoscience and Remote Sensing Letters, 9(3), 472-476. DOI: 10.1109/LGRS.2011.2182030

Watanabe, M., Thapa, R. B., Ohsumi, T., Fujiwara, H., Yonezawa, C., Tomii, N., et al. (2016). Detection of damaged urban areas using interferometric SAR coherence change with PALSAR-2. Earth, Planets and Space, 68(1), 131.

Wu, F., Gong, L., Wang, C., Zhang, H., Zhang, B., Xie, L. (2016). Signature analysis of building damage with TerraSAR-X new staring spotlight mode data. IEEE Geoscience and Remote Sensing Letters, 13(11), 1696-1700.

Xie, S., Duan, J., Liu, S., Dai, Q., Liu, W., Ma, Y., et al. (2016). Crowdsourcing rapid assessment of collapsed buildings early after the earthquake based on aerial remote sensing image: a case study of Yushu earthquake. Remote Sensing, 8(9), 759-774.

Yamaguchi, Y. (2012). Disaster monitoring by fully polarimetric SAR data acquired with ALOS-PALSAR. Proceedings of the IEEE, 100(10), 2851-2860.

Yamaguchi, Y., Moriyama, T., Ishido, M., Yamada, H. (2005). Four-component scattering model for polarimetric SAR image decomposition. IEEE Transactions on Geoscience and Remote Sensing, 43(8), 1699 – 1706.

Yamaguchi, Y., Sato, A., Boerner, W. M., Sato, R., Yamada, H. (2011). Four component scattering power decomposition with rotation of coherency matrix. IEEE Trans. IEEE Geoscience and Remote Sensing Letters, 49(6), 2251-2258.

Yamaguchi, Y., Yajima, Y., Yamada, H. (2006). A four-component decomposition of POLSAR images based on the coherency matrix. IEEE Geoscience and Remote Sensing Letters, 3(3), 292-296.

Yamazaki, F., Matsuoka, M. (2007). Remote sensing technologies in post-disaster damage assessment. Journal of Earthquake and Tsunami, 01(03), 193-210.

Yonezawa, C., Takeuchi, S. (2001). Decorrelation of SAR data by urban damages caused by the 1995 Hyogoken-nanbu earthquake. International Journal of Remote Sensing, 22(8), 1585-1600.

Yun, S. H., Fielding, E. J., Simons, M., Agram, P., Rosen, P., Owen, S., Webb, F. H. (2011). Damage proxy map of February M6.3 Christchurch earthquake using InSAR coherence. Fringe Workshop “Advances in the science and applications of SAR interferometry from ESA and 3rd party missions”, Frascati, Italy, https://earth.esa.int/documents/10174/1567329/Yun_FRINGE2011.pdf.

Yun, S. H., Fielding, E., Webb, F., Simons, M. (2015a). Damage proxy map from interferometric synthetic aperture radar coherence. Patent US9, 207, 318, B2, Dec. 8, 2015.

Yun, S. H., Hudnut, K., Owen, S., Webb, F., Simons, M. Sacco, P., Gurrola, E., Manipon, G., Liang, C., Fielding, E., et al. (2015b). Rapid damage mapping for the 2015 Mw 7.8 Gorkha earthquake using synthetic aperture radar data from COSMO–SkyMed and ALOS-2 Satellites. Seismological Research Letters, 86(6), 1549–1556.

Zebker, H. A., Villasenor, J. (1992). Decorrelation in interferometric radar echoes. IEEE Transactions on Geoscience and Remote Sensing, 30, 950–959.

Zhai, W., Huang, C. (2016). Fast building damage mapping using a single post-earthquake PolSAR image: a case study of the 2010 Yushu earthquake. Earth, Planets and Space, 68(1), 86. DOI: 10.1186/s40623-016-0469-2

Zhang, B., Wang, R., Deng, Y., Ma, P., Lin, H., Wang, J. (2019). Mapping the Yellow River Delta land subsidence with multitemporal SAR interferometry by exploiting both persistent and distributed scatterers. ISPRS Journal of Photogrammetry & Remote Sensing, 148, 157-173.

Zhang, X., Liu, W., He S. (2018). Urban change detection in TerraSAR image using the difference method and SAR coherence coefficient. Journal of Engineering Science and Technology Review, 11(3), 18-23. DOI: 10.25103/jestr.113.03

Zhao, C., Liu, C., Zhang, Q., Lu, Z., Yang, C. (2018). Deformation of Linfen-Yuncheng basin (china) and its mechanisms revealed by Π-rate InSAR technique. Remote Sensing of Environment, 218, 221-230.

Zhao, C., Lu, Z., Zhang, Q., Fuente, J. D. L. (2012). Large-area landslide detection and monitoring with ALOS/PALSAR imagery data over northern California and southern Oregon, USA. Remote Sensing of Environment, 124(9), 348–359.

Zhao, L., Yang, J., Li, P., Zhang, L., Shi, L., Lang, F. (2013). Damage assessment in urban areas using post-earthquake airborne PolSAR imagery. International Journal of Remote Sensing, 34(24), 8952-8966.